Thermal Modelling and Control of High Pressure Turbine Subsystems

Andrew van Paridon
St Catherine's College
University of Oxford

A thesis submitted for the degree of
Doctor of Philosophy

Hillary 2016

Dedicated to my parents

“We’ll soon design the bloody simplicity out of it”

- Lord Hives, director of Rolls-Royce, in response to Whittle’s jet engine design

“If we knew what it was we were doing, it would not be called ‘research’, would it?”

- Albert Einstein

“We choose to go to the moon in this decade and do the other things, not because they are easy, but because they are hard, because that goal will serve to organize and measure the best of our energies and skills, because that challenge is one that we are willing to accept, one we are unwilling to postpone, and one which we intend to win”

- President John F. Kennedy on the Apollo Program

Acknowledgements

Firstly, I would like to thank my supervisors Marko Bacic and Peter Ireland for their incredible support and guidance throughout my postgraduate tenure. Their belief and enthusiasm for the project has been an inspiration. I can not thank them enough for the opportunity to come to Oxford and be part of this department and University. I would also like to thank Andrew Dann, who took over the construction and commissioning of the Transient Heat Transfer Facility, for his support. His experience, feedback, and good humour have been invaluable.

Thanks goes to Paul Cox, Bill Godfrey, Hal Surtell, and Trevor Godfrey for their ideas and tireless effort in putting the rig together. Lots of appreciation goes to Rolls-Royce for funding the project. Specifically, I would like to thank Leo Lewis for project inspiration and guidance, and Chris Barnes and Carlo Ciccomascolo for all of their SC03 support.

A special thanks to Inés Usandizaga, not just for helping me vent in times of crises, but also for taking so many phone calls on my behalf when the project was getting underway. A special thanks also goes to Nathan Donaldson who saved me weeks of headaches trying to learn Veristand towards the end. Il Principe delicatessen gets a special mention for providing me with so many pizzas - saving my sanity, and to PhDComics for reassuring me that losing my sanity was just a natural part of the process.

To my wonderful girlfriend Daniela, who has been the greatest joy in my life, thank you for being there when I needed you most. Most of all, thanks to Mum and Dad for all the love you have given me, and for supporting me through all my academic pursuits all over the world. You have been my greatest champions.

Abstract

The control and monitoring of aircraft engine subsystems is one of the leading fields of research for improving overall performance. As engine sophistication increases, more sensor information becomes available to the digital control system, as well as options for active flow control technologies. It is important to develop control systems that can take full advantage of these developments. For instance, active control of the turbine casing can reduce excess rotor blade tip clearance; for every $0.0254mm$ of clearance eliminated, specific fuel consumption can be reduced by up to 0.1% and turbine entry temperature by up to $1K$. However, the tip clearance changes between $0.1mm$ and $0.4mm$ throughout a flight due to differences in the expansion of the rotor disc and seal casing. Active tip clearance control can be used to mitigate this variation and thereby minimise fuel burn. Equally, turbine discs and blades experience large temperature ranges that affect their lives. These can be also be improved by active cooling flow modulation. Clearly, both tip clearance problems and cooling flow modulation require sophisticated real-time models and actuation systems. This thesis has two key objectives; the validation of an active impingement system, and the development of reduced order models for discs and casings.

The thesis describes the design and development of a novel facility capable of reproducing typical conditions in a large civil engine's oversegment cavity. The facility recreates the air system at cruise-level temperatures ($770K$), pressures ($1.35MPa$) and mass flows ($1.0kg/s$), with a test casing that is instrumented to capture the complete three-dimensional thermal response. The facility has been designed specifically to validate a novel active clearance control concept - step climb alleviation (SCA). The SCA concept uses hot impingement jets from the oversegment cavity to heat the casing, providing a rapid thermal actuation system for tip clearance control during fast engine transients. Research at the facility allows better understanding of the circumferential heat transfer coefficients and the sealing effectiveness of the SCA impingement plates.

The development of the facility considers different air system architectural solutions. A novel concentric double-vessel has been designed to accommodate the high temperatures and pressures using predominantly low cost steels. The electric heater and flow bypass system can deliver rapid changes to the test air flow rate without compromising the temperature. The rail system allows rapid change out of test geometries and accommodates the thermal growth of the facility. The commissioning results of the rig show that it can recreate engine realistic conditions.

The facility has also been used to provide data for the development of reduced order models. In the second half of the thesis, a model of the test casing is developed using the newly defined LPV-SVD methodology. This method uses singular value decomposition (SVD) to identify modes of spatial coherence, and linear parameter varying (LPV) systems to model the non-linear dynamics. This is a low order thermal model capable of being run in real-time that requires only a small number of inputs already available in the engine measurement suite. When this is applied to the casing, an accuracy of $\pm 30K$ is achieved.

The LPV-SVD model is capable of being applied directly to other engine components, using either experimental or simulated data for system identification. As such, it has also been applied to modelling the axisymmetric temperature of an IP disc using simulated data from SC03. In this context, the model is built and validated using flight relevant trajectories. The disc model uses only spool speed, pressure altitude, and compressor exit temperature as inputs, and produces temperature distributions to an accuracy of $\pm 32K$, with all but a few points performing much better. The thesis also presents a Kalman filter augmentation to the LPV-SVD model, which helps track noisy trajectories outside the training data set. The filtered model has been validated against a previously unseen noisy flight profile, and achieves an accuracy of $\pm 30K$.

Finally, a second model of disc temperature has been developed using a physics based approach, a so called grey-box model. Heat transfer from air to disc is modelled using empirical rotor-stator aerodynamics matched to validated computational fluid dynamic analyses. Lumped capacitance models and simplified explicit conduction models simulate the heat diffusion through the axial and radial profile. This physics based model is also capable of being run in real-time, but proves to be less accurate than the LPV-SVD model in like-for-like comparisons. Overall, the LPV-SVD model recreates temperatures with far greater spatial resolution, making it a superior choice for disc life monitoring applications.

Contents

1 Introduction

List of Figures

Nomenclature

This is a list of the most common variables in this thesis.

Where two variables overlap, the pertinent chapter is listed in brackets ().

Other variables with specific use are defined within their own context.

Roman

a	inner radius of disc
alt	pressure altitude
A	surface area
$\mathbf{A}$	state (or system) matrix
b	outer radius of disc
$\mathbf{B}$	input matrix
c_p	specific heat at constant pressure
c_v	specific heat at constant volume
$\mathbf{C}$	output matrix
D	diameter
$\mathbf{D}$	feedthrough matrix
e	cost function
e_{max}	maximum absolute error
e_{RMS}	root-mean-square error
g	gravity
h	heat transfer coefficient
k	transfer function gain
k	thermal conductivity
L	length
$\mathbf{L}$	filter matrix
$\dot{m}$	mass flow rate
M	moment on one side of rotor
p	transfer function pole
p	static pressure of fluid
q	heat flux
$\dot{Q}$	heat transfer rate
r	matrix rank (3,4,5)
r	radial dimension (6)
R	gas constant (2)
R	recovery factor (6)
s	gap between rotor and stator disc
t	time
T	temperature
$\boldsymbol{u}$	input vector or forcing function
$\mathbf{U}$	matrix of left-singular vectors
v	velocity
$\boldsymbol{v}$	measurement noise
V	volume
$\mathbf{V}$	matrix of right-singular vectors
w	axial width
$\boldsymbol{w}$	process noise
$\boldsymbol{x}$	state vector
$\boldsymbol{y}$	output vector
z	transfer function zero

Greek

α	thermal diffusivity (2,3)
α	valve opening angle (4)
β	valve opening angle (4)
β_v	thermal expansion coefficient
ε	windage correction factor
θ	parameter vector
μ	dynamic viscosity
ν	kinematic viscosity
ρ	density
σ	singular value
Σ	diagonal matrix of singular values
τ	time constant
ϕ	rotational dimension
Φ	temporal variable
χ	position vector (3,4,5)
χ	correction factor for heat flux (6)
ψ	point targetted spatial function matrix (5)
ψ	combined correction factor (6)
Ψ	spatial variable
ω	angular speed of rotating core region
Ω	angular speed of rotor

Non-Dimensional Numbers

Bi	Biot Number	$\frac{hL_c}{k_{solid}}$	
C_M	Moment Coefficient on one side of rotor	$\frac{M}{\frac{1}{2}\rho\Omega^2 b^5}$	
C_W	Non-Dimensional Mass Flow	$\frac{\dot{m}}{\mu b}$	
Fo	Fourier Number	$\frac{\alpha t}{L_C^2}$	
G	Gap ratio	$\frac{s}{b}$	
Gr	Grashof Number	$\frac{g\beta_v\rho(T_s-T_\infty)L_C^3}{\mu^2}$	
L_c	Characteristic Length	$\frac{V}{A}$	
Ma	Mach Number	$\frac{v}{v_{sound}}$	
$\mathrm{Nu}_{(r)}$	Nusselt number (local)	$\frac{hb}{k_{fluid}}$	$\left(\frac{hr}{k_{fluid}}\right)$
Pr	Prandtl number	$\frac{\mu c_p}{k_{fluid}}$	
Ra	Rayleigh number	Gr Pr	
Re	Reynolds number	$\frac{\rho v D}{\mu}$	
$\mathrm{Re}_{\phi(,r)}$	Rotational Reynolds number (local)	$\frac{\rho\Omega b^2}{\mu}$	$\left(\frac{\rho\Omega r^2}{\mu}\right)$
St	Stanton Number	$\frac{\mathrm{Nu}}{\mathrm{Re}\,\mathrm{Pr}}$	
β	Core-swirl Ratio (6)	$\frac{\omega}{\Omega}$	
γ	Ratio of specifc heats	$\frac{c_p}{c_v}$	
λ_T	Turbulent Flow Parameter	$C_W Re_\phi^{-0.8}$	

	Acronyms
ACC	Active Clearance Control
CAD	Compter Aided Design
CFD	Computational Fluid Dynamics
CMS	Component Mode Synthesis
CNC	Computer Numerical Control
DN	Diametre Nominel (Nominal Diameter)
EGT	Exhaust Gas Temperature
FADEC	Full Authority Digital Engine Control
FE	Finite Element
IP	Intermediate Pressure
HP	High Pressure
HTC	Heat Transfer Coefficient
LC	Lumped Capacitance
LP	Low Pressure
LPV	Linear Parameter-Varying [System]
MIMO	Multi-Input/Multi-Output
MTO	Maximum Take-Off
NASA	National Aeronautics and Space Administration
NGV	Nozzle Guide Vane
PID	Proportional-Intergral-Derivative [Controller]
PLA	Pilot Lever Angle
PLC	Programmable Logic Controller
POD	Proper Othrogonal Decomposition
PT	Pressure Transducer
ROM	Reduced Order Model
SCA	Step Climb Alleviation
SISO	Single-Input/Single-Output
SLS	Sea-Level Static
SS	Stainless Steel
SVD	Singular Value Decomposition
TC	Thermocouple
TET	Turbine Entry Temperature
THTF	Transient Heat Transfer Facility

Chapter 1

Introduction

1.1 A Historic Context

Gas turbines have a come a long way from their humble origins in Roman Egypt, where Hero first described the *aeolipile* in the 1st century AD (see Figure 1.1). Regarded as a novelty at the time, “Hero’s Engine” demonstrated in rudimentary style many of the basic principles of a jet engine as they continue today; energy is instilled in to a fluid (i.e. steam) in the form of both heat and pressure, and then released in a controlled manner generating useful work. By utilising an axis of rotation and assuming a constant supply of fuel, the engine could be run continuously. In future turbomachinery, some of the extracted work would be re-routed into the initial compression stage to help improve efficiency, while some of the excess pressure would be directed rearwards to create a lateral thrust. But before compartmentalising and developing the individual subsystems, the science and mathematics would need to catch up, and it would be a long process.

In 1662 Hooke and Boyle demonstrated that the pressure and volume of an ideal gas under isothermal conditions are inversely proportional, giving us Boyle’s Law. In 1787 Charles showed that the volume and temperature of an ideal gas under isobaric conditions are directly proportional, leading to Charles’ Law. Together, these laws culminated in the ideal gas law as written by Clapeyron in 1834;

$$pV = nRT \tag{1.1}$$

where p is the pressure of the gas, V is the volume, n is the number of moles of the substance, R is the universal gas constant, and T is the temperature. By the end of the Industrial Revolution, thermodynamics had been identified as a scientific field in its own right. Fowler itemised the four laws of thermodynamics in 1935, following the observation and formalisation of the zeroth law.

Figure 1.1: Hero's Steam-Engine or *aeolipile* as drawn in Knight's American Mechanical Dictionary [69].

Concurrent to the fundamental scientific research, various steam and internal combustions engines were developed by Watt, Barber and others. This led to the formation of a variety of power cycles, which are constructions of the laws of thermodynamics into practical expressions for useful application. These cycles describe the engineering processes that are applied to a working fluid in some repeating pattern. The processes and end states of the fluid can be tailored depending on the desired output of the cycle. For instance the Carnot cycle (Figure 1.2), the most generic of the power cycles, describes the changing thermodynamic state of a fluid with the assumption that all processes are reversible. This greatly simplifies the calculation of each intermittent state. In this case, process $1 \rightarrow 2$ is isothermal expansion, $2 \rightarrow 3$ is adiabatic expansion, $3 \rightarrow 4$ is isothermal compression, and $4 \rightarrow 1$ is adiabatic compression. During compression work is applied to the fluid, and then extracted again during expansion. The net work out is defined by the area between the curves in the Figure. The cycle can be applied in either the forward direction as a heat engine, or in reverse direction as a refrigeration cycle. In the latter case, the net work is into the system, and the arrows in the Figure are reversed. The equation for the efficiency (η) of the Carnot heat engine is equivalent to the maximum thermal efficiency achievable for any cycle working between two thermal reservoirs;

$$\eta = 1 - \frac{T_{low}}{T_{high}} \tag{1.2}$$

The Carnot cycle represents an idealised case, but the principal that increasing the maximum working temperature leads to an increase in maximum efficiency holds across all power cycles.

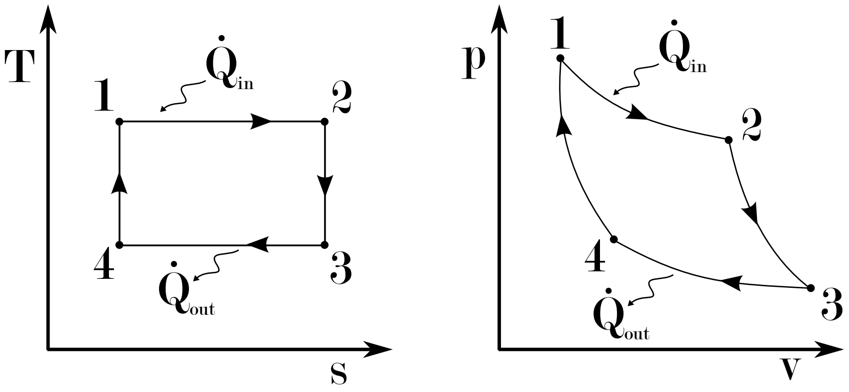

Figure 1.2: The Carnot Cycle. The processes in each stage are; 1 → 2 isothermal expansion, 2 → 3 isentropic and adiabatic expansion, 3 → 4 is isothermal compression, and 4 → 1 isentropic and adiabatic compression.

The development of power cycles was motivated by the desire to extract useful work from heat engines in the most efficient way possible. Another great body of work during the 19th century was developing the theories of fluid dynamics and aerofoil design using the experience of designing water wheels and windmills. Reaction and impulse turbines, shown in Figure 1.3, were invented by Parsons and De Lavel respectively. Both harness the change in the momentum of a fluid as it imparts rotational energy to a wheel.

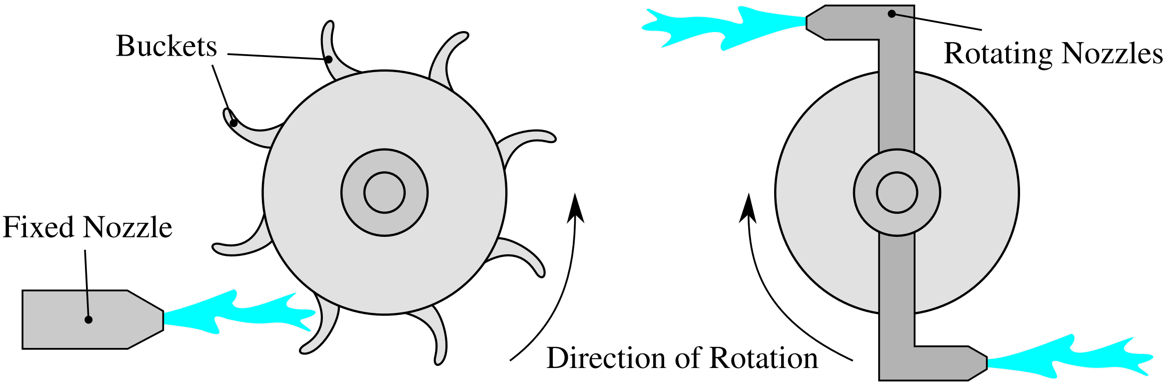

Figure 1.3: An impulse turbine (left) and reaction turbine (right).

Euler's equations for mass and momentum conservation can be used to calculate the power derived from these turbines. This is done by equating the change in the fluid's momentum with the force applied to the wheel. In modern turbines, the buckets on the reaction turbine, and nozzles on the impulse turbine, can be replaced with aerofoil shapes (blades) that work on the same principle. The governing design equations are then based on a vector analysis of the fluid's path through those blades. A standard example from an unwrapped turbine stage is shown in Figure 1.4, where the fluid path turns through the stator, impacts on the rotor where work is extracted, then turns again to leave the turbine.

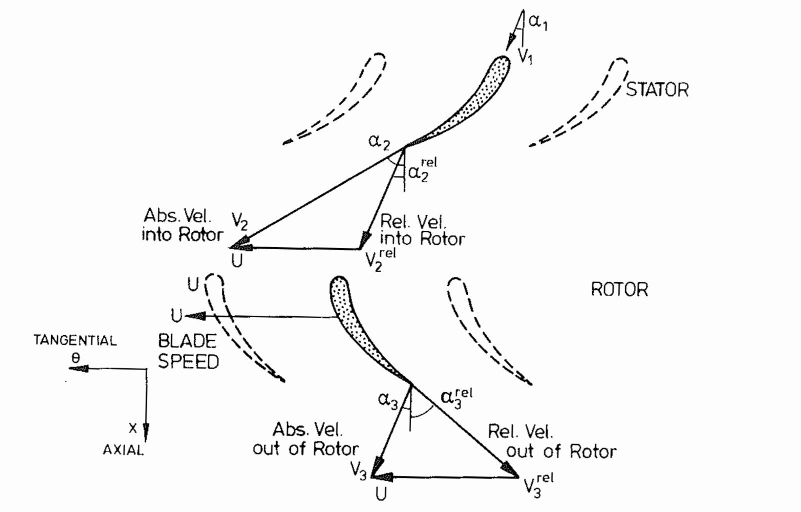

Figure 1.4: Vector analysis of the path of a fluid through a rotor-stator system.

Fluid enters the stator stage with velocity V_1, and is turned by the stator in the direction of the passing rotor blades to exit with a velocity V_2. The velocity in the rotor stage is considered in the relative frame, where the blade velocity is U and the relative entry velocity is V_2^{rel}. The power delivered to the rotor (assuming no losses) can be equated to the drop in enthalpy Δh, which is found using;

$$\Delta h = U(V_{3\theta}^{rel} - V_{2\theta}^{rel}) \tag{1.3}$$

Simply increasing U alone can help maximise the power output from the engine. However extracting work from rotating shafts at extremely high speed can be difficult as it puts large centrifugal loads on the blades. The process is usually broken down into multiple rotor-stator stages, with multiple changes in fluid velocity ΔV, all while operating on a single shaft with speed U.

The first modern jet engine that utilised all of these ideas was presented by Whittle in 1929 [135]. Whittle's design (see Figure 1.5) shows many elements which are still the norm in the majority of jet engines today; an axial intake compressor stage, injection of fuel and combustion, then an axially aligned turbine that underexpands the flow delivering both thrust to the aircraft and power back to the compressor. The design challenges might have changed, but the goals remain the same; to get planes flying in the air as efficiently as possible.

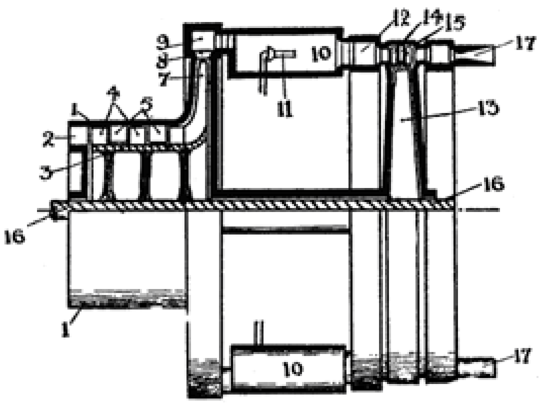

Figure 1.5: Reproduction of Whittle's first jet engine patent [135]. The numbered components are 1. Axial compressor casing 2. Intake 3. Compressor body 4. Compressor blades 5. Stator blades 7. Centrifugal compressor 8. Compressor outlet 9. Elbow 10. Combustion chambers 11. Fuel injector 13. Turbine disc 14. Turbine blades 15. Stator blades 16. Shaft 17. Divergent nozzle ring.

1.2 Modern Jet Engines

A jet engine's purpose is to provide thrust to the aircraft by accelerating a portion of the surrounding air backwards. Modern engines typically have two or three concentric shafts (as shown in Figure 1.6) that allow designers to optimise the turbine and compressor through each shaft separately. The combined shaft-turbine-compressor groupings are defined as the low pressure (LP), intermediate pressure (IP), and high pressure (HP) as applicable. The majority of the thrust for large civil engines is provided by the fan that is driven by the LP turbines, though some is still provided by the expansion of the exhaust gas in the nozzle as it exits the final turbine stage.

The power cycle for the engine is based on an open loop Brayton Cycle as shown in Figure 1.7, where the numbers 2,3,4,5 define the thermodynamic state of the fluid. This numbering system reflects typical industry practice; air entering the first compressor is always 2, and air exiting the turbine is 5. The ideal Brayton cycle operates under the following assumptions (where brackets show the alternative assumption used in practical, non-ideal cases);

2 → 3 Air enters the compressor stage and undergoes isentropic (adiabatic) compression,

3 → 4 Fuel is in injected under isobaric conditions, and combustion takes place,

4 → 5 The gases in the turbine stage expand isentropically (adiabatically) and work is extracted to drive the compressor.

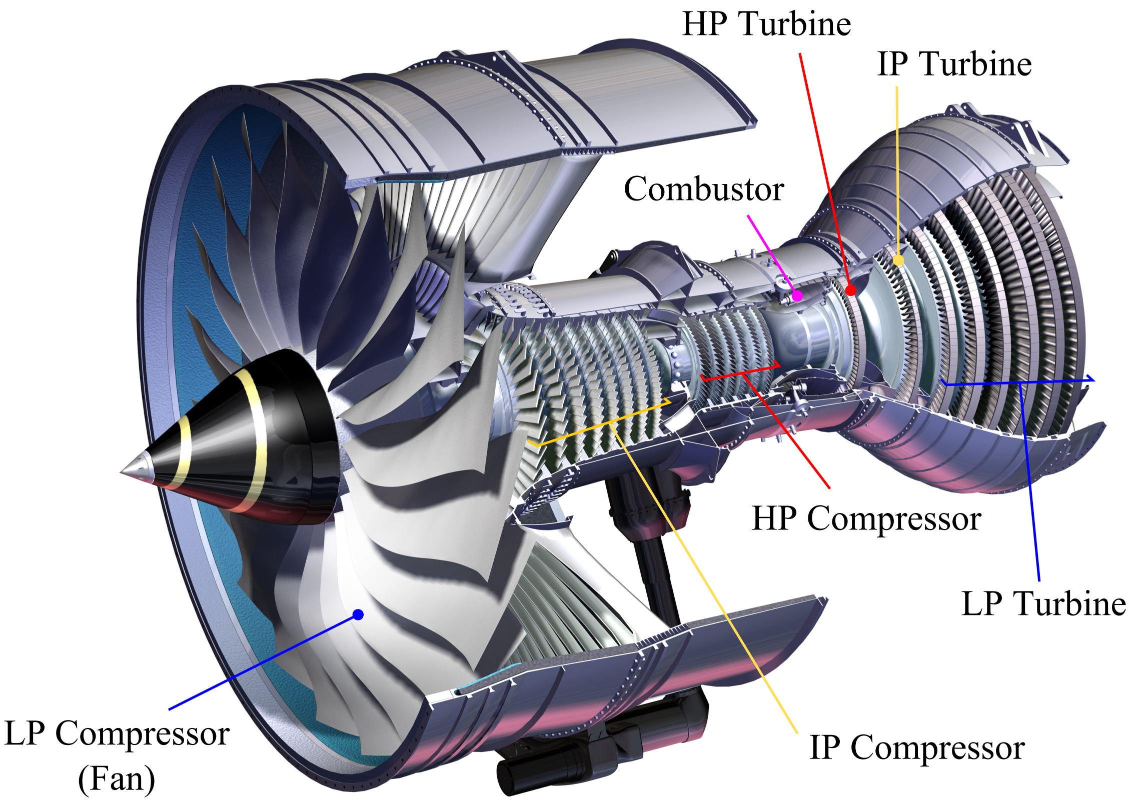

Figure 1.6: Example of a modern turbofan from Rolls-Royce [134].

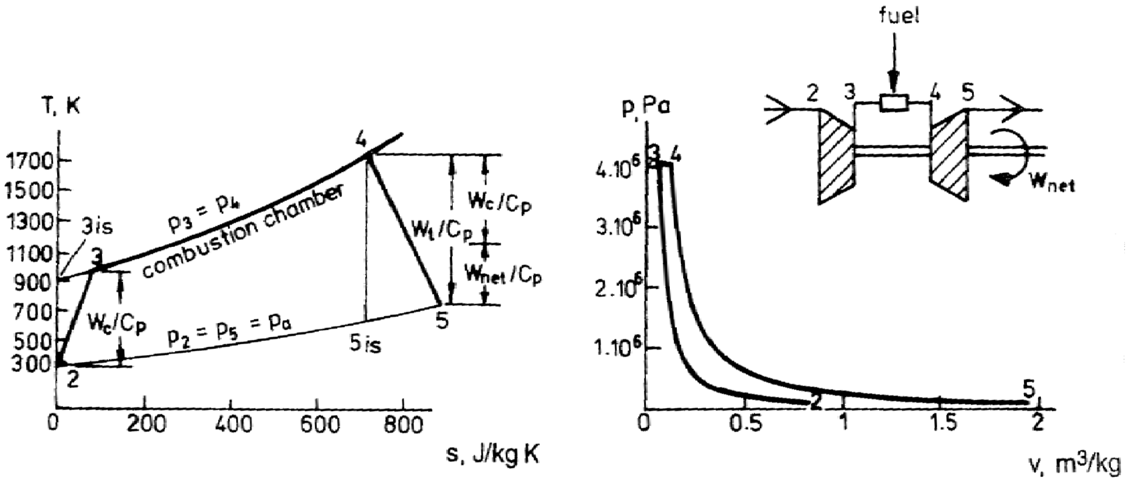

Figure 1.7: Brayton Cycle $T-s$ and $p-v$ diagrams [35].

The efficiency of the ideal Brayton cycle is given by;

$$\eta = 1 - \frac{T_2}{T_3} \tag{1.4}$$

Which can also be expressed in terms of the compressor pressure ratio (p_3/p_2);

$$\eta = 1 - \frac{1}{(p_3/p_2)^{(\gamma-1)/\gamma}} \tag{1.5}$$

Where γ is the gas's ratio of specific heats. Engine designers will often aim to improve their compression ratio (p_3/p_2) when striving for greater efficiency. This increases the temperature of the air entering the turbine (T_4). The turbine entry temperature (TET) peaks during take-off, and usually forms the limiting design factor of the engine. The progress of TET through history can be used to track the major engine developments necessary to meet increased demands for efficiency, as presented in Figure 1.8. In particular, this shows the dramatic effect that cooling technologies have had as materials limitations began to plateau.

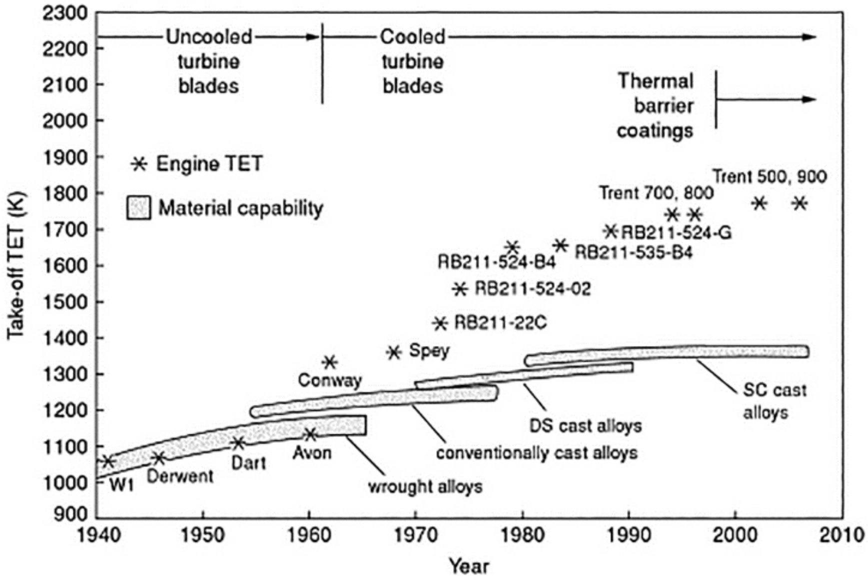

Figure 1.8: Increase in TET over time across different aircraft platforms [107].

As cooling technologies also begin to peak, some designers have shifted focus to minimising the aerodynamic losses of components. This can be achieved by optimising the 3D blade design and eliminating leakages and secondary flow structures. Another strategy is to ensure a long lifetime for components in order to save maintenance, down time, and replacement costs. All of the components of the turbine system and subsystem (including shafts, discs, and casing) operate in high temperature environments and thus experience exceptional stresses in their lifetimes. Closely monitoring fatigue and creep damage is an important strategy in avoiding excess maintenance and replacement costs.

1.3 Elements of the Turbine System

The complete turbine system from a large civil engine is shown in Figure 1.9. This example shows a three-shaft arrangement, where the main flow (orange) passes from the high pressure (HP), to the intermediate pressure (IP) and low pressure (LP) turbines in turn. The rotors and nozzle guide vanes (NGVs) make up the main system. The design of the blades and NGVs starts with the Euler equations, but generally utilise 2D and 3D methods to model the flow and improve the aerodynamic efficiency. Typically this will include investigating the rotor-stator interaction, the formation of vortices at the end walls, and leakage over the tip.

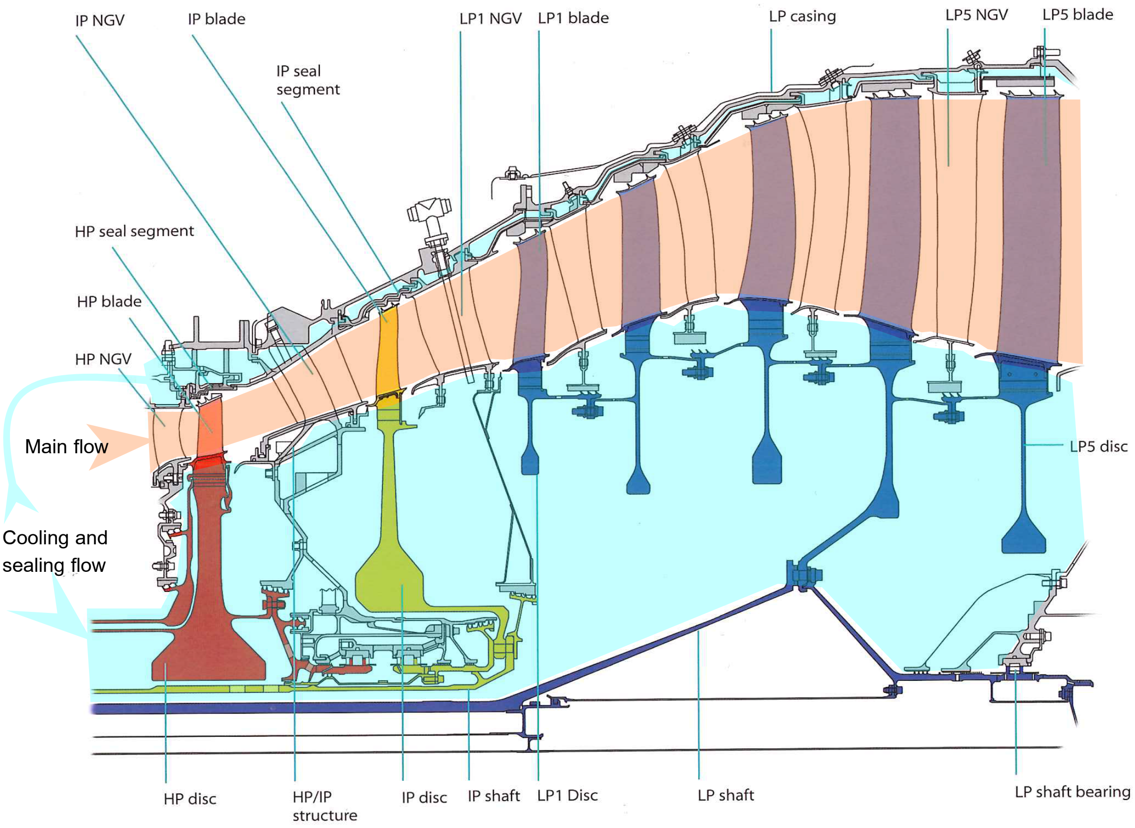

Figure 1.9: The components of a three-shaft turbine system [108].

Aside from aerodynamics, the blades must also be designed to resist the high TETs and the large stresses induced by the centrifugal loads. Cooling air from the secondary flow passes through the blades (as shown in Figure 1.10) by injection through the blade root. In turn, the discs that hold the rotor blades must also resist the harsh conditions imposed by the secondary flows and the centrifugal forces. The turbine subsystem is composed of all the components that are principally exposed to the secondary flows (blue region in Figure 1.9). This includes the casing, seal segments, discs and shafts.

The secondary flows themselves are used for both cooling components and ensuring that the primary flow remains sealed within its intended path. The secondary flow is drawn from various stages of the compressor, and as such has been heated to temperatures typically in the range of $500K \rightarrow 900K$ [108]. The path of the cooling flow through the blade shown in Figure 1.10 presents multiple techniques at work; ribbed passages, leading edge showerhead cooling holes, pressure side cooling holes, and the shroud cooling air.

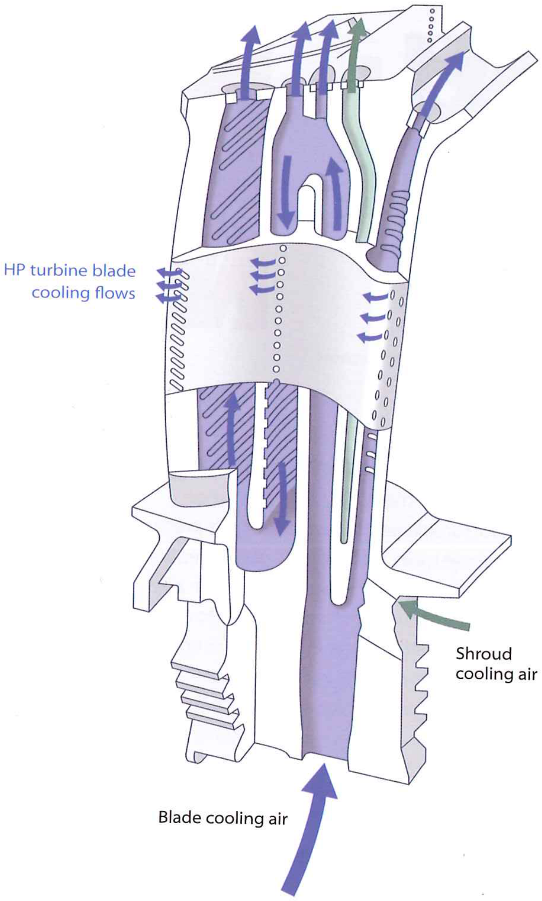

Figure 1.10: Cross-section of a turbine blade [108].

The subsystem components can be gathered into two groups, the outer system including the seal segment and casing, and the inner system including the discs and shafts. The casing is primarily responsible for providing containment and a robust seal around the turbine as a whole, while the seal segment provides a seal for the main flow above the rotor tip as shown in Figure 1.11. Tip clearance between the blade and seal segment is a major source of loss in aerodynamic performance, and thus it is an attractive target for technology development.

The discs and shafts are responsible for delivering the work from the blades to the compressors. Discs and shafts are designed primarily to limitations of fatigue and creep. This is evident in the tapered profile of the discs in Figure 1.9. The tapering is good for stress distribution, but consequently leads to increased temperature non-uniformity and thermal stresses. As such, discs become susceptible to thermomechanical fatigue, which has led to creative monitoring strategies - another motivator for technology development. Turbine technology relies on a suite of different techniques for improving their overall efficiency, so it is important to consider where the greatest improvements can be made.

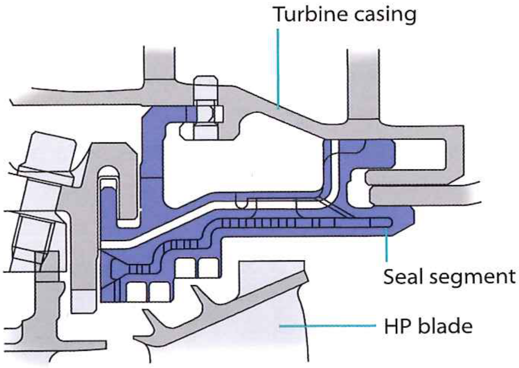

Figure 1.11: The components of a three-shaft turbine system [108].

1.4 Motivation

1.4.1 Industry Wide Factors

Airlines currently spend anywhere from 23% to 45% [10, 59, 93, 112] of their operating costs on fuel, depending on the airline. Fuel prices may have dropped dramatically in the last two years yet they continue to fluctuate and generally are rising, forcing airlines to adapt fuel hedging strategies [43]. The aviation industry continues to expand, with up to a 4.7% increase in air traffic predicted per annum, while at the same time accounting for roughly 2% of the CO_2 emitted into the atmosphere every year [61]. This has led to strict environmental targets as set forth by the Advisory Council for Aviation and Innovation in Europe (ACARE) [1], in turn forcing designers to lower manufacturing costs, operating costs, waste and emissions. The prospective outcomes are shown in Figure 1.12.

The results have been significant. Specific fuel consumption (SFC) has- and continues to- drop by about $1\% \rightarrow 2\%$ each year [10]. A jet aircraft coming off the production line today is around 80% more fuel efficient per passenger seat kilometre than one delivered in the 1960s. And while this is all promising, there is still demand for further improvement. Turbines in particular have a great potential for improvement as turbine efficiency directly reflects overall fuel costs. They have high unit and maintenance costs, and because turbines operate in the harshest engine environment, they also have strict service lives and often are

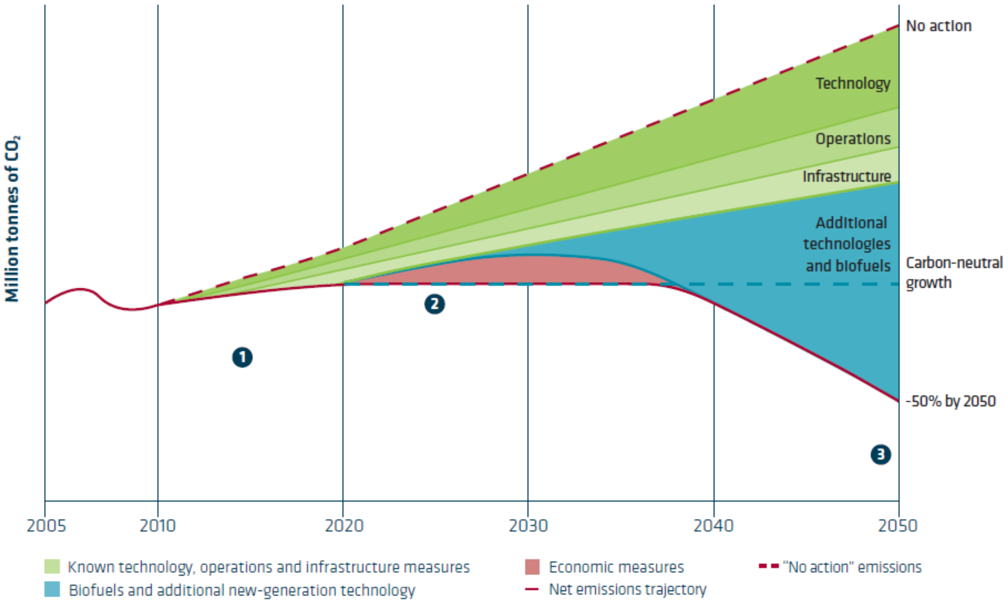

Figure 1.12: Commitments made by the global aviation industry. (1) Improve fleet fuel efficiency by 1.5% per year from now until 2020. (2) Cap net emissions from 2020 through carbon neutral growth. By 2050, net aviation carbon emissions will be half of what they were in 2005 [10].

retired without inspection [31]. Smart use of the advanced control systems to model and monitor the performance of components can help to improve efficiency and SFC [80]. On the other hand, research that focuses on extending the life of turbine parts has the most promise for meeting strategic cost demands [144].

1.4.2 Blade Tip Clearance

Improved sealing around the blade tip has shown promise in improving the aerodynamic efficiency of gas turbines. However, the gap is difficult to manage due to its dynamic response to the pressures, temperatures and inertial forces that the engine will encounter during any standard flight [73]. These effects can either be axisymmetric or asymmetric. One problem in particular is the sudden closure of the gap during take-off and mid-cruise accelerations. These closures are called pinch points and are shown at (b) in Figure 1.13. They occur because the response of the blade and disc to centrifugal and thermal grow is much faster than that of the casing. Engine casings and seal segments are usually run to a tolerance based on the maximum take-off (MTO) pinch point to ensure that there is minimal incursion of the blade tip, but subsequently this means that there is a large stand-off distance left when the aircraft enters extended cruise periods. Typically, turbine case cooling (TCC) is used throughout cruise in order to minimise the axisymmetric portion of the gap and reduce losses. This is achieved by impinging secondary flows on to the casing from the outside, cooling and shrinking the casing to create a tight clearance with the blade tips. Optimising the distribution and flow rate of these jets is an ongoing topic of research [3, 5, 30, 36, 40, 51, 57, 131].

However there is still room for improvement. TCC is designed to close some of the gap, but there is still a running clearance left above the blade tip during cruise to ensure that the tip does not interfere with the seal when a mid-cruise acceleration (otherwise called a *step climb*) is initiated. This running clearance presents an opportunity to further improve the work extracted by the turbine during the long periods of cruise. To claim this, an active clearance control (ACC) system is required to open the gap prior to the step climb pinch point. Research by Wiseman and Guo [144] shows that ACC can produce as much as 0.1% reduction in SFC and 1 °C reduction in exhaust gas temperature (EGT) for every $1 mil$ ($0.0254 mm$) of clearance eliminated.

Current ACC research focuses on either thermally or mechanically actuated systems. They rely on having measurements of the clearance to actively monitor and control the ACC mechanism. Instrumentation that can take these direct measurements represents a severe design challenge as they must survive in a hostile environment. A model of the tip clearance could prove to be an effective supplement to this system, as a good model would allow a single measurement to provide far greater detail about the greater turbine subsystem. Rather than modelling tip clearance directly, a model of component temperatures would suffice. This is because the relationship between temperature state and disc growth is well understood, but less so the link between engine conditions and disc temperature profile.

1.4.3 Disc Life Management

Designers will always pursue the efficiency advantage of operating at higher TETs even when improved aerodynamics could allow for cooler operation. As TETs increase, so does the temperature of the secondary flow system. In turn, this increases the thermomechanical damage accumulation on the discs. To understand this damage requires a cumulative damage model, but there is no agreed upon standard for these, so they are designed and applied on a case-by-case basis. As such, most specific examples are proprietary, and there is very little in the literature that directly links disc temperature to fatigue life.

Typically, and in the absence of specific engine real-time information, disc life is computed and declared at the design stage, applied across the whole fleet, using a probabilistic

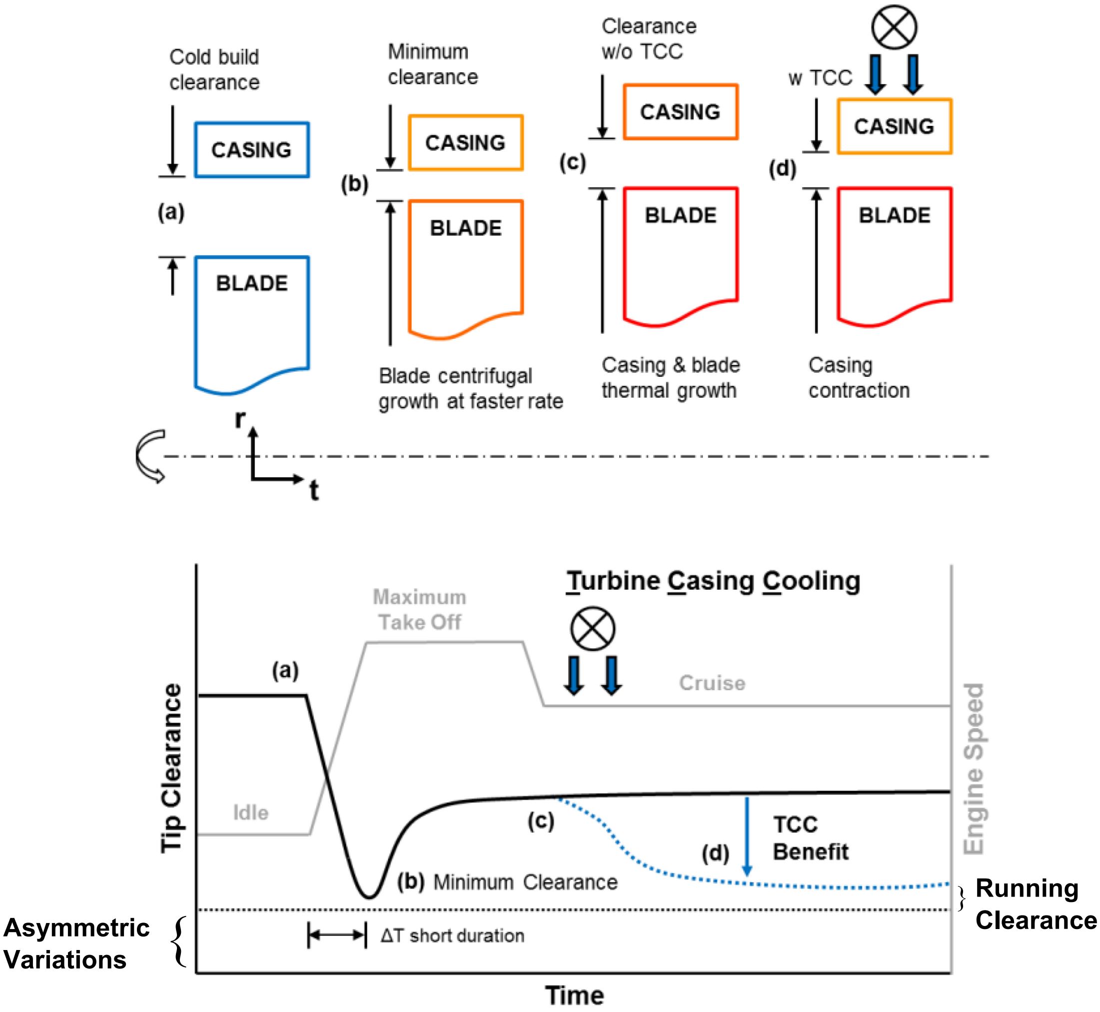

Figure 1.13: Tip clearance at the start of a standardised flight profile. Closure above dotted line is axisymmetric, below the line is asymmetric [30].

approach assuming worst case scenarios and flight profiles [23, 24, 88]. Stress evaluation is typically carried out through Finite Element (FE) computer simulation [31] in combination with Computational Fluid Dynamics (CFD). For some manufacturers and operators, the results are validated against experiments on discs that have been withdrawn early from service [23].

Because the FE/CFD approach uses of the 'worst case' flight profiles, the majority of the fleets' engines are taken off the wing for overhaul on the basis of a conservative life prediction. Statistical scatter in the prediction of disc life comes down to variations in five key parameters; geometry, manufacturing processes, service loads, surface finish and material defects [86]. By monitoring service loads on a flight-by-flight basis, the statistical scatter can be reduced [88]. Life consumption due to service loads is attributable to low-cycle fatigue, high-cycle fatigue, thermomechanical fatigue, creep, creep-fatigue interaction, and fatigue-oxidation interaction [145]. These mechanisms can behave independently or in combination; high temperature environments lead to thermal strain and creep, while also generating brittle oxides. Both of these mechanisms can lead to microcrack nucleation and propagation. A survey of analytical approaches to summing these mechanisms is provided by Changan *et al.* [29].

Knowledge of a disc's temperature can have a drastic improvement in the confidence with which its life is predicted [85], as can knowledge of the temperature gradient [56]. Monitoring temperatures on an individual basis in real-time can extend the declared disc life by up to 100% [85]. This leads to large savings when considering that replacement discs can cost up to 10 times the original purchase price or even lead to full engine replacement [115]. Using FE/CFD models to estimate transient temperatures, and therefore life, is computationally expensive [81] which makes them unsuitable for real-time applications. Furthermore, models that require the transmission of excessive data to a ground station post flight are expensive, so these methods are not being pursued. The best course of action is to develop a reduced order model (ROM) that operates within an engine's Full Authority Digital Engine Control (FADEC) system, and use the output from that model to track disc life usage.

1.4.4 FADEC Design

Figure 1.14 shows the FADEC concept for managing the control, diagnostics and prognostics of future gas turbine engines [48]. Where traditional engine control design is based on PI-controllers for independent components, the new system provides closed loop control

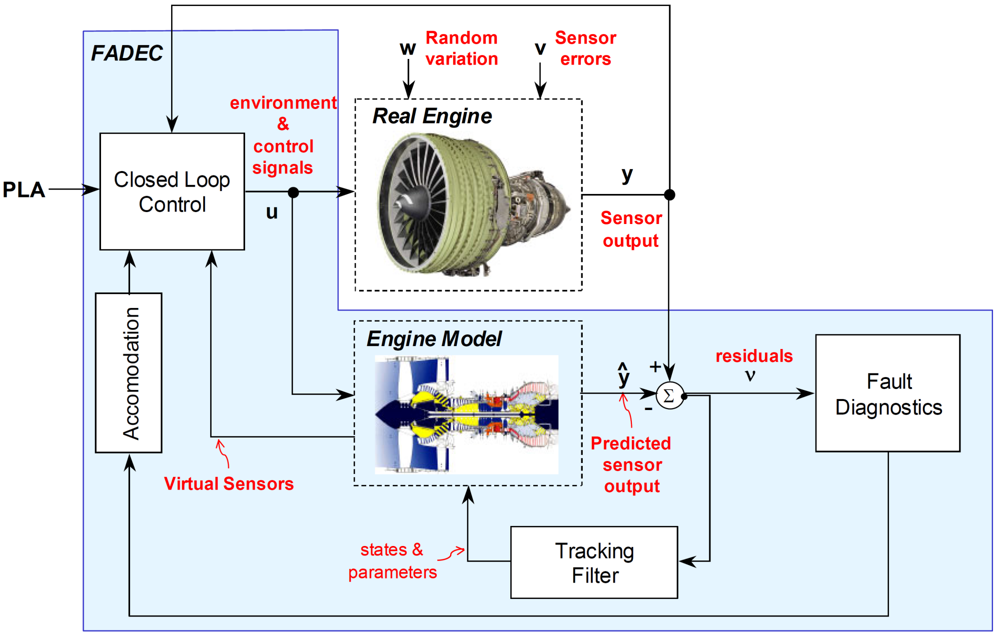

Figure 1.14: Future FADEC System for MIMO control.

for the entire multivariable architecture. The active regulation of interacting subsystems can optimise component efficiency, specific fuel consumption, and damage accumulation, as well as form a platform for performance failure detection. The figure shown is based on a FADEC system that is already in use, and is capable of multi-input/multi-output control. Inputs include pressure altitude, shaft speeds, gas flow temperatures and pressures. Comprehensive system models and controllers are at the forefront of exploiting current technology to the maximum effectiveness.

In support of ACC research, Garg *et al.* [48] have reviewed the current state-of-the-art with respect to FADEC systems and their potential to optimise engine performance. The challenge is to automate engine subsystems to actively mitigate undesirable features. These include inlet flow distortion and separation, compressor surge and stall, combustion instabilities, flow separation on aerofoils, flutter and high cycle fatigue, and engine noise. For this, instrumentation and sensor technology needs to meet minimum standards. For instance, ACC requires an actuator with a rate of movement greater than $0.1mm/s$, stroke of $3mm$, and resolution of $0.02mm$. Similarly, and in their specific case, the sensor should have a range of $2.5mm$ and resolution of $\pm 25\mu m$ accuracy. For effective turbine life management, they suggest flow and blade temperature measurements of $5K$ accuracy.

Beyond just improving the instrumentation and FADEC systems, ACC can also benefit from modelling the deterioration of the engine over time, as wear in the blade tip leads to increased clearance, and therefore increased EGT. Baptista *et al.* [14], identified that current engine sensors are not adequate for managing ACC effectively alone. They used an estimator engine model in conjunction with a real engine to predict the clearance deterioration throughout an engine's life. They found that they could reduce tip clearance by up to 25% from nominal, leading to a $7.5°C$ decrease in EGT, and a predicted 15% extension to engine life. Similar methods are utilised in the US Navy's Integrated Condition Assessment System, as presented by Byington *et al.* [27] for optimising the performance of power generation systems. A comprehensive study that combines all of these advances is presented by Lorenzo *et al.* [83] on the management of space shuttle subsystems.

1.4.5 Case Study - Space Shuttle Main Engine Turbine Blades

The space shuttle was one of the most advanced pieces of technology of its time, and only recently have we seen any promising successors. This is owing to the tremendous cost of the production and difficulty in providing a safe, reusable, manned delivery system for cargo en route to the International Space Station. As such, the space shuttle main engines (SSMEs) were pushed as far as they could go in terms of both performance and safe working life, and particular focus was put on the turbine blades within the propellant delivery system. Lorenzo *et al.* [83] detail how this was achieved using interconnected models of the engine subsystems, damage models of the blades, and advanced control systems for performance regulation with online feedback and nonlinear parameter optimisation. A brief overview is presented here as many of the methodologies used in the present thesis follow a similar development.

The SSME is a bipropellant rocket engine with a turbopump/turbine fuel delivery system as shown in Figure 1.15a. The description from Lorenzo is as follows: the propellants, namely, liquid hydrogen fuel and liquid oxygen, are individually pressurized by separate closed-cycle turbopumps. Pressurized cryogenic fuel and oxygen are pumped into two high-pressure preburners which feed the respective turbines with fuel-rich hot gas. The exhaust from each turbine is injected into the main combustion chamber where it burns with the remaining oxidizer and is expanded through the rocket nozzle to generate thrust. The oxygen flow into each of the two preburners is independently controlled by the respective servo-controlled valves. The turbine blades accumulate damage based on their operating temperature, which can be inferred from the fuel mix ratio and combustion temperature.

A model of the SSME plant has been devised using a series of interconnected first order lumped parameter models, featuring a total of 18 internal state parameters. Two inputs (servo-valve position angles) and two outputs (main thrust and O_2/H_2 mixture ratio)

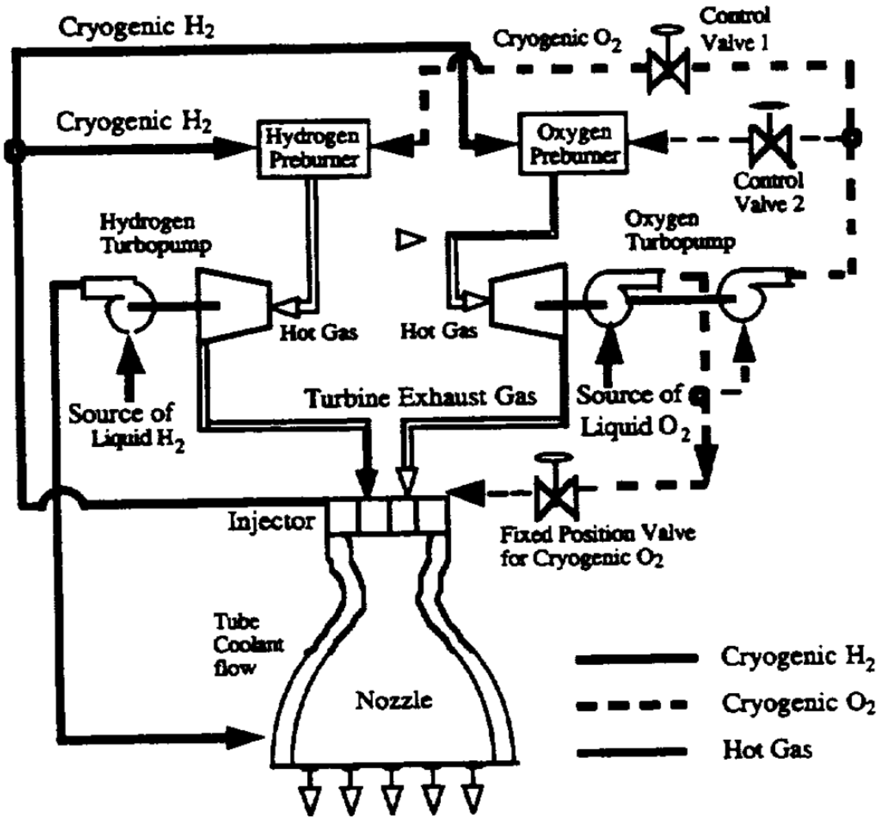

(a) Bipropellant Rocket Engine

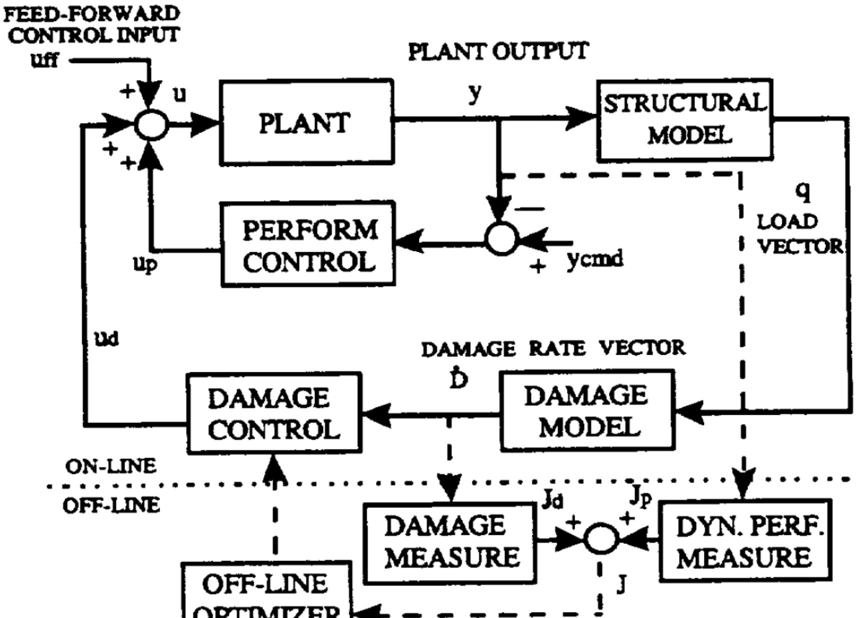

(b) Life extending control system

Figure 1.15: Schematics of the SSME and controller model.

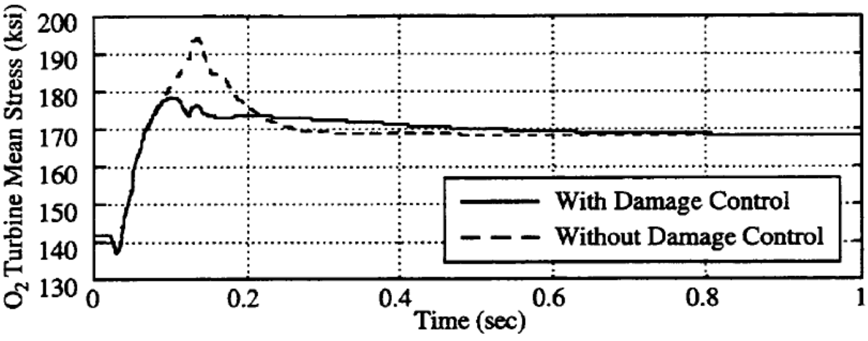

Figure 1.16: Mean stress in SSME O_2 turbine blades with and without damage control [83].

are observed. The model has then been linearised near to a central operating point, and then reduced to 13 state parameters in order to increase the efficiency of the real-time processing, whilst maintaining the original model characteristics. The accuracy and stability of the model is maintained with feedback as shown in Figure 1.15b. A separate model has been developed to summate the damage caused to the turbine blades using the output from the surrogate plant model, and then a controller is devised to minimise this damage, whilst regulating the performance of the engine. The damage is quantified as a series of penalties relating to the operating point.

The model was applied in simulated experiments. The result of the study was that the controller reduced the O_2/H_2 ratio by 1% temporarily during take-off, leading to a longer rise time in the chamber pressure. The reduction in stress in the O_2 turbine blades is shown in 1.16. The ratio representing the effective reduction in damage is reported to be 2.6 in the H_2 blades, and an astounding 35.4 in the O_2 blades, for transient manoeuvres. This study gives motivation, not just for the specific techniques of control, but the effectiveness with which control methods can exploit small internal system mechanisms for vastly improved overall performance.

1.5 Research Objectives

This thesis studies improvements to the turbine subsystem by focusing on two key ideas; regulating transient tip clearance and increasing disc life. The first objective was the development of a unique experimental test bed called the Transient Heat Transfer Facility (THTF). This facility allows for the testing of thermal ACC concepts and FADEC system designs under real engine conditions for pressure, temperature and mass flow rate. This represents a full size recreation of the oversegment cavity of a real civil aircraft. This facility provides an important stepping stone in developing FADEC and ACC technologies ahead of ground engine testing. Specifically, the facility provides the means to study:

1. The performance of various internal heat transfer and flow configurations.
2. The 3D spatial distribution of the heat transfer coefficients.
3. The transient 3D metal temperature behaviour during flight cycle changes and its impact on asymmetric and axisymmetric tip clearances.
4. The realistic seal leakage mass flow rates and its impact on metal temperatures.
5. Different plate and casing geometries, for either turbine or compressors sections.

Presently, the geometry of the casing test piece matches the target engine casing radius, length and thickness. The material used has well defined thermal properties that make it easy to map to the engine material, as the latter was not available. The air flows past the casing and impingement plates as it would in the engine, and the control valves operate at realistic speeds. The rig is instrumented to validate CFD predictions of the casing temperature during step climb transience; with and without ACC.

The second objective of this thesis was the development of two thermal models of subsystem components suitable for use in life monitoring and performance optimisation. The first model is based on linear parameter varying functions and singular value decomposition, such that there is no prior knowledge of the physical properties of the target component. The model methodology has been validated using data from the THTF and a simulated IP turbine disc. A second model has been developed in order to form a comparison case for the disc example. This model is based on an analysis of the physics of the disc and surrounding cavities. Both models are able to predict component temperatures under non-linear conditions with sufficient accuracy to implement both ACC concepts and life management systems. The suitability for real-time application is demonstrated through compilation of the models on a FADEC style computer.

1.6 Original Contributions

The design of the Transient Heat Transfer Facility (THTF) is a unique and important contribution to the literature. The THTF has been designed specifically for studying novel heat transfer concepts at realistic engine conditions. The only other facility that reflects these conditions is held at NASA Glenn Research Centre and is used to test mechanically actuated tip clearance mechanisms. The unique design of the THTF allows for it to be predominantly constructed from carbon steels and stainless steel, unlike the NASA rig which relies on Inconel. The THTF test piece has been arranged along the horizontal axis, which allows for realistic buoyancy effects to be observed. The space within the facility allows it to be adapted for a large variety of different test sections and instrumentation.

The thermal models developed are also new contributions to the literature. Firstly, the linear-parameter-varying - singular-value-decomposition (LPV-SVD) model is a unique combination of the LPV and SVD techniques for modelling 2D axisymmetric temperature distributions within non-linear systems. The creation of a model for real-time management of disc temperature with a Kalman filter FADEC system is also unique for turbine discs. The physics-based model is largely based off existing technologies, but the configuration of the techniques together is unique.

1.7 Thesis Outline

Chapter 2 of this thesis is an extended chapter outlining the development of the THTF. This includes a review of similar facilities, the design and development of the pressure vessel, and other analyses used to ensure that the facility can meet the required operating conditions in a safe environment. It goes on to predict the performance of the facility from an experimental perspective, and finishes by discussing the commissioning tests that validate the design objectives. Chapter 3 provides a literature review of reduced order models for thermal systems, culminating in the development of the theory for the proposed LPV-SVD model. The LPV-SVD model is adapted for use on the THTF in Chapter 4 in order to validate the methodology. It is then adapted for use with a simulated IP disc in Chapter 5. This chapter also develops a Kalman filter for the disc model that could be used as part of a closed-loop controller. Chapter 6 presents a counter example to the LPV-SVD model. It looks at the development of the physics-based reduced order model specific for the turbine disc, and presents a comparative study with the LPV-SVD model. Chapter 7 summarises the conclusions and recommendations of this thesis.

1.8 Publications

The following publications have been released alongside the production of this thesis;

Andrew van Paridon, Marko Bacic, Peter T Ireland, Chris Barnes, & Leo V Lewis. Reduced Order Transient Disc Temperature Models For Online Health Monitoring. In *Proceedings of ASME Turbo Expo 2014*, Düsseldorf, 2014. [137]

Andrew van Paridon, Marko Bacic, Peter T Ireland, & Ron Daniel. Disc Temperature Modelling Using Reduced Order Proper Orthogonal Decomposition Models. In *Proceedings of ASME Turbo Expo 2015*, Montréal, 2015. [138]

Andrew van Paridon, Andrew Dann, Peter T Ireland, & Marko Bacic. Design And Development Of A Full-Scale Generic Transient Heat Transfer Facility (THTF) For Air System Validation. In *Proceedings of ASME Turbo Expo 2015*, Montréal, 2015. [139]

One further paper has been accepted for publication;

Andrew van Paridon, Marko Bacic & Peter T Ireland. Kalman Filter Development for Real Time Proper Orthogonal Decomposition Disc Temperature Model. In *Proceedings of ASME Turbo Expo 2016*, Seoul, 2016. [136]

Chapter 2

Development of the Transient Heat Transfer Facility

2.1 Introduction

This chapter will discuss the design and development of a state-of-the-art test facility that simulates the secondary air system in a high pressure turbine oversegment cavity under realistic cruise conditions. This facility, named the Transient Heat Transfer Facility (THTF) and presented here for the first time in detail, is used to investigate a new method of thermal ACC called step climb alleviation (SCA). This concept provides a means to actively expand tip clearance at step climb pinch points. Results from this facility represent an important step in proving technology readiness prior to engine test bed experiments. The facility is a novel design that has multiple applications for future research, as well as providing data for developing reduced order models as discussed in Chapter 4.

The chapter proceeds as follows; Section 2.2 discusses current technologies in ACC, the strategy of the proposed SCA concept, and a short review of similar facilities that are investigating ACC and their impact on the design of the THTF architecture. Section 2.3 presents a full description of the final facility as constructed. Section 2.4 discusses the details of the design process of the pressure vessel, as this is a unique test bed with some novel concepts that require extensive investigation. Section 2.5 presents an analysis of the facility pipework used to predict and mitigate any problematic transient pressure effects that may occur during operation. Section 2.6 discusses the SCA impingement system and several analyses that predict its performance, and Section 2.7 describes the buoyancy effects that can be observed in the vessel cavities. The commissioning of the facility is finally presented in Section 2.8. A brief summary of conclusions is given in Section 2.9.

2.2 Background

2.2.1 Active Clearance Control of Pinch Points

Under normal cruise conditions, the cooling manifolds maintain a tight clearance of the casing around the blade tips, but they are not used to their full capacity. Whenever the pilot wants to increase their altitude the engine power is increased to initiate a climb. Consequently the rotor speeds and gas temperatures increase, leading to growth of both the blades and casing. As the blade time constant is much smaller than the casing's, this causes a change in clearance. Therefore an allowance is left for the tip growth to occur during a step climb pinch point. This change in clearance is similar to what is shown for the grounded reacceleration shown in Figure 2.1. The leakage through this gap is a source of aerodynamic efficiency losses, which leads to greater TET demand and increased SFC. By including an ACC system to offset the growth of the blades during step climb, the leakage during cruise can be reduced. The benefits of this can be realised for a large portion of the flight.

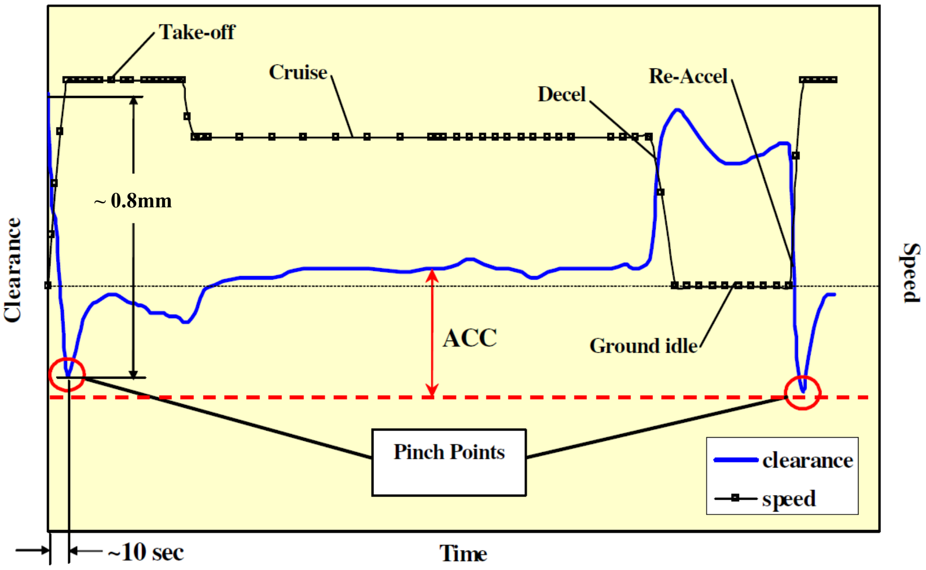

Figure 2.1: Pinch points at take-off and reacceleration [73].

The ability to control casing expansion can be achieved with either direct mechanical actuation or with direct heating that creates thermal growth. Direct mechanical actuation has shown promising results in maintaining tight clearances over an entire flight profile [42, 73, 129, 130]. The approach discussed in these papers uses an articulated seal carrier that is actuated from multiple fixed points outside the casing. The experimental setup can be seen in Figure 2.4. The actuators sit outside the casing and protrude in, creating leak paths along the actuator shafts. There are also leaks between the carrier segments. Despite this, the seals have proven to be effective enough that the mechanical ACC system produces a positive effect.

There are a few advantages to thermal actuation over mechanical methods. Direct heating means that leaks can be eliminated, thus there is less pressure loss in the turbine. Further, because the actuation occurs over a large distribution of points, it has the capacity to produce a more axisymmetric effect than the mechanical method. To make thermal ACC viable, the heating rate must be high enough to produce the required rate of radial growth. The challenge is to create a system that can provide this heating rapidly enough to match the performance demand of the pilot.

2.2.2 The Step Climb Alleviation Concept

The Step Climb Alleviation (SCA) concept is based on reversing typical TCC, by blasting the casing from the inside with the hot air available in the oversegment cavity [77]. The diagram from the original patents is shown in Figure 2.2. During cruise the casing usually sits at 500-600K and the air in the oversegment cavity is typically at 600-800K and 12-18bar. Air from the oversegment cavity (A,B) is drawn through holes in an existing heat shield (39,39'), creating jets that blast the casing (31). The air collects in a plenum (E) and passes through offtake tubes (41,41') into a low pressure region downstream as controlled by valves outside the casing (42). This creates a mechanism for heating the casing, thus expanding it on demand. The expansion of the casing in turn moves the seal segment (33) and that increases the tip clearance (G) between the seal segment and the rotor (32).

In later designs, the heat shield was been replaced by a set of 20 dedicated SCA impingement plates that include a continuous circumferential channel on their forward edge (as seen in Figure 2.3). When SCA is switched on the oversegment air (blue) is drawn through the holes and impacts on the surface, then reverses direction (orange) back into the channel. This channel feeds into one of four offtakes set at 90° intervals around the casing's outer surface. The air is exhausted into a lower pressure section of the engine. The present designs have eliminated the channel again, but the offtakes are in the same place and the path of the air has been maintained.

There are several challenges associated with researching the internal heat transfer in cavities such as this. The flow speed is often low, the flow pattern is not well understood and the total mass flow rate is significantly influenced by the leakages at the edges of the plenum. The seals for these leakages depend on the concentricity of the design and the type

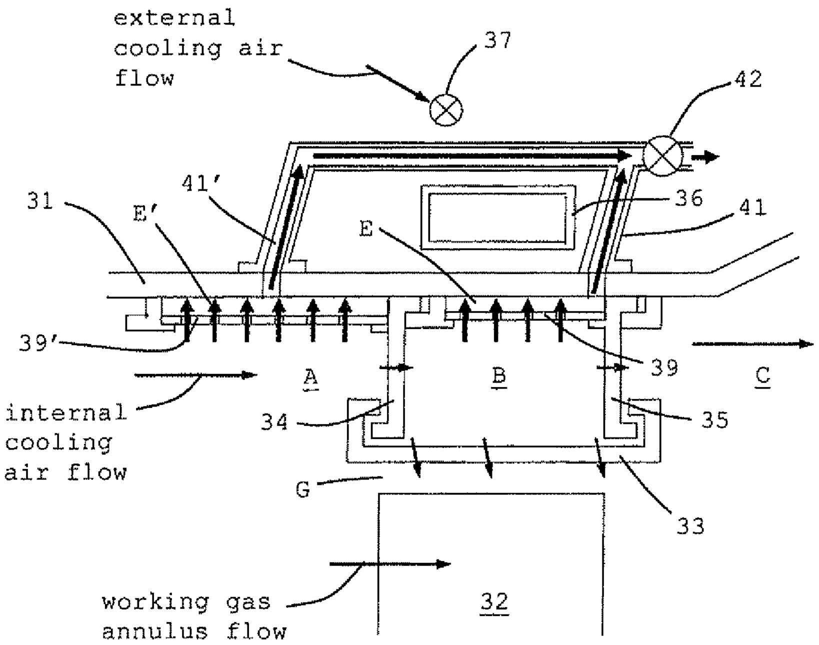

Figure 2.2: SCA concept for thermal actuation of the turbine casing from Lewis and Bacic [77].

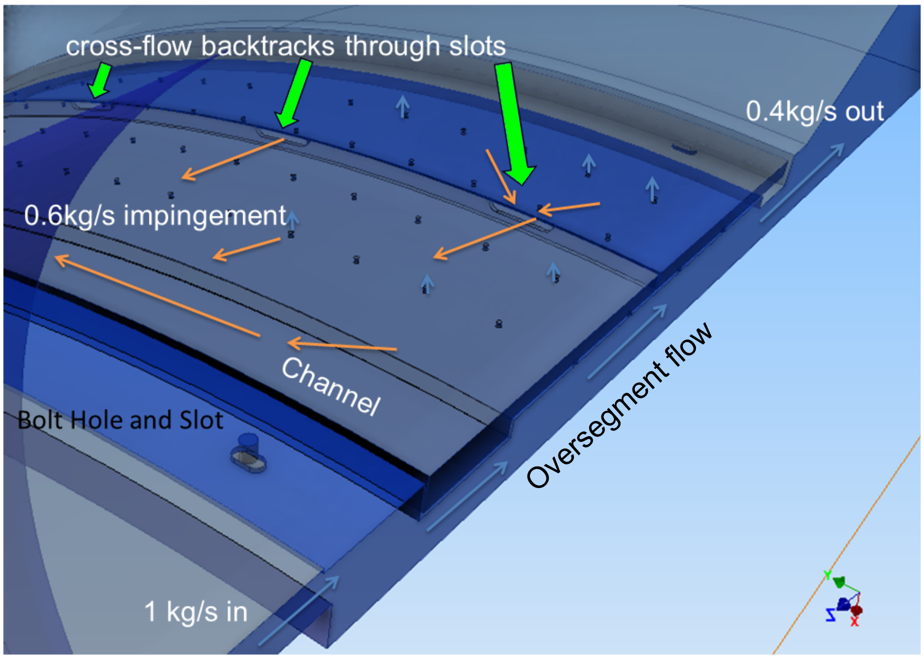

Figure 2.3: Close up view of the flow paths through the impingement system. Image taken from CFD model. The oversegment cavity air is shown in blue, it then passes through the holes, and the orange lines show where it turns back and enters the channel. The casing above the holes is transparent. The cross-flow slots exist in this configuration because the plate required the added bracing between the rows of holes.

of seal being used, which in turn make them highly temperature dependent. This makes such cavities difficult to study in small scale, room temperature experiments. Consequently the internal heat transfer, and its impact on cruise clearance, cannot be well understood until much later in the engine development program than desired. The only way to gain a better understanding of these characteristics before the engine development program starts is through a full-scale facility that replicates the engine geometries and sealing systems.

2.2.3 Facility Requirements

The THTF has been designed to recreate engine cruise conditions, as well as off-design conditions above and below the norm. Formally, this represents a technology readiness level 5 (TRL5) facility as per guidelines set forth by NASA [91]; a facility intended to identify and offset the problems that may be expected when moving to ground engine testing. The aim of the facility is to study the following research areas:

1. The performance of various internal heat transfer and flow configurations.
2. The 3D spatial distribution of the heat transfer coefficients.
3. The transient 3D metal temperature behaviour during flight cycle changes and its impact on asymmetric and axisymmetric tip clearances.
4. The realistic seal leakage and its impact on metal temperatures.
5. Different plate and casing geometries, for either turbine or compressors sections.

To achieve this, the geometry of the casing is representative of a real engine casing radius, length and thickness. The real engine material, Waspalloy, is not available, so it is important that the material of the casing has well defined thermal properties so that the results can be analysed with a non-dimensional approach. The air must flow past the casing and impingement plate as it would in the engine. The test section must be instrumented to validate the CFD predictions of the casing temperature transience and impingement plate pressure drop. Therefore thermocouples and pressure tappings must have a minimum sampling rate of $5Hz$, and be spaced sufficiently to observe any circumferential variations. The designated requirements based on large engine cruise conditions are listed in Table 2.1.

Parameter	Value	Tolerance
Inlet Air Pressure	10.3-17.2bara	5%
Inlet Air Temperature	≤810K	5%
Inlet Air Mass Flow Rate	≤1kg/s	5%
Mass Flow through each SCA Valve	≤0.6kg/s	5%
Pre-experiment Casing Temperature	≤670K	5K
Experiment Duration	10s	0.1
SCA Valve Opening Time	≤0.1s	-

Table 2.1: Facility Operating Conditions

2.2.4 Review of Similar Facilities

True scale facilities are rare as testing at low scale conditions can often yield sufficient results with the use of suitable non-dimensional analyses. This is especially common for rotating facilities, where it is difficult to replicate all aspects of component interaction, sealing, gas temperatures and pressures. Three such examples of scaled facilities are the Oxford Turbine Research Facility which generates heat using a free piston in order to measure turbine efficiency [15], the Cooled 1.5 Stage Facility at Ohio State University that uses a honeycomb matrix of resistive heating elements to create a sophisticated combustor emulator [94, 95, 96], and the upgraded Sussex Turbine Stator Well Facility that uses a Dart RDa 12 engine to drive a centrifugal compressor that provides the main annulus flow [33]. These facilities, operating at non-dimensional equivalent conditions to the real engine, provide technology readiness level 4 (TRL4) [91]. Facilities that can produce TRL5, and run at realistic pressure and temperature conditions, are less common, the main reasons being that:

1. Generation of mid- to high-stage HP compressor air is prohibitively expensive and sometimes involves the use of a small gas turbine (e.g. Corren *et al.* [33]).
2. Thermomechanical design challenges of such facilities usually require them to be built from high temperature materials that greatly increase the overall cost of the facility (e.g Lattime *et al.* [74]).
3. The harsh test environment adds significant challenges to instrumentation and data acquisition.
4. The complex nature of the build means that there is significant trouble to change out test geometries without major rebuild or re-instrumentation.

With these challenges considered, the focus remains on creating a facility that provides TRL5 results, including full 3D geometry, representative secondary air conditions, variable test configurations and the need to consider the leakage effects. One example that proves very instructive is the NASA Tip Clearance Control facility [74]. As stated earlier, the purpose of this facility is to evaluate novel mechanical ACC concepts under aircraft cruise conditions. The target conditions are similar to the objective targets in the present facility. An overview of the facility is shown in Figure 2.4 and a detail view is provided in Figure 2.5.

The NASA TCC rig recreates cruise conditions at 815°C and 827kPa. The test piece itself (the seal carrier assembly in Figure 2.4), sits directly inside an annular pressure vessel and has its own radiant heater to reach initial conditions. The fact that the vessel is both directly heated and heavily insulated means that it needs to be designed to resist creep. In this case the designers have assumed that it reaches 815°C uniformly. Furthermore, the annular-rectangular design of the vessel leads to large stress concentrations. These two factors make it necessary to construct the vessel from Inconel 718. The disadvantage of this high strength steel alloy is that it is expensive, has a large lead time and is difficult to machine.

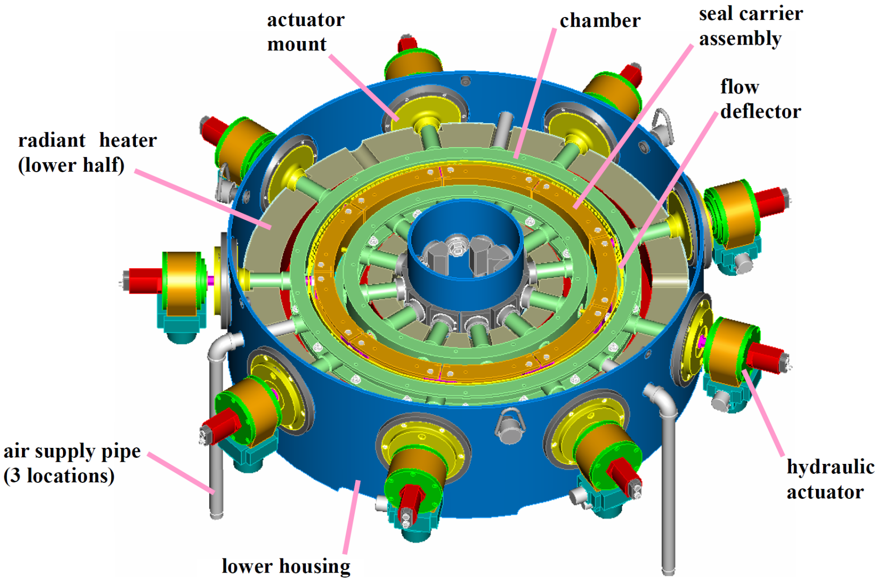

Figure 2.4: Overview of the NASA TCC facility with the housing lid removed [74].

The most useful feature inspired by the NASA TCC rig is the provision of the high temperature/high pressure air via the dual electric heaters. These heaters, designed and manufactured by Osram Sylvania, proved to be highly reliable at maintaining set point

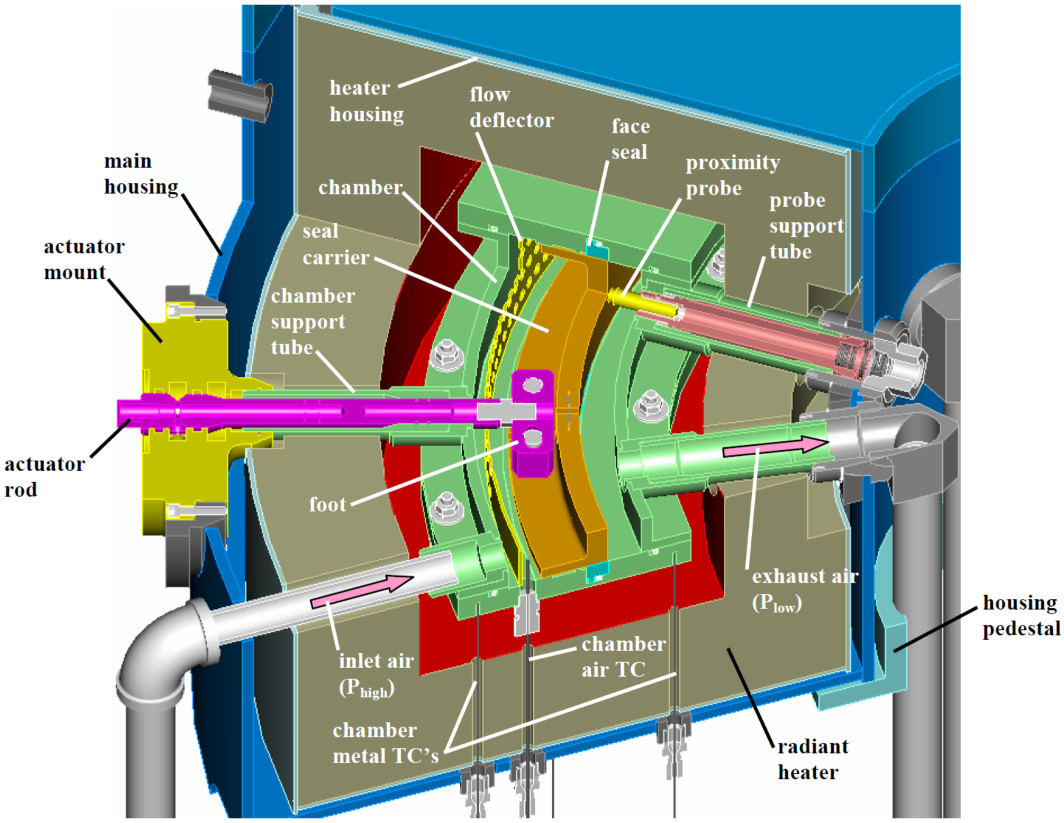

Figure 2.5: Detailed cutaway of the NASA TCC facility [74].

temperatures with relatively little pressure drop across them. However, the design only produced $72kW$ of heat input, while the objective of the THTF is to produce $1kg/s$ at $527^{\circ}C$ and $17.2bar$, which requires at least $500kW$ of heat input. There are three other methods of achieving these conditions as conceived from the literature;

1. Pass high pressure air through a heat exchanger, where the hot side is driven by a low pressure stream from a propane or methane burner, as described by Ireland and Jones [62]. (See Figure 2.6)

2. Use bleed air from a small gas turbine, such as a Viper or a Dart, as described by Coren *et al.* [33].

3. Use a gas fired burner to heat a ceramic pebble bed over a long time period, then use high pressure air pumped back through the bed to produce hot air for the test, as developed by Shreeve and Richmond [121]. (See Figure 2.7)

The heat exchanger has the benefit of using liquid fuel that has a high energy density, making it a cheaper source of energy than an electric heater. However, the hot side of the exchanger would be powered from a gas burner which usually operates at significantly lower pressures ($15-30kPa$). This means that the air density, and therefore mass flow rate, would be very sensitive to changing conditions on the cold side of the exchanger. So this design was ruled out as being very cumbersome from a control point of view. Moreover, the operating pressure difference between the sides of the heat exchanger presented severe mechanical challenges, and the lead time for a suitable, nickel-steel heat exchanger ruled this option out completely.

Another problem with bleeding air from a gas turbine engine or using a burner is that it would require careful management of the storage and supply of fuel causing an extra regulatory burden. Additionally, a gas turbine would have to be custom modified for this application and would require a costly installation.

The pebble bed facility would have produced an unsteady temperature stream, which would have made it very difficult to satisfy constant heat delivery objectives. Calculations showed that a pebble bed of viable size would also have taken approximately 6 hours to heat to the correct temperature and only provided hot air at a steady temperature for 4-5 minutes, leading to a very elongated test schedule.

As all of these alternative have significant problems, the most suitable and cost effective option is to heat the air using a custom-designed $650kW$ electric air heater. Effectively, a larger version of those used in the NASA TCC rig. The benefits include simple installation, flexible operation, consistent output, and high reliability. However, the consumption of air and electrical power for this option are both considerable, so a transient test procedure was developed to optimize the design of the new facility (Section 2.4.2). The design of the valve sequence, the heater power, and control valve settings of the THTF ensure that the facility can be brought to test conditions without exhausting the pressure margin of the supply air.

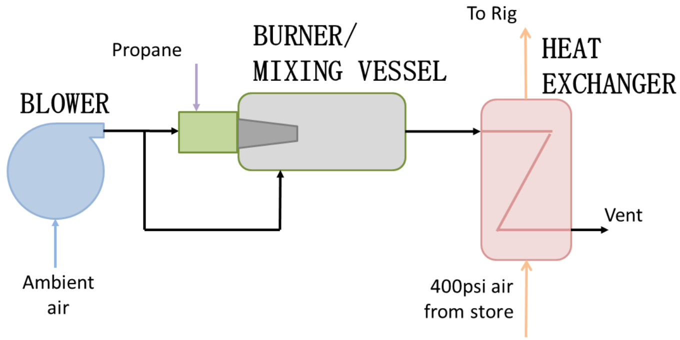

Figure 2.6: Heat exchanger assembly as an alternative heater design.

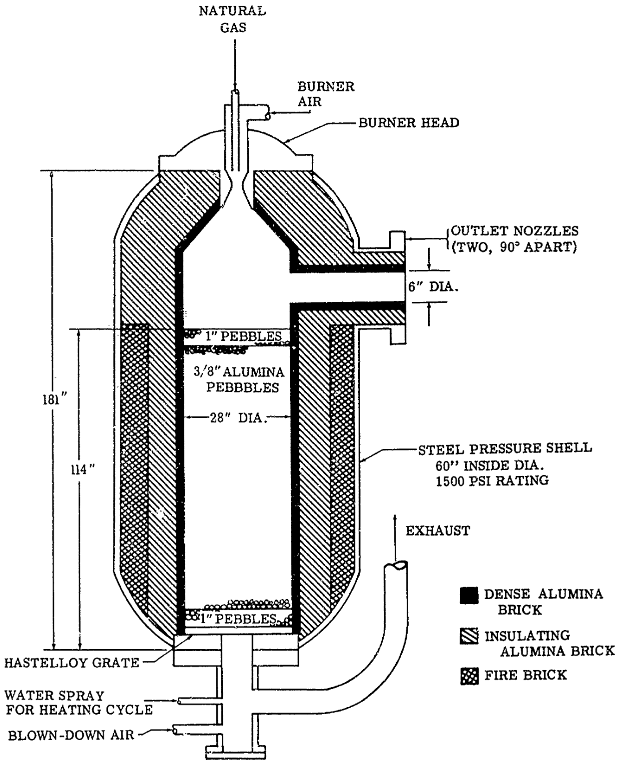

Figure 2.7: Pebble bed heater used in the BSRL Windtunnel Facility [121].

2.3 Facility Description

2.3.1 Casing and SCA Impingement Plates

The test casing is built from 316 stainless steel (316SS) and resembles engine geometry (see Figure 2.8). There are four offtakes built into the casing which draw air through the plenum created by the impingement plates. The SCA offtakes attach to flexible hoses that pass the hot gas to pipes, which in turn pass through the vessel wall (see Figure 2.11). Flexible hoses are used to accommodate differences in thermal expansion between components.

So far, two sets of impingement plates have been constructed. The hole pattern of the first set of plates have been designed following CFD analysis by Morris [100]. Their profile includes structurally important elements that would be required in the real engine that could affect the flow (see Figure 2.9). The second set of plates is more generic and has been used for fundamental research. Both sets of plates have been milled from 316SS by a CNC machine. There are a total of 20 plates in each set. Only results from the first set of plates are presented in this thesis. Each plate in the set has exactly the same design, though the instrumentation at the location of each plate is different. A detailed view of the plates and their instrumentation is included in Appendix A.

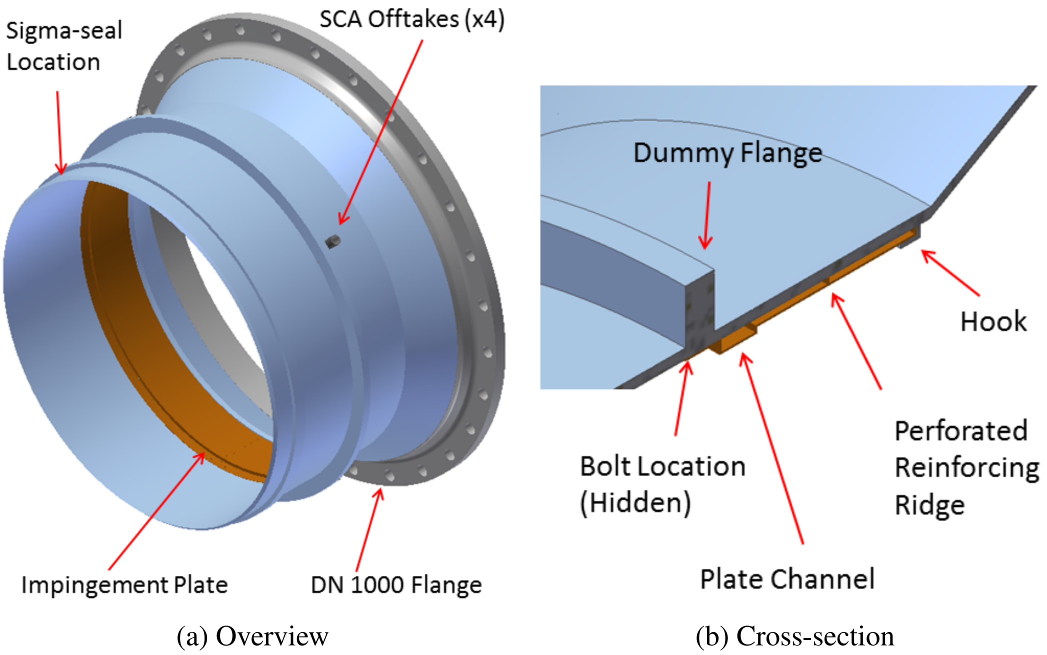

(a) Overview (b) Cross-section

Figure 2.8: Test casing replica of real casing design. The light blue matches basic real engine geometry. The orange section is impingement plate. The grey flange is for assembly purposes rather than experiment necessity.

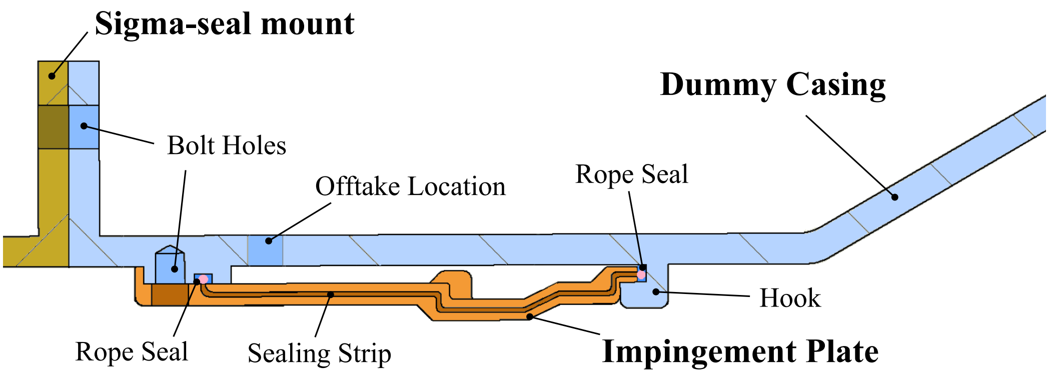

Figure 2.9: Sealing arrangement on impingement plates.

Many features of the real plates, that weren't necessary from an experimental point-of-view, found their way into the test plate design as they proved to be the only practical method to install and seal the system. For instance, the rear edge of the plates slot into a hook in the casing, and the front ends are bolted into the casing using bolts that span between the arcs of the plates (see Figure 2.10). The front and rear edges have been sealed with a rope seal supplied by Rolls-Royce. In order to seal the tangential gap between plates, there is a $1mm$ groove along their axial edge where a thin strip of metal has been cemented. These strips are only cemented into one edge of each plate in sequence, such that they slot freely into the groove of the neighbouring plate. The plates are also designed so that their arc length is 17.6°, just less[1] than the 18° necessary for the total to be 360°. This way, when the plates are installed in sequence, they can be forced together leaving a large enough gap for the final plate to be installed before they are all shuffled back to their intended position and finally bolted into place.

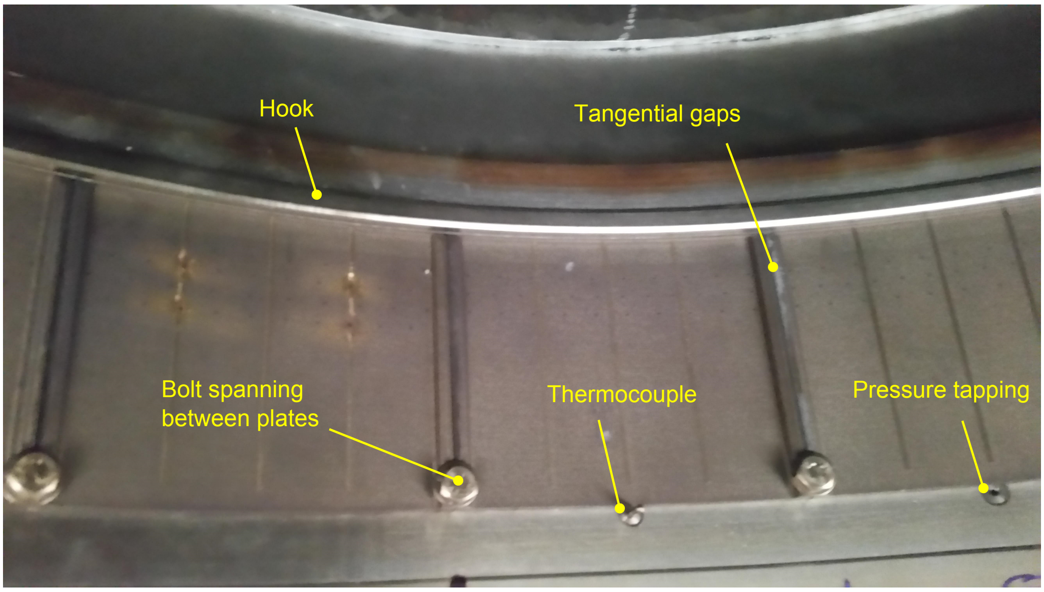

Figure 2.10: Picture of the plates installed in the casing.

The casing has been designed and built in conjunction with the pressure vessel that contains it. The test casing forms a closed volume within the pressure vessel by sealing at both the front and rear surfaces (see Figure 2.11, an early design of the vessel). The rear edge is attached via a standard DN1000 flange. The front end has a custom design compression seal with a "sigma" shaped cross-section. This is squeezed up against a machined surface in the front half of the vessel when closed. Finite element studies have shown that

---

[1] $0.4^\circ \approx 1mm$

the sigma-seal needs to accommodate strain ranging from 2*mm* of compression to 4*mm* expansion during an test cycle. The seal is formed from Inconel 718 using custom tooling.

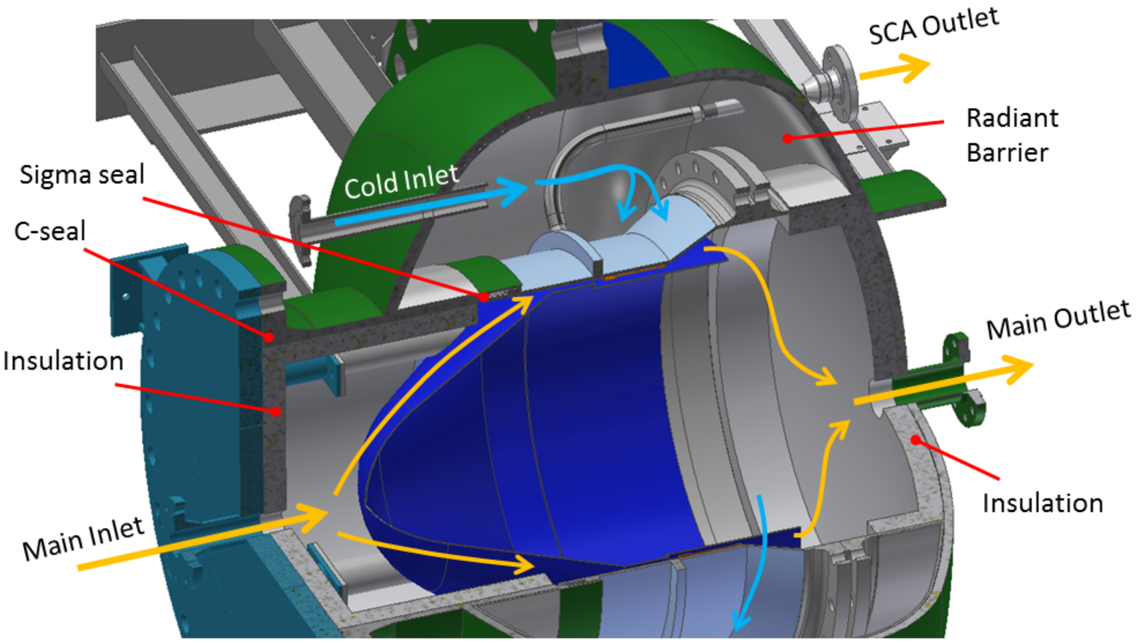

Figure 2.11: Internal flow paths and vessel features. The cold flow circulates around the entire outer cavity and exits from the bottom of the vessel.

2.3.2 Pressure Vessel

The vessel splits into four main sections as shown in Figure 2.12. It is 1800*mm* in diameter with a torispherical front end and hemispherical rear end. The front end has a 900*mm* flange that allows access to the internal test section without opening the entire vessel. The outer cavity between the casing and vessel wall provides thermal and pressure containment for the experiment. The extra space leaves room for future modification to the experiments. All sections of the vessel wall are insulated on their inner surface with 316SS sheets to keep the working fluid hot and the vessel walls cool.

The vessel has a design pressure and temperature of 1.9*MPa* and 300°C respectively. The vessel is protected from high temperatures by its sheer bulk and the short duration of the heating period. The low design temperature allows the pressure vessel to be built from the relatively cheap P355NL1 steel. However, at the inlet and outlet nozzles where convective heating is highest, Inconel 718 inserts have been used to provide thermal protection. Further analysis of this design is included in Section 2.4. The 900*mm* front flange is sealed with a Waspalloy c-ring similar to the sigma-seal (Figure 2.11), however the 1800*mm* flange uses a rubber o-ring because the air is kept relatively cool in this region. The other inlet, outlet, and instrumentation nozzles are sealed with graphite gaskets for the high temperature flows.

The fourth section of the vessel that has not yet been discussed is the central 'bullet' section. Hot air that enters the vessel through the central inlet first encounters the bullet and is distributed uniformly to the annular cavity of the test section. This central body increases the Reynolds number at the test section to 3000, similar to the oversegment cavity in the real engine. In this case, the characteristic length for determining the Reynolds number is based on the radial clearance between the bullet and impingement plates.

The hot air within the central cavity can exit the vessel via either the four SCA offtakes (CV2) or through the main outlet that is controlled by a variable globe valve (CV1). The vessel outer cavity has one inlet and one outlet. The outlet is split in two, one path through a ball valve (CV3) that allows the air to be dumped quickly as required, and one path through an orifice plate that cannot be closed and safeguards the vessel against ever being left pressurised. A full pipeflow diagram that includes these valves is shown in Figure 2.14.

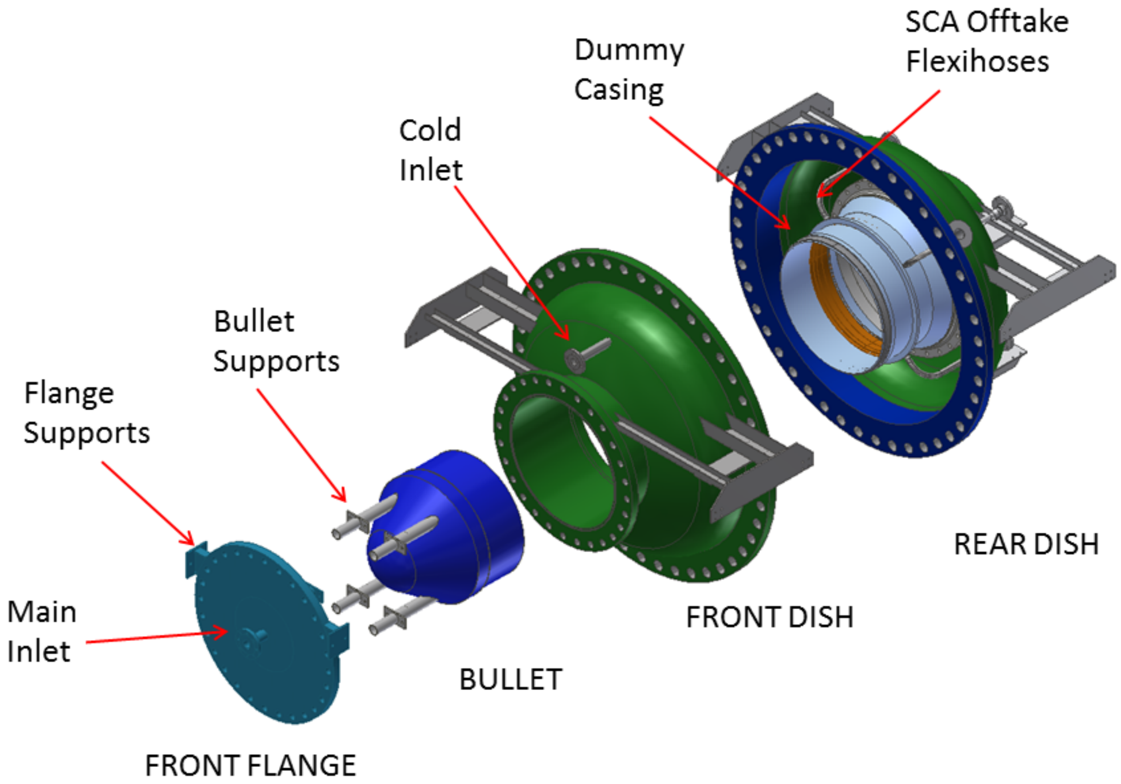

Figure 2.12: Exploded view of the vessel assembly. The bullet is bolted to the front flange. Each other section is supported on a rail system that allows each piece to move independently when unbolted.

2.3.3 Air Heater

The electric air heater is shown in Figure 2.13. When first procured, the 650kW air heater was a unique design from the manufacturer though it has since been copied for similar projects. It consists of a stainless steel housing with 48 parallel resistive heating elements made of copper coils. It is capable of delivering up to $1kg/s$ of air heated to $530°C$ as demonstrated in commissioning, though there is potential for more. The heater is controlled via power thyristors using 3-phase $415V$ supply and providing up to $1200A$ of continuous current. There are four thermocouples providing overheat protection positioned downstream of the heating elements spaced circumferentially 90° apart. One of these thermocouples is used in a PID loop to regulate the gas exit temperature, which can reach a set point accuracy of $\pm2^\circ$ under steady state conditions. There is an additional mass flow sensor to detect low-flow or no-flow conditions to prevent the heater potentially over-heating its elements.

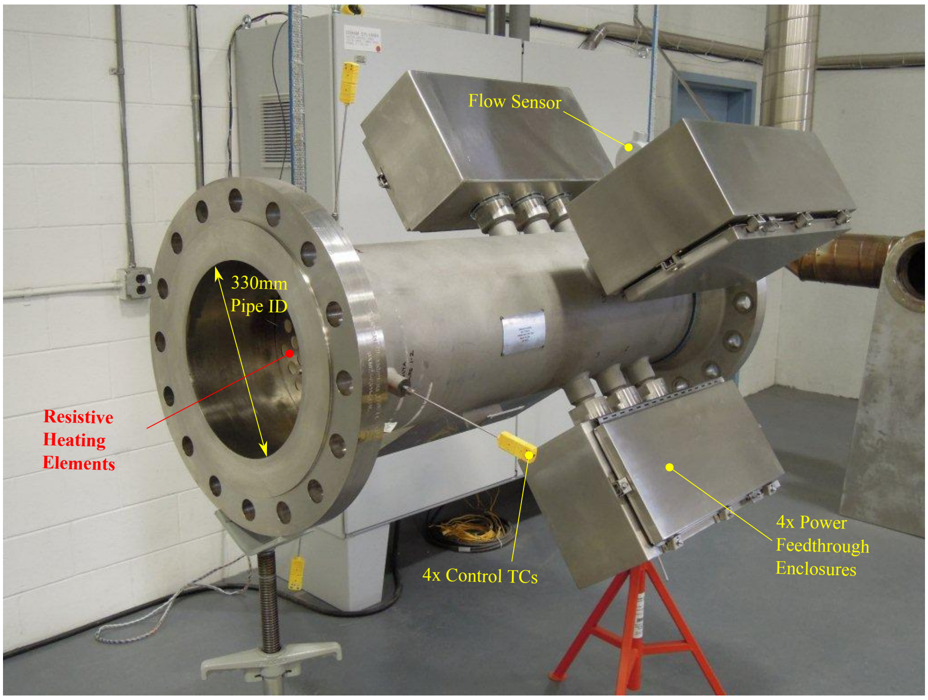

Figure 2.13: Osram Sylvania Ultra-High Temperature Air Heater.

2.3.4 Rail System and Power Supply

The heater and vessel are both suspended on a rail system in order to accommodate movement during both thermal expansion and for opening of the vessel. The rails maintain the alignment of the components when it is pulled apart. The rail height is set above the centre of gravity of the both the vessel and heater so that they don't tip while being moved. The vessel itself is 500mm above the floor so that the lower bolted connections can be accessed. The power supply to the heater has its own flexible track that enables the heater to be moved without the need to disconnect any electrical connections.

2.3.5 Valves and Pipes

The complete set of valves used in the THTF are shown in Figure 2.14 (a simplified version and description of operation is shown in Figure 2.16 and Section 2.3.8 respectively). The control of the flow through the facility is based on pressure regulation upstream of the test piece, with flow regulation downstream. This recreates the mechanisms governing flow in the real engine. All flow paths are maintained at choked conditions in order to simplify the calculation of mass flow rate. For instance, CV1 and CV4 have a known discharge coefficient curve related to their opening angle provided by the manufacturer. The flow is controlled in closed loop on the basis of the valve upstream pressure and temperature measurements giving mass flow accuracy of $\pm 0.05 kg/s$ at the nominal facility operating flow rate of $1 kg/s$. The mass flow through the CV2 valves is governed by choked orifice plates calibrated to British Standards BS1092, and monitored with upstream pressure and temperature measurements. The valves themselves have actuators capable of providing full flow in under $0.1 s$.

The heated bypass line that passes through IV4 and CV4, shown in Figure 2.14, solves an important design problem. The offtakes in the SCA system must be able to switch on quickly, drawing additional mass flow through the vessel inlet. At the same time, the core flow that passes through the test piece without going to the SCA system must be maintained (usually about $0.5 kg/s$). This means that extra hot air must be delivered from the air heater. In a real engine this extra demand is small (0.4-0.6kg/s) compared to the throughput of the primary flow (200-300kg/s). However, the air heater would not be capable of providing the air so rapidly as it takes time to adjust to the new power requirements. By including a bypass line, the extra air can be pre-emptively bypassed around the vessel until such time that it is required. A detailed analysis was undertaken to co-ordinate the valve sequencing and predict any problematic responses of the complete air system. This is shown in Section 2.5.

The bypass line has two valves; a butterfly valve (IV4) that can match the actuation speed of the CV2 valves, and a globe valve (CV4) that grants the operator a high level of control over the flow. Fine control is required because the pressure drop of the impingement

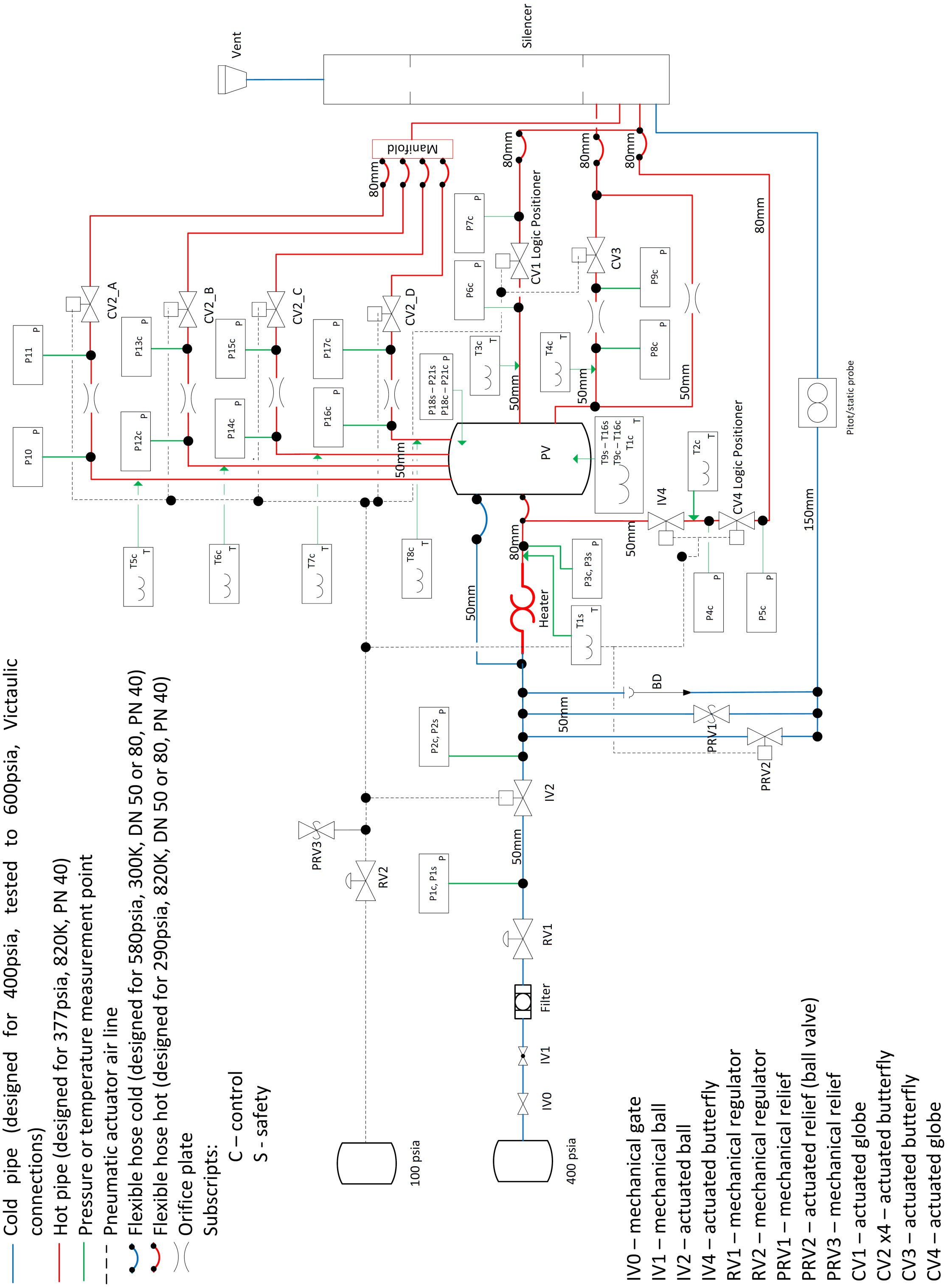

Figure 2.14: Overview of THTF pipework and instrumentation.

plate is unknown. The required discharge rate through CV4 is managed heuristically every time the pressure regulator is set. Once CV4 is first set correctly it can be left for the remainder of the experiment as the mass flow is not strongly correlated with temperature.

The cold flow pipework is constructed using Victaulic couplings for ease of assembly and re-assembly. Hot flow pipework uses a combination of stainless steel pipes and reinforced hoses, all of which are insulated in order to both ensure maximum heat is delivered to the vessel and to protect facility operators. The hoses also accommodate differences in thermal expansion, just as they do inside the vessel. The silencer, exhaust ductwork and chimney are also stainless steel, and have been designed to prevent ingress of weather back into the facility.

All of the valves are fitted with mounting kits designed to limit the amount of heat conducted up into the actuators. The actuators are all either pneumatically single- or double-acting, using air from a separate $690 kPa$ supply line. The actuated valves are controlled centrally from the control room computer via two programmable logic controllers (PLC).

2.3.6 Control and Safety Systems

To ensure safe operation, the facility control systems and safety systems are separated. All rig control valves are ultimately controlled by a purpose built ‘control’ PLC which is further monitored by a second independent ‘safety’ PLC. These two PLCs have internal software to ensure that the vessel’s pressures and temperatures stay within the design limits. The operator controls the valves via a Labview interface on a desk top computer that then communicates with the control PLC via an ethernet link. The control PLC vets those commands to ensure safety and operability. The safety PLC monitors the facility conditions directly and shuts it down if preset design limits are exceeded. Examples include over-pressure, over-temperature, and uneven pressure distributions.

2.3.7 Instrumentation

The facility is fitted with pressure transducers (PTs) and thermocouples (TCs) for data acquisition, live control, and safety. The position of the 21 PTs and 20 TCs for control and safety are shown in Figure 2.14. There’s a further 48 PTs and 88 TCs directly at the casing reserved exclusively for data acquisition. Of the 88 TCs, four measure the air in the annulus free stream, four measure the air in the offtake tubes, and 40 each are spot welded on to the outside and inside of the casing to measure the metal temperature. The casing

TCs are shown in Figure 2.15. A more detailed account of all of the experimental TCs and PTs are contained within Appendix A.

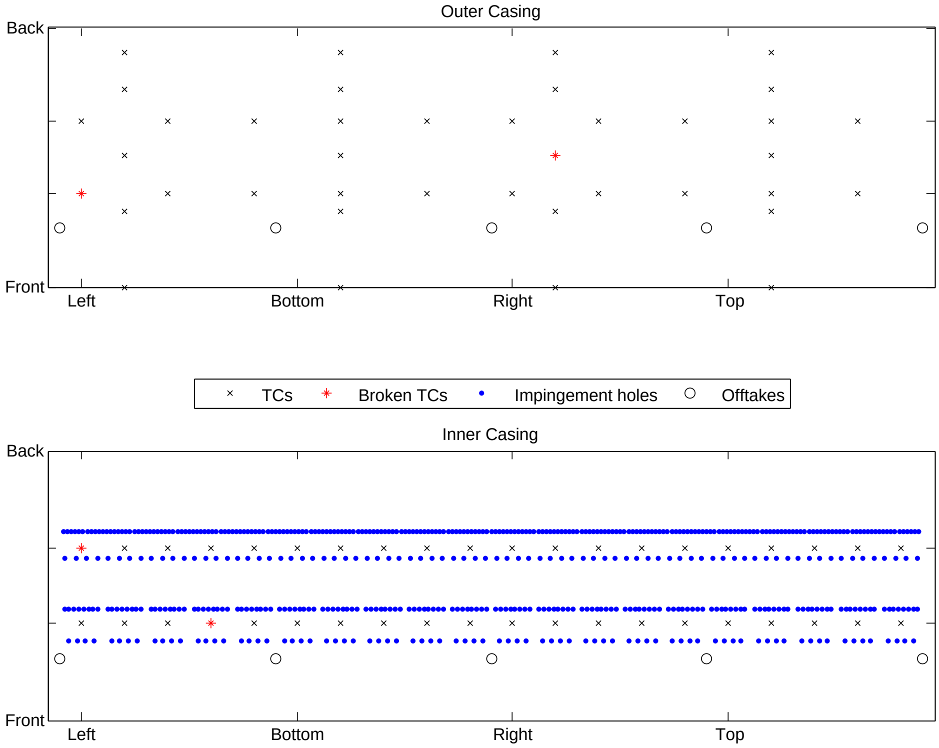

Figure 2.15: Position of temperature measurements in the casing.

The control PT located before IV2 (i.e. P1c) has a range of $0-35bara$, while all remaining PTs have a range of $0-20bara$. All the PTs have an accuracy of 0.3% full scale. All of the TCs are K-type with a range of $273-1373K$ and an accuracy of $\pm 2.5K$ for $233-606K$ and $\pm 0.75\%$ for $606-1473K$.

The experimental data is recorded at $10Hz$ using a National Instruments PXI/SCXI combination chassis system. This incorporates SCXI-1102 thermocouple amplifiers and a PXI-6225 multifunction data acquisition device.

2.3.8 Overview

A CAD diagram of the general arrangement of the facility is shown in Figure 2.16a, with a basic overview of the pipework shown in Figure 2.16b. Other components that have been installed as part of the facility include the data acquisition system, the heater control system, the heater power supply, the fence enclosure and the control room built for the facility operators. Air is supplied from two onsite reservoir tanks with a capacity of $30m^3$ each at $27.6barg$. There is a separate air system which provides $690kPa$ of pressure to the valve actuators. The supply of air to the experiment is controlled by a large, swing-lever ball valve. Once this is turned on, there are two further manually operated isolation valves which are dedicated specifically for this facility (IV0,IV1). Having two valves creates a redundancy safety mechanism. Furthermore, IV1 is a gate valve that gives an operator fine control of the rate of pressurisation. The air initially pressurises only a small section of the facility up to the oil filter, the pressure regulator and the isolation valve IV2. Full facility pressurisation is managed via IV2 remotely, so that the operators can work from the control room. The pressure regulator is manually set by the operator prior to full facility pressurisation, with a target pressure about 10% higher than the target value under free flow conditions. The remaining valves in the system can all be actuated remotely as well. The control signals of all the actuated valves, heater commands, and any other commands, are issued via the PLCs.

A picture of the pressure vessel is shown in Figure 2.17. During normal operation, the air heated by the electric heater enters the vessel's inner cavity via the central inlet nozzle. This can be seen on the left side of the photo. Cold air enters the outer cavity of the vessel at the inlet as shown at the bottom left. On the right of the photo are the multiple exit paths through which all the air from the vessel flows; one hot outlet from the central volume, four hot outlets from the SCA system, and one cold outlet from the outer cavity. Two of the eight instrumentation nozzles can also be seen. All of the air flow paths, including the bypass line and the emergency relief system (hidden), exhaust to atmosphere through the silencer. The silencer has the same pressure capacity as the vessel, and can pass twice the air flow, whilst providing acoustic protection to operators.

2.4 Design of the Pressure Vessel

2.4.1 Analytical Approach

Pressure vessels that are built to British Standards are either designed "by formula" (as given in the standards) or "by analysis" using detailed thermal and structural FE simulations. Since the pressure vessel houses dual inner volumes and has a complex geometry with very particular dynamic heat transfer effects, this requires an FE analysis. The FE software SC03 [4, 8, 63, 126, 127] has been used to model the vessel, casing and test section. The design was conducted in two stages, first the preheat cycle analysis, and then the

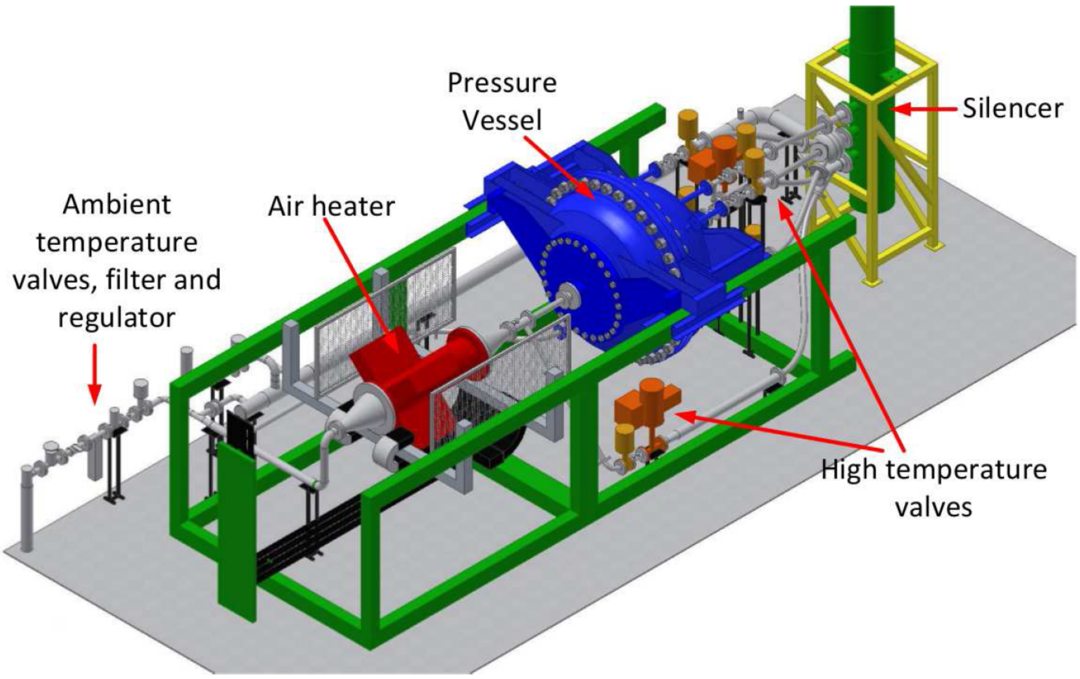

(a) CAD model

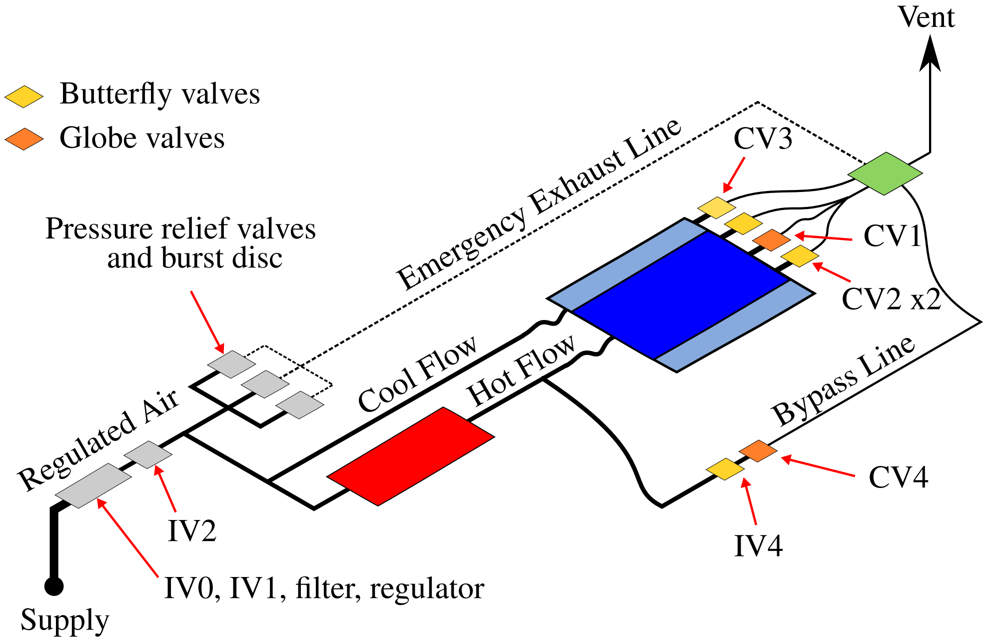

(b) Basic outline of pipes, valves and key components

Figure 2.16: Overview of the Transient Heat Transfer Facility.

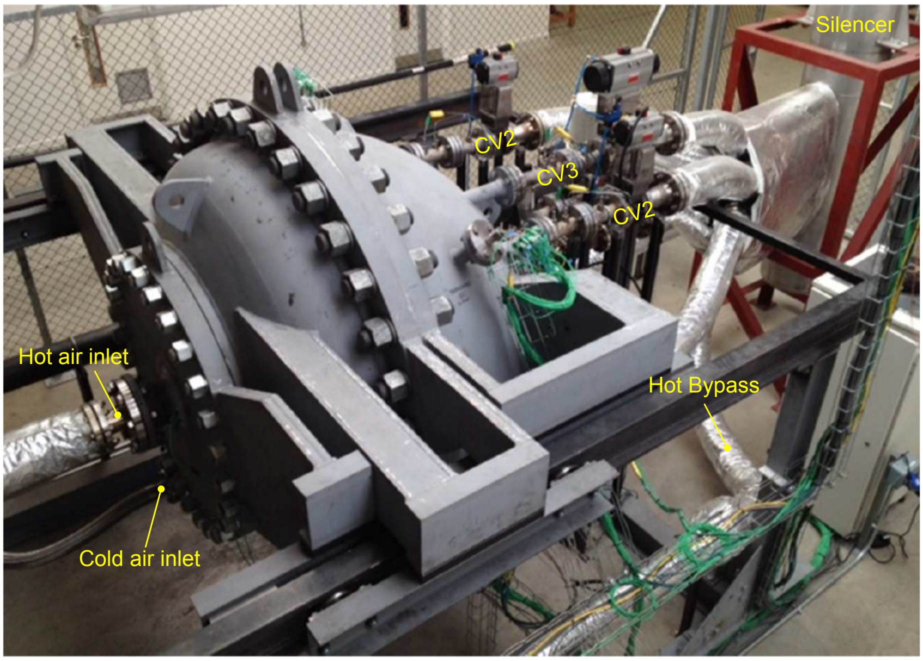

Figure 2.17: Photo of the pressure vessel, rail system, hot valves, pipes and instrumentation.

thermomechanical analysis. To simplify the design process, only 2D axisymmetric models of the vessel are considered. 3D components, such as nozzles and lifting points, are easy to add to the final design following standard design procedures. The vessel wall, nozzle and flange thicknesses are selected to satisfy British Standard PD5500 using Ohmtech Visual Vessel Design software [9]. The Ohmtech software is effectively a codified version of PD5500 into a vessel design program, but unfortunately the design task was too complicated to manage completely within the Ohmtech environment. However, for the outer parts of the vessel, this software proved invaluable. The initial design choices for the wall and flange thicknesses were consistent through to the final design.

For each iteration of the design, SC03 generates an unstructured mesh using triangular elements. Each edge is given thermal boundary conditions, usually one convective and one radiative, and SC03 is able to integrate the 3D axisymmetric heat flux over each surface. The boundary condition treatment for the final model is shown in Figure 2.18. Radiation boundary conditions are either ‘external’ or ‘internal’. External radiative heat transfer $\dot{Q}_{rad,ext}$ is calculated as;

$$\dot{Q}_{rad,ext} = \varepsilon \sigma_{SB} A (T_w^4 - T_{amb}^4) \tag{2.1}$$

Where ε is the emissivity of the surface, σ_{SB} is the Stefan-Boltzmann constant ($5.67 \times 10^{-8} W/m^2/K^4$), A is the projected surface area, T_w is the wall temperature and T_{amb} is the temperature of the ambient fluid far from the surface. Internal radiation is calculated by integrating the view factor between any two surfaces that have been manually identified as having significant radiative heat exchange. The internal radiative heat transfer between two surface elements (1 and 2, as highlight in Figure 2.18) can be calculated as;

$$\dot{Q}_{rad,int} = \frac{\sigma_{SB}(T_1^4 - T_2^4)}{\frac{1-\varepsilon_1}{A_1\varepsilon_1} + \frac{1}{A_1 F_{12}} + \frac{1-\varepsilon_2}{A_2\varepsilon_2}} \tag{2.2}$$

Where the view factor, F_{12}, is geometry dependent and represents the fraction of the energy emitted by surface 1 that impacts surface 2. The convective boundary conditions are calculated based on the wall temperature, the fluid boundary temperature (T_f) and the heat transfer coefficient (h);

$$\dot{Q}_{conv} = hA(T_f - T_w) \tag{2.3}$$

For external surfaces, it is assumed that h obeys natural convection, typically $20W/m^2K$, and that the ambient temperature is $293K$. Natural convection also dominates the inner surfaces of the outer cavity of the vessel, but the air temperature is partially dictated by a slow flow from the cold inlet. In this case, the program assumes that the volume of fluid acts like it has a single heat capacity. All the surfaces tend towards thermal equilibrium by assuming that the air transfers heat to every other surface in the cavity, while at the same time slowly extracting some heat through the cooling flow. The cooling flow heat loss is expressed as a power term P_{input}. The fluid temperature can be calculated as;

$$\rho V c_p \frac{\partial T_f}{\partial t} = \int h(T_f - T_w).dA + P_{input} \tag{2.4}$$

The inner cavity takes this process a step further. The flow has a designated start and finish along each surface. Heat can be picked up and deposited along the flow path. Where the volume opens up, the mass flow is divided between the two facing surfaces. Heat transfer coefficients for narrow passages are calculated using the correlation created by Nunner [101] which use Re, Pr, friction factor (f), and boundary layer development term (f/f_0) to give an approximation of the local Nu;

$$\mathrm{Nu} = \frac{\frac{f}{8}\,\mathrm{Re}\,\mathrm{Pr}}{1 + 1.5\,\mathrm{Re}^{-1/8}\,\mathrm{Pr}^{-1/6}(\mathrm{Pr}\frac{f}{f_0} - 1)} \tag{2.5}$$

By using conservative estimates for values such as HTC, it is possible to create 'worst case' scenarios that can be used for proof-of-concept warm up cycles (Section 2.4.2) and structural design extremes (Section 2.4.3). Inputs such as pressure, temperature and mass flow can all be specified for the intended design cycle in a similar fashion.

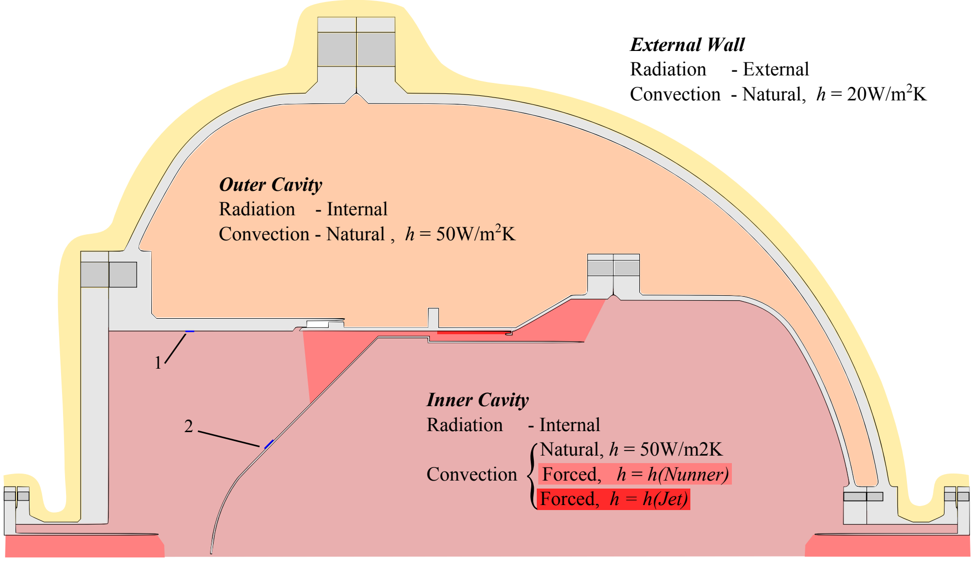

Figure 2.18: Thermal boundary conditions used in SC03 analyses. Surface elements 1 and 2 are examples for the calculation of internal radiation.

2.4.2 Preheat Cycle Proof-of-Concept

Experiments in the THTF are usually carried out with a starting gas temperature of $770K$, and casing temperature of $600K$. However, the facility has limitations on supply air and electrical power that places constraints on the preheating process. Preheating the experiment with natural convection would take several hours, however the presence of an impingement system allows us to speed up the process by an order of magnitude. It was important to design an operating sequence that would heat the casing to test conditions under the worst case scenario within a reasonable time scale. To that end, an analysis was undertaken in SC03 to predict the thermal response of the casing during the warm up period. The restrictions on operating conditions were;

1. Only the impingement system could be used for heating the casing. No external heat blanket or similar are provided. CFD by Morris [100] showed that the impingement should produce $990W/m^2K$ with $0.6kg/s$ input, and that the HTC is roughly proportional to the mass flow.

2. The emissivity of steel is taken to be 0.7. No insulation or radiant barriers are included.

3. The air heater takes 5 minutes to reach $500kW$ of output. This was the longest quoted time from the manufacturer. The analysis assumes that the time required to achieve

any fraction of this power is directly proportional.

4. The SCA offtakes limit the flow to $0.2kg/s$ at maximum pressure. This is based on the orifice plate with the smallest opening as per the test program.

5. The average HTC on the external surface of the casing is $50W/m^2K$. This is a conservatively large estimate for free convection.

6. The maximum available air from the supply receivers is $375kg$ without using the compressors for top up. This is the most air that can be taken from the $30m^3$ capacity before pressure drops below $1.72MPa$.

7. The supply air can be supplemented by compressors, but this is limited to 0.27kg/s. This is the combined output for two $90kW$ Bauer "A28.3" compressors currently onsite. Once the facility draws more than this, the air receivers will begin to deplete. We also assume that only one receiver is available.

8. The minimum volumetric flow through the air heater is $150cfm$ ($0.071m^3/s$). This is suggested by the manufacturer to avoid tripping the low flow sensor.

The proposed heat up cycle is shown as Stage 1 and Stage 2 of the full test cycle, as illustrated in Figure 2.19. In the full cycle, Stage 3 represents the period where the section is at correct temperature and pressure conditions, but the mass flow has been directed into the bypass line is provides an opportunity to tune CV4. Stage 4 is the test itself and Stage 5 is the cool down. As for the preheat cycle, Stage 1 uses just the compressors to allow the heater to warm up to full temperature without draining the receiver. There is a limit to the maximum pressure that can be achieved using the maximum compressor flow rate and minimum heater flow rate (conditions 7 and 8). This pressure is given by the perfect gas law;

$$\rho = \frac{\dot{m}}{\dot{V}} = \frac{0.27}{0.071} = 3.8kg/m^3 \tag{2.6}$$

$$P = \rho RT = 3.8 \times 287 \times 810 = 880kPa \tag{2.7}$$

This is 52% of $1.72MPa$, the maximum pressure, therefore the total flow through the SCA offtakes in Stage 1 is limited to 52% of the mass flow rate at maximum pressure, which works out to roughly $0.1kg/s$ (condition 4). Because the inter-hole spacing of the impingement plate is large, we can further assume that the HTC achieved under the plate is proportional to the mass flow [55], so the maximum HTC during Stage 1 is about $165W/m^2K$.

Stage 2 of the warmup procedure is the controlled pressurisation of the facility to desired test conditions using a high mass flow rate. This is when all the receiver begins to drain. Even if not all of the flow is diverted into the impingement plates, the increased flow rate decreases the overall warm up time further because there is proportionally less heat lost to the vessel. Stage 2 of the cycle pushes the total flow rate across both systems to $1kg/s$. A plot of the casing temperature responding to the prescribed warmup cycle is shown in Figure 2.20.

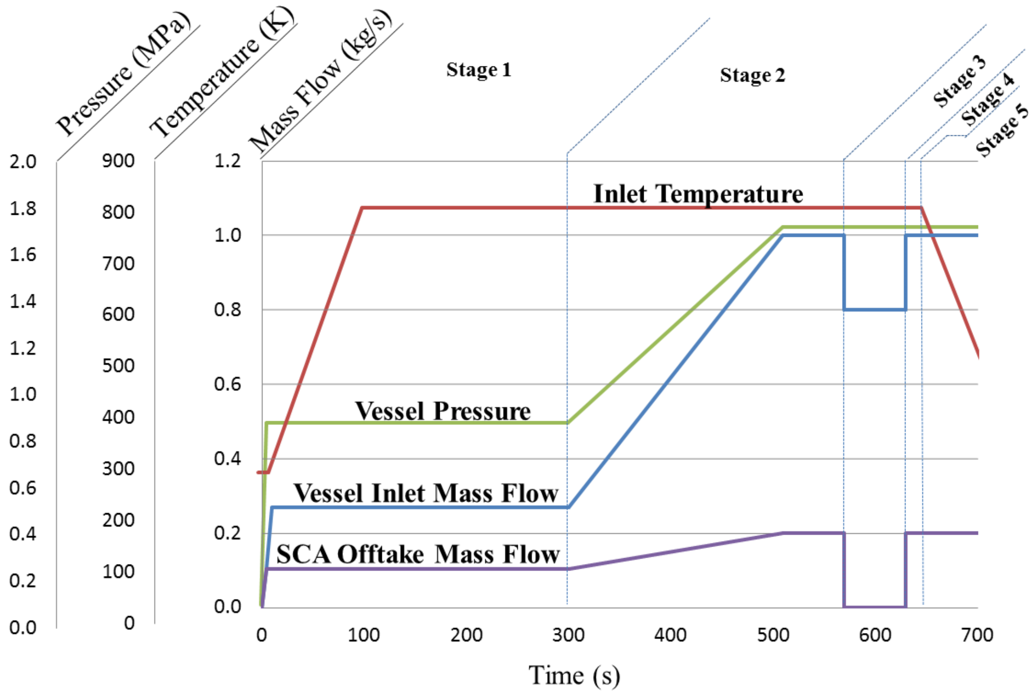

Figure 2.19: Inlet conditions for the preheat and test cycles. The five stages shown are 1. Low Flow Power Up, 2. High Flow Power Up, 3. Bypass Line Tuning, 4. Experiment, and 5. Cool Down.

The results show that pre-experiment temperatures can be achieved within 500 seconds. The total air used up to the end of the test stage (for the cycle shown) is $330kg$, of which only a net of $170kg$ has been depleted from the receiver, meaning that the test pressure can be maintained. The temperature profile at the peak of the cycle is shown in 2.21 (note that this analysis was conducted on an early model of the vessel).

From this analysis it was observed that radiation barriers on the inside of the vessel wall could reduce wall temps by up to $80K$. Insulation and thermal barrier coatings on the vessel wall and bullet respectively could help keep the air temperature at the plate higher

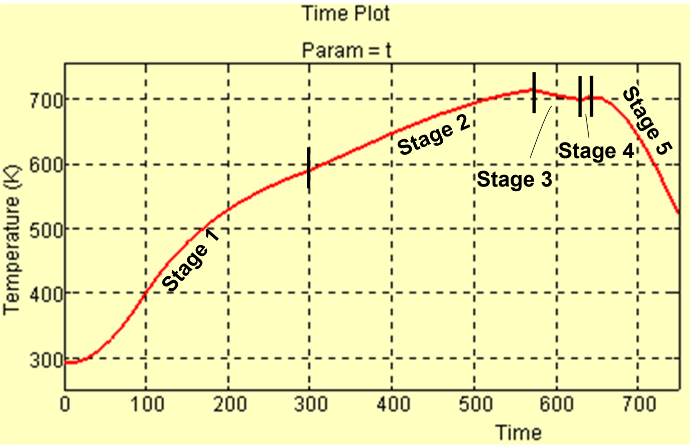

Figure 2.20: Test casing temperature during the preheat and testing cycle.

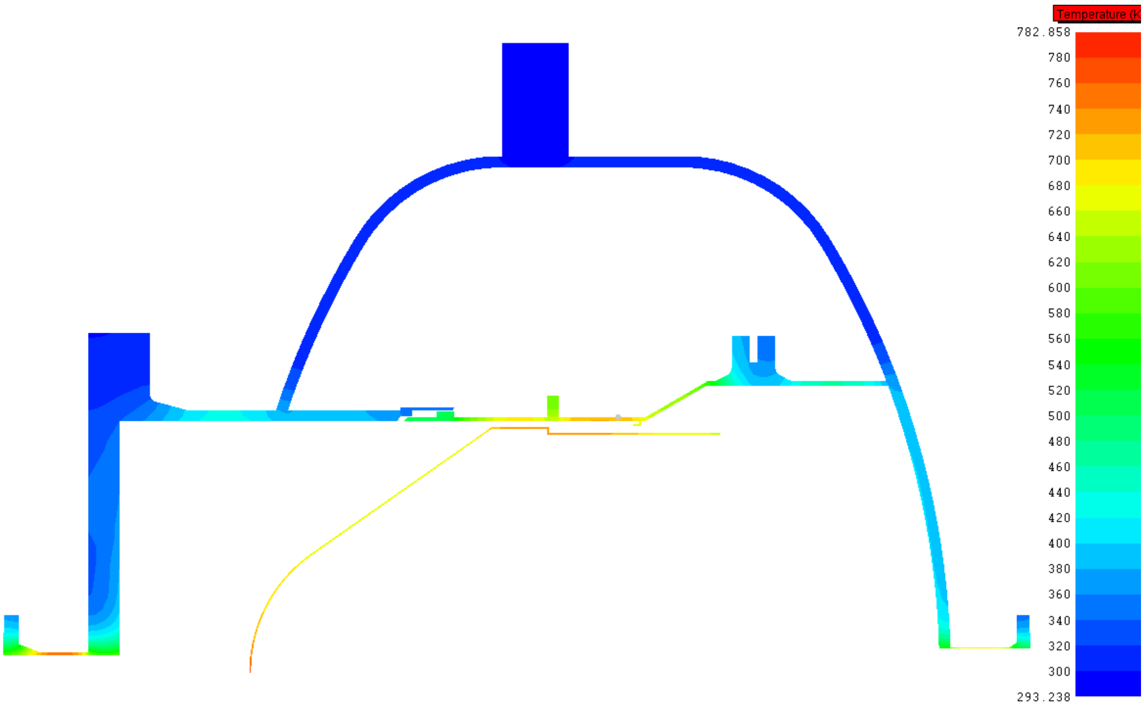

Figure 2.21: Temperature Profile of the vessel at 570s through the cycle.

as well. Finally, thermal protection is absolutely required in the nozzle entry points due to the excessive local HTCs. A validation experiment for this preheat cycle is presented in Section 2.8.2.

2.4.3 Vessel Design Iteration with SC03

The vessel design shown in Figure 2.21 represents one of the first designs to undergo a full thermomechanical assessment. The vessel has a design pressure and temperature of $1.9MPa$ and $300°C$ respectively. There are two reasons to target $300°C$. Boiler steels operating up to $300°C$ do not need to be designed for creep failure. Secondly, the design strength of carbon steels falls drastically with temperature, and are not allowable at all above $400°C$. So by keeping the design temperature low allows for more flexibility in the material selection. However, this creates tough design challenge as the desired operating air temperature is $497°C$.

The thermal and mechanical properties of the materials used in this facility, and for the casing (Waspalloy), are shown in Table 2.2. This table also shows the sudden loss of strength of the boiler steel (PN355NL1) above $300°C$. An uninsulated vessel containing hot air under steady state conditions will naturally tend towards an average wall temperature halfway between the internal and external air temperatures, assuming similar rates of convection. This is under the assumption that the vessel is large enough that the wall thermal profile can be approximated by a 1D infinite plate heat transfer process. So, for the present vessel, this average temperature would be $260°C$. For the vessel to actually uniformly meet this temperature is physically impossible from a maximum energy point of view. Suppose that $500kg$ of air was available (as a worst case) and this is heated at $1kg/s$ with the $650kW$ heater. The energy delivered ($325MJ$) could only heat the $6000kg$ vessel by $110°C$. As such, we can limit the scope of the analysis to the real concerns, which are the heat and stress concentrations, by applying inputs with an energy total above $315MJ$.

Conservative inputs are considered for running simulations to ensure that any design that passed the simulation will be overdesigned in reality. These inputs include that the pressure starts at $1.9MPa$ throughout the vessel, there is a maximum flow of $1kg/s$ entering the inner cavity ($0.6kg/s$ to the SCA offtakes, $0.4kg/s$ to the main outlet) and only a minimal cooling flow ($0.05kg/s$ to outer cavity). We ignore the heater warm up time, and assume the air starts at $810K$. By limiting simulation run times[2] to $1000s$ the total energy

---

[2] $1000s$ was considered as a good compromise between achieving suitable test conditions and limiting the heat that could be absorbed by the vessel.

input is roughly 525MJ based on the theoretical power delivered by the heater. This is far higher than any real experiment could deliver.

Property		Carbon Steel PN355NL1	Stainless Steel 316	Inconel 718	Waspalloy AMS 5544
Yield Strength (MPa)	at 20°C	345	260	1 100	910
	at 300°C	225	155	1 000	826
	at 500°C	N/A	135	980	770
Young's Modulus (GPa)	at 20°C	203	193	200	213
	at 300°C	185	179	185	198
	at 500°C	150	168	173	186
Conductivity (W/mK)	at 20°C	14.9	16.2	11.4	11
	at 300°C	18.4	20.0	15.7	14.2
	at 500°C	21.0	21.4	18.9	17.4
Coefficient of thermal expansion ($\mu m/mK$)		17	17.5	13	13.9
Specific Heat Capacity (J/kgK)		455	500	435	520
Density (g/cm^3)		7.8	8.0	8.2	8.2

Table 2.2: General material propeterties for metals used in the THTF. Precise values rely on final treatments.

The design is progressed in iterations using a limit of 50% yield stress as a bench mark for the average Von Mises stress across the thickness of the wall, and 100% yield stress as the maximum for stress concentrations. These are based on discussions with stress experts on failure analysis and the desired service life of the vessel (20 000 cycles). Figure 2.22 shows an example of a mesh used for a thermomechanical simulation. The thermal BCs were shown in Section 2.4.1. The model assumes that there is no insulation or radiative shielding. The pink lines on the mesh highlight where the geometry is discontinuous near bolted faces. When modelling bolts in FE simulations it is necessary to break up the contact between flange faces to allow appropriate flexure of the rest of the shell, however, any stresses at the bolted faces can be ignored as artifacts of the simulation. Bolted connections can be readily designed according to standard design codes.

Figure 2.23a shows the worst principal stresses in an early vessel design. The associated thermal profile is shown in Figure 2.23b. The combination of heat and pressure produces many complex stress interactions, particularly as caused by disparities in radial growth. Below is a list of the key design decisions that lead from the early model (shown in Figure 2.21) to the final model (shown in Figure 2.22). The numbers in the list match to the numbers in Figure 2.23.

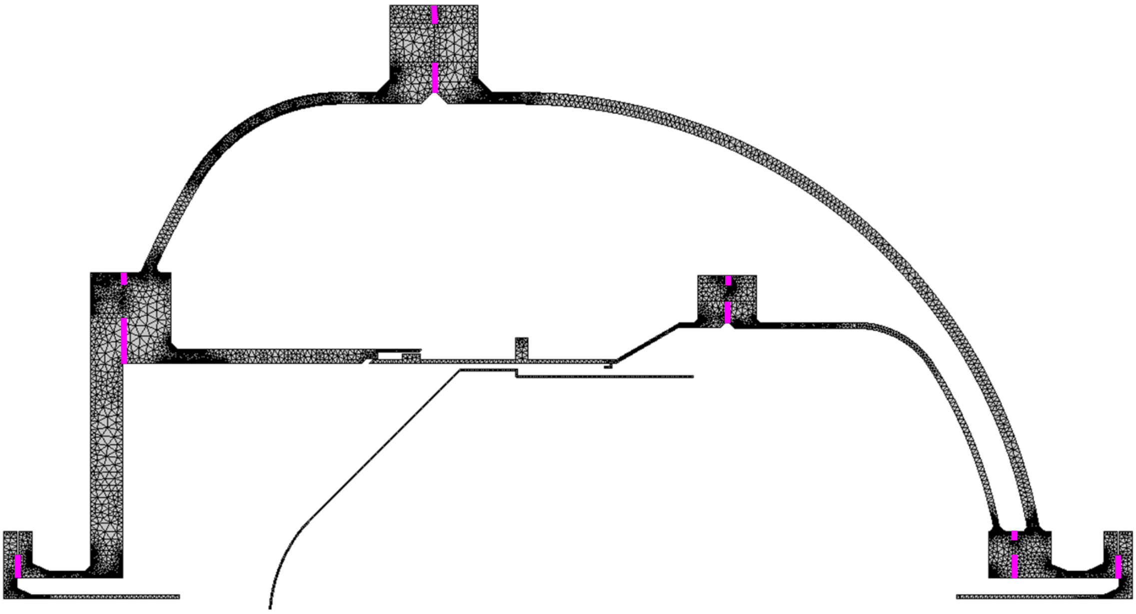

Figure 2.22: Mesh used for the thermomechanical study in SC03.

1. The maximum temperature in the inlet and outlet nozzles is near to $480°C$ due to the extremely high local HTCs. It is assumed that the same feature would exist at the SCA offtake nozzles. Even stainless steel would struggle to meet the strength requirements for these temperatures without substantial thickening of the part. Instead, a series of Inconel inserts (see Figure 2.24a) were designed that can handle the high temperature. These are bolted into the nozzles and allow for thermal growth without transmitting the strain into the nozzle. Stresses in the insert themselves are still high so the tensile strength of the Inconel is still necessary.

2. The high compressive stresses on the inner corner of the vessel nozzles are the limiting factor in fatigue life calculations. The inclusion of the Inconel inserts reduces the stresses in these regions by half.

3. The highest tensile stresses are found in the concave corner on the outside of the vessel, where the $900mm$ opening meets the dish end and connects to the inner cavity wall. This is eliminated by welding the $900mm$ flange directly into the dish, which also bulks up the connection.

4. Similar to front end, the connection of the central cavity wall to the rear dish end is also a location of substantial tension. The stress is partly pressure induced, and partly due to thermal growth of the central sections. In the final design, the vessel wall is hemispherical and the casing has been mounted onto a $1000mm$ dish that is bolted to

the rear dish near the outlet nozzle. The bolted connection allows for thermal growth much like the inserts. The added material provides strength and thermal mass that absorbs more heat without substantial growth, substantially reducing stresses in the outer wall. As the joint is completely contained within the vessel there is no seal between the flanged faces.

5. The location of the sigma-seal is measured for displacement so that the seal compression-extension can be adequately absorbed. It is found that under pressure load only, the gap grows by $2mm$, while thermal growth of the casing reduces the gap by $4mm$ compared with no load at all.

6. Stresses in the outer wall near the bolted connection as pictured here are mostly due to the modelling procedure. Once the bolts have been modelled appropriately as per the discussion above, these stresses reduce and do not need to be considered further in the fatigue analysis.

2.4.4 Final Analysis of Vessel

This pressure vessel has been designed to the British Standard PD5500 [26], and in accordance with that standard the FE model can only be verified by a certified specialist. This is because the application of the code is subjective. It requires that stresses are categorised as primary or secondary based on output from FE models that are grid dependant. However, it is the responsibility of the user to specify the design case, and finding a suitable ‘worst case’ is not a straight-forward process; the thermal expansion of the vessel can often relieve some of the stresses caused by pressurisation, yet the increased temperature of the metal also reduces the design strength. Furthermore, the inner and outer cavities can contain different pressures, yet the standard only assumes a maximum working pressure and/or temperature throughout the whole. The input condition matrix for finding the worst case scenarios is shown in Table 2.3.

Cases 1,2,3 represent different configurations of the hot flow at a single stated design pressure. The hot air could be distributed throughout the inner cavity, both cavities, or neither. Each is considered for both static and fatigue loading. Cases 4,5,6 represent the same temperature distributions but with the largest allowable pressure differential that could be expected between the cavities. This would only occur under transient conditions, either when the vessel is first pressurised or during an emergency shutdown. These events would be extremely rare, as it requires a failure of the PLC and is limited by the fact that the

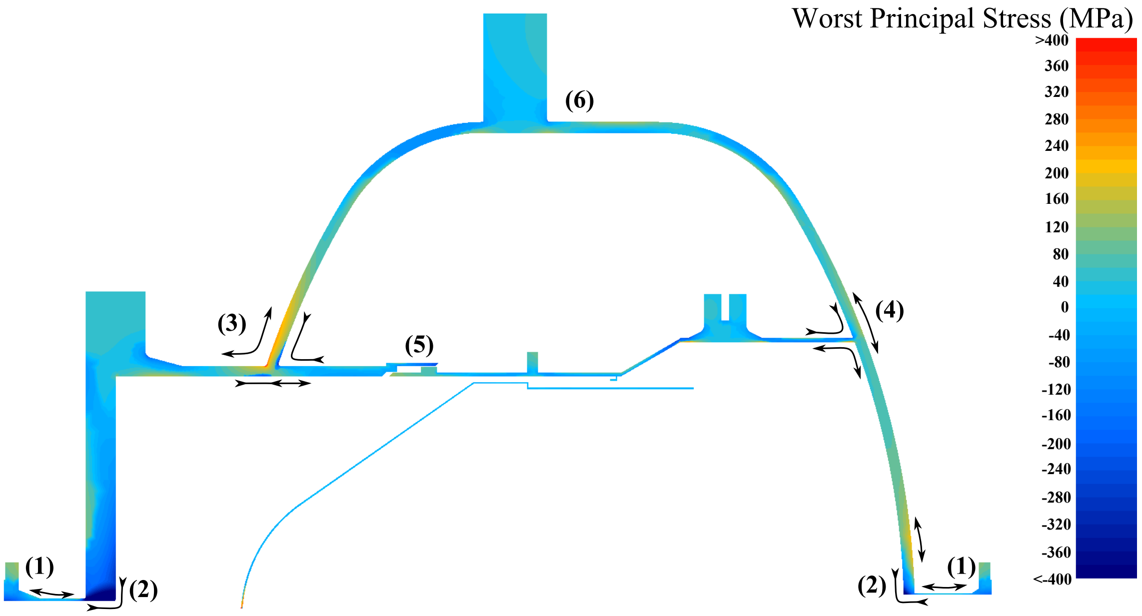

(a) Worst Principal Stresses. Tension is red and compression is blue.

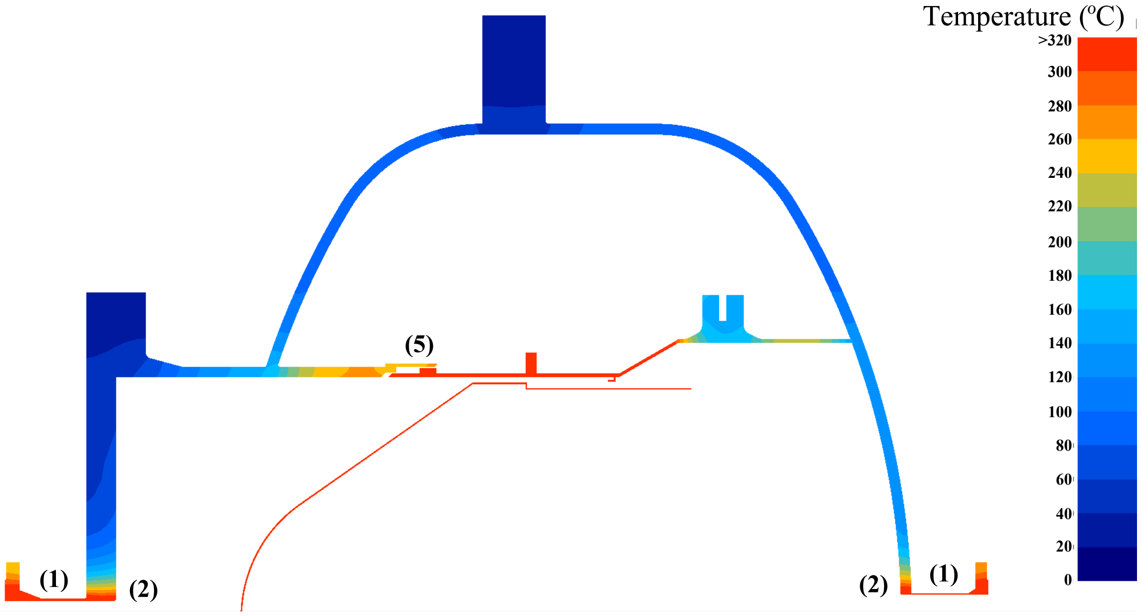

(b) Temperature after 1000*s* of heating. Any contour in red exceeds the design temperature.

Figure 2.23: Structural and thermal analysis of an early vessel design

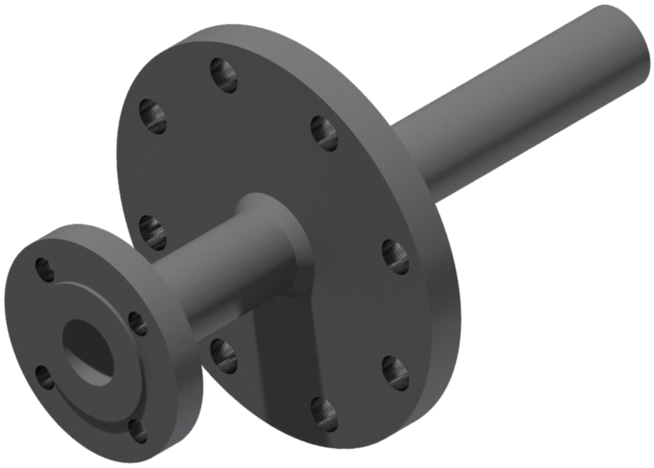

(a) Main inlet insert made of Inconel 718

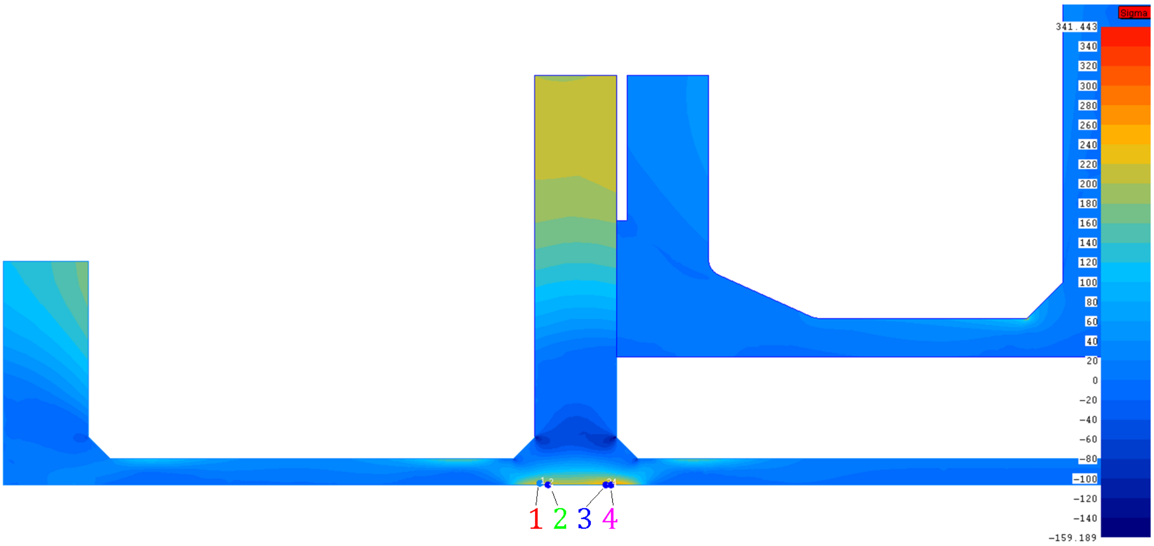

(b) First principal stress after 1000s of heating

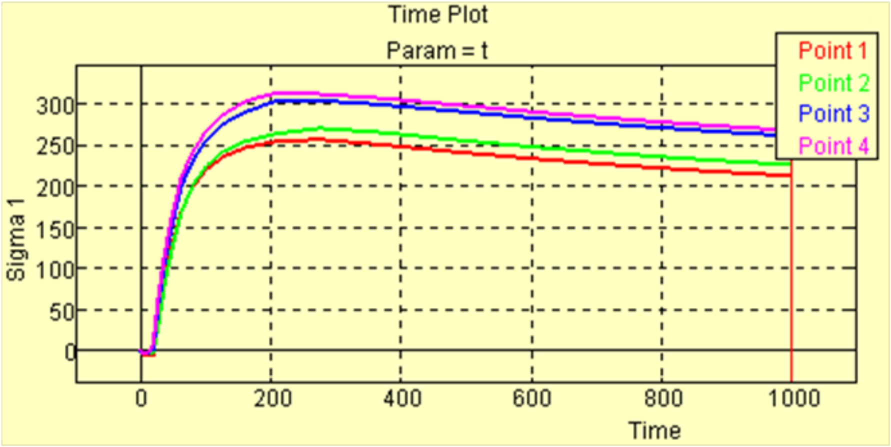

(c) Change in first principal stress over time

Figure 2.24: Main inlet insert used to protect vessel from high temperature flows.

Case	T_{inner}	T_{outer}	p_{inner}	p_{outer}	Description	Considered under
1	810	810	1.9	1.9	Maximum design pressure	Static and fatigue
2	810	293	1.9	1.9		
3	293	293	1.9	1.9		
4	810	810	1.9	1.4	Maximum pressure differential	Static only
5	810	293	1.9	1.4		
6	293	293	1.9	1.4		
7	770	293	1.6	1.6	Normal operation	Fatigue only
8	293	293	3.45	3.45	Hydrostatic test	Static only

Table 2.3: Simulation matrix of inlet air temperature (K) and pressure (MPa).

cavities are linked directly via the duct work. As such they have only been considered under static loading. Case 7 represents regular operating conditions, including a slow temperature ramp up, and was only considered for fatigue. Case 8 represents the vessel's hydrostatic test conditions. This test is done once; the vessel is filled with water and taken up to a test pressure (p_t) calculated by the manufacturer based on design pressure (p_{des}) and PD5500;

$$p_t = 1.25 p_{des} \left(\frac{\sigma_{nom}}{\sigma_{des}} \times \frac{t}{t-c} \right) \tag{2.8}$$

where σ_{nom} is the nominal strength of the material, σ_{des} is the strength of the material at the design temperature, t is the main wall thickness, and c is the corrosion allowance. This case is considered under static conditions only. The final vessel passed the hydrostatic test without incident.

For a static analysis, the membrane stress in the vessel is interpreted as an average of the principal stresses through a hypothetical cut. All cases were simulated, and the worst tensile stresses are consistently found in the connection between the rear hemisphere and padded flange at the exit nozzle (Figure 2.25). The design limit is that the membrane stress should less than 50% of the yield stress. Every case was found to be allowable, so the 'worst case' focuses on fatigue cases only.

When considering fatigue loading, the steep temperature gradient of case 2 creates the highest stresses. The operating conditions (case 8) provide a more accurate prediction of fatigue life, but choosing case 2 as the 'worst case' gives a good safety margin. The temperature of the vessel under these conditions is shown in Figure 2.26b, with selected points of interest shown in Figure 2.26c, and the worst principal stresses shown in Figure 2.26a. The temperatures and pressures were considered by the external expert who found that the vessel should have a fatigue life of 63 600 full cycles. This was conducted on an early design of the vessel (similar to that shown in Section 2.4.3), and stresses have since

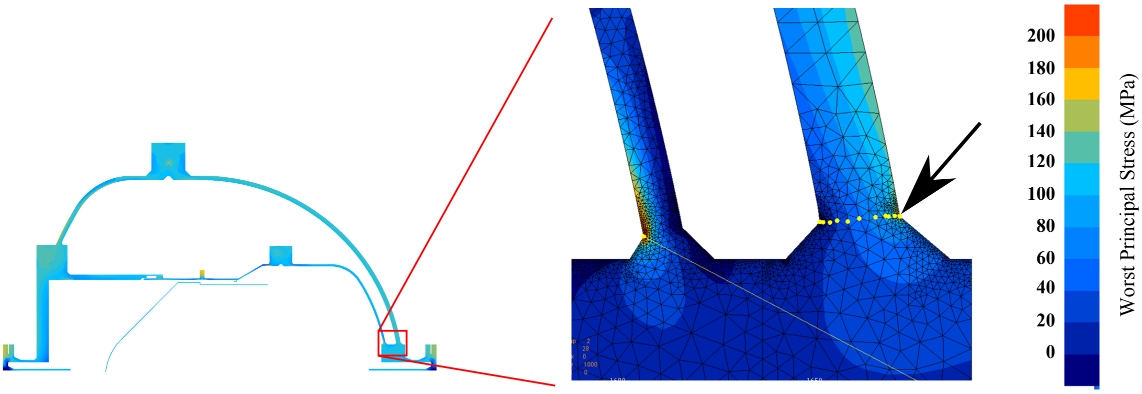

Figure 2.25: Location of the most critical stresses in the pressure vessel.

been reduced further, so one could expect a higher fatigue limit still. As it is, the limit imposed for operation has been chosen as 20 000 cycles, which under present test schedule would last over 100 years.

Separate static stress analyses were conducted on each of the Inconel inserts. The stresses in the inserts at label (8) in Figure 2.26a are very high, but well within the capacity of the Inconel. Individual simulations of each insert demonstrate that they all capable of withstanding the local stresses. The stresses in the casing and at the base of the internal dish (9) are not safety critical as they are fully contained by, and isolated from, the outer wall.

2.5 Flow Control Analysis

2.5.1 Lumped Parameter Pipe Flow Model

A lumped parameter analysis [104] was performed on the facility pipe and valve network using MATLAB's Simulink. The analysis helps predict the temperature lost to the pipework during test cycles, as well as pre-empt any other unexpected effects caused by operation of the valves. For instance, the heater manufacturer states that a $69kPa$ pressure drop across the heater could cause damage, and that a sustained temperature spike could trip the emergency cut-off, so both of these scenarios should be mitigated. The scope of the pipework modelled in this study is shown in Figure 2.27. The model assumes that there is an infinite volume of air available, delivered at constant pressure by the regulator. The downstream valves (IV4, CV1, CV3 and 4×CV2) and related orifice plates are modelled under the assumption that they all remain choked.

The numerical model for the air in the pipes is based on the continuity equations for

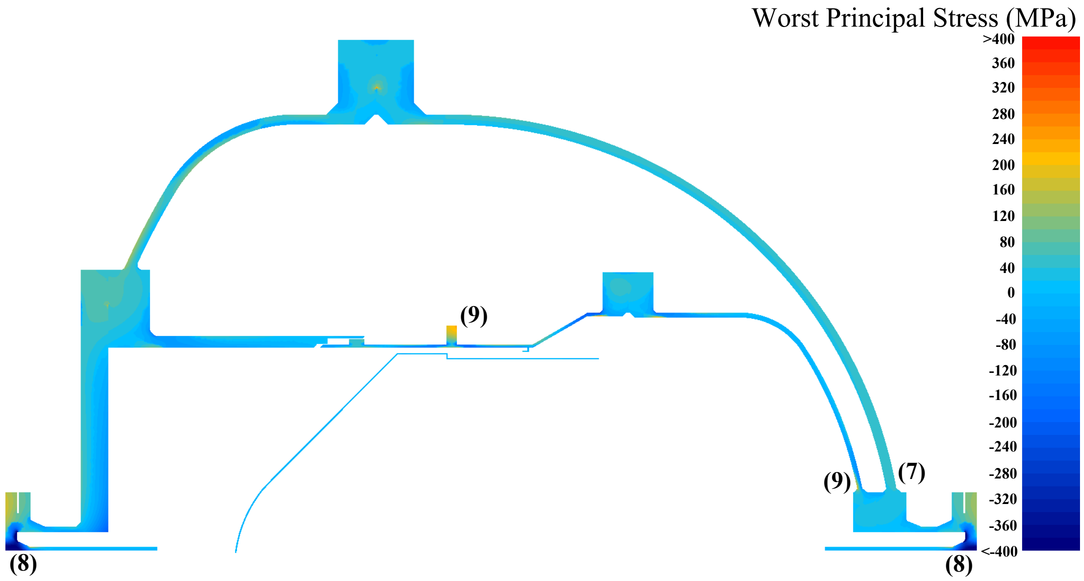

(a) Worst Principal Stresses

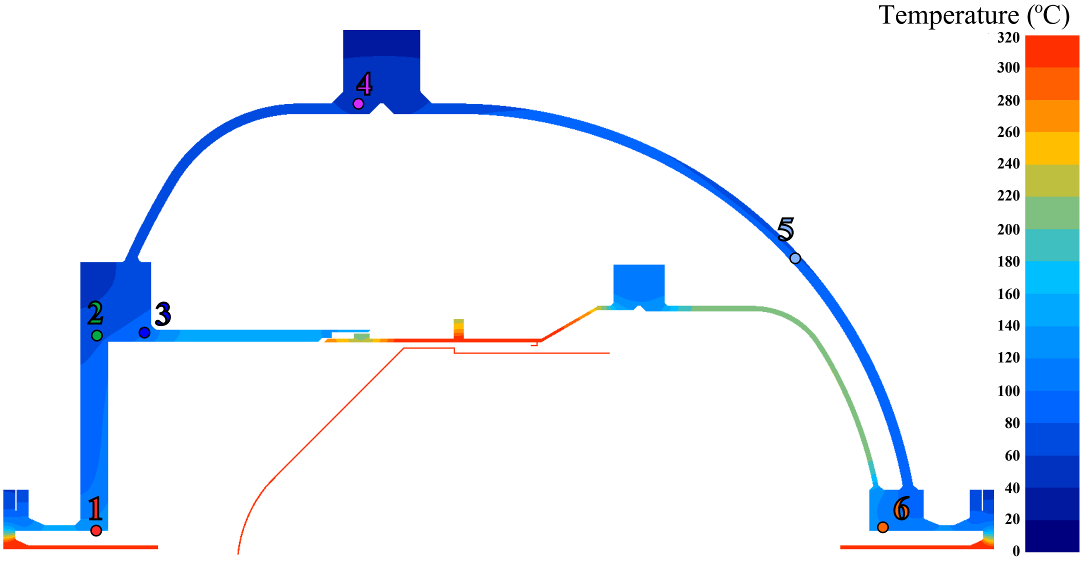

(b) Temperature after 1000*s* of heating

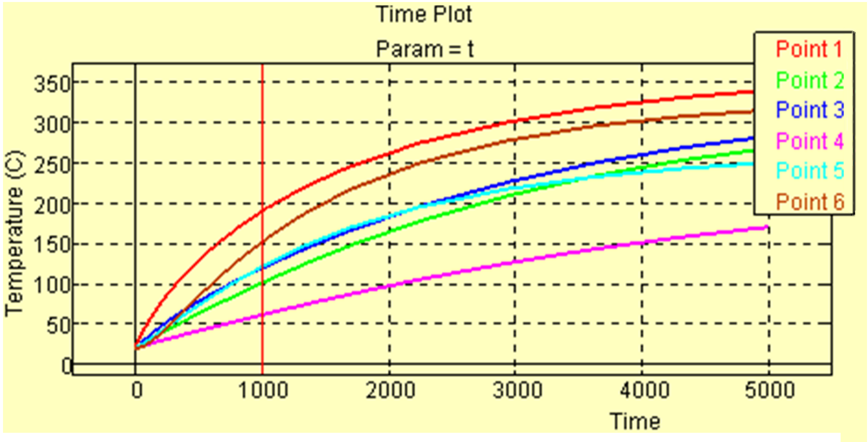

(c) Temperature of points indicated in (b). The red line at 1000s indicates the operating temperature

Figure 2.26: Structural and thermal analysis of the final vessel design.

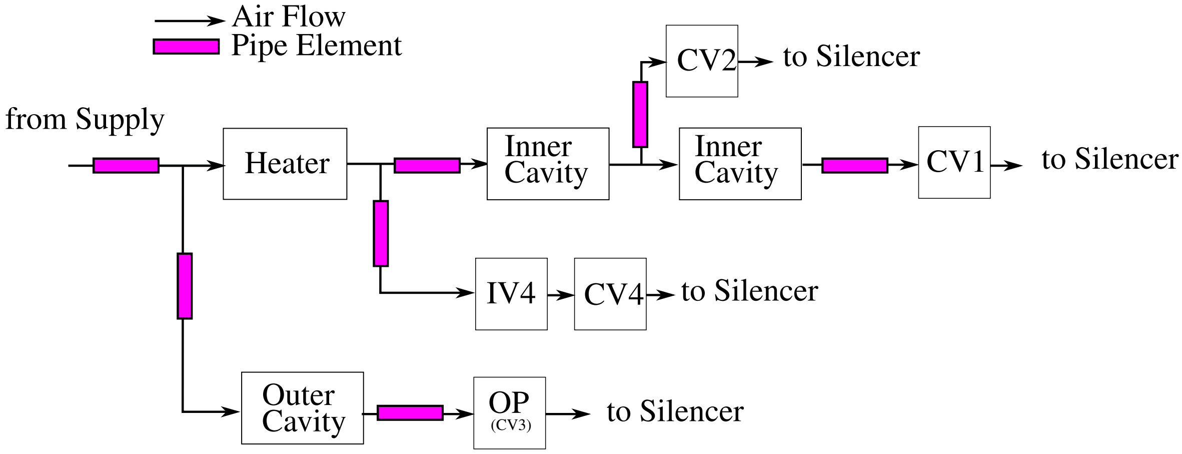

Figure 2.27: Extent of pipework modelled in Simulink.

mass and momentum. These equations have been applied to the control volumes shown in Figure 2.28. Mass continuity is considered between two mass flow nodes ($\dot{m}_i$, $\dot{m}_{i+1}$), such that the volume is at uniform pressure (p_{i+1}), whereas momentum continuity is considered between pressure nodes (p_i , p_{i+1}) where the volume has constant mass flow ($\dot{m}_i$). Thus the volumes overlap, and the two equations are formalised in tandem to fully resolve the flow.

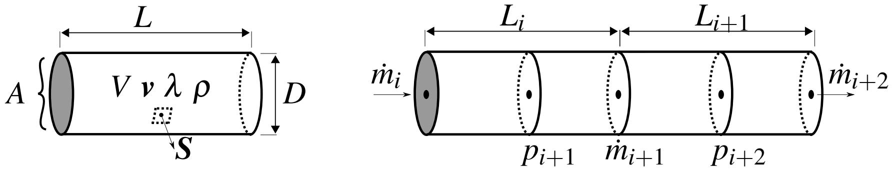

(a) Discrete length of pipe.

(b) Pressure and mass flow nodes.

Figure 2.28: Finite volumes used in discretisation of the continuity equations.

Consider the control volume between $\dot{m}_i$ and $\dot{m}_{i+1}$. Let this volume have density ρ, volume V, the outwards pointing surface vector $\boldsymbol{S}$, and velocity vector $\boldsymbol{v} = (u, v, w)$. The equation for mass continuity can be expressed as the balance between the mass accumulating in the volume with the net flux of mass exiting the surface of that volume;

$$\oint_V \frac{\partial \rho}{\partial t} dV = - \oint_S (\rho \boldsymbol{v}) d\boldsymbol{S} \tag{2.9}$$

From Green's theorem, the right side of the equation can be expressed as a volume integral;

$$\oint_V \frac{\partial \rho}{\partial t} dV = \oint_V \nabla (\rho \boldsymbol{v}) dV \tag{2.10}$$

and thus;

$$\frac{\partial \rho}{\partial t} = \nabla (\rho \boldsymbol{v}) \tag{2.11}$$

The control volumes only have flow along the x dimension, and the mass flow passes through two equally sized surfaces of area A, thus;

$$\frac{\partial \rho}{\partial t} = \frac{\partial}{\partial x}\frac{\dot{m}}{A} \tag{2.12}$$

Discretising the equations gives;

$$\frac{\rho_{i,j+1} - \rho_{i,j}}{t_{j+1} - t_j} = \frac{1}{A}\frac{1}{(x_{i+1} - x_i)}(\dot{m}_{i,j} - \dot{m}_{i+1,j}) \tag{2.13}$$

Finally, assume that the volume obeys the ideal gas law ($\rho = p/RT$), the space discretisation can be generalised ($x_{i+1} - x_i = L_i$), and that all time steps are equally sized ($t_{j+1} - t_j = \Delta t$), then;

$$\frac{p_{i,j+1} - p_{i,j}}{\Delta t} = \frac{RT_i}{A_i L_i}(\dot{m}_{i,j} - \dot{m}_{i+1,j}) \tag{2.14}$$

Next, consider the control volume between p_i and p_{i+1}, and the equation for momentum continuity;

$$\frac{\partial}{\partial t}\oint_V \rho \boldsymbol{v}.dV + \oint_S \rho \boldsymbol{v}.d\boldsymbol{S}\boldsymbol{v} = -\oint_S p.d\boldsymbol{S} + \oint_V \rho \boldsymbol{f} dV + \boldsymbol{F}_{viscous} \tag{2.15}$$

Momentum continuity can be expressed as the balance between changes in momentum both within the volume (first term LHS) and across the surface boundary (second term LHS), with the forces acting on the fluid (RHS). These forces, respectively, are the pressure acting on the fluid's surface (first term RHS), the external forces ($\boldsymbol{f}$) acting on the internal volume (second term) and the viscous forces acting within the fluid itself (collectively bundled into the term $\boldsymbol{F}_{viscous}$).

For the numerical simulation, we assume that the volume has a uniform density and velocity, and therefore the second term on the left is zero. For pipe flow, we assume that there are no external forces ($\boldsymbol{f} = 0$) so the second term on the RHS goes to zero. The pipe diameter remains constant, and thus $\dot{m} = \rho v A$. The remaining integrals can then be evaluated as;

$$\frac{\partial \dot{m}}{\partial t} L_i = (p_i - p_{i+1})A_i + \boldsymbol{F}_{viscous} \tag{2.16}$$

To model the viscous forces, we consider the flow when it is under steady state, thus $\partial \dot{m}/\partial t = 0$;

$$\boldsymbol{F}_{viscous} = -(p_i - p_{i+1})A_i \tag{2.17}$$

Next, take the Darcy-Weisbach equation for headloss;

$$p_{i+1} - p_i = \lambda_i \frac{L_i}{D_i}\frac{\rho_i v_i^2}{2} = \frac{\lambda_i L_i}{2\rho_i A_i^2 D_i}\dot{m}_i^2 \tag{2.18}$$

where λ_i is the Darcy-Weisbach friction factor. Substitute this into Eq. 2.17 gives;

$$\boldsymbol{F}_{viscous} = -\frac{\lambda_i L_i}{2\rho_i A_i D_i}\dot{m}_i^2 \tag{2.19}$$

and applying this to Eq. 2.16 and discretising gives

$$\frac{\dot{m}_{i,j+1} - \dot{m}_{i,j}}{\Delta t} = (p_i - p_{i+1})\frac{A_i}{L_i} - \frac{\lambda_i L_i}{2\rho_i A_i D_i}\dot{m}_i^2 \tag{2.20}$$

Each pipe section can now be modelled using Equations 2.14 and 2.20. Time steps are calculated automatically by Simulink. Each pipe has a surface roughness that has been assumed based on a stainless steel finish, and this is used to identify the local λ_i. The equivalent head loss through a flexible hose has been quoted as 1.5 times the equivalent pipe. The head loss at the impingement plate is based on CFD by Morris [100] which show 15% pressure drop. The head loss through corners and diffusers is modelled simply as a minor loss acting at a point between the pipe volumes as modelled above. The minor loss coefficient (ζ) is found from the literature, and applied as;

$$\Delta p = \zeta \frac{1}{2}\rho v^2 \tag{2.21}$$

2.5.2 Thermal Model

Equations 2.14 and 2.20 together form the pipe flow model but do not account for the heat lost from the air to the pipe walls. For worst case conditions, we consider the pipework to be uninsulated and model the convection and radiation to the environment. The thermal model assumes a lumped capacitance approach whereby the streamwise heat conduction is low compared with convection (i.e. $\mathrm{Nu} \geq 10$) and the temperature in the pipe wall is evenly distributed at all times (i.e. $\mathrm{Bi} \leq 0.1$). For a pipe of known internal diameter (D) and air flow of known viscosity (μ) and mass flow rate ($\dot{m}$), the Reynolds number (Re) can be calculated via;

$$\mathrm{Re} = \frac{\rho v D}{\mu} = \frac{\dot{m}}{A}\frac{D}{\mu} = \frac{4\dot{m}}{\pi D \mu} \tag{2.22}$$

The local Prandtl number (Pr) for air at the conditions considered here is assumed to be 0.69. The Nusselt number (Nu) for internal flow through a pipe can be found from the Dittus-Boelter correlation;

$$\mathrm{Nu} = 0.023\,\mathrm{Re}^{0.8}\,\mathrm{Pr}^{0.33} \tag{2.23}$$

For the largest pipe ($D = 80mm$) and the lowest flow rate ($\dot{m} = 0.1kg/s$) we find a minimum $\mathrm{Nu} = 134$, thus the lumped capacitance assumption for negligible streamwise convection holds. The local heat transfer coefficient (h) can be found from the conductivity (k_{air}) and the definition of Nu;

$$\mathrm{Nu} = \frac{hD}{k_{air}} \tag{2.24}$$

and from this the Biot number can be calculated as;

$$\mathrm{Bi} = \frac{hL_c}{k_{metal}} \tag{2.25}$$

where L_c is the characteristic length defined by the cross-sectional area of the pipe wall thickness divided by the internal circumference. For the pipe between the heater and the vessel, $\mathrm{Bi} \leq 0.1$ for $\dot{m} \leq 0.7kg/s$. For higher mass flows, the assumption of lumped capacitance becomes less valid.

The fluid temperature (T_f) and pipe wall temperatures (T_w) are calculated in tandem, similar to the continuity equations. The temperature of the pipe wall, having mass (m_w) and specific heat capacity ($c_{v,w}$), is governed by the energy balance;

$$m_w c_{v,w} \frac{dT_{w,i}}{dt} = \dot{Q}_{conv,i} - \dot{Q}_{conv,e} - \dot{Q}_{rad,e} \tag{2.26}$$

where the internal convection ($\dot{Q}_{conv,i}$) is calculated using h from above, and the pipe internal surface area $A_{s,i}$;

$$\dot{Q}_{conv,i} = hA_{s,i}(T_{w,i} - T_{f,i}) \tag{2.27}$$

The external convection ($\dot{Q}_{conv,e}$) is approximated as natural convection with $h = 20W/m^2K$, and the external radiation ($\dot{Q}_{rad,e}$) is calculated as;

$$\dot{Q}_{rad,e} = \varepsilon \sigma_{SB} A_{s,e}(T_{w,i}^4 - T_{amb}^4) \tag{2.28}$$

The change in gas temperature (T_f) across the length of pipe is calculated using the $\dot{Q}_{conv,i}$ as;

$$T_{f,i+1} - T_{f,i} = \frac{hA_{s,i}(T_{w,i} - T_{f,i})}{\dot{m}_i c_p} \tag{2.29}$$

Each section of pipe or flexi-hose in the final model uses the four equations (2.14, 2.20, 2.26, 2.29) together. The simulink model of a pipe section is shown in Figure 2.29.

The heater, the heater diffusers, and the inner cavity of the vessel have also been modelled in the same way for this simple approach. The inner cavity is divided into two, one section before the offtakes and one after. The temperature change of the air across the heater is governed by the extraction of heat from the resistive elements. This has been modelled using a PI controller based on the manufacturer's specifications as shown in Figure 2.30. The heater's time constant to reach maximum output is quoted as 180s.

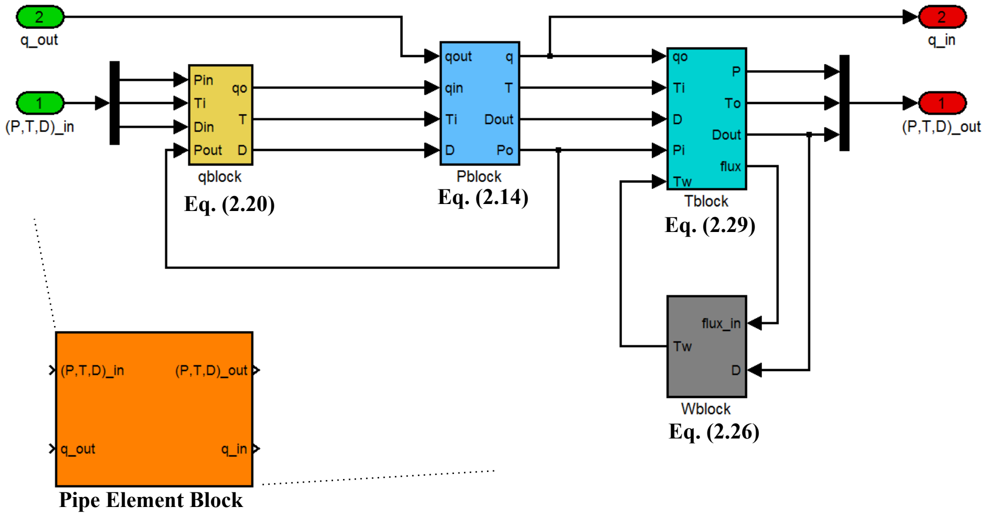

Figure 2.29: Simulink pipe element.

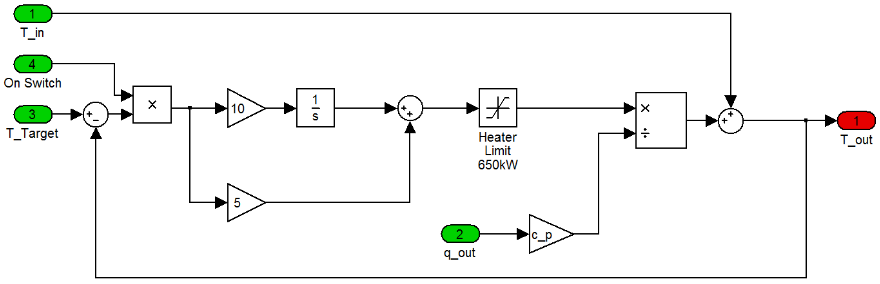

Figure 2.30: PI controller that simulates air heater response time.

2.5.3 Valve Model

To complete the pipe network simulation, we need to calculate the mass flow exiting through each valve. The mass flow through each CV2 valve is calculated based on the orifice plate area (A_{OP}), a known flow coefficient (C_D), and the isentropic flow equations. We also assume that the static pressure and static temperature measurements at the valves are equal to the total pressure and total temperature respectively ($p = p_0, T = T_0$) due to relatively low flow velocity at the valve. The mass flow at the throat is given by;

$$\dot{m}^*_{OP} = \rho^* v^* C_D A_{OP} \tag{2.30}$$

We know the ideal gas law, the Mach number (Ma), and the speed of sound in a gas are defined as, respectively;

$$p^* = \rho^* R T^* \tag{2.31}$$

$$\mathrm{Ma} = v^* / v_{sound} \tag{2.32}$$

$$v_{sound} = \sqrt{\gamma R T^*} \tag{2.33}$$

Substituting these back into Equation 2.30 we get;

$$\begin{aligned} \dot{m}^*_{OP} &= \frac{p^*}{RT^*} \sqrt{\gamma R T^*}\, \mathrm{Ma}\, C_D A_{OP} \\ &= C_D A_{OP} \sqrt{\frac{\gamma}{R} \frac{p^{*2}}{T^*} \mathrm{Ma}^2} \end{aligned} \tag{2.34}$$

Next, from the isentropic flow relations, we have equations for conditions at the throat;

$$T^* = T_0 \left(1 + \frac{\gamma - 1}{2} \mathrm{Ma}^2\right)^{-1} \tag{2.35}$$

$$p^* = p_0 \left(1 + \frac{\gamma - 1}{2} \mathrm{Ma}^2\right)^{\frac{-\gamma}{\gamma-1}} \tag{2.36}$$

Substituting these into Equation 2.34, setting Ma = 1 and rearranging gives;

$$\dot{m}^*_{OP} = p_0 C_D A_{OP} \sqrt{\frac{\gamma}{RT_0} \left(\frac{2}{\gamma + 1}\right)^{\frac{\gamma+1}{\gamma-1}}} \tag{2.37}$$

The C_D for the plates is 0.9 by design according to British Standard BS1092. For the globe valves (CV1 and CV4), the equation requires the substitution $C_D A_{OP} = C_V N$, where C_V is the flow coefficient as a function of the valves stroke position (α), and N is a constant factor for units and area, both found from the manufacturer's specifications.

$$\dot{m}^*_{GV} = p_0 C_V N \sqrt{\frac{\gamma}{RT_0} \left(\frac{2}{\gamma + 1}\right)^{\frac{\gamma+1}{\gamma-1}}} \tag{2.38}$$

The CV2 and IV4 valves are expected to have an actuation time of $0.15s$ which has been incorporated into the model.

2.5.4 Facility Network Study

The model was first run under steady input conditions for $1000s$ to demonstrate the temperature drop between the heater, the vessel inlet, and the casing. The results are shown in Figure 2.31. Some of the later experimental observations of the actual air temperature at the casing are also shown for context. The predicted temperature loss at both the vessel inlet and casing drops off with increasing mass flow rate, which could be expected, and is in agreement with the observed results. The temperature drop within the vessel is much greater that in the upstream pipework, due to the long residency time and large thermal mass of the vessel. It is believed that the difference between the observed results and the model is that the air in the front of the vessel actually has a higher HTC than expected, mostly due to the inadequacy of the Nunner correlation in this context. The buoyancy of the air likely leads to a local heat plume and impingement, as theorised in Section 2.7.

The model does provide some further insights though. The walls of the vessel are still rising in temperature at the end of $1000s$, as shown in Figure 2.32, so insulating the outside of the vessel would not help maintain the internal temperature much (nor be appropriate under the Standards for vessels as previously outlined). Insulating the pipework will reduce losses before the start of the vessel, so the final construction of the facility includes insulation along all the upstream flexible hoses and pipework. Insulation on the inside of the vessel is also used in the final design to help preserve some of the air temperature.

The model was next run such that the CV2 valves are switched on and off under maximum flow conditions. These tests led directly to the implementation of the bypass line, but here we are only considering the model after the bypass had been included for brevity. Figure 2.33 shows the flow through the core, the impingement system and the bypass lines, with the effect of the switch from the bypass to the offtakes (or vice-versa) when they are not perfectly synchronised. Test (1) is a regular switch between valves, assuming that there is a $0.1s$ delay in the synchronisation, such that both lines are open. Test (1a) is the impingement switching on, and Test (1b) is switching off. Test (2) considers the flow if the bypass switches off suddenly, and test (3) consider a similar scenario for the impingement system.

There is a mass flow spike in test (1), but it is slower than the flow sensor's response time of $2s$, so it is unlikely to trip the safety switch. However, the tests have associated pressure

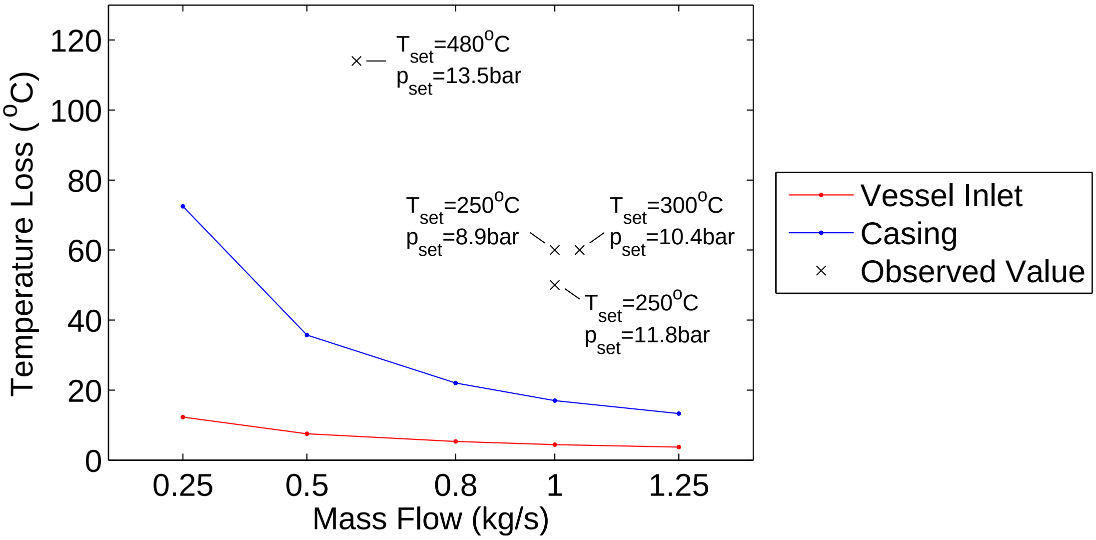

Figure 2.31: Temperature drop between the heater exit, and the vessel and casing at $T_{set} = 500°C$ and $p_{set} = 16bar$. The experimental observations are at the conditions shown.

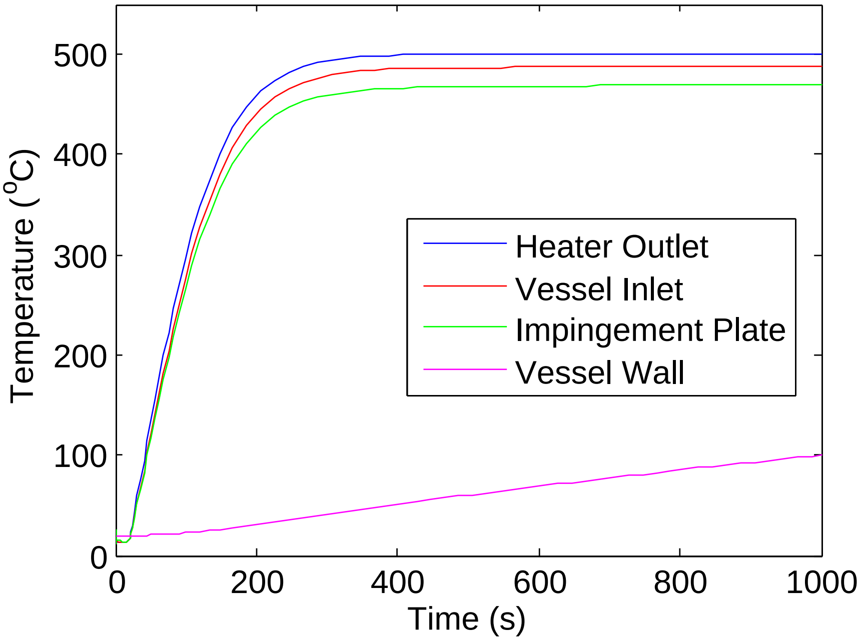

Figure 2.32: Comparison of the metal temperatures under steady state conditions.

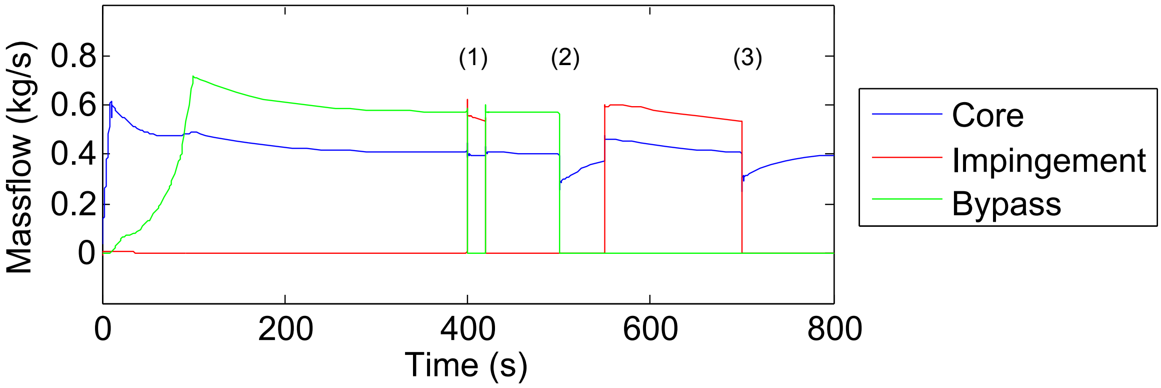

Figure 2.33: Comparison of the mass flow rates through each exit. Spikes in the flow are caused by the quick acting valves.

spikes that warranted further investigation to ensure they do not damage the heater, and these are shown in Figures 2.34. The greatest pressure wave found peaks at $4kPa$, which is less than the $69kPa$ limit to prevent heater damage.

The spikes oscillate at a frequency of $4.3Hz$ for just under $1s$ before dissipating. The cause for the oscillation is likely to be Helmholtz resonance between the vessel and the inlet pipe. The frequency of Helmholtz resonance (f_H) is calculated as;

$$f_H = \frac{v_{sound}}{2\pi}\sqrt{\frac{A}{V_0 L_{eq}}} \tag{2.39}$$

where v_{sound} is the speed of sound ($552.6m/s$), A is the throat area of the pipe leading into the vessel ($0.08m$), V_0 is the volume of the inner cavity in the vessel ($1.27m^3$), and L_{eq} is the equivalent length of the pipe entering the vessel. For the Helmholtz frequency observed in the simulation L_{eq} is found to be $1.65m$. This could be easily interpreted as the combined length of the heater and pipe used in the model, validating the theory that this is Helmholtz resonance. It is plausible that it would occur in the real facility, however, the installed instrumentation only has a 1% accuracy and $0.1Hz$ sample rate. Furthermore, the flexible hoses would dampen the effect, so it is unlikely we can observe the frequency in the measured response.

The network model was validated during the installation and commissioning of the heater. In that case, the vessel had not yet been installed and the heater was directly attached to CV1 to exhaust through the silencer. The pressure and mass flow through the system was verified against the Simulink pipe model, having been truncated to the same network. The prediction of the pressure at the heater exit was found to be in good agreement with the experimental measurement as shown in Figure 2.35. This confirms that the empirical loss and geometric parameters used in the model are correct.

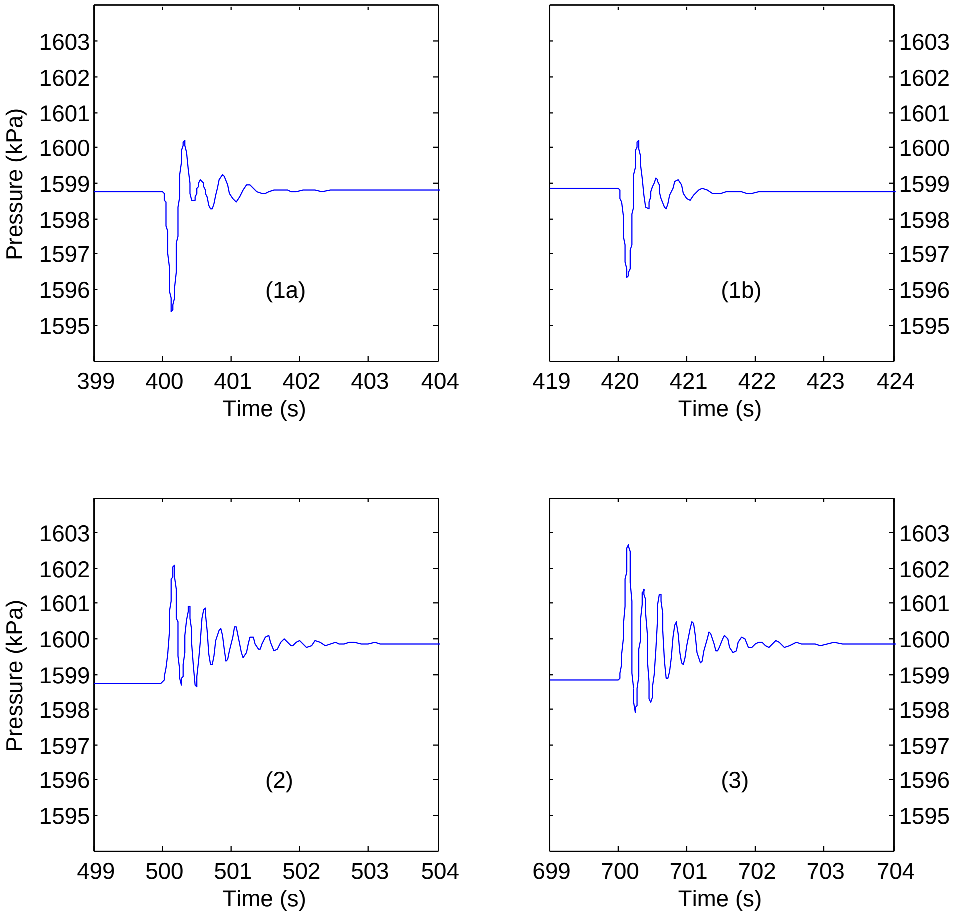

Figure 2.34: Pressure spikes at the heater representing the tests in Figure 2.33. (1a) Regular test start, (1b) Regular test end, (2) Sudden bypass shut off, (3) Sudden offtake shutoff.

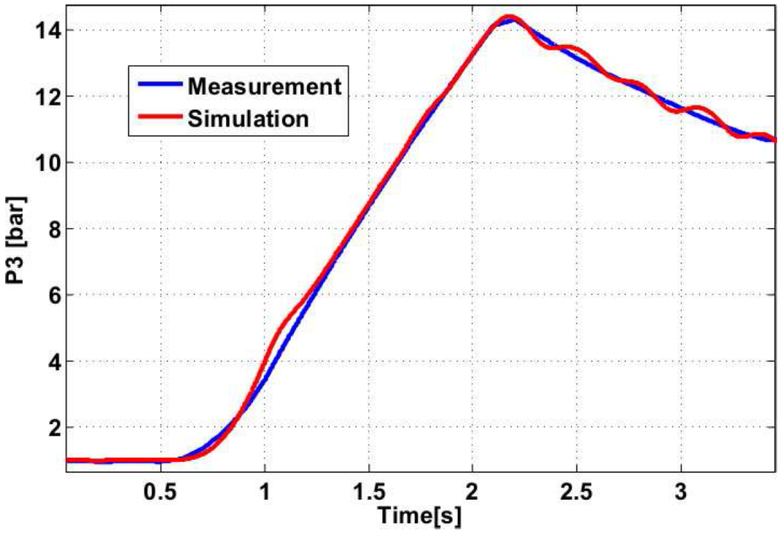

Figure 2.35: Comparison of the heater exit pressure as predicted and measured.

2.6 Impingement Plate and HTC Prediction

2.6.1 Theoretical Nusselt Number

Impingement jets have been a subject of considerable research, and the experiment and analysis by Goldstein and Seol [51] is similar to the four rows of holes in the SCA impingement plates. Goldstein and Seol consider a row of circular jets with square edges and diameter D, exhausting cold air on to a set of stainless steel heating foils (see Figure 2.36). If z is the distance downstream of the row, and S is the interhole spacing, the range of parameters that have been tested are shown in Table 2.4. Heat transfer coefficient (h) is defined as;

$$h = \frac{q_w}{T_w - T_{0,ad}} \tag{2.40}$$

where q_w is the convective wall flux, T_w is the wall temperature and $T_{0,ad}$ is the adiabatic wall temperature of the fluid. The paper found that the Nu can be approximated by the function;

$$\frac{\mathrm{Nu}}{\mathrm{Re}^{0,7}} = \frac{2.9}{22.8 + (S/D)(L/D)^{0.5}} e^{0.09(z/D)^{1.4}} \tag{2.41}$$

Applying this equation to the present case gives the results listed in Table 2.4. The jet diameter to height ratio (L/D) matches the set up in the present impingement plate. The Reynolds number (Re) for row 3 is the same as considered by Goldstein, and the other hole rows are still within, or near to, the turbulent region for jet flows Re > 3 000. The inter-hole spacing (S/D) is wider than Goldstein considered, so it is likely that the holes in the casing will act less as a contingent row, and more as isolated jets. Furthermore, it is more likely that there is interaction between jets of neighbouring rows, particularly between rows 3 and 4.

Parameter	Goldstein and Seol	Row 1	Row 2	Row 3	Row 4
D, mm	6.4	1	1	2	1
L/D	$2 \leq L/D \leq 8$	4	4	4	4
S/D	4,8	51.1	25.5	25.5	20.4
Re	$10\,000 \leq \mathrm{Re} \leq 40\,000$	2 900	5 800	23 300	7 300
Nu_{max}		11.6	17.0	44.8	23.0

Table 2.4: Impingement Hole Rows in Goldstein and Seol [51] and the THTF.

Bearing these limitations in mind, it is useful to construct a prediction for Nu over the surface of the casing. This is calculated assuming that the z/D at each point on the casing is the distance from each jet individually, and not the axial distance from the row. For points that had significant Nu contribution from multiple holes, only the hole with greatest

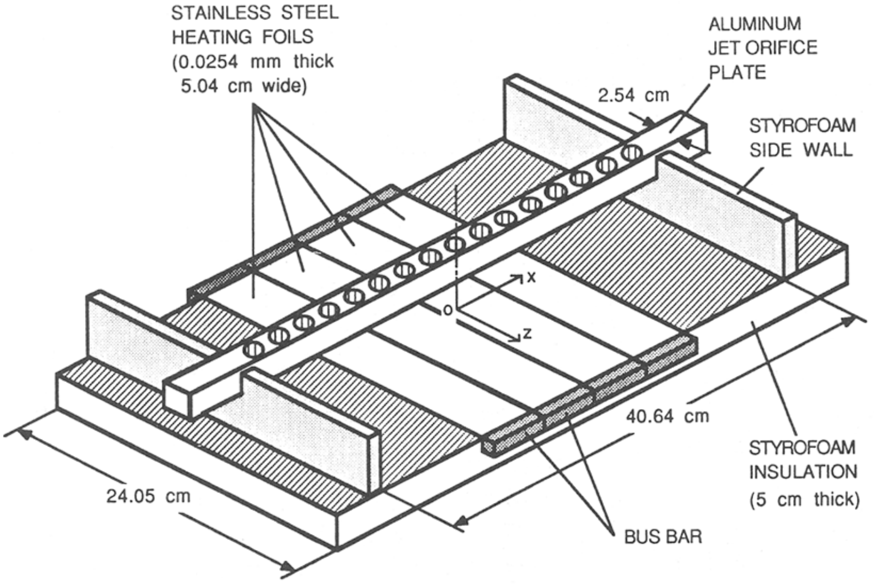

(a) Overview

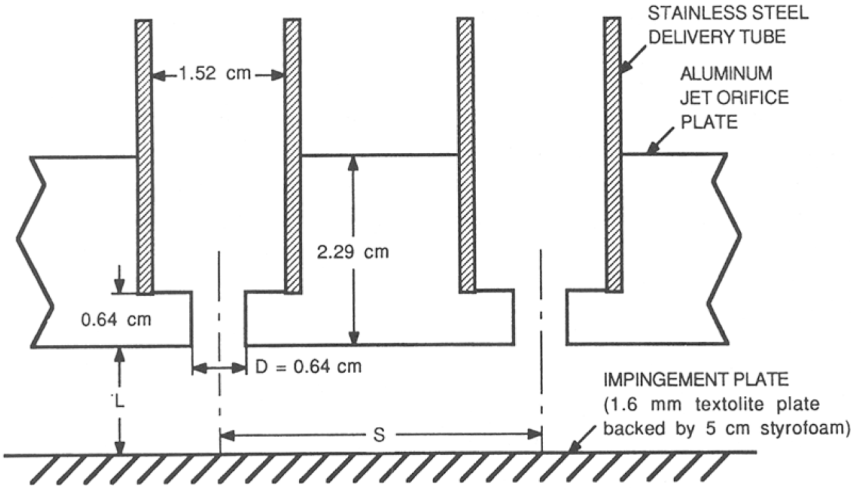

(b) Hole exit detail

Figure 2.36: Experiment row of impingement jets from Goldstein and Seol [51].

influence was counted. This gives an overall value of Nu lower than should be expected, however the results still prove insightful. The contours are shown in Figure 2.37.

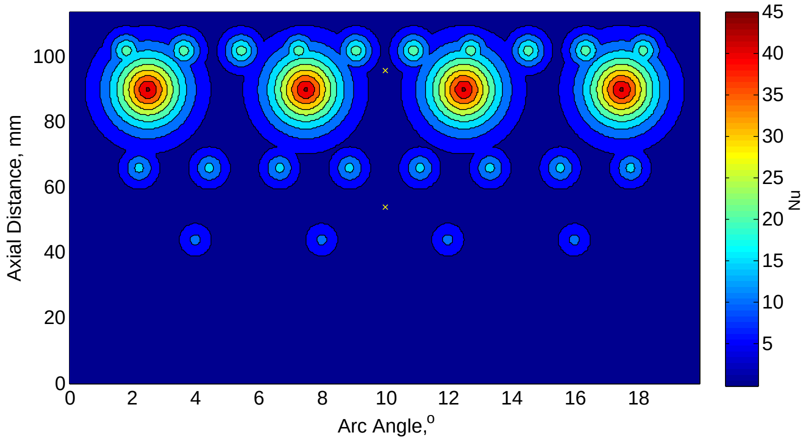

Figure 2.37: Theoretical Nu under the impingement jets for each plate.

The yellow crosses indicate the approximate position of the two TCs on the inside of the casing. As TCs are sparsely distributed compared with the impingement holes, only general trends HTC are likely to be identifiable in the experiment. The figure shows that the heat transfer is likely to be dominated by row 3 of the cooling holes, followed by row 4, 2 and 1 respectively.

2.6.2 Casing Average Temperature

The uniformity of the casing temperature is an important characteristic for maintaining an axisymmetric tip clearance. As such the results discuss both the average casing temperature and the variation of the temperature profile. The average temperature of the casing can be calculated by finding the average temperature of the inner ($\bar{T}_{ic}$) and outer ($\bar{T}_{oc}$) surfaces separately, and then assuming a particular temperature profile between the two surfaces. The temperature profile through the thickness of the casing can be calculated using the heat equation numerically, however there is no analytical solution for a 1D wall of finite thickness under transient conditions. A close approximation, that can be verified through CFD and experiment and shown in Figure 2.38, is a quadratic profile between the two surfaces based on the radial depth (x);

$$T(x) = C_1x^2 + C_2x + C_3 \tag{2.42}$$

Although there is a changing area with radius in cylindrical coordinates, the outer and inner radii are only 1% different, which is then the same for the exposed convecting surface

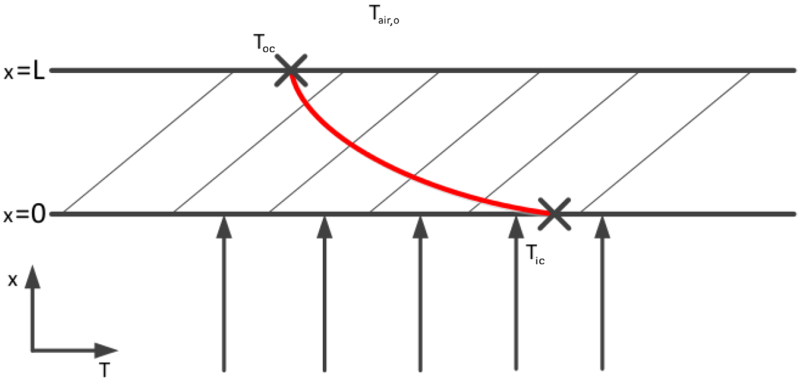

Figure 2.38: 1D Temperature profile through a cross-section of the casing wall.

area. Thus the effect of changing surface area is assumed to be negligible. Three equations are needed to solve for the three constants (C_1, C_2, C_3). For the first two, let the inner surface $x_{ic} = 0$ and the outer surface $x_{oc} = L$, then evaluate Equation 2.42 at each surface;

$$\bar{T}_{ic} = C_3 \tag{2.43}$$

$$\bar{T}_{oc} = C_1 L^2 + C_2 L + C_3 \tag{2.44}$$

Thirdly, Fourier's Law can be evaluated at either surface, and we choose the outer surface;

$$\left.\frac{dT}{dx}\right|_{x=L} = -\frac{h_{oc} L}{k}(T_{air,oc} - \bar{T}_{oc}) \tag{2.45}$$

where h_{oc} is the heat transfer coefficient on the outer surface, k is the conductivity of the metal, and $T_{air,oc}$ is the air temperature in the outer volume of the vessel. The constants can then be evaluated as;

$$C_1 = \frac{\bar{T}_{ic} - \bar{T}_{oc}}{L^2} - \frac{h_{oc}}{kL}(\bar{T}_{ic} - \bar{T}_{oc}) \tag{2.46}$$

$$C_2 = \frac{2(\bar{T}_{oc} - \bar{T}_{ic})}{L} - \frac{h_{oc}}{k}(\bar{T}_{air,oc} - \bar{T}_{oc}) \tag{2.47}$$

$$C_3 = \bar{T}_{ic} \tag{2.48}$$

Then the average temperature through the thickness of the casing ($\bar{T}$) can be evaluated by integrating the temperature between x_{ic} and x_{oc} and dividing by the thickness L;

$$\bar{T} = \frac{1}{L}\int_0^L T.dx \tag{2.49}$$

$$= \bar{T}_{oc} + \frac{\bar{T}_{ic} - \bar{T}_{oc}}{3} + \frac{h_{oc} L}{6k}(\bar{T}_{air,oc} - \bar{T}_{oc}) \tag{2.50}$$

Finally we know that $h_{oc} \approx 20 - 50W/m^2K$ (based on free convection in the outer vessel), $k = 18.6W/mK$ for stainless steel, and $L = 6.3mm$, so the coefficient of the last term equates to 3×10^{-3}. So we consider the final term negligible, and simplify the equation to;

$$\bar{T} = \frac{2\bar{T}_{oc} + \bar{T}_{ic}}{3} \tag{2.51}$$

2.6.3 Unsteady Conjugate CFD

A numerical simulation of the SCA design was performed by Dann *et al.* [39] using the ANSYS CFD Flow Solver. It considered both the flow and casing structure in a conjugate CFD analysis of a 90° sector of the test section, using the geometry as shown in Figure 2.39. The inlet is set just downstream of the nose of the bullet, the outlet for the main flow is downstream of the plate, and the outlet for the offtake flow through a long stretch of pipe similar to the offtake hose. This ensures that the flow exiting the offtake is fully developed. This stops the offtakes from unnaturally affecting the impingement jets and helps the solution converge faster. The initial conditions are based on a CFD solution of the steady state prior to the SCA offtake switching on. This setup has assumed that there is negligible buoyancy in the region under the plate in order to understand the impingement system independently and reduce the overall size of the calculation.

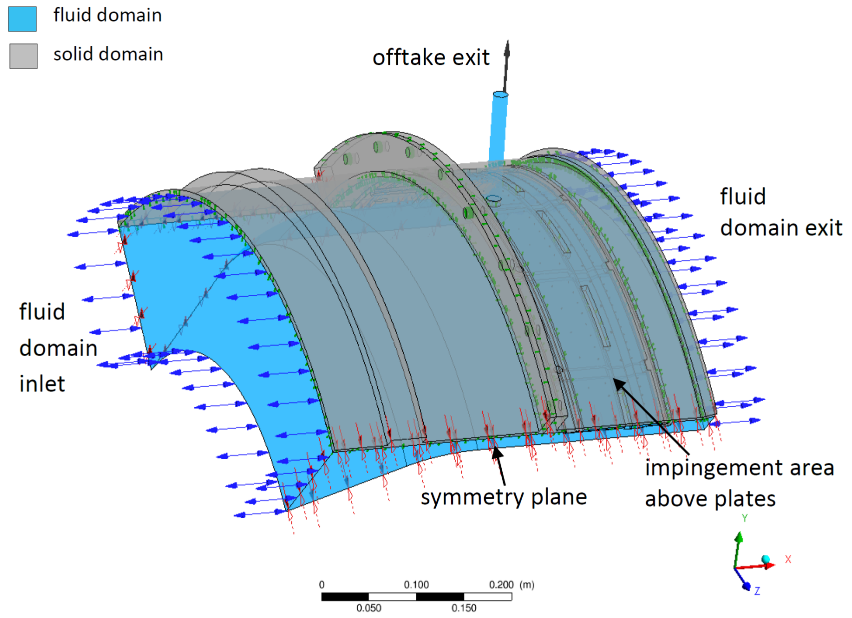

Figure 2.39: Conjugate CFD domains for simulating a quarter arc of the THTF [39].

The model was meshed in ANSYS using tetrahedral elements in the free stream, and structured inflation layers near the surfaces to model boundary layers. The fluid model had

20.9 million elements, while the solid model had 2.1 million. The shear stress transport (SST) k-ω turbulence model was chosen in order to best model the relatively low Re values, and $y+ < 1$ is maintained underneath the impingement jets. The metal sections all have thermal properties consistent with 316SS. Under steady-state initial conditions the driving air temperature was $770K$, the metal temperature was $630K$, while the outer surface had a constant heat loss based on an HTC of $20W/m^2K$ and an outside temperature of $373K$.

The analysis by Dann *et al.* [39] concluded that the conjugate CFD had matched the experimental results to 10% accuracy for absolute temperature. For the purposes of this thesis, only the results of the temperature distribution in the casing will be considered as they are most pertinent to the SVD analysis and simulation in Chapter 4. The casing inner and outer surface temperature profiles are shown in Figure 2.40. The results clearly show that the impingement holes towards the rear of the casing produce a much larger temperature rise than the forward holes. There is some smearing of effectiveness in the region of the offtake, where the temperature rise is greater overall, but the peaks in HTC are reduced directly underneath the individual holes. This suggests that the sparsely distributed TCs in the experiment will not pick up the effect of the offtake pipe.

One feature that is interesting is that the temperature distribution on the inside of the casing closely mirrors the temperature distribution on the outside. This is because the radial thickness is small and the radial conduction is faster than in the circumferential and axial directions. This is an important feature for later analysis of the full casing, as any features that don't show up on both surfaces are likely to be due to instrumentation error. The pattern and strength of the jets matches closely with the theoretical model shown in Figure 2.37.

The CFD has also been used to validate the quadratic temperature profile approximation that is derived in Section 2.6.2 and later used in discussion of experimental results. The temperature profile through the thickness of the casing is shown in Figure 2.41. The point temperatures at element corners within these profiles have been extracted and plotted against thickness in Figure 2.42. These figures validate that a quadratic can be used to produce a reasonable approximation of the average temperature of the casing.

The CFD model has a few short comings that may influence temperature distribution in the full model. The experiment itself only measures temperatures at discrete locations and won't pick up individual jet effects, so careful placement of the TC beads away from impingement points is necessary to alleviate local anomalies. The flow at the inlet to the vessel (upstream of the bullet) and on the outside of the casing has not been modelled. As

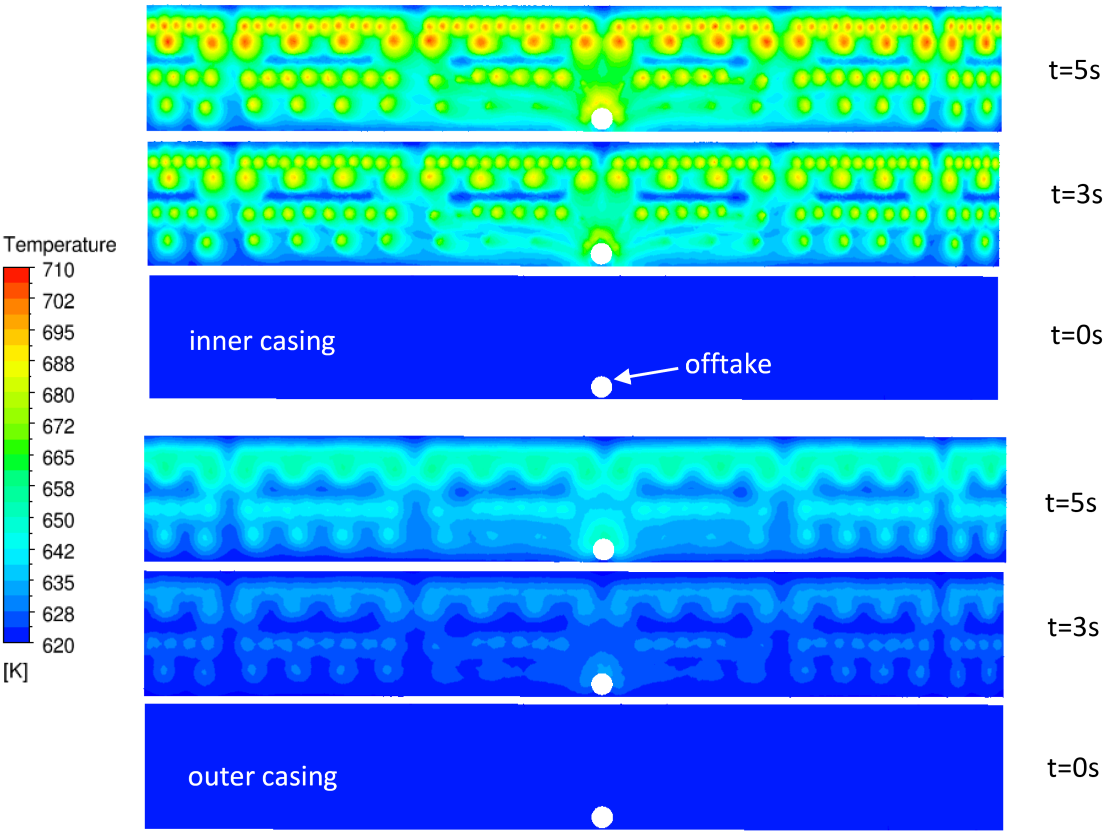

Figure 2.40: Instantaneous surface temperatures at $0, 3, and 5s$ of the CFD simulation showing the effects of the individual holes [39].

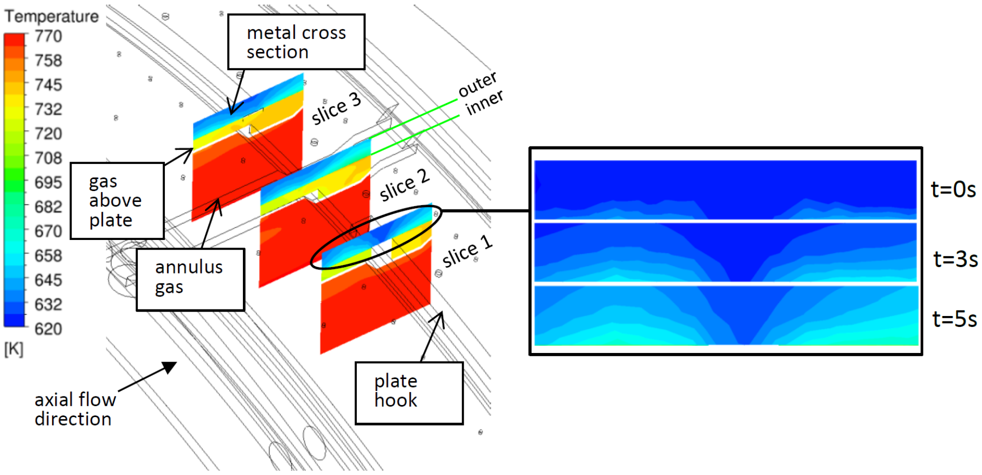

Figure 2.41: Radial slices of the casing for the first $5s$ of the CFD simulation showing the rate of conduction [39].

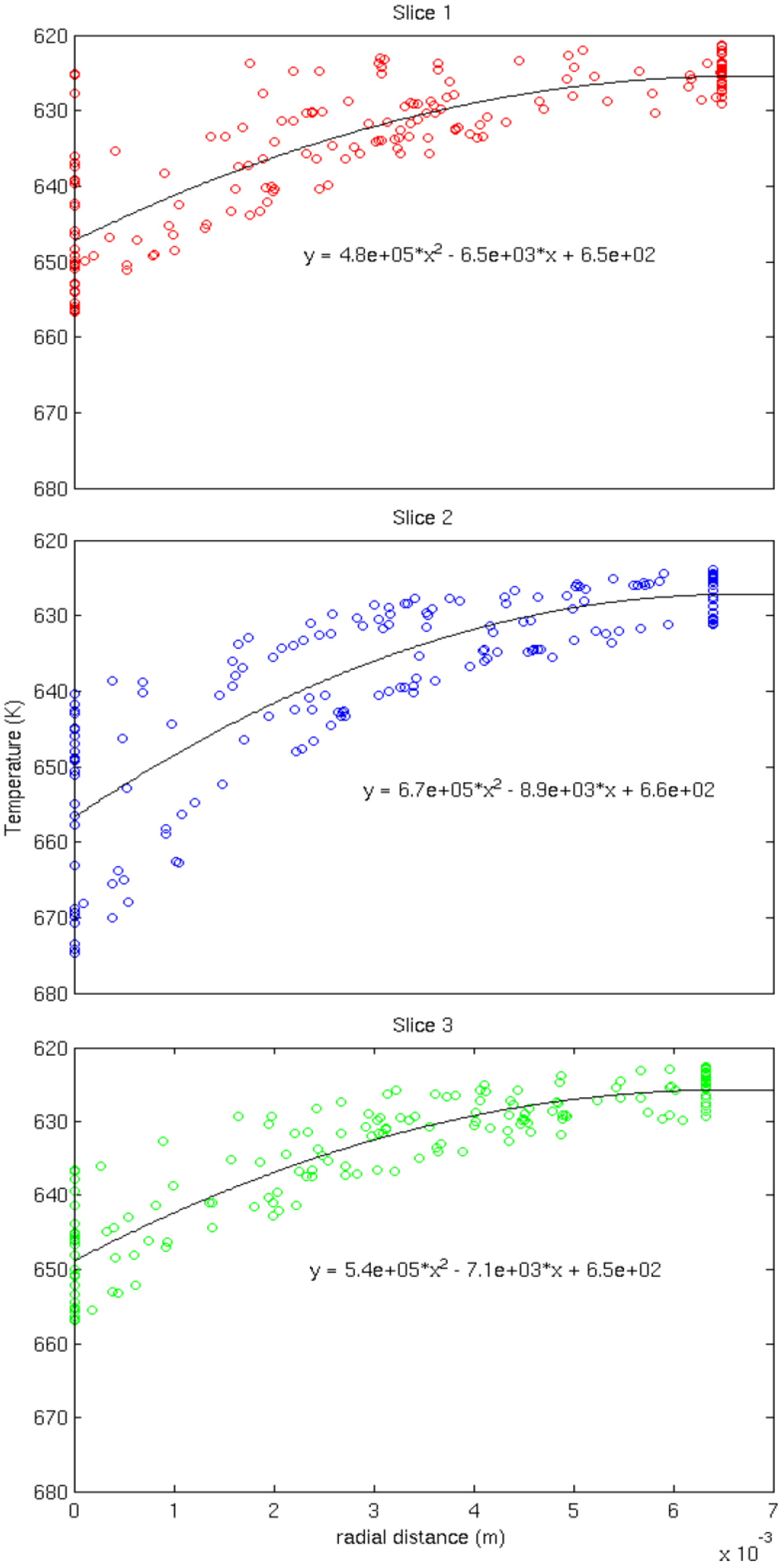

Figure 2.42: Quadratic fit of the point temperatures extracted from Figure 2.41 [39].

this air flow has a low velocity compared to the test section flow, there is a tendency for it to become buoyant and create thermal gradients, and this is considered further in the next section.

2.7 Buoyancy Effects in the Vessel

2.7.1 Theoretical Grashof Number

To assess the relative effect of buoyancy and momentum, we consider the ratio of the Grashof Number (Gr) with the Reynolds number squared (Re^2), both for the inner and outer cavity. Gr and Re can be calculated as;

$$\mathrm{Gr} = \frac{g\beta_v(T_f - T_s)L_c^3\rho^2}{\mu^2} \tag{2.52}$$

$$\mathrm{Re} = \frac{\rho v L_c}{\mu} \tag{2.53}$$

which can then be combined as

$$\frac{\mathrm{Gr}}{\mathrm{Re}^2} = \frac{g\beta_v(T_f - T_s)L_c}{v^2} \tag{2.54}$$

where g is gravity, β_v is the thermal coefficient of expansion, T_f is the fluid temperature and T_s is the surface temperature. Typically, buoyancy effects can be considered negligible if $\mathrm{Gr}/\mathrm{Re}^2 << 1$. The ratio for the internal cavity has been plotted against axial distance in blue in Figure 2.43. The ratio in the outer cavity has been calculated for a single location as it is reasonably constant. These plots consider a high flow rate and with $\mathrm{Re} = 22500$ at the plate.

Figure 2.43 shows that buoyancy will be an important factor in both cavities. In the outer cavity, the ratio remains above 100. The buoyancy effects are likely to be further reinforced by the inlet and outlet, as the inlet tube is positioned at the bottom of the cavity, and the outlet positioned at the top. For the inner cavity, it appears that buoyancy is unlikely to be evident at the plate, however, it is possible that the extended residency time of the air at the nose of the bullet will lead to some buoyancy forces creating a vertical thermal gradient. This gradient could be carried forward and seen at the plate, however, without CFD, this largely 3D flow is hard to assess directly and is not considered further.

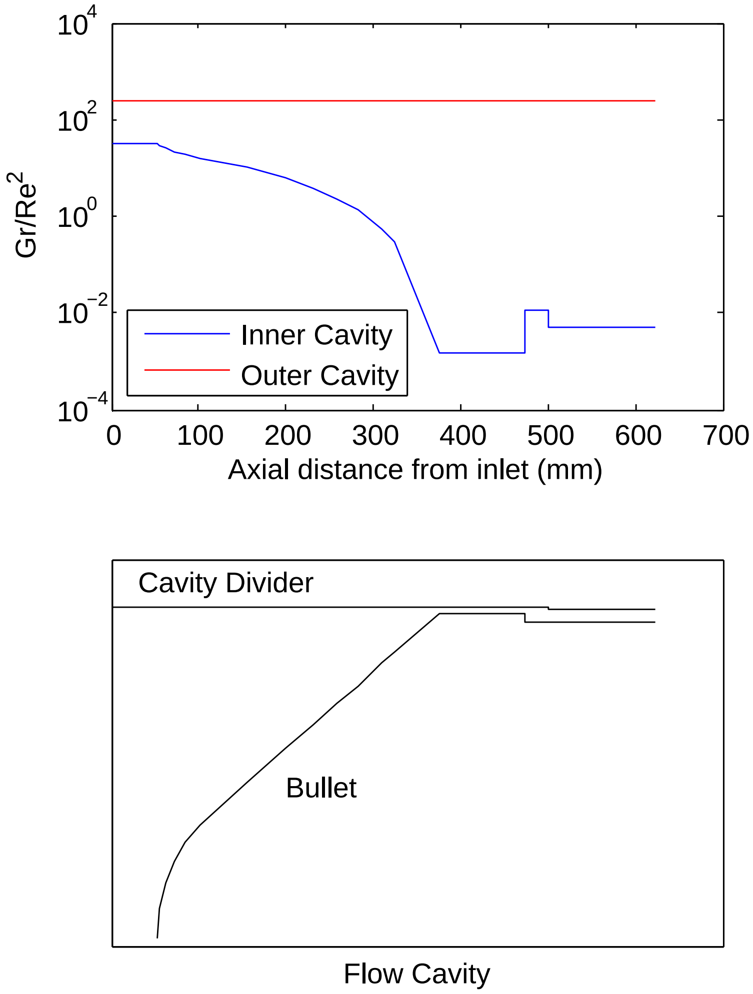

Figure 2.43: Buoyancy vs momentum vs axial location within the THTF cavities.

2.7.2 Outer Cavity Free Convection

To assess the overall effect of buoyancy in the outer cavity, consider the free convection observed within concentric, horizontal annuli. Heat transfer within concentric annuli have been investigated for the purpose of nuclear reactor design, aircraft cabin insulation, and engine cavity cooling [70]. Typically, the annulus is made of concentric cylinders, with either a horizontal or vertical axis, but eccentric and off-centre systems have been investigated as well [2]. Kuehn and Goldstein [70, 71] developed an empirical relation for the Nu on both the inner and outer concentric cylinders with a horizontal axis under steady-state conditions. Systems dominated by buoyancy convection are defined by their Rayleigh Number ($\mathrm{Ra} = \mathrm{Gr}\,\mathrm{Pr}$). In Kuehn and Goldstein's method, the inner and outer surfaces have separate Ra, defined as;

$$\mathrm{Ra}_{Di} = \frac{g\beta_v(T_i - \bar{T}_B)D_i^3}{\nu\alpha} \tag{2.55}$$

$$\mathrm{Ra}_{Do} = \frac{g\beta_v(\bar{T}_B - T_o)D_o^3}{\nu\alpha} \tag{2.56}$$

Where D_i and D_o are the inner and outer cylinder diameters, T_i and T_o are the inner and outer cylinder temperatures, $\bar{T}_B$ is the bulk air temperature, ν is the air kinematic viscosity and α is the air thermal diffusivity. Initially, $\bar{T}_B$ must be estimated, but as the equations are calculated, eventually $\bar{T}_B$ can be recalculated and the process is iterated towards a stable solution. Usually it takes 4-5 iterations. The second step is to calculate the inner and outer Nu;

$$\mathrm{Nu}_i = \frac{2}{\ln\left(1 - \frac{2}{((0.5\,\mathrm{Ra}_{Di}^{1/4})^{15} + (0.12\,\mathrm{Ra}_{Di}^{1/3})^{15})^{1/15}}\right)} \tag{2.57}$$

$$\mathrm{Nu}_o = \frac{2}{\ln\left(1 - \frac{2}{((\mathrm{Ra}_{Do}^{1/4})^{15} + (0.12\,\mathrm{Ra}_{Do}^{1/3})^{15})^{1/15}}\right)} \tag{2.58}$$

Finally, $\bar{T}_B$ can be recalculated from;

$$\frac{\bar{T}_B - T_o}{T_i - T_o} = \frac{\mathrm{Nu}_i}{\mathrm{Nu}_i - \mathrm{Nu}_o} \tag{2.59}$$

Francis *et al.* [45] showed that this method is accurate for $10^5 < \mathrm{Ra} < 10^8$, which covers the upper laminar and transitional flow regimes. For $10^8 < \mathrm{Ra} < 10^{10}$, as is the case for the vessel outer cavity, the Kuehn and Goldstein model over predicts the convective heat transfer, but not by much.

The flow structure in such an annulus tends to be represented by the streamlines and isotherms shown in Figure 2.44 assuming that the central cylinder at the higher temperature.

The system produces a hot plume above the central cylinder that impinges on the top of the outer cylinder creating the highest HTC in the system. The air cools and flows down the outer cylinder before reaching a stagnant region at the bottom. Air drawn from the bottom of the annulus cools the bottom of the inner cylinder, creating the highest HTC local to the inner surface. According to Kenjeres and Hanjalic [67], as Ra increases, the recirculation and turbulence at the top of the annulus increases (the streamlines become more pronounced) leading to increased mixing in the upper region. In turn, this leads to a larger stagnant region at the bottom.

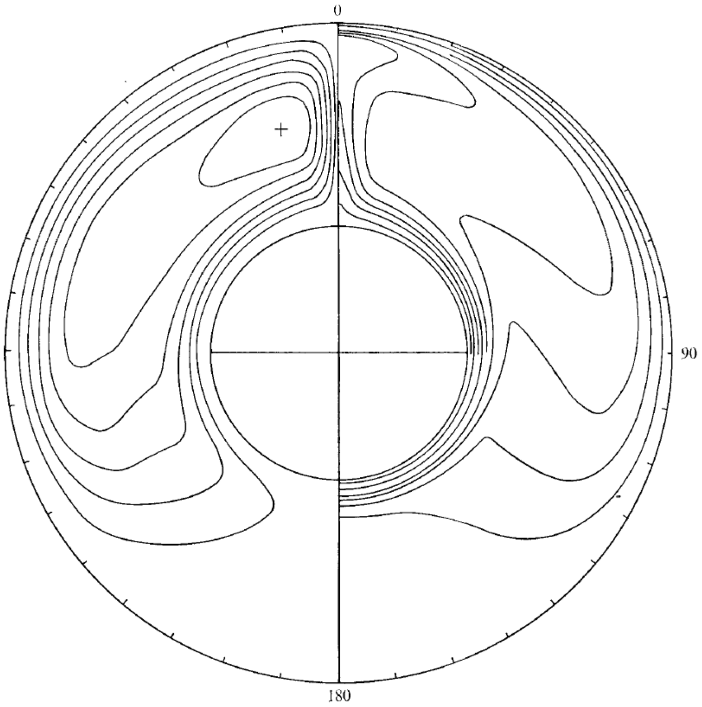

Figure 2.44: Streamlines (left) and isotherms (right) of steady laminar flow in a concentric annulus with $\mathrm{Ra} = 10^5, \mathrm{Pr} = 5.0$ [70].

Overall Ra is usually calculated as

$$\mathrm{Ra}_L = \frac{g\beta_v(T_i - T_o)L^3}{\nu\alpha} \tag{2.60}$$

Where $L = D_o - D_i$. The papers mentioned so far typically deal with $T_i - T_o \approx 3K$ and $0.5m < L < 3m$. Compare this to the THTF outer cavity, which has $T_i - T_o \approx 300K$ $L = 0.9m$. This driving temperature typically pushes Ra to $\sim 10^{10}$. However, the apparent Ra is likely much greater due to the inlet and outlet of the cooling flow exacerbating the conditions. This would drive a significant thermal gradient in the outer cavity. Furthermore, the fact that the inlet and outlet are off-centre lead to an eccentric skew in the streamlines' profile. This has knock-on effects on the HTCs.

For insight into eccentric regimes, consider the angled ellipse and flat tubes as studied by Abed *et al.* [2] and Sakr [113]. The streamlines and isotherms from the former are shown in Figure 2.45. These show, perhaps unsurprisingly, that the regions of higher velocity near the inner surface lead to higher to higher HTCs and lower temperatures. These results can help explain the overall temperature distributions in the context of the THTF commissioning tests.

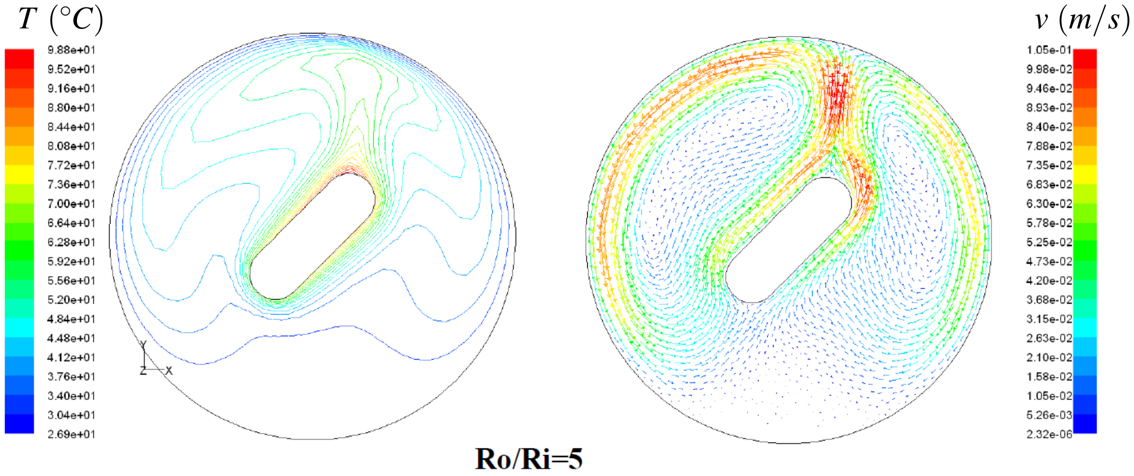

Figure 2.45: Isotherms (left) and velocity vectors (right) for a flat tube in an annulus [2].

2.8 Commissioning of Facility

2.8.1 Experiment Procedure

A series of experiments were undertaken to validate the design and demonstrate the safe operability of the THTF. Each experiment has some variation in procedure, so as a general case it is instructive to look at the results of a typical experiment as shown in Figure 2.46. The lower graph has dual y-axes; pressure on the left, and temperature on the right. The temperature data includes the heater output measurement, and 76 of the casing TCs (four returned faulty data. The time instances in brackets in Figure 2.46 match the experimental procedure as follows;

1. Upstream valve (IV2) is opened with the core flow (CV1) set to a very low flow in order to pressurise the vessel and pipework.

2. The core flow is increased allowing the heater enough mass flow to be turned on safely.

3. The impingement system valves (CV2s) are opened for a short period to help warm up the casing to initial conditions.
4. The bypass system is opened (via IV4) and adjusted (via CV4) such that the mass flow matches the expected flow through the impingement system.
5. First test starts. Once quasi-steady state conditions have been established (in this case, the target heater temperature is $150°C$), the flow is diverted quickly from the bypass to the impingement system. The tests typically last $60 \rightarrow 90s$.
6. First test complete, impingement turned off and bypass turned on. The switch from the impingement to the bypass is not automated, so there is a temporary loss in mass flow and thus a spike in the heater temperature. The heater set point is then reset to $250°C$.
7. Second test starts. It can be seen that between (6) and (7) the bypass flow rate has been adjusted in this example. This is not typical as the overall mechanical similarity of the systems should be maintained.
8. Second test complete.
9. The heater is switched off. At this point, because of the lost PID control at the heater, the data collected is no longer valid for construction of the model.
10. The impingement system is turned on briefly to aid the cooling down process.
11. The vessel is depressurised and allowed to cool. If tests are completed in the morning, and then again later in the day (after $3hrs$), then the casing will still be about $50°C$, but because tests are conducted much above this temperature, this is considered sufficient cooling time to ensure no effect on the important results.

2.8.2 Validation of Preheat Cycle

A test was undertaken to validate the preheating cycle developed in Section 2.4.2 (see Figure 2.19) and establish an understanding of the true vessel behaviour. The flow rate and timing of the preheat cycle is used as a target operating point. In order to recreate the ramp up of pressure and mass flow for ‘Stage 2’, the air is manually throttled at the inlet at IV0 and balanced with the outlet exhaust at CV1. The results are shown in Figure 2.50.

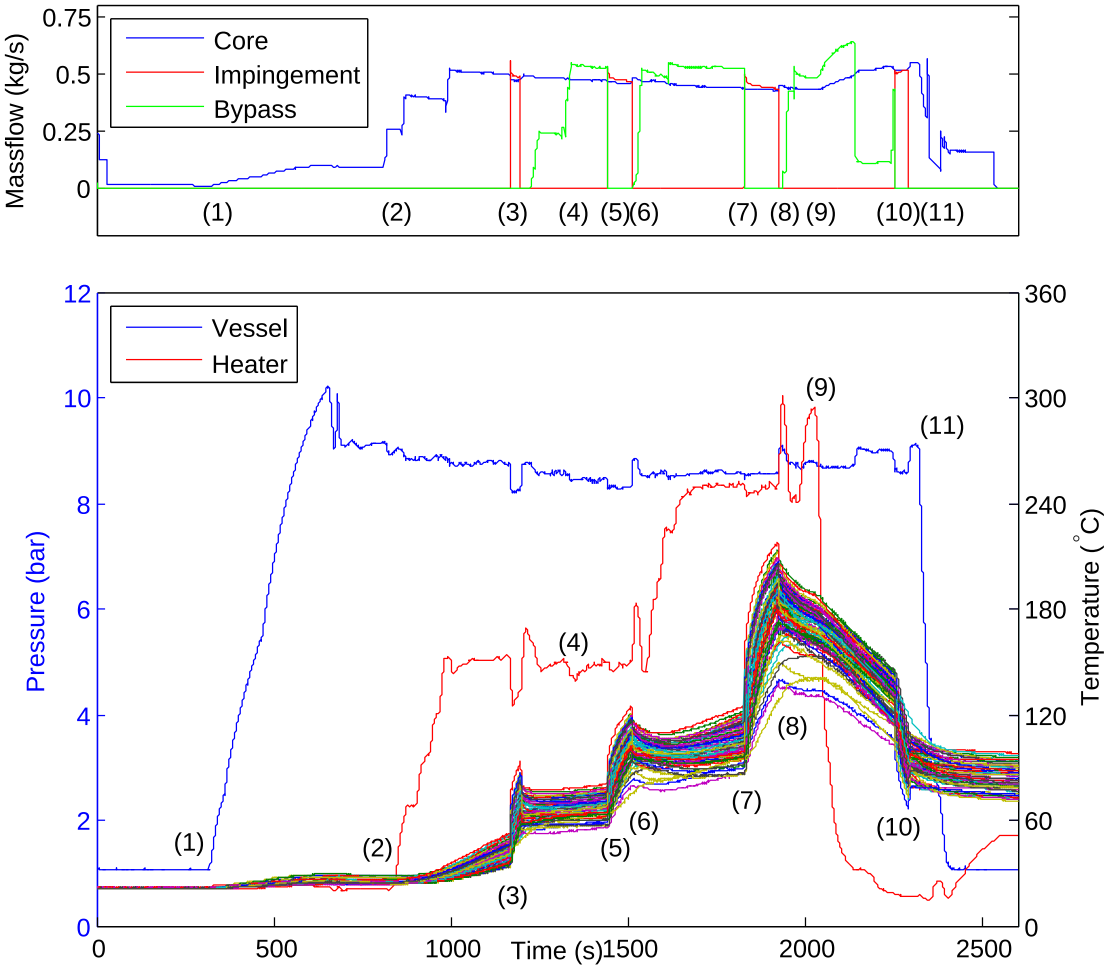

Figure 2.46: Typical experiment output for a test cycle conducted in the THTF. The multi-coloured lines represent the casing TC output. In brief, the time stamps represent; (1) upstream valve open, (2) heater on and CV1 opened, (3) impingement engaged to speed warm up, (4) bypass flow started, (5,6) first test, (7,8) second test, (9) heater off, (10) impingement engaged to speed cool down, (11) rig depressurised.

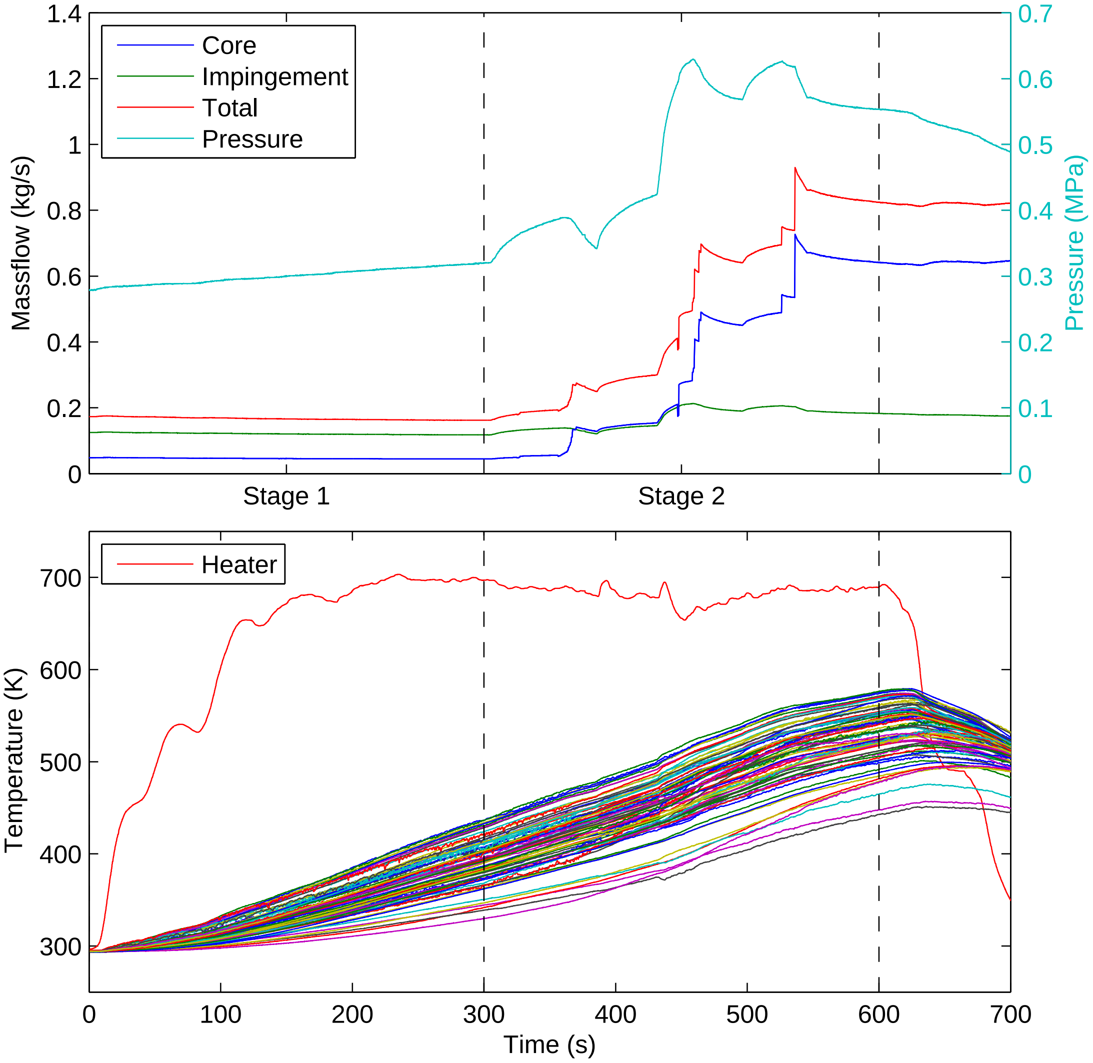

Figure 2.47: Preheat cycle as tested in the THTF.

The heater target temperature is limited to $693K$, compared with the original target of $810K$. There was oil residue in some of the flexible hosing that emitted fumes at higher temperatures, so this has been avoided as a safety precaution until it can be probably cleaned off. The heater PID does an excellent job of maintaining a constant output through the dynamic change in mass flow rate. The CV1 (Core) flow rate is initially lower than the target flow rate because the compressors are not actively compensating the system. Instead, the overall flow rate is maintained at a high enough rate to avoid tripping the low flow condition in the heater.

The flow rate through the impingement system (rather than the pressure) is one of the most important variables governing the HTC of the impingement system, and this matches the target reasonably well. The preheat cycle assumes that a flow rate of $0.1kg/s$ would produce $h_i = 165W/m^2K$. This value can be calculated from the experiment by applying an unsteady 1D energy balance to the section of the casing that is bounded by TC stations 4 and 8 as shown in Figure 2.48. Here, we assume isothermal boundary conditions at the edge of the casing, and an even HTC distribution both axially and circumferentially.

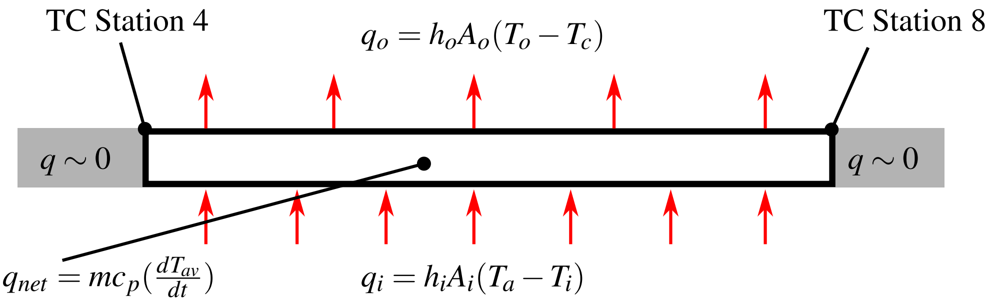

Figure 2.48: Model of heat flow through casing.

The temperature of the annulus air (T_a) is assumed to be evenly distributed, and equal to the average of the 4 annulus TCs. The temperature of the outer vessel cooling air (T_c) is assumed to remain equal to the metal starting temperature. The casing outer and inner temperatures (T_o and T_i) and the casing average temperature (T_{av}) have been found from the average of the TCs within each surface, and then across the thickness respectively, as performed in Section 2.6.2. In this case, only the TCs on the outer surface between stations 4 and 8 (inclusive) have been used. These temperatures can be shown comparatively in Figure 2.50. In practice, some of the TCs provided unrealistic data (see Appendix C for examples). However it was never more than two (out of 32 for the outer surface, and 40 for

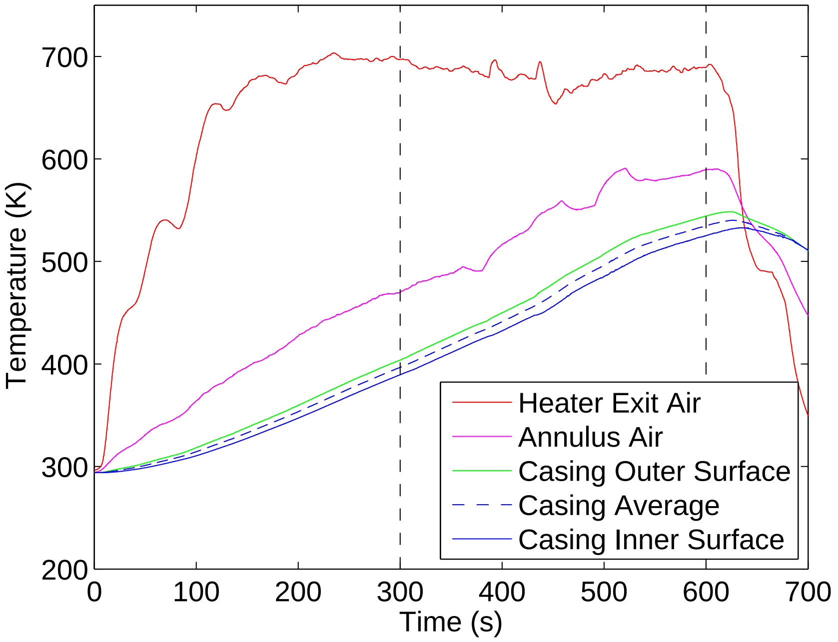

Figure 2.49: Average temperature of air and surfaces during preheat cycle.

the inner surface). To compensate for this and provide a balanced estimate, the TCs that mirror the location of the broken TCs about the vertical plane (on the opposite side of the casing) were counted twice in calculating the average surface temperatures. .

The net heat flux that warms the casing (q_{net}) is equal to the difference between the convective heating on the inside (q_i) and the outside (q_o) of the casing, therefore;

$$h_i = \frac{q_i}{A_i(T_i - T_a)} = \frac{q_{net} + q_o}{A_i(T_i - T_a)} \tag{2.61}$$

The total heat loss on the outside is unknown, but we can bound our prediction by applying an upper and lower bound to the outer HTC such that $15W/m^2K < h_o < 30W/m^2K$. The resulting prediction for the impingement HTC is shown in Figure 2.50. This figure shows that the starting HTC is precisely as predicted in during Stage 1, about $165W/m^2K$. It doesn't increase as much as expected in Stage 2, where a doubling of the HTC should happen in line with the mass flow. This is possibly due to the fact that only two SCA valves have been used to generate the flow, and as such there isn't an even distribution of the flow through the plates. There were no plates available with small enough orifices that would allow the combined four offtakes to pass the desired flow. However, this just means that the worst case scenario is not as bad as originally expected, so we should expect any better results when all four valves are used. The initial spike in the HTC (at $0 \rightarrow 20s$) is likely to be a calculation error due to a breakdown of the assumptions near the starting conditions,

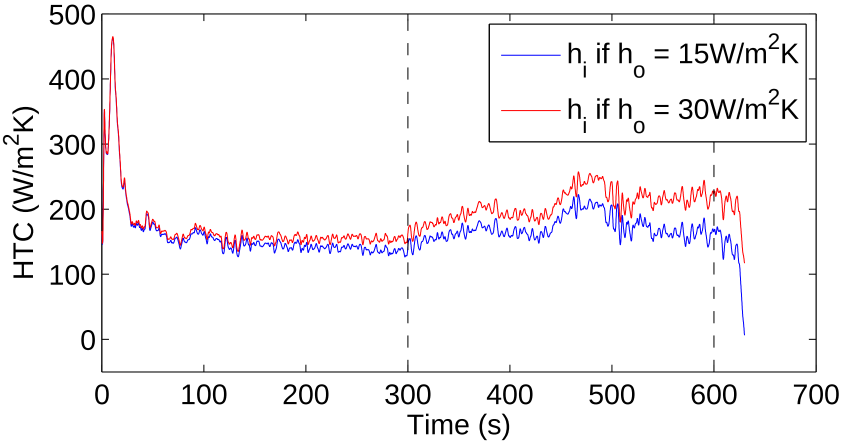

Figure 2.50: HTC of impingement system during preheat cycle.

particularly the assumption of isothermal boundary conditions. For the same reason, the calculation is also not valid above 600s.

Looking back to the results in Figure 2.49, the casing temperature rises at a constant rate up until the heater is switched off. The original prediction in Figure 2.20 was that the temperature would rise quickly initially, and then at a constant rate. The difference, particularly during Stage 1, is a significant under prediction in the temperature lost between the heater and impingement plates. This can be observed by noting that the annulus air temperature increases slowly. This, and the fact that the driving temperature is only 693K compared with the 810K target, means that the final T_{av} is only 526K, much less than the 715K predicted. Better insulation along the hot air flow path would greatly improve the prediction.

The preheat cycle was conceived to ensure that the total mass of air used in the warm up cycle was restricted as much as possible. The total mass used to the end of Stage 2 was 246kg. At an average consumption of $1kg/s$, this implies that the test could continue for 129s before the supply pressure drops to 1.72MPa. This would leave some time for the vessel to be pressurised and a test to be completed. In practice, these maximum pressure conditions are not tested often. In fact, the tests conducted in Chapter 4 use 408kg, 429kg, 384kg and 473kg in their preheat cycles respectively.

Overall, the test proved to be a sound validation of the preheat cycle as conceived. The trajectory of the casing temperature relative to the annulus temperature matches well, as the HTCs have been predicted successfully. The overall temperature will improve as more of the SCA valves are used. A replacement IV0 valve with actuator control will allow the process to be smoother, and to be optimised through experience. It is highly likely that a test at maximum temperature and pressure conditions could be readily achieved if higher mass flow is allowed through the impingement system.

2.8.3 Ability to Establish Engine Conditions

These tests considered whether or not the facility could produce the required engine steady state conditions, and to find out what accuracy could be achieved, in line with the requirements in Section 2.2.3. Tests were conducted at three pressures from $0.96 \rightarrow 1.35 MPaa$. In each test, the mass flow through CV1 is set to $0.6kg/s$, and then the set point temperature for the heater is chosen. The air temperature at the annulus has been recorded under steady state conditions and shown in Table 2.5.

Pressure ($MPaa$)	Heater Exit (K)	Annulus Air (K)
0.96	773	600
1.20	763	650
1.35	753	620

Table 2.5: Steady state measurements for validating engine conditions.

The results for the pressure and temperature measurements at the test section are shown in Figure 2.51 and Figure 2.52 respectively. In each case, only a sample of $500s$ has been shown. The vertical dashed bars indicate where steady conditions have been achieved for $50s$, and these time stamps are equivalent across both Figures. The tests have demonstrated that the facility is capable of delivering constant air flow at steady pressures and temperatures within the target specifications. The drop in pressure after each of the steady periods indicates where the SCA valves were opened, but no bypass was used. Maintaining a steady gas temperature is extremely difficult for the high end targets as the large thermal mass of the vessel continues to warm.

2.8.4 Vessel Wall Temperatures compared to the Design Case

The SC03 simulations of maximum wall temperatures from Section 2.4.4 can be validated by comparison with the temperatures recorded during facility operation. Several TCs are positioned on the internal and external surfaces of the outer wall of the pressure vessel, and

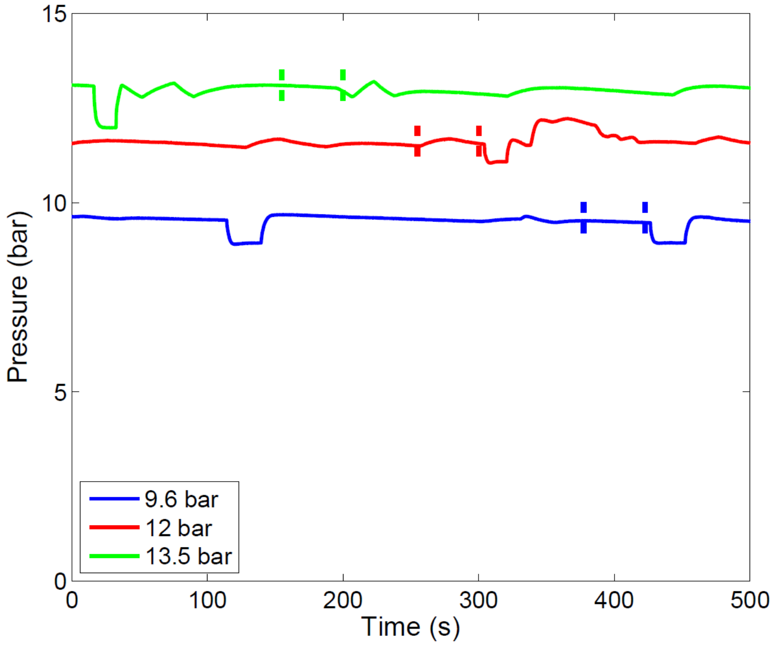

Figure 2.51: Sample data from commissioning test showing steady pressure at 9.6, 12 and 13.5*bar*. The dashed vertical lines on each pressure trace represent a period of 50 seconds where the level is approximately constant. These periods are concurrent with Figure 2.52.

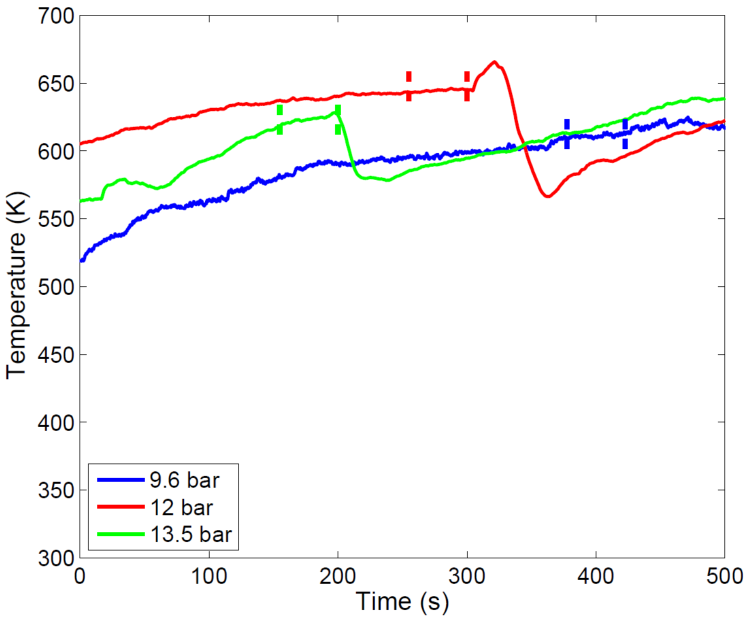

Figure 2.52: Sample data from commissioning test showing steady temperature at 9.6, 12 and 13.5*bar*. The dashed vertical lines on each temperature trace represent a period of 50 seconds where the level is approximately constant. These periods are concurrent with Figure 2.51.

these locations have been similarly sampled in the SC03 simulations, as shown in Figure 2.53.

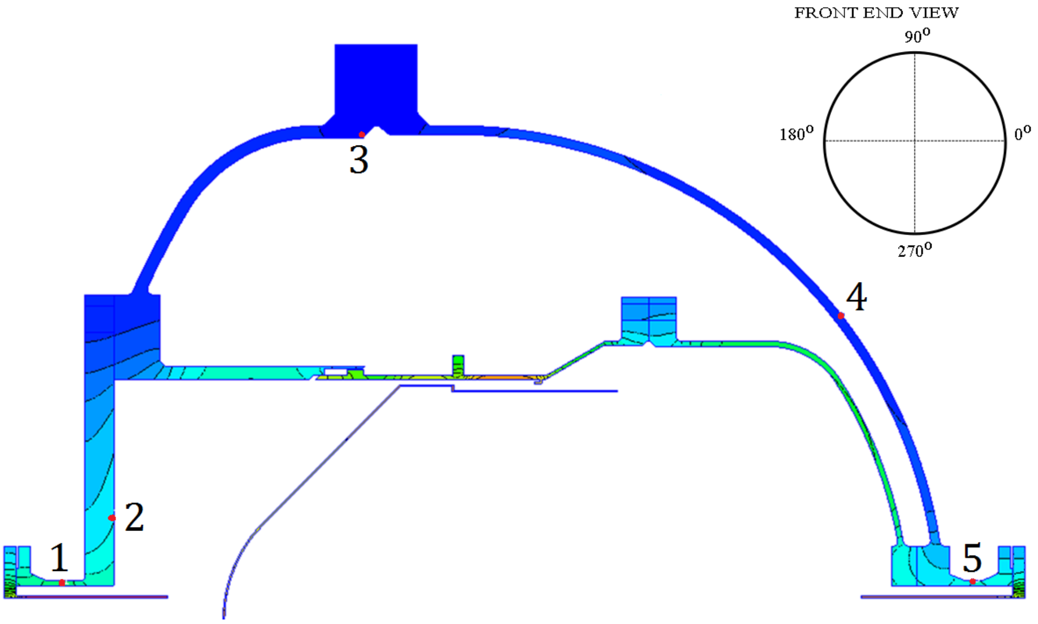

Figure 2.53: Locations measured in the THTF experiments, and sampled in the SC03 simulations, as shown in Figure 2.54.

A comparison of the design case ($810K$,$19bara$,$1kg/s$) vs the regular experiment conditions is shown in Figure 2.54. It is clear that the regular operating point is well within the design case. At locations (1,2,3,5) the actual temperature of the outer vessel wall is much lower than those of the simulation. For location (4), the temperature is $10K$ higher at the end of $1000s$. This could possibly be due to a thermal plume coming off the inner dished end. It is still far from the design limit of $573K$.

To further validate the setup of the SC03 model, the simulation is rerun with an updated cycle to match the actual input conditions from one of the experiments. The results for the wall temperature and casing are shown in Figures 2.55 and 2.56 respectively. The simulation retains the same internal HTCs as before, with the exception of the impingement plate which has been scaled to $900W/m^2K$ from maximum conditions as predicted during the design phase.

The facility has two TCs at each of locations 2 and 5, but at clocked positions. For position 5 the average of the TCs is shown, but at location 2 both TCs are shown individually. The higher value TC is directly above the inlet (90° in Figure 2.53), whereas the second TC is off centre ($\sim 150^\circ$). The difference in the response is likely due a heat plume coming off the inlet, similar to the annulus free convection. Certainly, a heat plume in the outer cavity would explain the higher temperature at location 3 compared to the SC03 study

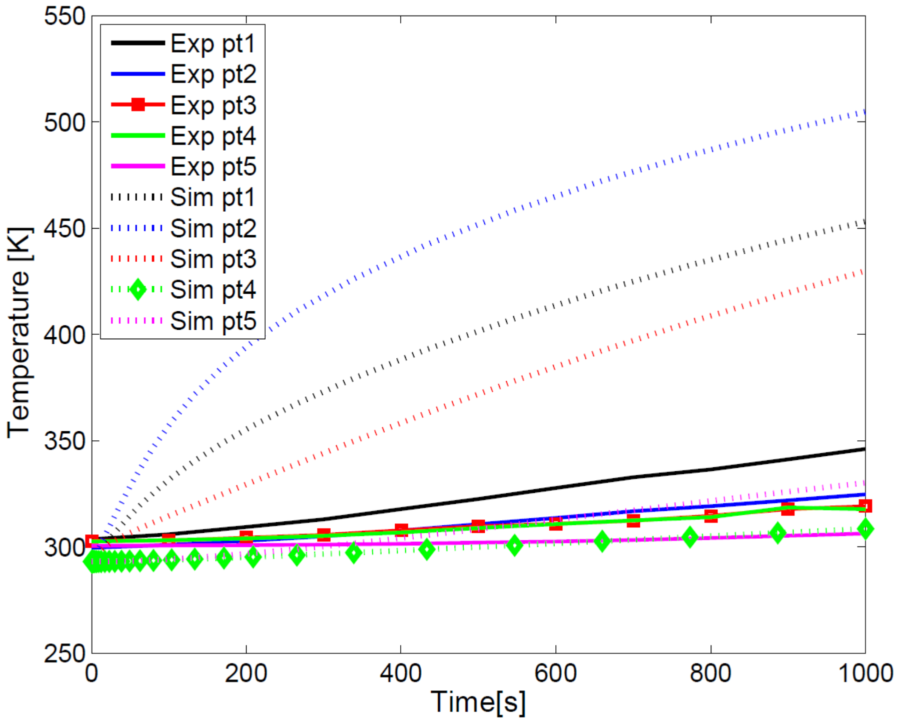

Figure 2.54: Comparison of wall temperatures under regular operation in the experiment, and under maximum design conditions in the simulation.

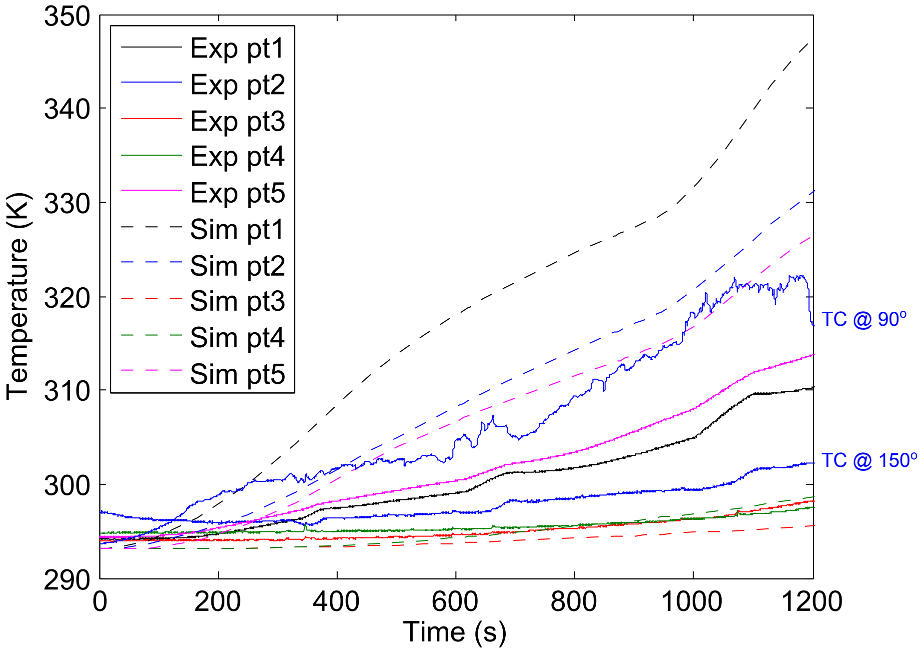

Figure 2.55: Comparison of wall temperatures under regular operation from both experiment and simulation.

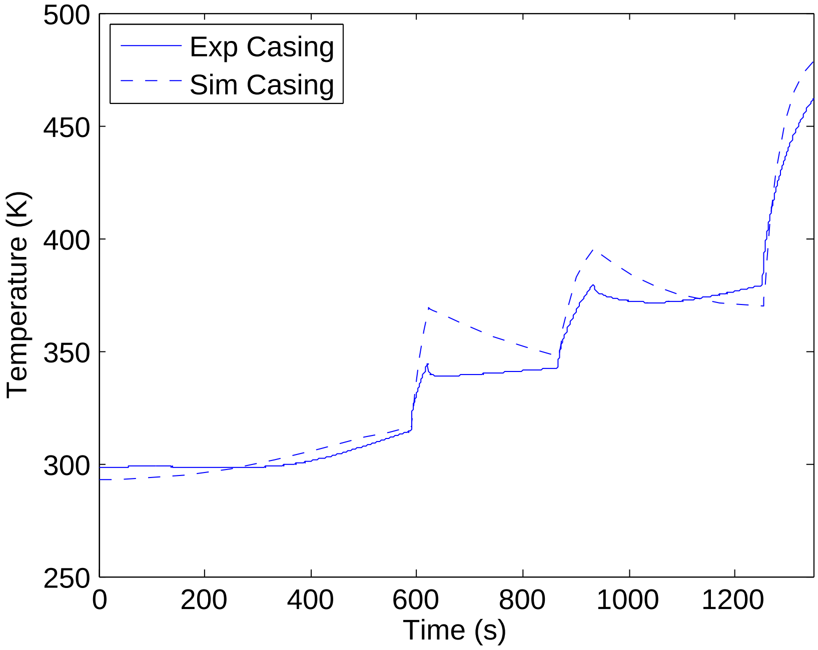

Figure 2.56: Comparison of test casing temperature under regular operation from both experiment and simulation.

that didnt account for bouyancy. Aside from location 3, the SC03 results over predict the experimental results, which means that the design was adequately conservative.

2.8.5 Casing Temperature Uniformity

Temperature uniformity of the casing is critical to understanding the achievable axisymmetric tip clearance. Figure 2.57 shows the circumferential temperature distribution of the inside of the casing at two instances in time (t_1 and t_2) during a typical test, with temperature on the radial axis. Figure 2.57a shows measurements at the forward TCs, and Figure 2.57b shows the aft TCs. The test was conducted at $13.5 bara$, and the average gas temperatures at the annulus is $265°C$ and $290°C$ for t_1 and t_2 respectively.

The region from approximately $0° \rightarrow 120°$ exhibits a temperature approximately $25K$ higher than the other circumferential positions. There also appears to be a cooler region from $230° \rightarrow 280°$. This effect could be explained by the presence of a hot plume forming on the outside of the casing, but off-centre, much like it was shown for the angled tube in Section 2.7.2. It is off-centre because the cooling flow inlet and outlet in the outer cavity of the vessel are located at 250° and 70° respectively.

To illustrate this further, the steady state temperature profile for both the inner and outer TCs has been interpolated as unwrapped contour plots in Figure 2.58. This example is taken

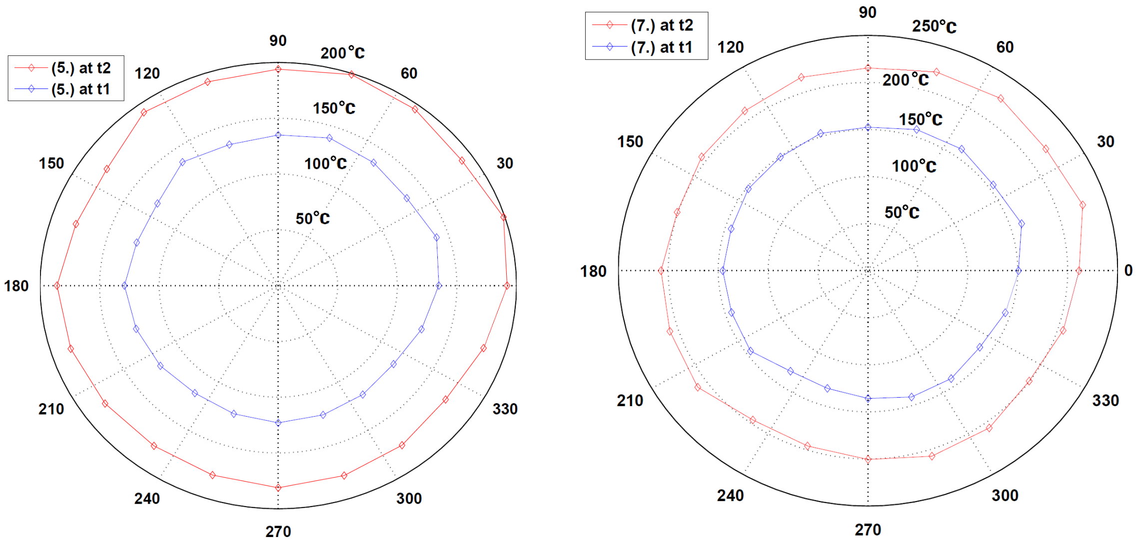

(a) Measurement point (5.)

(b) Measurement point (7.)

Figure 2.57: Circumferential temperature uniformity of the inner TCs at different times. The angular position of the TCs are shown in degrees, with 90° at the top and 270° at the bottom. The radial steps are $50°C$ in between.

from a test at $9.0bara$ pressure and average gas temperature of $180°C$. The resolution of this Figure does not capture the individual impingement holes as shown in the CFD results in Section 2.6.3, but this is expected. Instead, it does illustrate the prediction that the holes towards the rear of the plate will create a larger temperature rise than those at the front. Further, it shows that the overall temperature distribution is dominated by both the impingement system and the annulus free convection. To help isolate these effects, it is proposed that a manifold or some other insulating surface is installed around the outside of the casing to match the annulus conditions of the target engine.

2.8.6 Casing Temperature Transient Response

The casing currently being tested in the THTF is constructed from 316SS, however the real engine casing is constructed from Waspalloy that has different thermal properties (as shown in Table 2.2). The point of the THTF is that most properties of the system such as L_c, h, and T match very closely with the target system. The properties that don't are the conductivity (k) and by extension, the thermal diffusivity (α). The ratio from stainless steel to Waspalloy for k and α are 1.23 and 1.31 respectively. Therefore, it is necessary to perform a non-dimensional study of the results to show that the SCA system working with a Waspalloy casing can produce a temperature rise of $25K$ in $5s$. This analysis is summarised from work done by Dann *et al.* [39] and is included for completeness.

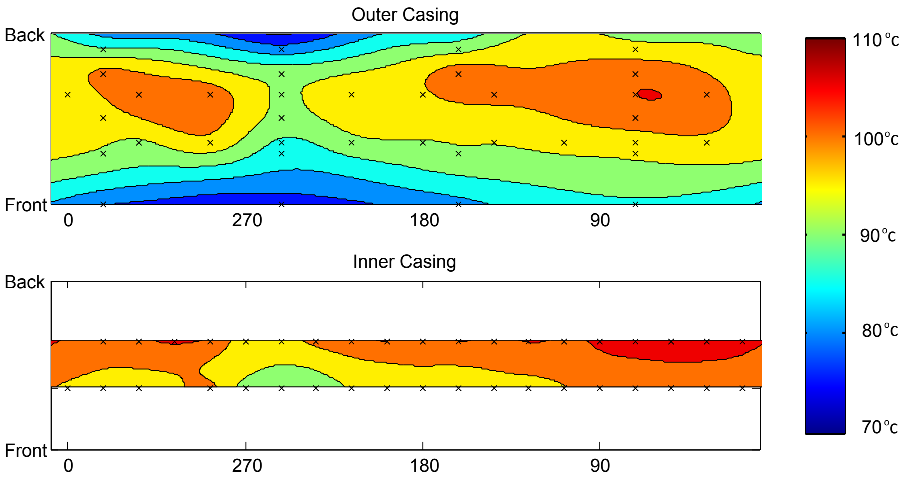

Figure 2.58: Contour plot of the unwrapped temperature profile. Crosses mark locations of TCs. The temperature between TCs has been interpolated linearly across each surface.

An example time response for the average casing temperatures is shown in Figure 2.59 which includes the average inner surface temperature, the average outer metal temperature, and the volume average metal temperature ($\bar{T}$) as calculated in Section 2.6.2 and using a HTC of $50W/m^2K$ for free convection on the outer surface. This data was taken from a test at $13.5bara$ where the air increases from $265°C \rightarrow 290°C$ over $100s$. The resulting $\bar{T}$ varies by $\pm 1.6K$ around the circumference.

The results of several tests have been evaluated using the non-dimensional groups of Biot number (Bi), Fourier number (Fo) and non-dimensional temperature (Θ);

$$\Theta = f(\text{Bi}, \text{Fo}) \tag{2.62}$$

$$\frac{T - T_0}{T_\infty - T_0} = f(\frac{hL_c}{k}, \frac{\alpha t}{L_c^2}) \tag{2.63}$$

where T is the average metal temperature, T_0 is the average metal temperature at the beginning of the test, T_∞ is the temperature of the air at the annulus, and t is time. The h has been calculated using Equation 2.61, and a selection of the best performing results are shown in Figure 2.60. This figure also shows the target function (in black) based on a Waspalloy casing and the target rate of $25K$ in $5s$. The performance of the system showed good agreement with the CFD results. Furthermore, the latest CFD results for new hole pattern designs show an increased HTC. Therefore, Dann *et al.* concluded that the overperformance of the system in the THTF suggests that SCA is sound and warrants investigation in a ground engine test.

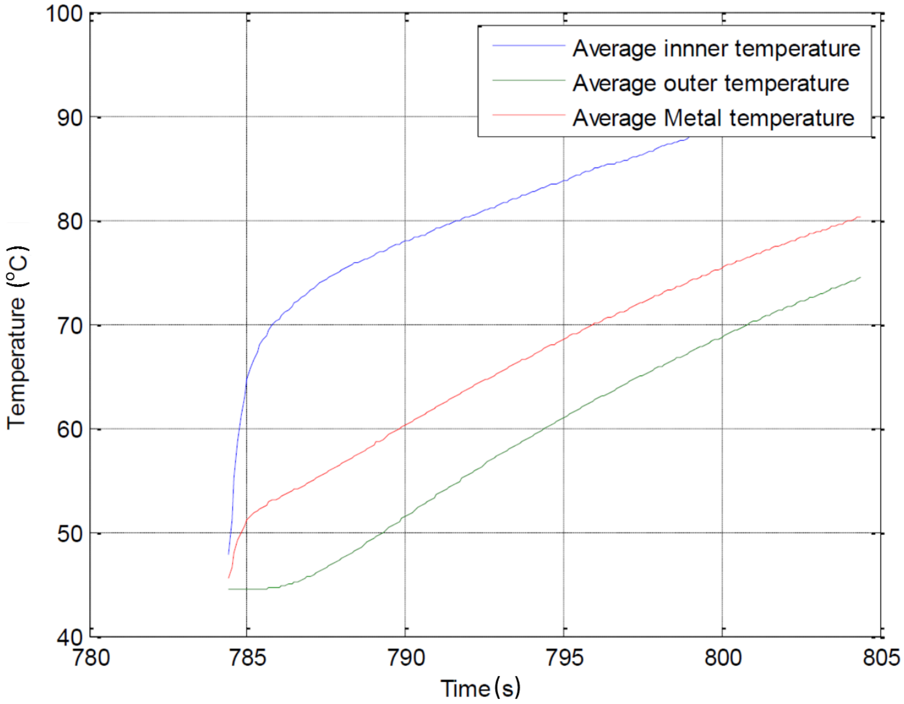

Figure 2.59: Example of the average rise in T_i, T_o and $\bar{T}$ after the SCA valves are opened.

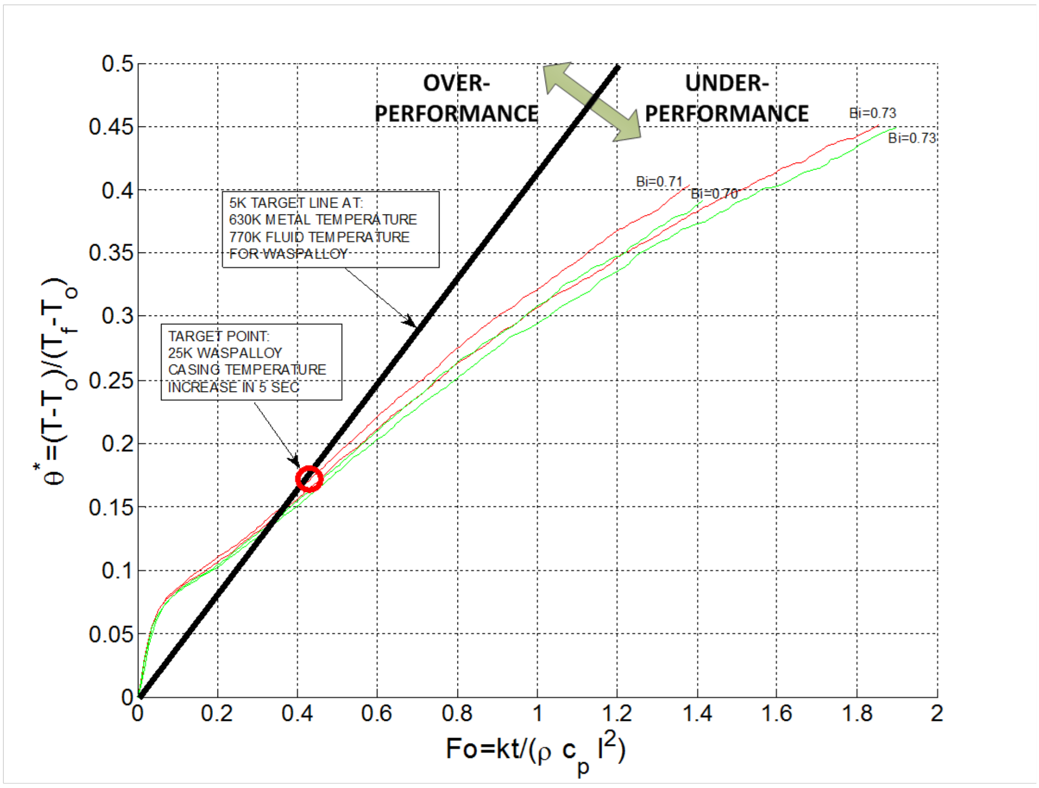

Figure 2.60: Non-dimensional groups $(\Theta, \mathrm{Bi}, \mathrm{Fo})$ corresponding to different test arrangements compared with the target profile in the real engine [39].

2.9 Conclusions

This chapter has presented the design and commissioning of the THTF, a new facility capable of producing engine realistic test conditions. The test piece is representative of a full size HP turbine casing from a large civil engine. The test air has been successfully run at $13.5bar$ pressure, $770K$ temperatures and $1kg/s$ flow rates under test conditions. A preheat cycle has demonstrated that the test casing can be preheated with a controlled warm up of the facility, such that the average starting temperature is $526K$. This allows the facility to carry out up to two transient impingement tests of 10s each in a single experiment run at maximum conditions. More tests can be undertaken if intermediate conditions are also tested. The impingement plates create the highest heat fluxes at the aft holes, as had been predicted through theoretical analysis and CFD studies, and confirmed through experiment. The results show that the SCA system should be successful and that the target rate of $25K$ in $5s$ can be achieved. The construction of the vessel using predominantly boiler steel and stainless steel has made it substantially cheaper than the closest alternative facilities. The fatigue life of the pressure vessel has been calculated as 20 000 cycles based on an extensive finite element analysis. There are some buoyancy effects creating hot spots and temperature gradients within the test piece and vessel. It is yet to be determined how similar these effects will be to the real engine environment.

Chapter 3

Review of Reduced Order Models for Thermal Systems

3.1 Introduction

As outlined in Chapter 1, reduced order models of thermal systems are necessary for any flow control application. Both casing expansion and disc lives are dependent on induced temperature transients, so tracking those transients online is beneficial. Models are built using known physical laws that link together the plant's otherwise independent sensor information. Measurements of the model can then be used to investigate internal states, mitigate sources of noise in the sensor measurements, identify performance issues and/or optimise the control of the new mechanisms. For use in real-time applications in aircraft, it is important that the model is sufficiently low order for execution on a standard FADEC system task.

This chapter will review the literature with regards to creating reduced order models of thermal systems that are suitable for real-time application. Section 3.2 reviews the fundamentals of the dynamic systems and control theory. Section 3.3 discusses the heat equation and how it can be solved analytically. Section 3.4 develops lumped parameters models as a method of solving the heat equation with ODE approximations and different variants. Section 3.5 discusses how a linear single-input/single-output model can be used to simulate non-linear plants using linear parameter varying systems. Section 3.6 briefly discusses balanced realisation which is a common control theory technique for generating practical low order models that has been used in thermal applications. Section 3.7 introduces the singular value decomposition and how it can be applied as an excellent approximation of the heat equation.

3.2 Preliminaries

3.2.1 Dynamic Systems

Consider the open loop dynamic system, or *plant*, shown in Figure 3.1a which could represent any engine component. A given input signal $u(t)$ drives the plant's internal state $x(t)$, which in turn is measurable by an output $y(t)$. The input signal will typically encounter some process noise/disturbance $w(t)$ before it has the chance to affect the plant, and the output measurement will have some sensor noise $v(t)$.

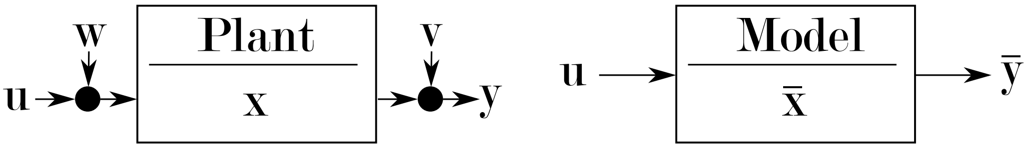

(a) Plant (b) Model

Figure 3.1: Block diagrams representing inputs and outputs of dynamic systems.

A surrogate model of the plant, with the same input $u(t)$, would have the approximate internal state $\bar{x}(t)$ and output $\bar{y}(t)$ as shown in Figure 3.1b. The purpose of the model is to replicate the plant behaviour, ensuring that the error $y-\bar{y}$ is minimised according to a given metric. The advantage of the model is it allows direct access to useful information about the internal state via $\bar{x}(t)$. To build a model, we start by considering systems represented by linear ordinary differential equations (ODEs) that have parameters that do not change with time, so called *linear time invariant* (LTI), and with a single input and output.

3.2.2 System Identification

An effective method of identifying the parameters (k,p,z) from a continuous, rich data set is to use optimisation over a horizon of samples. This is a method of *parametric identification.* Start by taking the step response of the system by applying the input;

$$u(t) = \begin{cases} 0, t \leq 0 \\ 1, t > 0 \end{cases} \tag{3.1}$$

The output $y(t)$ is then sampled at N equa-spaced time intervals. The noise is assumed to be normally distributed with a zero mean. Then, assume a transfer function $G(s)$ of the form;

$$G(s) = \mathrm{k}\frac{\prod_{i=1}^{m}(s-\mathrm{z}_i)}{\prod_{i=1}^{n}(s-\mathrm{p}_i)} \tag{3.2}$$

The side of m and n can often be chosen by inspection for low order systems. In either case, the parameters themselves are found by optimising the cost function e;

$$\begin{aligned} &\underset{\mathrm{k},\mathrm{p}_1\ldots\mathrm{p}_n,\mathrm{z}_1\ldots,\mathrm{z}_m}{\text{minimise}} && e \\ &\text{subject to} && e = \frac{1}{N}\sum_{i=1}^{N}\big(G(s)u(t_i) - y(t_i)\big)^2 \end{aligned} \tag{3.3}$$

The optimisation process can be automated through off-the-shelf routines, such as in MATLAB's System Identification toolbox.

3.2.3 Transfer Functions

Consider the dynamics of an LTI plant that can be approximated by the set of n^{th} order linear ODEs;

$$\begin{gathered} y^{(n)} + a_1 y^{(n-1)} + \ldots + a_{n-1} y^{(1)} + a_n y = \\ b_0 u^{(m)} + b_1 u^{(m-1)} + \ldots + b_{m-1} u^{(1)} + b_m u \end{gathered} \tag{3.4}$$

where the superscript (n) represent the n^{th} order of differentiation. It is useful to construct a transfer function that dictates the direct relationship between u and y. It is easiest to define this in the discrete Laplace-domain, so we take the Laplace transform of the equation;

$$\begin{gathered} \mathscr{L}\left\{y^{(n)} + a_1 y^{(n-1)} + \ldots + a_{n-1} y^{(1)} + a_n y\right\} = \\ \mathscr{L}\left\{b_0 u^{(m)} + b_1 u^{(m-1)} + \ldots + b_{m-1} u^{(1)} + b_m u\right\} \end{gathered} \tag{3.5}$$

$$(s^n + a_1 s^{n-1} + \ldots + a_{n-1} s + a_n) Y(s) = (b_0 s^m + b_1 s^{m-1} + \ldots + b_{m-1} s + b_m) U(s) \tag{3.6}$$

which can then be rearranged to give the transfer function $G(s)$;

$$G(s) = \frac{Y(s)}{U(s)} = \frac{b_0 s^m + b_1 s^{m-1} + \ldots + b_{m-1} s + b_m}{s^n + a_1 s^{n-1} + \ldots + a_{n-1} s + a_n} \tag{3.7}$$

Furthermore, by appropriate factorisation of the numerator and denominator, the transfer function can be expressed in zero-pole-gain form such that;

$$G(s) = \mathrm{k}\frac{\prod_{i=1}^{m}(s - \mathrm{z}_i)}{\prod_{i=1}^{n}(s - \mathrm{p}_i)} \tag{3.8}$$

This is useful, because the poles (p_i) and zeros (z_i) will often have physical significance.

3.2.4 State-Space Formulation

Another useful formulation of an ODE is the state-space representation. Starting again from Equation 3.4, we can rearrange the equation by invoking the state vector $x_i = y^{(i-1)}$, such that;

$$\begin{bmatrix} y^{(n)} \\ y^{(n-1)} \\ \vdots \\ y^{(1)} \\ y \end{bmatrix} = \begin{bmatrix} x_{n+1} \\ x_n \\ \vdots \\ x_2 \\ x_1 \end{bmatrix} = \boldsymbol{x} \tag{3.9}$$

This leads to the set of differential equations;

$$\begin{aligned} \dot{\boldsymbol{x}}(t) &= \mathbf{A}\boldsymbol{x}(t) + \mathbf{B}u(t) \\ y(t) &= \mathbf{C}\boldsymbol{x}(t) + \mathbf{D}u(t) \end{aligned} \tag{3.10}$$

where;

- **A** is the state (or system) matrix; represents the physics of the system.
- **B** is the input matrix; which dictates the controllability of the system, i.e. the ability of u to affect x.
- **C** is the output matrix; which dictates the observability of the system, i.e. the ability of y to accurately describe x.
- **D** is the feedthrough matrix; which has been included for completeness. In almost all physical systems $\mathbf{D} = 0$ as there is no process in nature that responds truly instantaneously.

The state-space equations are shown in block diagram form in Figure 3.2. The state-space is an incredibly useful representation of a set of ODEs, because it works for both single-input/single-output (SISO) and multi-input/multi-output (MIMO) systems where the input and output are vectors $(\boldsymbol{u}, \boldsymbol{y})$.

It is possible to convert between a SISO state-space model and the transfer function formulation. However, there are more parameters in $\mathbf{A}, \mathbf{B}, \mathbf{C}, \mathbf{D}$ than there are in the numerator and denominator of the transfer function, therefore the construction (or *realisation*) of the state-space is not unique. An infinite number of realisations exist that will accurately represent the original system. To gain access to such realisations requires a *transformation* matrix (**T**) such that;

$$\begin{aligned} \mathbf{A}_{trans} &= \mathbf{TAT}^{-1} & \mathbf{B}_{trans} &= \mathbf{TB} \\ \mathbf{D}_{trans} &= \mathbf{D} & \mathbf{C}_{trans} &= \mathbf{CT}^{-1} \end{aligned} \tag{3.11}$$

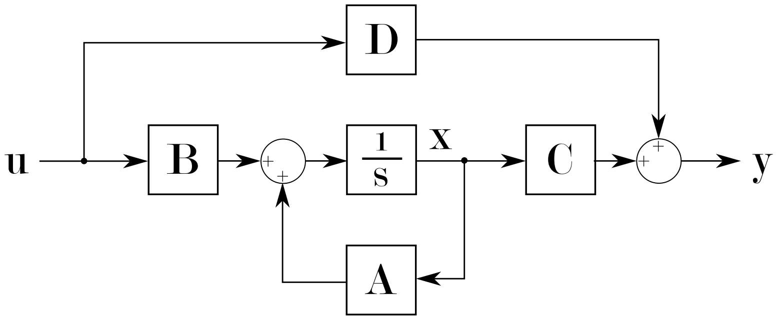

Figure 3.2: Block diagram of state-space model.

When constructing a state-space control system, choosing an appropriate realisation can help a designer to optimise the controllability and/or observability of the model [99]. This is important when converting from transfer functions to state-space representation. In this thesis, systems will be identified using transfer function parametric identification first, then converted into state-space formulation for modelling. Unless expressed otherwise, the feedthrough matrix will always be assumed to be zero.

3.3 The Heat Equation

3.3.1 Analytical Solutions

The following sections will present a series of methods for modelling thermodynamic systems based on different abstractions of the above processes. Ultimately, models emulate the physical reality of heat diffusion, which has the governing equation;

$$\frac{\partial T}{\partial t} = \alpha \nabla^2 T \tag{3.12}$$

This partial differential equation (PDE) relates the spatial temperature distribution T to the rate of change in time within a material that has thermal diffusivity α. The thermal diffusivity is calculated from the materials conductivity k, density ρ and heat capacity c_v as;

$$\alpha = \frac{k}{\rho c_v} \tag{3.13}$$

Analytical solutions for the heat equation exist for simple geometries and idealised cases. However, for systems with complex boundary conditions such as gas path processes, or shapes of highly specialised geometries, this is an intractable problem and a different approach is needed. The following sections will review different techniques to model the heat equation, and how their usefulness depends on the application, availability of information and target accuracy. A good review of current methodologies for modelling partial differential equations (PDEs) is provided by Li and Qi [78]. In this section, we consider two transient analytical solutions that have been solved in the literature.

3.3.2 Transient Solutions for Semi-Infinite Media

Analytical transient solutions only exist for a small variety of semi-infinite cases without resorting to separation of variables (see Section 3.3.3). For example, Figure 3.3 shows the case of a semi-infinite wall. We consider the initial value - boundary problem, where the temperature of the wall starts at $T(x,0) = T_0$, and the boundary is suddenly "quenched" under the isothermal condition $T(0,t) = T$. The solution is given as the *error function*;

$$T(x,t) = T_0 \, \mathrm{er}f\left(\frac{x}{2\sqrt{\alpha t}}\right) \tag{3.14}$$

This solution typically appears briefly at the boundaries of finite element simulations before the effects of the geometry shape are seen. For instance, this was observed by the author in Chapter 2 for the wall of the vessel, and Chapters 5 and 6 at the surface of the disc.

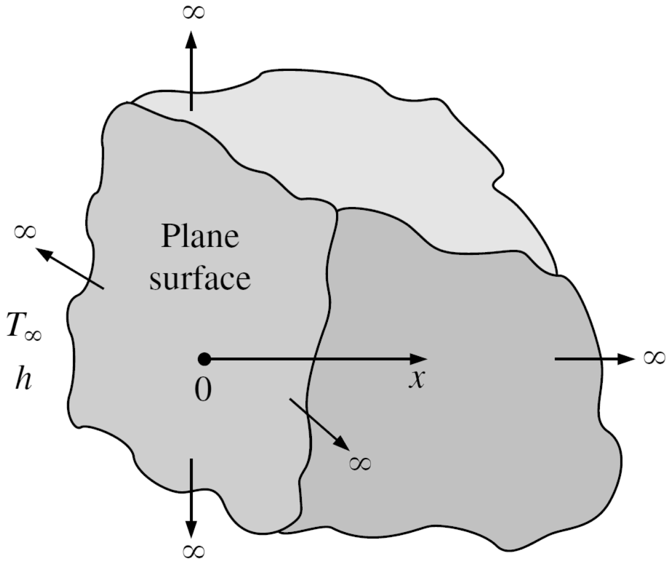

Figure 3.3: Co-ordinate system for a semi-infinite wall [60].

3.3.3 Transient Solutions for Finite Media

For a finite media case, consider the 1D infinite plate shown in Figure 3.4. Again, this is based on a "quench" case, where a solid of some temperature in an environment at T_i is suddenly immersed in a fluid environment at T_∞. The fluid remains at the same temperature throughout, and the solid gradually shifts into equilibrium. In this case, we consider an initial temperature distribution $T(x,0) = f(x)$ and Dirichlet boundary conditions, where $T(0,t) = T(L,t) = 0$. We solve this using the method of separation of variables. Assume that the solution has the form;

$$T(x,t) = \Psi(x)\Phi(t) \tag{3.15}$$

Substitute this into the heat equation and rearrange;

$$\frac{\partial \Psi\Phi}{\partial t} = \alpha \frac{\partial^2 \Psi\Phi}{\partial x^2} \tag{3.16}$$

$$\frac{1}{\alpha\Phi}\frac{d\Phi}{dt} = \frac{1}{\Psi}\frac{d^2\Psi}{dx^2} \tag{3.17}$$

We can solve each side of this equation individually, but to do so we make both sides equal to the constant $-w^2$ in order to preserve the similitude between the equations.

$$\frac{1}{\alpha\Phi}\frac{d\Phi}{dt} = -w^2 \tag{3.18}$$

$$\frac{1}{\Psi}\frac{d^2\Psi}{dx^2} = -w^2 \tag{3.19}$$

Solving the equations by direct integration gives;

$$\Psi(x) = A'\cos(wx) + B'\sin(wx) \tag{3.20}$$

$$\Phi(t) = C\big(-w^2\alpha t\big) \tag{3.21}$$

which in turn can be substituted back into the original equation, combining the coefficients into A and B;

$$T(x,t) = \big(A\cos(wx) + B\sin(wx)\big)\exp\big(-w^2\alpha t\big) \tag{3.22}$$

The next step is to solve the equation using the boundary conditions. Solving the equation at $x = 0$ implies that $A = 0$. Solving the equation at $x = L$ implies that $\sin(wx) = 0$. As such, there are an infinite number of independent solutions that satisfy the boundary conditions, and they can be solved simultaneously as;

$$T(x,t) = \sum_{n=1}^{\infty} \Big(B_n \sin\big(\frac{n\pi x}{L}\big)\Big)\exp\Big(-\big(\frac{n\pi}{L}\big)^2\alpha t\Big) \tag{3.23}$$

where n are positive integers. Finally, solve for the initial condition;

$$T(x,0) = \sum_{n=1}^{\infty} B_n \sin\left(\frac{n\pi x}{L}\right) = f(x) \tag{3.24}$$

Which can be recognised as a Fourier's series representation of $f(x)$. To find the coefficients B_n we can take advantage of the orthonormality of the solutions. Multiply the initial condition by $\sin(\frac{n\pi x}{L})$, integrate from 0 to L and normalise by half the length;

$$B_n = \frac{2}{L}\int_0^L f(x)\sin\left(\frac{n\pi x}{L}\right)\,dx \tag{3.25}$$

For the case where $f(x) = T_i$, the solution is shown in Figure 3.4 and the equation is;

$$T(x,t) = \frac{4T_i}{\pi}\sum_{n=0}^{\infty}\frac{1}{(2n+1)}\sin\left(\frac{(2n+1)\pi x}{L}\right)\exp\left(-\frac{n^2\pi^2\alpha t}{L^2}\right) \tag{3.26}$$

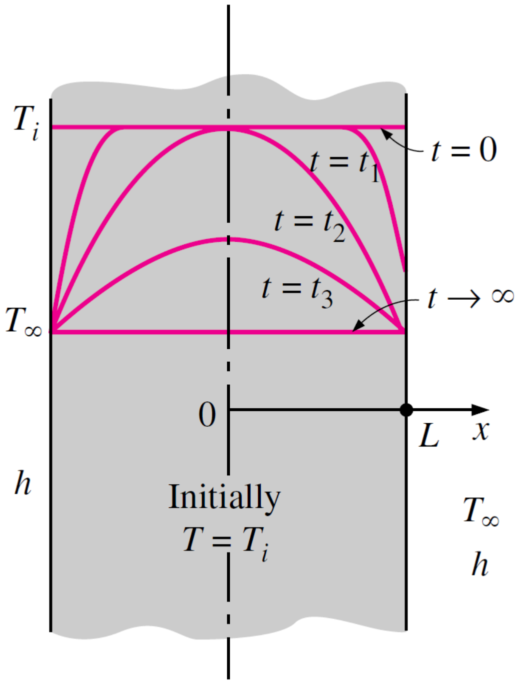

Figure 3.4: Example of 1D transient conduction through a quenching process [60].

3.4 Lumped Parameter Models

3.4.1 Lumped Capacitance

It has been shown that exact solutions to the heat equation are not available for transient boundary conditions. So, in order to create practical models, we start to make some simplifying assumptions about the domain and material properties. The broadest simplification is that the body responds as a whole to the boundary conditions, and that there is no internal temperature gradient. These models are called lumped parameter models (LPMs), and are typically used to model ODEs. They are often applied where the requirement for spatial resolution of the temperature field is less important than the computational efficiency. As such, LPM design requires an objective accuracy and then relies on simplifying the model topology into singular elements that can meet that objective. This can be done in stages or all at once, depending on the physics that are being considered. Consider the example from Incropera *et al.*[60] based on the lump of material shown in Figure 3.5.

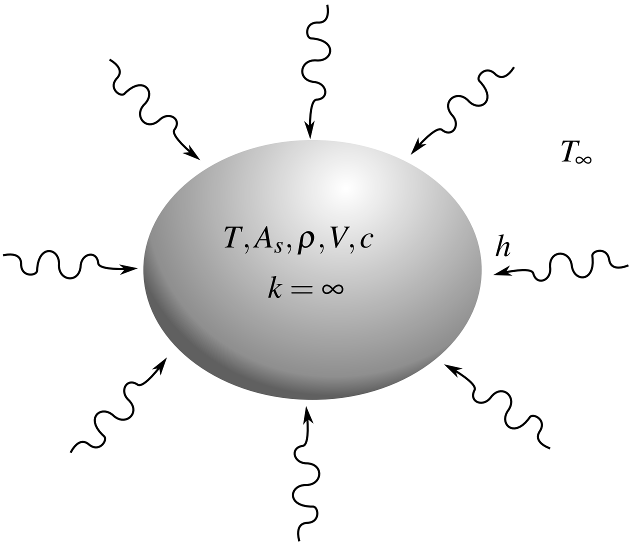

Figure 3.5: A 'lumped' piece of material with infinite conductivity, sitting in a fluid reservoir with both infinite thermal capacity and conductivity.

This example considers a solid of infinite conductivity (thus the internal temperature gradient is negligible) suspended in a fluid of sufficient volume that the presence of the solid does not affect the temperature of the far field. Heat transfer in to the materials is given by;

$$\dot{Q} = -hA_s(T - T_\infty) \tag{3.27}$$

where h is the heat transfer coefficient (HTC), A_s is the surface area of the solid, T is the uniform temperature of the solid, and T_∞ is the temperature of the fluid in the far field. The rate of change of temperature of the solid is given by;

$$\rho V c \frac{dT}{dt} = -hA_s(T - T_\infty) \tag{3.28}$$

where V is the volume of the solid. Integrating from initial conditions gives;

$$\frac{\rho V c}{hA_s} \int_{T_0 - T_\infty}^{T - T_\infty} \frac{dT}{(T - T_\infty)} = -\int_0^t dt \tag{3.29}$$

Evaluating the integral and rearranging gives;

$$\frac{\rho V c}{h A_s} ln \frac{T - T_\infty}{T_0 - T_\infty} = t \tag{3.30}$$

$$\frac{T - T_\infty}{T_0 - T_\infty} = e^{-(\rho V c / h A_s) t} \tag{3.31}$$

Furthermore, consider that the non-dimensional temperature (Θ), characteristic length (L_c), Biot number (Bi) and Fourier number (Fo) can be defined as;

$$\Theta = \frac{T - T_\infty}{T_0 - T_\infty}, \qquad L_c = \frac{V}{A_s}, \qquad \mathrm{Bi} = \frac{h L_c}{k}, \qquad \mathrm{Fo} = \frac{\alpha t}{L_c^2} \tag{3.32}$$

the temperature of the solid can be written as;

$$\Theta = e^{-\mathrm{Bi}\,\mathrm{Fo}} \tag{3.33}$$

Non-dimensional analysis can be exploited for appropriating experimental data to engine conditions, thus allowing the experiment to be undertaken at manageable lab conditions. Such an analysis was performed by Dann *et al.* [39] as presented in Section 2.8.6. In that case, the function relating the parameters was unknown. Equation 3.33 is used when the temperature of a solid can be modelled as a consolidated object, and this is called the lumped capacitance method. Lumped capacitance models are usually applied to situations where the Biot number Bi < 0.1, implying that a solid's temperature can be modelled as uniform because the temperature is dominated by the convective heating boundary conditions. For higher Biot numbers it is necessary to consider the transient conduction of heat through the material, so additional augmentation of the model is required.

3.4.2 Extended Methods

Keshavarz and Taheri have augmented the lumped capacitance method with a polynomial approximation to the temperature profile within the solid [68]. This approach assumes that the temperature of the solid as calculated above is only the average temperature of the model. Thus, there still exists some temperature distribution through the thickness of the model. The form of this distribution can be linear, quadratic, or something more complex. This method has been applied in Chapter 6.

Similar approaches using zero- and first-order Hermite integrals have proven to be very effective for monitoring the health of lithium-ion batteries [90]. In that example, the method was applied in a 1D axisymmetric case. However, generalising this approach to 2D cases is much more difficult, and so far there is no solution in the literature.

Alternative approximations using the basic LPM method divide the system into a series of smaller sections and focus on generating equations for approximating the transmission of heat between the sections, while still treating each section as a lumped model. This has been applied in modelling multi-layer slabs of differing thermal properties by Stephenson and Mitalas [125]. This method has been extended to multidimensional systems by Laurenti *et al.* [75] who considered blocks of similar geometry. The overall method proved accurate to 10% for Biot numbers up to 6.0.

3.4.3 Component Mode Synthesis

Finite element (FE) models take the lumped capacitance method to the extreme by subdividing the topology into many thousands of elements. They can be highly accurate for even the most complex boundary conditions, but the disadvantage of this method is the computation intensity that makes them unsuitable for online application directly. Instead, FE models can be reduced using Component Mode Synthesis (CMS) which identifies regions of thermal coherence within a dynamic system [89]. CMS has a multitude of different approaches, and a good overview is provided by De Klerk *et al.* [41]. Most methods start from the original definition of CMS by Hurty [58] and the modification produced by Craig and Bampton [34].

This method has been used to model the temperature field of a turbine disc by Botto *et al.* [22]. In that study, the target accuracy was $\pm 10K$, and the FE model was reduced from 6114 degrees of freedom down to 30 by visually selecting the most important eigenmodes. The model was used to investigate the disc's response to a 'hot-slam' cycle with a temperature range of roughly $350K$. Some of the eigenmodes that were found are shown in Figure 3.6.

Though the paper has identified the need to select the most important modes, which can be aided with some numerical indicator, the exact process remains subjective. Another limitation of this approach is that the material properties and HTCs are kept constant throughout the simulation in order to generate a linear model. In fact, the CMS method relies on knowledge of the FE models explicitly, including all thermal properties, boundary conditions, element location and connectivity, and has limited applicability with non-linear HTCs. It also doesn't provide direct insight into the temporal dynamics of the system.

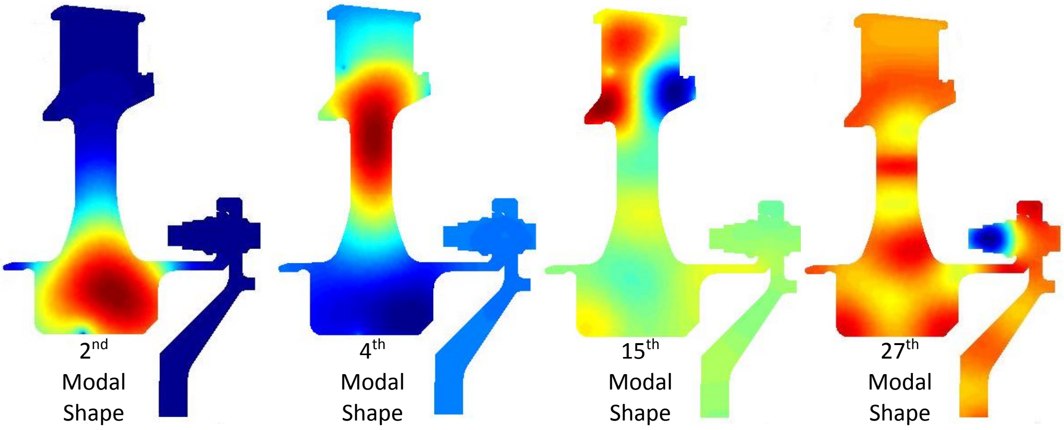

Figure 3.6: Temperature modal shapes of the disc identified with CMS from Botto *et al.* [22].

3.5 Linear Parameter Varying Models

3.5.1 General Theory

The only state-space models that have been presented so far have been LTI, however the thermal problems considered in engines don't often obey linear dynamics, as their boundaries are governed by non-linear aerodynamics. Non-linear behaviour can be modelled by adapting different control parameters to different operating points, a process called *gain-scheduling*. One such class of models are called linear parameter varying (LPV) systems. In an LPV system, the parameters of the ODEs behave linearly between local operating points. Their value is dependent on some exogenous signal (θ) whose trajectories are unknown *a priori* but are bounded by some compact set and can be measured online. The state-space model of an LPV system was first described by Shamma [116] and is defined as;

$$\begin{aligned} \dot{\boldsymbol{x}}(t) &= \mathbf{A}(\theta)\boldsymbol{x}(t) + \mathbf{B}(\theta)\boldsymbol{u}(t) \\ \boldsymbol{y}(t) &= \mathbf{C}(\theta)\boldsymbol{x}(t) \end{aligned} \tag{3.34}$$

The signal θ is called the parameter vector (or scheduling variable). In aircraft applications, the parameter vector is usually compiled of the power demand, altitude and Mach number of the engine, as supported by the work of Henrion *et al.* [54]. Bruzelius *et al.* [25] identified that despite having a rich source of signals to choose from when selecting the scheduling variables, it is important to choose a small number that are independent of each other in order to avoid creating a conservative controller. This also leads to a simpler LPV model which in turn leads to a simpler controller.

There are no strict methods for creating LPV models, and most require choices by the designer that are problem dependent. As such there has been a very wide variety of methods presented in the literature [132]. A lot of early work to analyse LPV systems for stability and apply them in the context of gain-scheduled controllers has been done by Shamma *et al.* [28, 117, 118, 120, 119], Becker *et al.* [16, 17] and Apkarian *et al.* [6, 7]. Recent surveys by Rugh & Shamma [111] and Leith & Leithead [76] generally divide LPV synthesis into either linearisation theory or quasi-LPV approaches, the latter of which includes models identified through experimental results, though there is also some overlap between the techniques. Henrion *et al.* [54] also identified models using a computationally simulated turbofan rather than from laboratory experiment data.

3.5.2 Linearisation Approach

Linearisation (or Jacobian Linearisation) comes from the Taylor series expansion and truncation of a nonlinear system $f(t)$ in the neighbourhood of an equilibrium point t_a;

$$f(t) = f(t_a) + f'(t)(t-t_a) + \frac{f''(t)}{2!}(t-t_a)^2 + \frac{f^{(3)}(t)}{3!}(t-t_a)^3 + \ldots + \frac{f^{(n)}(t)}{n!}(t-t_a)^n \quad (3.35)$$

An LPV model can be created by aggregating the solutions of a family of equilibrium points covering a large number of operating conditions. The model works by switching between solutions based on the parameter vector θ. In this case θ must be strictly made up of exogenous signals and/or output signals ($\boldsymbol{y}$) and not be dependent on the state ($\boldsymbol{x}$). Definition of the family of equilibrium points and the selection of θ are problem dependent.

The effectiveness of the model depends on the validity of the linearisation far from equilibrium points, and the requirement that the parameter vector varies slowly and smoothly [111]. It is necessary to ensure that there is a smooth transition of the parameters with respect to the trajectory of θ as the model switches from point to point throughout the entire thermal space.

Linearisation methods have found particular use in wind turbine regulation [11, 20, 21], where the equations governing the mechanical behaviour of the blades, shafts, and mounting are well understood.

Jacobian linearisation has been compared and contrasted with velocity based linearisation in an attempt create a model using experimental data by Reberga *et al.* [106]. Velocity based linearisation uses the derivative of the state-space;

$$\begin{aligned}\ddot{\boldsymbol{x}}(t) &= \frac{\partial}{\partial \boldsymbol{x}}\Big(\mathbf{A}(\theta)\boldsymbol{x}(t)+\mathbf{B}(\theta)\boldsymbol{u}(t)\Big)\dot{\boldsymbol{x}}+\frac{\partial}{\partial \boldsymbol{x}}\Big(\mathbf{A}(\theta)\boldsymbol{x}(t)+\mathbf{B}(\theta)\boldsymbol{u}(t)\Big)\dot{\boldsymbol{u}}\\ \dot{\boldsymbol{y}}(t) &= \frac{\partial}{\partial \boldsymbol{x}}\Big(\mathbf{C}(\theta)\boldsymbol{x}(t)+\mathbf{D}(\theta)\boldsymbol{u}(t)\Big)\dot{\boldsymbol{x}}+\frac{\partial}{\partial \boldsymbol{x}}\Big(\mathbf{C}(\theta)\boldsymbol{x}(t)+\mathbf{D}(\theta)\boldsymbol{u}(t)\Big)\dot{\boldsymbol{u}}\end{aligned} \tag{3.36}$$

in order to generate a quasi-LPV model, as the parameter vector is dependent on the state. This would provide advantages in a model far from equilibrium points, however, this advantage was lost when the analytical solution was not given. The two approaches were implemented with a military turboreactor, where the input vector is made up of the nozzle area and fuel flow, the output vector is the pressure in the combustion chamber, and the parameter vector is a combination of the Mach number, altitude and pilot lever angle (PLA). There were 18 different step cycles used to train the model, starting from ground idle and reaching maximum take-off (MTO). The functions governing each model were identified using two methods, piecewise linear interpolation and polynomial interpolation. These produced almost indistinguishable results. The final models are of comparable quality as shown in Figure 3.7. Neither closely match the steady-state case, though it is remarked that this can be corrected simply. The reason for the inclusion of the **D** matrix is unclear, and it would appear that removing it from the framework may have improved results.

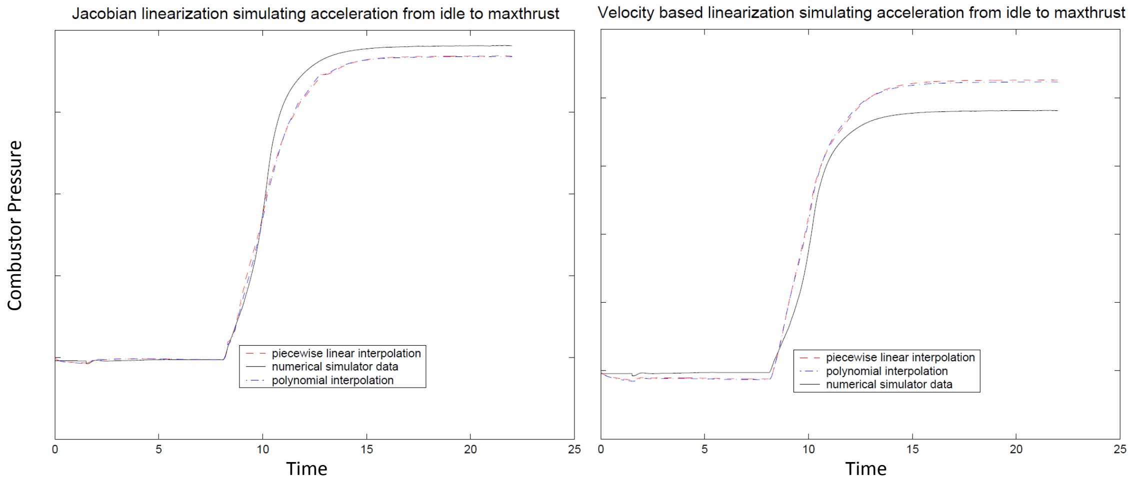

Figure 3.7: Two different LPV methods for modelling combustor pressure from Reberga *et al.* [106] .

3.5.3 Quasi-LPV Approach

The quasi-LPV approach to LPV models generates a state-space system with a θ that is dependent on both the exogenous signals and the state ($\boldsymbol{x}$). In this system there is only a single equilibrium point at the origin and the non-linearities are disguised within the relationship between the state-space parameters and θ. Such a system can be analysed for stability much like an LTI at any particular operating point.

Quasi-LPV systems are useful in guidance applications because the equations of motion governing each axis do not need to be assessed independently. This has been applied for the control of a generic missile [128], a 747 aircraft [92], turbofan shaft speed [79] and for a twin rotor model [110]. Lu and Wu [84] have demonstrated that for large variations in parameters it is possible to use a family of LPV systems and switch between them in order to generate better performance from a controller overall. Kwiatkowski *et al.* [72] has also attempted to create an automated system for creating the quasi-LPV model, and highlight the wide selection of options available to a designer to create different models for the same nonlinear plant which may or may not give optimal results.

3.5.4 LPV System Identification

A more general process of identifying quasi-LPV systems based on experimental data is another methodology that has shown an increased popularity recently, again primarily in motion control. Analytically derived models can be difficult to produce, and will often miss key dynamics necessary for creating accurate models for control. This is particularly true for modelling the dynamics of lightweight structures, as investigated by Tóth *et al.* [133], who advocate data-driven identification of the LPV model. There are two methods presented in the literature; (1) techniques that identify LPV models based on one set of measurements with time-varying parameters, and (2) techniques based on multiple different sets of measurements using ‘frozen values’ of the scheduling variable [103]. Bamieh & Giarré [13] developed compact formulae to solve the latter approach, in order to identify the polynomial based relationship between the parameters of the transfer function and the scheduling variable using recursive-least-squares and least-mean-square algorithms. This has been applied to great effect by Steinbuch *et al.* [124] first to resolve the frequency response of a mechanical linkage system, and later to a build a gain-scheduled controller for a robot arm [53]. This thesis will also utilise an application of the ‘frozen value’ method as it is most easily formulated from the available experimental and FE data.

Different techniques for synthesising LPV controllers have been summarised by Balas [12], including linear fractional transformations, single quadratic Lyaponov functions and parameter-driven quadratic Lyaponov functions. Balas’ work explores the differences between the linearisation based models, quasi-LPV models, and models based on system identification, though there is some overlap between them. They are successfully applied in the context of a full simulation of a Pratt & Whitney twin spool, after burning turbofan. Their conclusion is that the guaranteed and actual performance and robustness of the the rate-bounded LPV control designs far outweighs their computation time expense.

3.6 Balanced Realisation Models

One advantage of the LPV system identification is that it does not require special insight into the governing equations in order to create the model. Whether or not a model is built on the heat equation directly, it is useful again to consider another method of reducing the order of the model for real-time application. From a control point of view, a typical route to reduce the order of a stable transfer matrix would be to find a balanced realisation of the model state-space as proposed by Moore [99]. A balanced realisation is one that balances the observability and controllability of the model.

This approach has been applied to thermal models of buildings by Ménézo *et al.* [97]. In that case, both 1D and 2D elements were considered in creating the model of the floor and walls, and the model accounts for non-linear conduction, convection and radiation effects. The model shows good tracking through a series of step responses. However, the range of temperatures spanned is small compared with aircraft systems, and the temperatures are averaged over large volumes meaning that there is poor spatial resolution.

3.7 Singular Value Decomposition Models

3.7.1 Mathematical Description

Stepping back from modelling theory, it is important to introduce a mathematical process for analysing matrices called the singular value decomposition (SVD). Let $\mathbf{Q}$ be an $m \times n$ matrix. It is possible to decompose $\mathbf{Q}$ into three matrices $\mathbf{U}, \Sigma, \mathbf{V}$ that satisfy;

$$\mathbf{Q} = \mathbf{U}\Sigma\mathbf{V}^{\mathsf{T}} \tag{3.37}$$

where Σ is an $m \times n$ matrix with non-zero elements strictly along the main diagonal, and where $\mathbf{U}$ and $\mathbf{V}$ are square matrices of rank m and n respectively. Each column of $\mathbf{U}(U_i)$ links uniquely with a single element of $\Sigma(\sigma_i)$ and column of $\mathbf{V}(V_i)$. Moreover, the columns of both $\mathbf{U}$ and $\mathbf{V}$ are internally orthonormal, such that the inner product;

$$\langle U_i, U_j \rangle = \begin{cases} 1, i = j \\ 0, i \neq j \end{cases} \tag{3.38}$$

and

$$\langle V_i, V_j \rangle = \begin{cases} 1, i = j \\ 0, i \neq j \end{cases} \tag{3.39}$$

This makes the SVD a form of proper orthogonal decomposition (POD). Depending on the application it can also be known as Karhunen-Loéve decomposition or principal component analysis [105].

The SVD can be used to identify patterns of coherence in the structure of the original matrix. The column vectors $(U_1, U_2 \dots U_m)$, also known as *singular vectors*, are equivalent to the normalised eigenvectors of $\mathbf{Q}\mathbf{Q}^\mathsf{T}$;

$$\mathbf{Q}\mathbf{Q}^\mathsf{T} U_i = \lambda_i U_i \tag{3.40}$$

$\mathbf{U}$ is found by compiling the results into a single $m \times m$ matrix and finding the normalisation. In this process, an equal number of eigenvalues $(\lambda_1, \lambda_2 \dots \lambda_m)$ are also produced and stored. The columns of $\mathbf{V}$ are found by applying the same theory to $\mathbf{Q}^\mathsf{T}\mathbf{Q}$;

$$\mathbf{Q}^\mathsf{T}\mathbf{Q} V_i = \lambda_i V_i \tag{3.41}$$

This results in a $n \times n$ matrix. By virtue of this approach, and assuming that $m < n$, there are m eigenvalues that appear in each solution[1]. The *singular values* (σ_i) of $\mathbf{Q}$ are equal to $\sqrt{\lambda_i}$ for each value up to λ_m. The matrix Σ can be constructed by setting σ_i along the main diagonal and zeroes everywhere else. The decomposition is then completed as;

$$\mathbf{U}\Sigma\mathbf{V}^\mathsf{T} = \begin{bmatrix} U_1 U_2 \dots U_m \end{bmatrix} \begin{bmatrix} \sigma_1 & & & 0 & \\ & \sigma_2 & & & \\ & & \ddots & & \\ 0 & & & \sigma_m & \end{bmatrix} \begin{bmatrix} V_1^\mathsf{T} \\ V_2^\mathsf{T} \\ \vdots \\ V_m^\mathsf{T} \\ \vdots \\ V_n^\mathsf{T} \end{bmatrix} \tag{3.42}$$

Typically, the elements are ordered such that $\sigma_i > \sigma_{i+1}$, and the order of the vectors in $\mathbf{U}$ and $\mathbf{V}$ are rearranged to match. As the final columns of Σ are zero, they can be discarded, along with the final rows of $\mathbf{V}^\mathsf{T}$. The final result can be written as;

$$\mathbf{Q} = \begin{bmatrix} U_1 U_2 \dots U_m \end{bmatrix} \begin{bmatrix} \sigma_1 & & & \\ & \sigma_2 & & \\ & & \ddots & \\ & & & \sigma_m \end{bmatrix} \begin{bmatrix} V_1^\mathsf{T} \\ V_2^\mathsf{T} \\ \vdots \\ V_m^\mathsf{T} \end{bmatrix} \tag{3.43}$$

---

[1] and vica-versa if $n < m$.

Alternatively, $\mathbf{Q}$ can also be represented by the sum;

$$\mathbf{Q} = \sum_{i=1}^{m} U_i \sigma_i V_i^{\mathsf{T}} \tag{3.44}$$

The SVD has applicability across fields as diverse as climatology [98, 142], brain imaging [64], turbulent fluid flows [18] and big data compression [19].

3.7.2 Approximation of a Temperature Field

The use of SVDs to model thermal systems with was set forth by Gay and Ray [49]. They exploit the properties of SVD truncation to select only the most significant spatial and temporal modes of the system, and use this to reduce the model. In this way, SVD models behave functionally like an intermediate blend of balanced realisation and CMS. However, unlike CMS, SVD models don't require previous knowledge of material properties or physical boundary conditions. The original demonstration by Gay and Ray is general for all PDEs but here we start from the heat equation in 3D;

$$\frac{\partial T}{\partial t} = \alpha \nabla^2 T \tag{3.45}$$

When solving PDEs analytically we often resort to solution with separation of variables, where dependence in space and time is separated. We therefore assume that we can represent a solution to the heat equation as:

$$T(x,y,z,t) = \sum_{l=1}^{M} \Psi_l(x,y,z)\Phi_l(t) \tag{3.46}$$

This representation is not unique, and will depend on our choice of model for Ψ_l and Φ_l. For example we can represent Ψ_l with a Fourier series which would then give a corresponding specific set of time functions $\Phi_k(t)$. For SVD models, we assume that $\Psi_l(x,y,z)$ can be represented by an orthogonal set of functions, such that;

$$\iiint \Psi_i(x,y,z)\Psi_j(x,y,z)dxdydz = \begin{cases} 1, i = j \\ 0, i \neq j \end{cases} \tag{3.47}$$

To find $\Psi_l(x,y,z)$ analytically would require knowledge of the boundary conditions along the curved surface of the body, instead SVD models use system identification to derive the responses from experimental data. Consider subsampling the temperature field of a body at discrete locations $\chi_i = \chi(x_i, y_i, z_i)$ and at times t_k during a transient manoeuvre to get the matrix $T(\chi,t)$. We postulate can be represented as a POD of the form;

$$T(\chi,t) = \sum_{l=1}^{M} \Psi_l(\chi)\Phi_l(t) \tag{3.48}$$

This is immediately identifiable as a equivalent to the SVD of the data set;

$$T = \sum_{i=1}^{M} U_i.\sigma_i V_i^{\mathsf{T}} \tag{3.49}$$

It follows that each vector can be approximated as $\Psi_l = U_i$ and $\Phi_l = \sigma_i V_i^{\mathsf{T}}$. System identification can be performed on $\sigma_i V_i^{\mathsf{T}}$ to identify each of the temporal functions Φ_l. By ordering the elements of the SVD such that $\sigma_i > \sigma_{i+1}$, the relative importance of each successive term is diminished. Selecting only the first r terms, an approximation for temperature, $\hat{T}$ is given by;

$$\hat{T} = \sum_{i=1}^{r} U_i \sigma_i V_i^{\mathsf{T}} \tag{3.50}$$

Thus, it is possible to create a reduced order model by identifying the first r modes of the system. The selection of 'r' is chosen to satisfy some predetermined criteria of accuracy.

Gay and Ray applied the above technique to the modelling and control of a 1D metal slab with a series of 21 TCs and 20 controlled heating zones [49]. Data was generated by running 20 step cycles of differing inputs that excited as many modes of the system as possible. Because the setup is 1D and the TCs equally span the domain, the resulting vectors appear like B-splines of different order of control. The model was reduced from 20 to 6 modes based on the SVD.

Zheng and Hoo [148] create a similar model for a tubular chemical reactor, using an eighth order SVD-Karhunen-Loève expansion model. A grey-box style model featuring nonlinear boundary conditions is demonstrated by Romijn *et al.* [109]. SVD models have been extended to 2D temperature models as well, including thermal bridges and multizone buildings [146] and metal slabs with active cooling control [140, 50]. This thesis will develop a model similar to Gay and Ray [49] in Chapter 4. The SVD has been chosen because it can be created directly from temperature data, and the spatial and temporal modes can be readily adapted for changing boundary conditions using the LPV system approach.

3.7.3 Applications Similar to the SVD

Jones *et al.* [65] use the method of Galerkin projections and eigenfunctions to obtain a reduced order model of temperature distribution for a spray deposition process. The heat equation is first converted into an infinite dimensional set of ordinary differential equations, before being reduced down to a few first order ordinary differential equations by selecting the most important eigenmodes. This allows for efficient real-time implementation of the model for the purposes of the closed loop control of the process. Further, in direct relation to turbine metal temperatures, Widrich *et al.* [143] tested a variety of simulation techniques using a combination of SVD identified modes and multi-layer feedforward neural networks to accommodate the nonlinear dynamics. The range of temperatures they simulated was in the region of $280K$ using the first 5 modes of the POD. It is unclear what accuracy they achieve during transients as there are no difference plots, however they identified the importance of choosing modes which optimally represent general system behaviour because the accuracy of modes is limited from one data set to another.

Chapter 4

Development of LPV-SVD Methodology

4.1 Introduction

This chapter presents the proposal and validation of the LPV-SVD methodology through the application of the model to the Transient Heat Transfer Facility (THTF). The literature review of the previous chapter has set the mathematical framework for approximating a temperature field with SVDs. This model is augmented by applying a quasi-LPV process to the data acquisition. In developing the model for application to the THTF, the model inputs are based on measurements of the pressure and temperature of the air entering the vessel, and the state of the SCA offtake mechanism. The desired output is the temperature profile of the casing based on the locations of the TCs. The methodology has been evaluated using the model to simulate unseen experiments.

Section 4.2 develops the mathematical theory behind the LPV-SVD model. Section 4.3 presents the scope and methodology behind creating a model of the casing from the experimental results. This includes a detailed analysis of the SVD process and the system identification process. Section 4.4 presents a full overview of the model. Section 4.5 presents the validation process used to ensure that best model has been developed, and then compares the simulated results with experimental data from both the validation test cycle, and an earlier test from the original THTF experiments. The final conclusions are presented in Section 4.6.

4.2 Theory

Based on the literature in Chapter 3, a new method is developed that incorporates non-linear modelling from quasi-LPV methods with the spatial resolution of SVD analysis. This method is applicable for modelling high Bi components subject to complex aerodynamic environments such as studied here. We start from the SVD based model of a thermal system, which has the structure;

$$T(\chi,t) = \sum_{i=1}^{m} \Psi_i(\chi)\Phi_i(t) \tag{4.1}$$

However, in our case and most turbomachinery cases, there are non-linear boundary conditions that cannot be neglected, and the above model structure is not fit for purpose. Instead, consider an LPV-SVD formulation;

$$T(\chi,t) = \sum_{i=1}^{m} \Psi_i(\chi)\Phi_i(\theta,t) \tag{4.2}$$

where $\Phi_i(\theta,t)$ are found through quasi-LPV identification. By introducing the parameter vector (θ), the spatial modes can be adapted for a wide range of operating conditions. Firstly, θ is selected such that it adequately parameterises the system's aerodynamics. The functions are identified from experimental data using the 'frozen-value' method. In this approach, a series of experiments are undertaken where each experiment uses a constant value of θ and a step change in $u(t)$. The parameters of each $\Phi_i(\theta,t)$ are identified following the method in Section 3.2.2, where the poles (p), zeros (z) and gains (k) are stored in lookup tables for later interpolation. As such, it is important that the numbers of poles and zeros for each $\Phi_i(\theta,t)$ are consistent across all θ. If this can't be achieved, then the model doesn't work, and this can become a limiting factor in the rank of the final model, and possibly the accuracy.

When the model is put together, the p,z,k values are recalled for use in state-space representation such that $\Phi_i(\theta,t) = \boldsymbol{y}_i(\theta,t)$;

$$\begin{aligned} \dot{\boldsymbol{x}}_i(t) &= \mathbf{A}_i(\theta)\boldsymbol{x}(t) + \mathbf{B}_i(\theta)u(t) \\ \boldsymbol{y}_i(\theta,t) &= \mathbf{C}_i\boldsymbol{x}(t) \end{aligned} \tag{4.3}$$

Notice that $\mathbf{C}$ in this realisation is not dependent on θ. This is necessary to keep the construction of the state-space consistent across each Φ_i as there are more variables in the state-space than there are poles and zeroes in the transfer functions. To see how the identified variables are utilised, consider $\boldsymbol{y}_i$ that has been identified with the transfer function;

$$Y(s) = \mathrm{k}(\theta)\frac{s-\mathrm{z}(\theta)}{(s-\mathrm{p}_1(\theta))(s-\mathrm{p}_2(\theta))}.U(s) \tag{4.4}$$

this can be realised in state-space form;

$$\begin{aligned} \dot{\boldsymbol{x}}(t) &= \begin{bmatrix} \mathrm{p}_1(\theta) & 0 \\ \mathrm{p}_2(\theta)-\mathrm{z}(\theta) & \mathrm{p}_2(\theta) \end{bmatrix}\boldsymbol{x}(t) + \begin{bmatrix} \mathrm{k} \\ 0 \end{bmatrix}\boldsymbol{u}(t) \\ \boldsymbol{y}(\theta,t) &= \begin{bmatrix} 1 & 1 \end{bmatrix}\boldsymbol{x}(t) \end{aligned} \tag{4.5}$$

The proof of this is shown in Section 4.3.9. The elements of **C** are Boolean (0 or 1) in any such realisation. When the final model is built, $\Psi(\chi)$ can be incorporated directly by multiplying the vector $\mathbf{C}_i$ with the spatial vector $\mathbf{U}_i$;

$$\Psi_i(\chi) = \mathbf{C}_i\mathbf{U}_i = \begin{bmatrix} 1 & 1 \end{bmatrix} \mathbf{U}_i \tag{4.6}$$

Consequently, the final model will directly produce the temperature output;

$$\begin{aligned} \begin{bmatrix} \dot{\boldsymbol{x}}_1(t) \\ \dot{\boldsymbol{x}}_2(t) \\ \vdots \\ \dot{\boldsymbol{x}}_m(t) \end{bmatrix} &= \begin{bmatrix} \mathbf{A}_1(\theta) & & & 0 \\ & \mathbf{A}_2(\theta) & & \\ & & \ddots & \\ 0 & & & \mathbf{A}_m(\theta) \end{bmatrix} \begin{bmatrix} \boldsymbol{x}_1(t) \\ \boldsymbol{x}_2(t) \\ \vdots \\ \boldsymbol{x}_m(t) \end{bmatrix} + \begin{bmatrix} \mathbf{B}_1(\theta) \\ \mathbf{B}_2(\theta) \\ \vdots \\ \mathbf{B}_m(\theta) \end{bmatrix} \boldsymbol{u}(t) \\ T(\theta,\chi,t) &= \begin{bmatrix} \Psi_1(\chi) & \Psi_2(\chi) & \dots & \Psi_m(\chi) \end{bmatrix} \begin{bmatrix} \boldsymbol{x}_1(t) \\ \boldsymbol{x}_2(t) \\ \vdots \\ \boldsymbol{x}_m(t) \end{bmatrix} \end{aligned} \tag{4.7}$$

The model can be easily reduced by selecting the first r functions from the m that have been identified. The basis for this can then be determined by the designer. This model has been applied to the experimental results from the THTF casing in this chapter, and to the simulated results from an IP disc in Chapter 5.

4.3 Methodology

4.3.1 Model Scope

The LPV-SVD model has been used to simulate the casing temperature of the THTF. Unlike the engine that takes a smooth trajectory through different operating points, the THTF is designed to simulate one steady operating point and the response of the casing to a step change in conditions. As such, the model has been designed to replicate this limited aspect of operation. The proposed model uses measurements of the THTF as the input signal and parameter vector, and a prediction of the casing temperature as the output.

The scope of the model is limited to the following conditions;

- The facility is already pressurised.
- The bypass has been tuned to perfectly match the mass flow through the CV2 valves.
- All four of the CV2 valves act together, and simultaneously with IV4.
- There is no change in the impingement plate geometry.

- There is no active change in CV1 position.

The measurement suite of the THTF that was considered in constructing the model is shown in Figure 4.1. These are limited to measurements in the hot path - downstream of the heater. The control signals are also shown, but they are not recorded during experiments as the model is expected to respond to physical measurements of the THTF and not the input signals. This is to replicate the perceived development in future engine applications. The accuracies of each of the measurements are shown in Table 4.1.

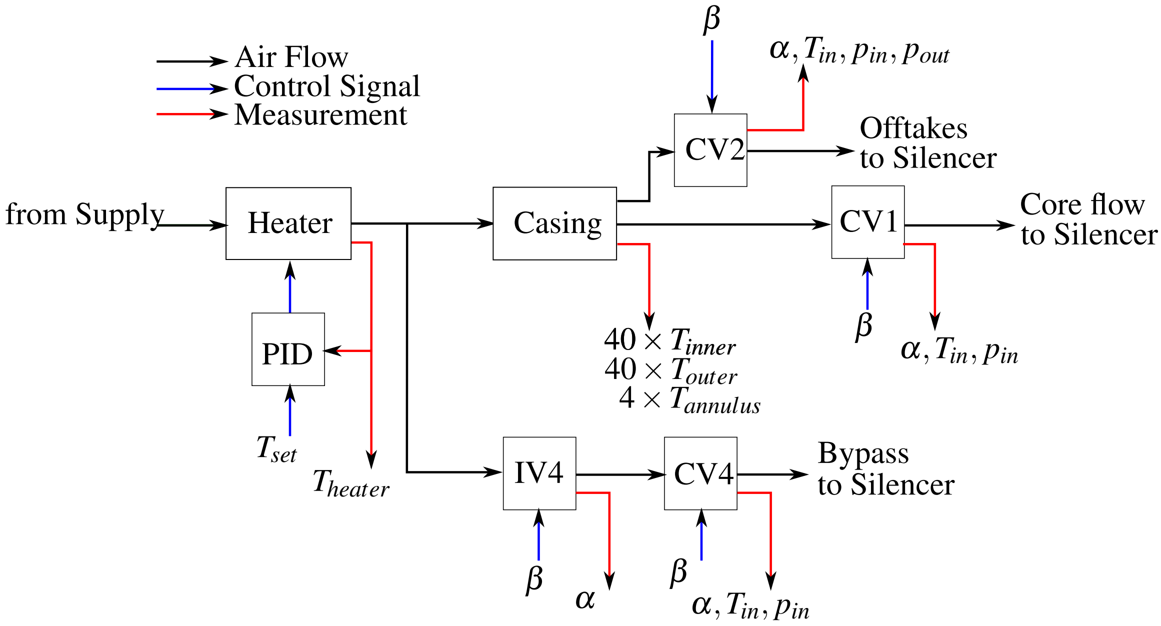

Figure 4.1: Instrumentation and control signals downstream of the heater in the THTF. The command for the opening angle is β, while α is the measured feedback.

4.3.2 Signal Selection

The output of the model is based on the casing inner and outer TC measurements, T_{inner} and T_{outer} respectively, as shown in Figure 4.2. However, the input signal and parameter vector were not so simply defined as there are several signals that could be selected and/or combined. The heater set point temperature (T_{set}), the heater output temperature (T_{heater}) and the average of the four annulus measurements ($T_{annulus}$) were considered for the input signal. The aim of the model is to set a foundation for later engine testbed experiments, so it is counter-productive to rely on measurements of the annulus flow that would not be available so close to the casing in the real engine, so $T_{annulus}$ is ignored. The set point temperature (T_{set}) is discarded as the model is not expected to recreate the dynamics of the PID controller that governs the heater elements. As such, T_{heater} is used as the basis for the

Description		Number	Recorded Unit	Expected Error ($\pm$)	Model Vector
Casing	$T_{outer}*$	40	K	$2.5K$	y
	$T_{inner}*$	40	K	$2.5K$	y
	$T_{annulus}$	40	K	$2.5K$	
Heater	T_{heater}	1	K	$2.5K$	u
CV1	T_{in}	1	K	$2.5K$	
	p_{in}	1	$bara$	0.3%	θ
	α	1	%	-	
CV2	T_{in}	4	K	$2.5K$	
	p_{in}	4	$bara$	0.3%	
	p_{out}	4	$bara$	0.3%	
	α	4	%	-	θ
CV4	T_{in}	1	K	$2.5K$	
	p_{in}	1	$bara$	0.3%	
	α	1	%	-	
IV4	α	1	%	-	θ

Table 4.1: Data collected from the THTF used in developing the LPV-SVD model. *These measurements are metal temperatures, all other temperature measurements are of the gas flow.

input signal, normalised by ambient temperature T_0 and the maximum set point temperature T_{max} (500°C).

The parameter vector for the model is based on the pressure at the inlet of CV1 (p_{in}), and the current CV2 discharge area (A_{CV2}) multiplied by the average opening angle of the CV2s (α_{CV2}), which ranges from $0 \rightarrow 1$. The pressure at CV1 is a good measure of the average pressure in the vessel generally, which is roughly constant within the scope of the model, and this gives a good characterisation of the mass flow when combined with the discharge area. Thus, we have a robust parameterisation of the jet HTC.

The opening angle of the CV2 valves (α_{CV2}) would ideally be based on the signal β sent to the control valves, however, there is a slight delay between the signal and actuation due to the fill time of the actuator and the feedline. Also, because the feedline to each actuator is slightly different in length, the delays are not synchronous. Using an average of the four α measurements makes for a good approximation.

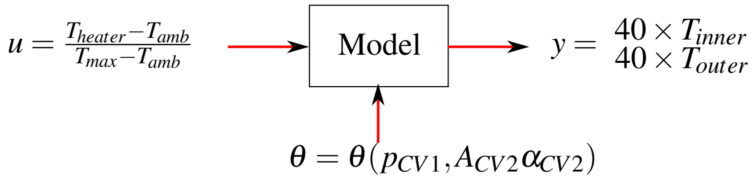

Figure 4.2: Model of the casing using inherited signals from the hot path system.

4.3.3 Acquisition of Training Data

Typical experiments in the THTF (such as those performed in Chapter 2) have short run times that are unsuitable for accurate system identification. Furthermore, they don't follow the assumptions about the model listed in Section 4.3.1. Usually there is some change in CV1 and CV4 opening angles or the number of CV2 valves used. So, for the purposes of model development, four major tests were conducted; three for system identification (P,Q,S) and one for validation (R). These tests were conducted at typical operating conditions as shown in Table 4.2. Each test contains two or three subtests where the impingement system is turned on once creating a 'step' response. The data from broken TCs have been discarded. An example of the raw data is shown in Figure 4.3, with the broken TCs highlighted in black. This has been taken from Test Q, which is used as an example throughout this chapter. The full results are included in Appendix C.

Test		T_{set} $(^{\circ}C)$	p_{CV1} (MPa)	D (mm)
(P)	1	200	1.18	10.2
	2	200	1.18	10.2
	3	250	1.18	10.2
(Q)	1	150	0.92	10.2
	2	250	0.92	10.2
(R)	1	150	1.04	10.2
	2	250	1.04	10.2
	3	300	1.04	10.2
(S)	1	150	0.89	10.2
	2	250	0.89	10.2

Table 4.2: Major test and subtest operating points.

Another consideration is the calculation of the casing average temperature as outlined in Section 2.6.2. Because some TCs were broken, there are some missing values from the circumference of the casing that could skew the average values. To compensate for this, TCs that mirror the location of the broken TCs about the vertical plane (on the opposite side of the casing) were counted twice in calculating the average surface temperatures.

The experimental data is logged at a $10Hz$ sample rate, and each subtest is found by sampling the raw data over a 70s period, giving a total 701 time steps. This results in a 76×701 matrix of data for each subtest (P1,P2, etc.) The opening of the CV2 valves is always locked to the 101^{st} step. This is important in order to keep SVDs of the data consistent by maintaining constant matrix size. The identification process is shown in Section 4.3.8.

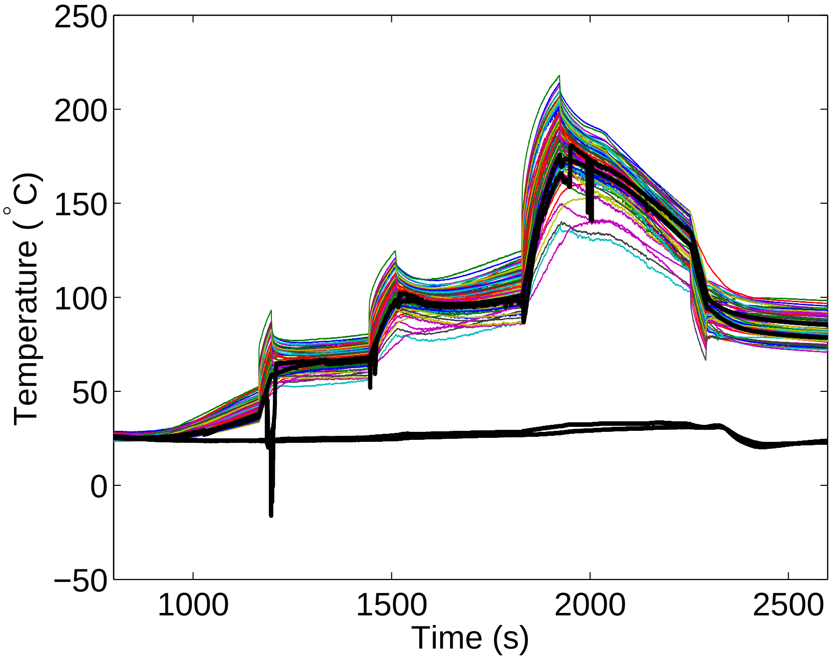

Figure 4.3: Complete TC data from Test Q highlighting the data from broken TCs.

4.3.4 Model Structure

The LPV-SVD model was intended to model heat conduction inside a solid of high Bi and non-linear boundary conditions. However, the casing in the THTF is relatively thin (thus a low Bi) and all of the TCs are spot welded on the surface rather than embedded within the material. Furthermore, the inner and outer surfaces have very distinct thermal characteristics as the impingement system is only applied to the inside surface. As such, the casing has been analysed and modelled via SVD twice, once as a 'combined' system that considers all of the TCs together, and once as a 'split' system where the inner and outer TCs are considered separately.

The average temperature of the inner and outer TCs during a step change is shown Figure 4.4. This shows that the internal surface has an immediate response, and the outer surface has a delay as the heat diffuses through the thickness of the casing. Both surfaces quickly come into a quasi-steady equilibrium as they heat up together. A model based on the combined SVD analysis would reflect an average of the inner and outer case measurements which might ultimately compromise the accuracy of the model, thus the motivation to explore both approaches.

For each test in the combined system, the data from the 76 TCs (excluding the 4 broken

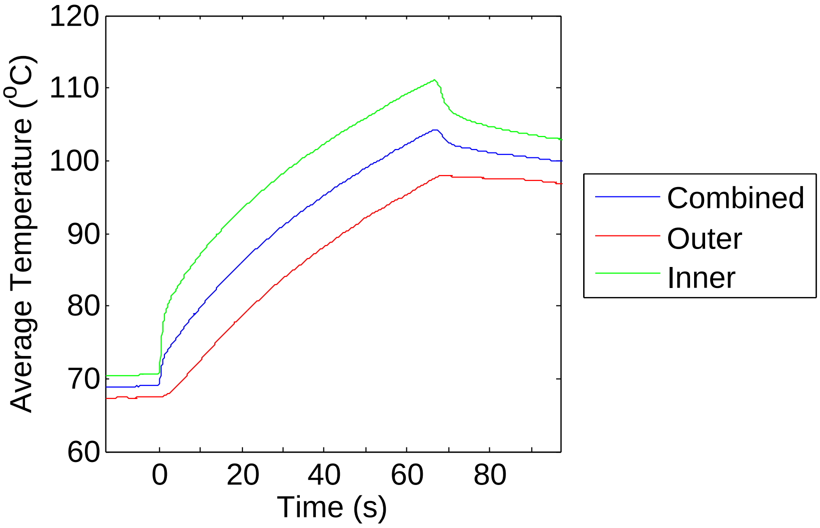

Figure 4.4: Comparison of average inner and outer TC measurements at subtest Q1.

TCs) is stored as matrix T_{comb}, and the SVD calculated as;

$$T_{comb} = (\mathbf{U}\Sigma\mathbf{V}^{\mathsf{T}})_{comb} \tag{4.8}$$

where the singular vectors U_i represent the spatial modes of the temperature profile, and the singular vectors V_i represent the temporal modes. The split system performs the same analysis to inner measurements (T_{inner}) and outer measurements (T_{outer}) separately;

$$\begin{aligned} T_{inner} &= (\mathbf{U}\Sigma\mathbf{V}^{\mathsf{T}})_{inner} \\ T_{outer} &= (\mathbf{U}\Sigma\mathbf{V}^{\mathsf{T}})_{outer} \end{aligned} \tag{4.9}$$

The present analyses use an equal number of points for both the inner and outer casing. This was fortuitous as of the four TCs that broke, two were from each side of the casing. If there were an unequal division of points, then the inner and outer responses would be weighted similarly either towards or away from the combined response.

4.3.5 Truncation Rank Accuracy

With either the combined or split system, the model is truncated to some rank r, such that;

$$\hat{T} = \sum_{i=1}^{r} U_i \sigma_i V_i^{\mathsf{T}} \tag{4.10}$$

We must consider a measure of fidelity that ensures the accuracy of the model, yet is sufficiently low order that the identified functions have a consistent structure over every training set. There are two methods of measuring the accuracy of interest - The L_∞ norm (maximum error);

$$e_{max} = ||\hat{T} - T||_\infty \tag{4.11}$$

and the root-mean-square error;

$$e_{rms} = \sqrt{\frac{\sum_{i=1}^{n}(\hat{T}_i - T_i)^2}{n}} \tag{4.12}$$

The values for these are plotted against truncation rank as shown in Figure 4.5 and Figure 4.6. For a rank 1 truncation, choosing the combined model over the split model results in at least a $10K$ (50%) increase in maximum error. For e_{max}, the improvement in the result drops off significantly above rank 3 for the combined SVD, or rank 2 for the split model. Based on this, the analysis in the next section will continue by focusing on the first two vectors only.

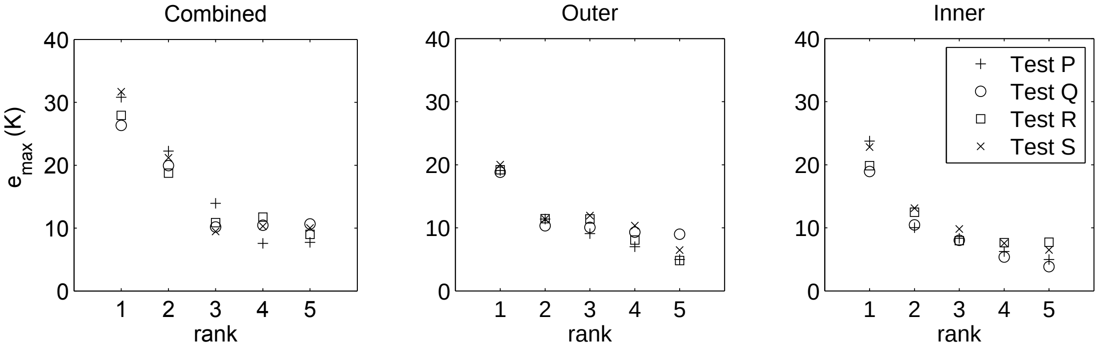

(a) Combined (b) Split - Outer (c) Split - Inner

Figure 4.5: Comparison of e_{max} resulting from different SVD truncation ranks.

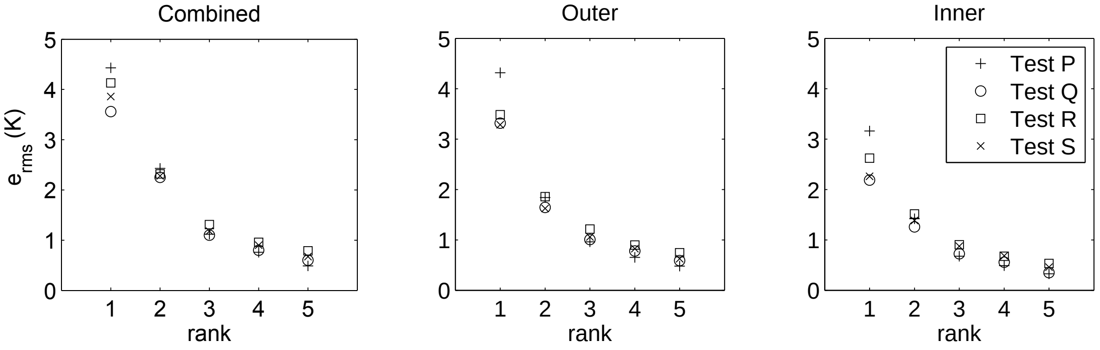

(a) Combined (b) Split - Outer (c) Split - Inner

Figure 4.6: Comparison of e_{rms} resulting from different SVD truncation ranks.

4.3.6 Spatial Singular Vector Analysis

Although both the split and combined models have been fully developed for comparison, the spatial vectors (U_1, U_2) are qualitatively very similar in these cases, so only the split results are presented here. The spatial vectors (U_i) relating to each V_i help a designer to understand the physical meaning that each response represents, which then aids in the decision on which U_i to use in the final model.

U_1 and U_2 have been calculated for each of the four tests, and the results are overlaid as unwrapped contour plots in Figures 4.7 and 4.8 respectively. The values of the contours are interpolated at all points away from the original TC locations. This produces an effective visualisation of the vectors, though it is strictly qualitative. The contours are calculated along the inner and outer surfaces separately (there is no interpolation of points through the thickness of the casing), which is why the inner casing is limited to a narrow axial band within the impingement hole rows.

As the experiments never truly reach steady states, U_1 captures characteristics of the dominant quasi-stable temperature profile as shown in Section 2.8.5. There are three distinct effects that can be identified in Figure 4.7;

- The casing is hotter at the top and cooler at the bottom, with a slightly off-centre alignment due to convection in the outer cavity.
- The rear impingement jets are stronger than the forward ones.
- There is a cool patch near the top, that is so far unexplained.

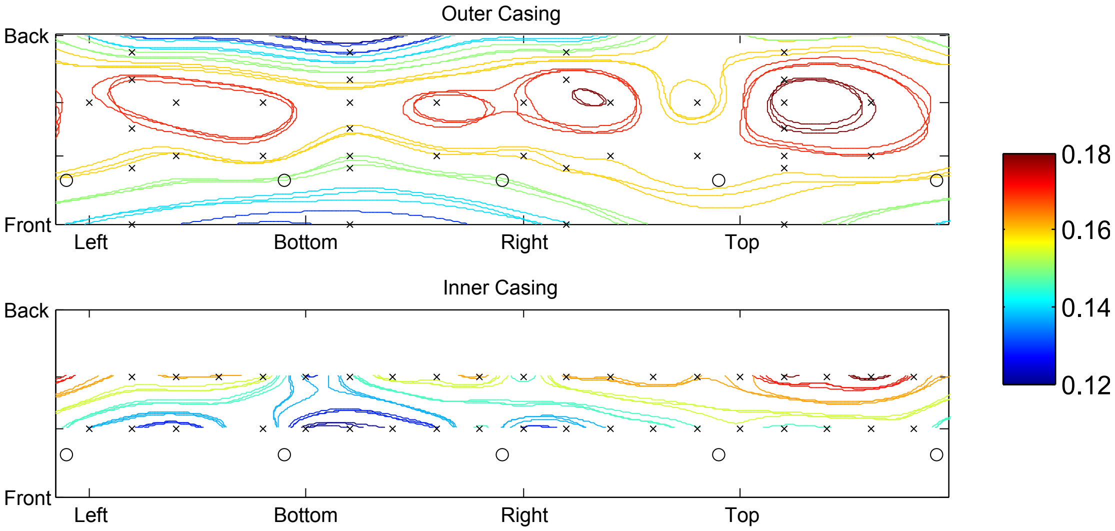

Figure 4.7: Overlay of U_1 for tests P,Q, and S under the split system. Test R is left out as it is used for validating the final model.

Figure 4.8 shows U_2 and highlights the effects associated with transient conditions at each step test. Interestingly, the *bottom* of the outer casing has the highest peak. This shows the effect that the driving temperature has on heat flux. When the impingement system is switched on, the cooler bottom section of the casing has a large temperature difference with the extra air rushing in from the heater. This difference is larger than for the upper, hotter section of the casing. This means that the bottom section has a higher local heat flux and higher rate of temperature change.

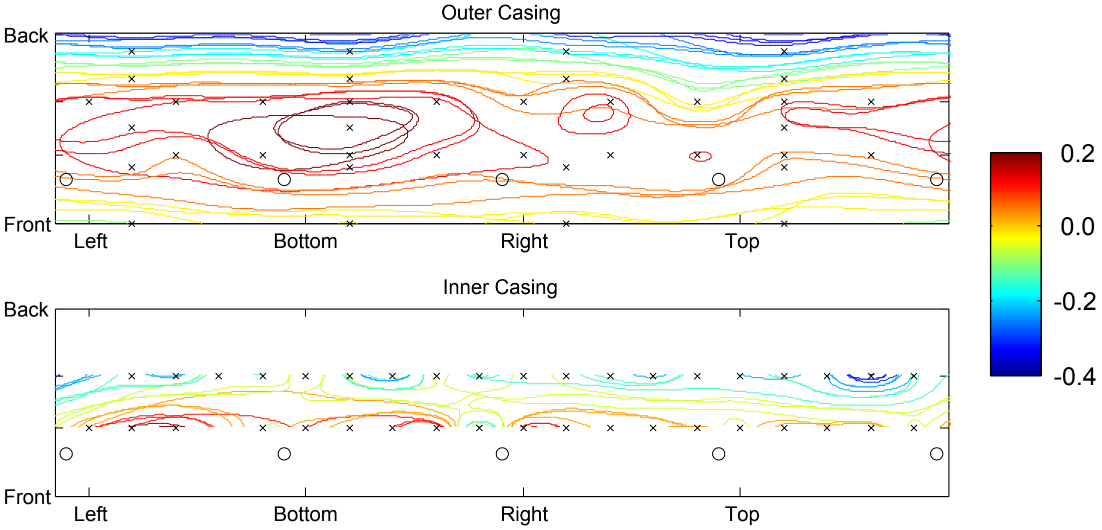

Figure 4.8: Overlay of U_2 for Tests P,Q, and S under the split system.

The spatial vectors used in the final model are created by concatenating all the available training data and selecting the appropriate U_i from the decomposition. This provides an effective average of the overlaid U_i identified above. The model's Ψ_i are created by multiplying these U_i by the $\mathbf{C}_i$ as identified in the system identification process (Section 4.3.8).

4.3.7 Temporal Singular Vector Analysis

The first two temporal vectors (V_1, V_2) have been assessed for both the combined and split analyses to understand their ease of identification and reproducibility. Figure 4.9 shows V_1 and Figure 4.10 shows V_2, both for test Q. Both plots show that the combined system represents an average of the inner and outer responses, as would be expected. This is more obvious in Figure 4.9 but the trend is present in Figure 4.10 as well. It is important to note that the experiments never truly reach a steady state for any length of time. This influences the significance of the spatial modes, and becomes a limiting factor in system identification.

The comparison of V_2 indicates why a rank 2 combined model is ineffective compared to a rank 2 split model. The forms of the inner and outer responses are very different. When

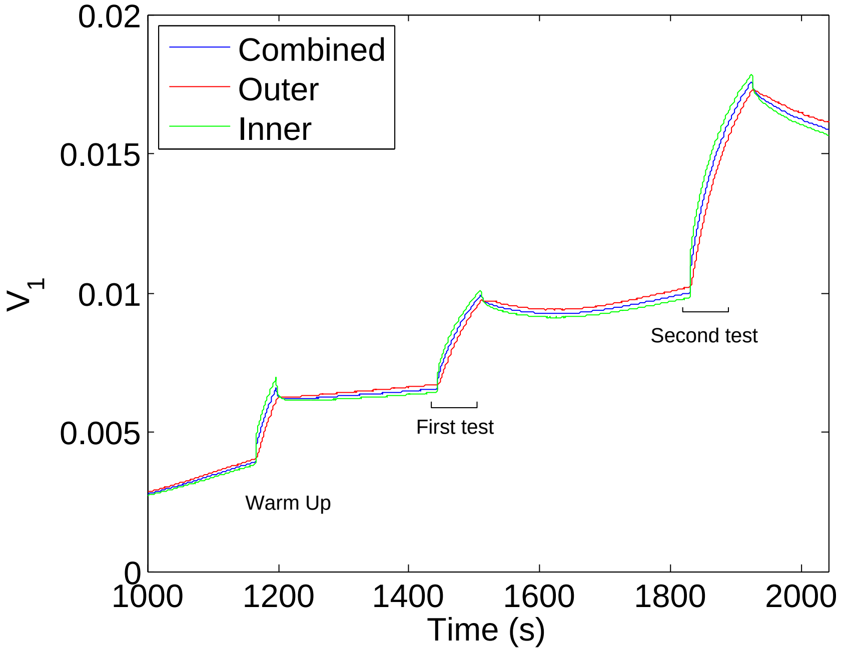

Figure 4.9: Comparison of combined and split system V_1 from Test Q. The first and second subtests Q1 and Q2 are also shown.

a test starts the inner system peaks quickly and begins to die away in what is possibly a second order response. However, the outer system does not even come close to reaching its peak value. The combined system is a compromise between two very different responses. In fact, a rank 2 combined model would perform no better than a split model of rank 1 (as also indicated by the error plots above). Higher order responses (i.e. $V_3, V_4 ...$) show an even greater distinction between the outer and inner systems.

4.3.8 System Identification

Now that the appropriate temporal vectors V_i have been identified, it it necessary to identify the first two temporal functions Φ_i so that the final model can be constructed;

$$T(\theta,\chi,t) = \sum_{i=1}^{2} \Psi_i(\chi)\Phi_i(\theta,t) \tag{4.13}$$

System identification is performed according to the 'frozen-value' method of quasi-LPV identification. In the 'frozen-value' method, many different step responses are recorded, each with a single constant operating point $\theta = \theta(p_{in}, A_{CV2}\alpha_{CV2})$. The parameters of the best fit function used to define the model at that particular θ are found using the optimisation;

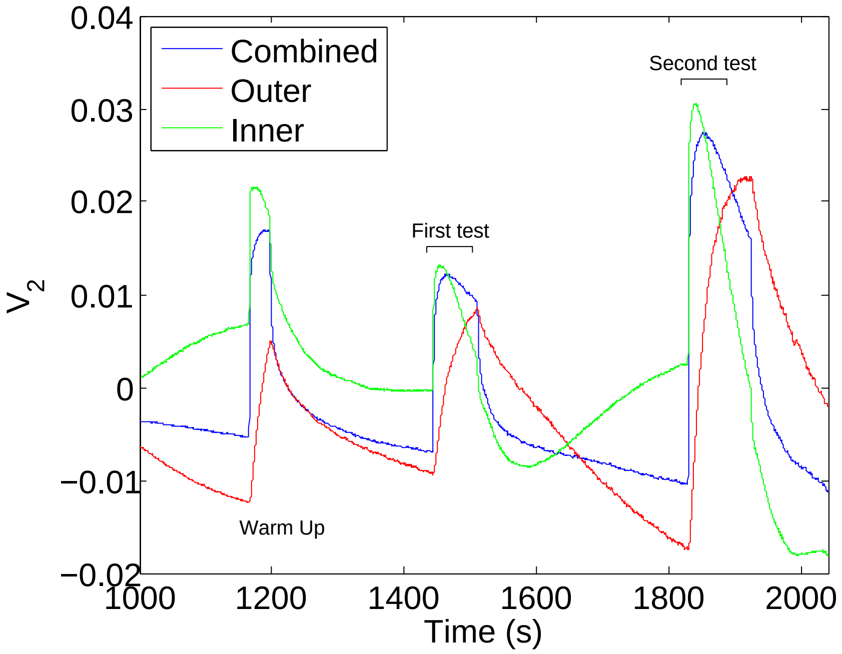

Figure 4.10: Comparison of combined and split system V_2 from Test Q.

$$\begin{aligned} \underset{\mathrm{k},\mathrm{p}_1\ldots\mathrm{p}_n,\mathrm{z}_1\ldots,\mathrm{z}_m}{\text{minimise}} \quad & e \\ \text{subject to} \quad & e = \frac{1}{N}\sum_{i=1}^{N}\big(G(s)u(t_i)-y(t_i)\big)^2 \end{aligned} \tag{4.14}$$

When the model is run, it recalls the parameters according to θ, or linearly interpolates values in between. This way, the applicable operating envelope of the model can cover many different conditions. Identification using $\sigma_i V_i$ rather than V_i alone allows for easier validation against an SVD from a full test, as it normalises the results against the length of the time series. The input signal $u(t)$ is modelled on;

$$u(t) = \frac{T - T_0}{T_\infty - T_0} \tag{4.15}$$

Plots of the Φ_i identification process are shown in Figures 4.11 and 4.12. Respectively, Figures 4.11a and 4.11b are for $\sigma_1 V_1$ and $\sigma_2 V_2$ for the outer TCs, and Figures 4.12a and 4.12b are for $\sigma_1 V_1$ and $\sigma_2 V_2$ for the inner TCs. The data is shown in red and the fitted model in blue.

Upon investigation, it was found that different model structures were appropriate for the inner and outer TC responses. Generally, the best fit transfer functions were;

$$
\begin{aligned}
\Phi_{inner,1} &= \mathrm{k}\frac{(s-\mathrm{z}_1)}{(s-\mathrm{p}_1)(s-\mathrm{p}_2)} & \Phi_{outer,1} &= \mathrm{k}\frac{1}{(s-\mathrm{p}_3)(s-\mathrm{p}_4)} \\
\Phi_{inner,2} &= \mathrm{k}\frac{(s-\mathrm{z}_2)}{(s-\mathrm{p}_5)(s-\mathrm{p}_6)} & \Phi_{outer,2} &= \mathrm{k}\frac{(s-\mathrm{z}_3)}{(s-\mathrm{p}_7)(s-\mathrm{p}_8)}
\end{aligned}
\tag{4.16}
$$

However, as will become clear from the figures, these have varying degrees of applicability. Starting from the outer TCs in Figure 4.11, it is clear that the datasets never truly reach steady state. This means that the final values of the transfer functions must be extrapolated. This could be a source of error in the final model. Generally, both $\Phi_{outer,1}$ and $\Phi_{outer,2}$ are matched well, and each of the (z,p,k) can be stored in relation to θ.

In Figure 4.12, $\Phi_{inner,1}$ matches very well, but $\Phi_{inner,2}$ is not consistent. There are not enough data points to resolve where the asymptote of the function is, and the initial step is very difficult to capture. More data could be taken but the experiments are time consuming and the overall result is unlikely to improve. The experiments themselves are not robust, as they do not start from the same initial temperature distribution, particularly for the sake of higher order responses. This enhances any differences found in the repeated SVDs. Following this investigation, and in order to be consistent for the inner and outer models, the final model relies only on the first functions $\Phi_{outer,1}$ and $\Phi_{inner,1}$.

4.3.9 Realisation of the State-Space

The transfer functions need to be realised as a state-space in the final model. For $\Phi_{inner,1}$, the transfer function has the form;

$$
Y(s) = \mathrm{k}(\theta)\frac{s-\mathrm{z}(\theta)}{(s-\mathrm{p}_1(\theta))(s-\mathrm{p}_2(\theta))}.U(s) \tag{4.17}
$$

This can be represented in state-space form using the matrices;

$$
\mathbf{A} = \begin{bmatrix} \mathrm{p}_1 & 0 \\ \mathrm{p}_2-\mathrm{z} & \mathrm{p}_2 \end{bmatrix} \quad \mathbf{B} = \begin{bmatrix} \mathrm{k} \\ 0 \end{bmatrix} \quad \mathbf{C} = \begin{bmatrix} 1 & 1 \end{bmatrix}
$$

To prove this is true, start with the state-space form and work backwards. The full state-space form of the equation is;

$$
\begin{aligned}
\begin{bmatrix} \dot{\boldsymbol{x}}_1(t) \\ \dot{\boldsymbol{x}}_2(t) \end{bmatrix} &= \begin{bmatrix} \mathrm{p}_1 & 0 \\ \mathrm{p}_2-\mathrm{z} & \mathrm{p}_2 \end{bmatrix} \begin{bmatrix} \boldsymbol{x}_1(t) \\ \boldsymbol{x}_2(t) \end{bmatrix} + \begin{bmatrix} \mathrm{k} \\ 0 \end{bmatrix} \boldsymbol{u}(t) \\
\boldsymbol{y}(t) &= \begin{bmatrix} 1 & 1 \end{bmatrix} \begin{bmatrix} \boldsymbol{x}_1(t) \\ \boldsymbol{x}_2(t) \end{bmatrix}
\end{aligned}
$$

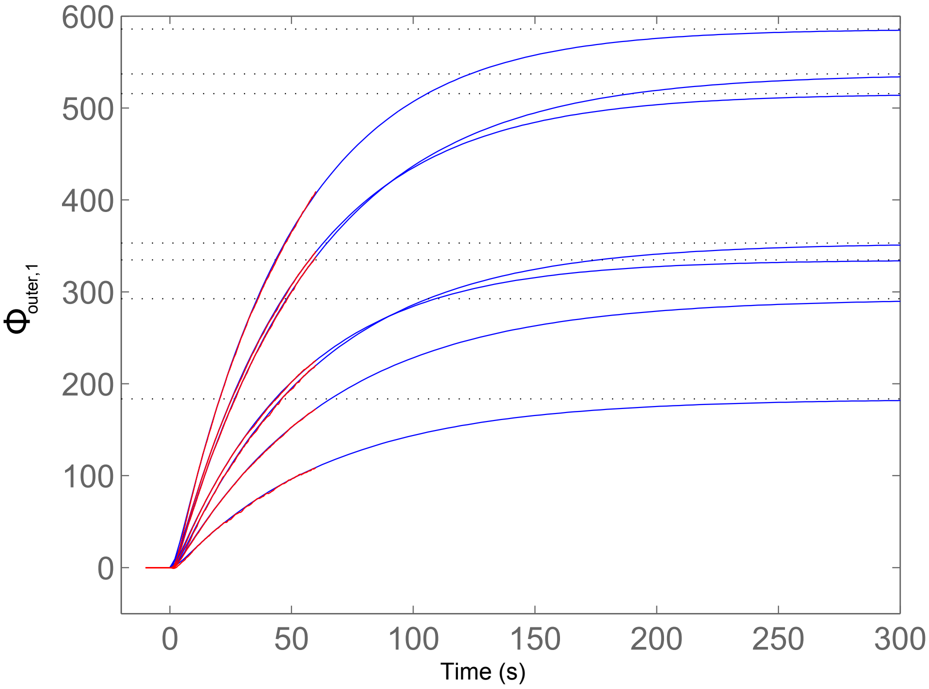

(a) First singular vector

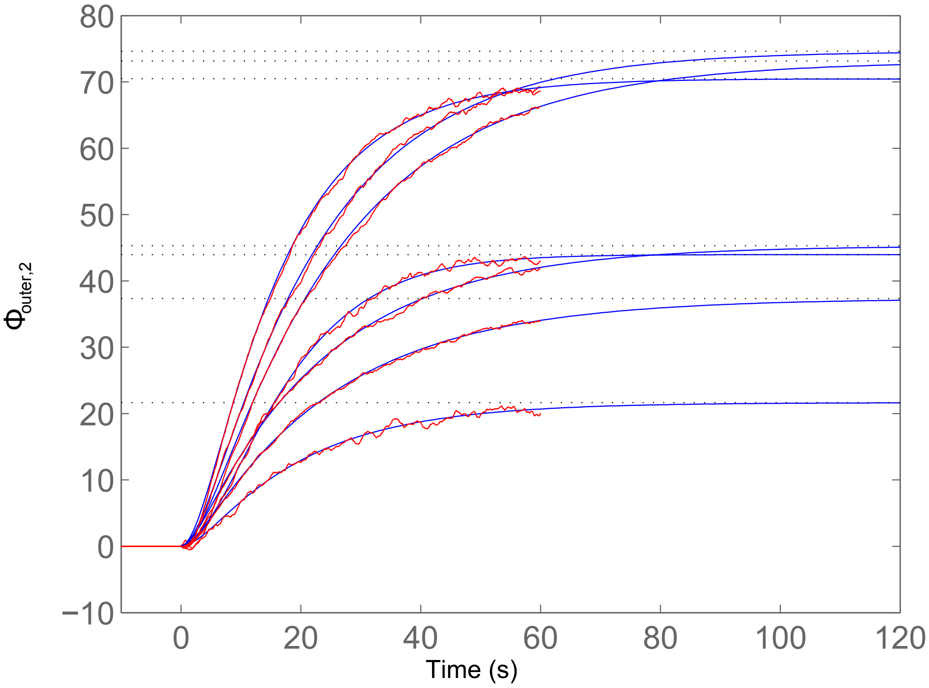

(b) Second singular vector

Figure 4.11: System identification of the outer TCs. The red line is the data for $\sigma_i V_i$, the blue line is the identified function Φ_i.

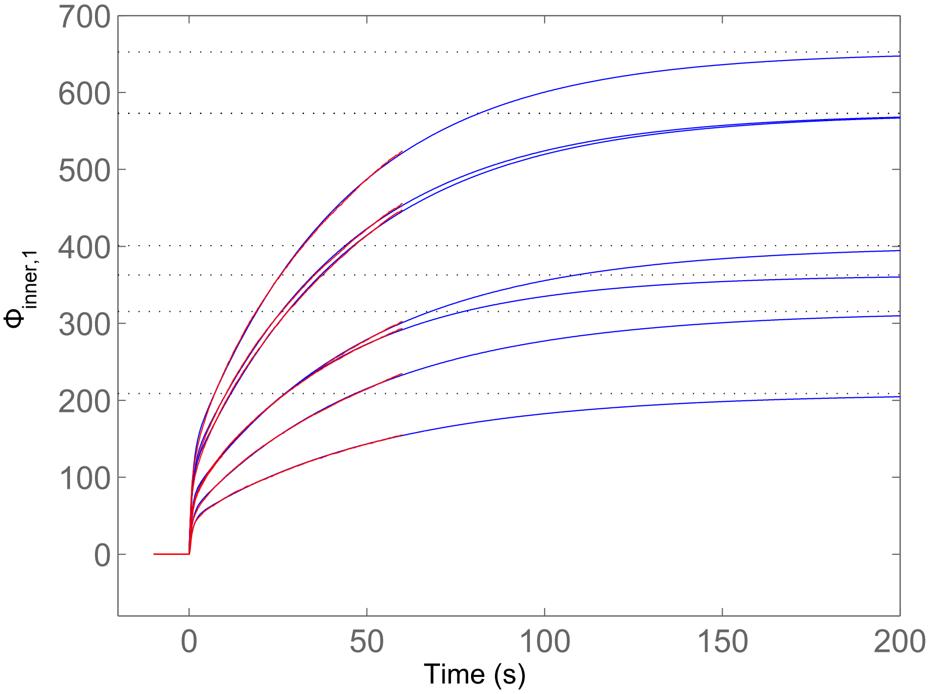

(a) First singular vector

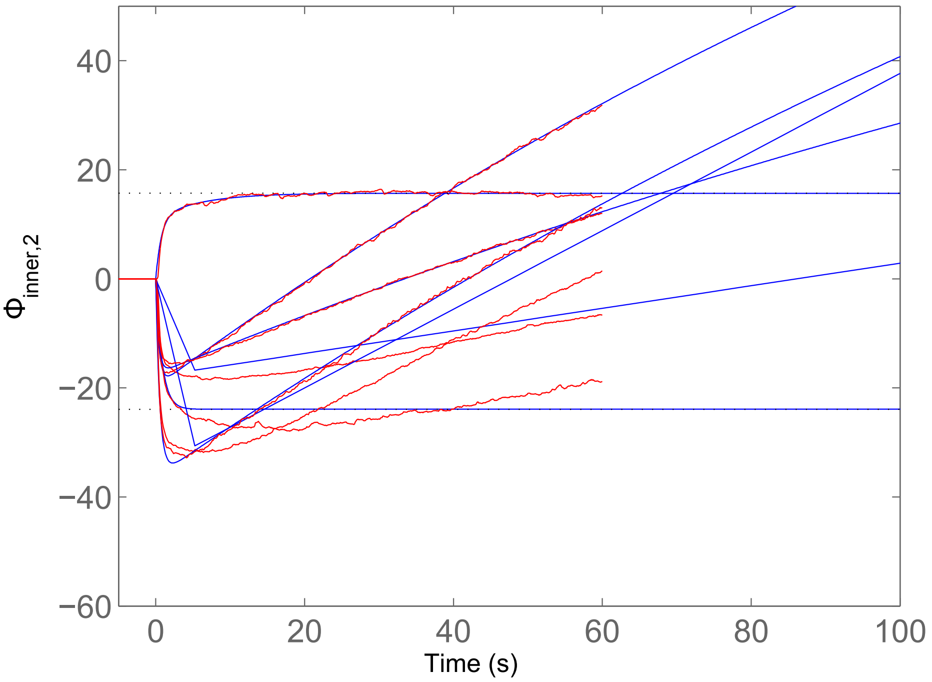

(b) Second singular vector

Figure 4.12: System identification of the inner TCs. The red line is the data for $\sigma_i V_i$, the blue line is the identified function Φ_i.

Expanding this gives three simultaneous equations;

$$\dot{x}_1(t) = \mathrm{p}_1 x_1(t) + \mathrm{k}u(t) \tag{4.18}$$

$$\dot{x}_2(t) = (\mathrm{p}_2 - \mathrm{z})x_1(t) + \mathrm{p}_2 x_2(t) \tag{4.19}$$

$$y(t) = x_1(t) + x_2(t) \tag{4.20}$$

The Laplace transforms are then;

$$s.X_1(s) = \mathrm{p}_1.X_1(s) + \mathrm{k}.U(s) \tag{4.21}$$

$$s.X_2(s) = (\mathrm{p}_2 - \mathrm{z}).X_1(s) + \mathrm{p}_2.X_2(s) \tag{4.22}$$

$$Y(s) = X_1(s) + X_2(s) \tag{4.23}$$

Rearranging (4.21) and (4.22) respectively gives

$$X_1(s) = \frac{\mathrm{k}}{(s - \mathrm{p}_1)}.U(s) \tag{4.24}$$

$$X_2(s) = \frac{(\mathrm{p}_2 - \mathrm{z})}{(s - \mathrm{p}_2)}.X_1(s) \tag{4.25}$$

Substituting (4.24) into (4.25);

$$X_2(s) = \frac{(\mathrm{p}_2 - \mathrm{z})}{(s - \mathrm{p}_2)} \frac{\mathrm{k}}{(s - \mathrm{p}_1)}.U(s) \tag{4.26}$$

Then substituting (4.24) and (4.26) into (4.23) and rearranging;

$$Y(s) = \frac{\mathrm{k}(\mathrm{p}_2 - \mathrm{z})}{(s - \mathrm{p}_1)(s - \mathrm{p}_2)}.U(s) + \frac{\mathrm{k}}{(s - \mathrm{p}_1)}.U(s)$$

$$Y(s) = \mathrm{k}\left(\frac{(\mathrm{p}_2 - \mathrm{z}) + (s - \mathrm{p}_2)}{(s - \mathrm{p}_1)(s - \mathrm{p}_2)}\right).U(s)$$

$$Y(s) = \mathrm{k}\left(\frac{s - \mathrm{z}}{(s - \mathrm{p}_1)(s - \mathrm{p}_2)}\right).U(s) \tag{4.27}$$

Thus equation (4.27) is equivalent to (4.17). It is trivial to complete a similar proof for $\Phi_{outer,1}$, and show that it has the parameter matrices;

$$\mathbf{A} = \begin{bmatrix} \mathrm{p}_3 & 0 \\ 1 & \mathrm{p}_4 \end{bmatrix} \quad \mathbf{B} = \begin{bmatrix} \mathrm{k} \\ 0 \end{bmatrix} \quad \mathbf{C} = \begin{bmatrix} 1 & 1 \end{bmatrix} \tag{4.28}$$

4.4 Final Model Structure

The final concatenated form of the LPV-SVD model can be expressed as;

$$
\begin{aligned}
\dot{\boldsymbol{x}}(t) &= \begin{bmatrix} \mathrm{p}_1(\theta) & 0 & 0 & 0 \\ \mathrm{p}_2(\theta)-\mathrm{z}_1(\theta) & \mathrm{p}_2(\theta) & 0 & 0 \\ 0 & 0 & \mathrm{p}_3(\theta) & 0 \\ 0 & 0 & 1 & \mathrm{p}_4(\theta) \end{bmatrix} \boldsymbol{x}(t) + \begin{bmatrix} \mathrm{k}_1(\theta) \\ 0 \\ \mathrm{k}_2(\theta) \\ 0 \end{bmatrix} \frac{T_{heater}(t)-T_{min}}{T_{max}-T_{min}} \\
T(\theta,\chi,t) &= \begin{bmatrix} U_1 & U_1 & U_2 & U_2 \end{bmatrix} \boldsymbol{x}(t)
\end{aligned}
\tag{4.29}
$$

where each parameter (z,p,k) can be resolved via interpolation according to $\theta = \theta(p_{in}, A_{CV2}\alpha_{CV2})$. The model is constructed in the Simulink environment based on the diagram shown in Figure 4.13. The rounded green boxes represent variable inputs, the squared green box represents a constant input, the brown boxes represent the 1D and 2D look-up tables, the pink block represents a typical state-space function in block form, and the rounded red box represents the output.

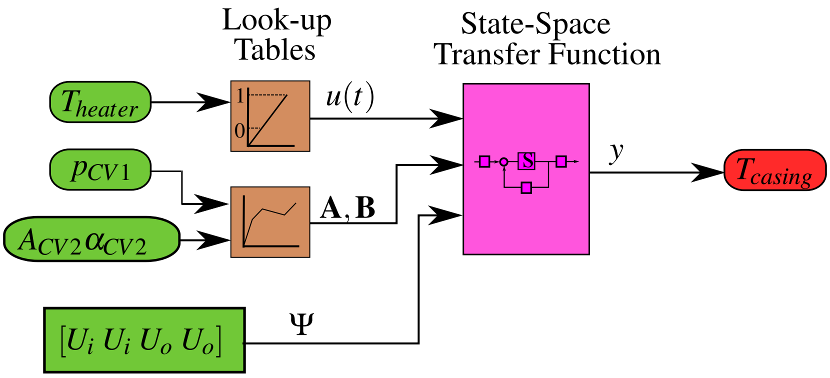

Figure 4.13: Full Architecture of the LPV-SVD Model. The flow diagram of signal path is above, and the mathematical expressions from the look up blocks is below.

4.5 Validation and Discussion

4.5.1 Reproduction of Temporal Singular Vectors

As part of model development, it is useful to consider how well the functions of Φ match the equivalent σV from the SVD of a full length experiment run (i.e. not truncated to a single step). A typical result is shown in Figure 4.14 for both the inner and outer surfaces. It is immediately clear that the model solution (blue) matches best with the target data (red) at the second two steps. These instances have been used explicitly to create the model, whereas away from these points the relevant state-space parameters have been interpolated.

There is a distinct mismatch of $\Phi_{inner,1}$ to the data between steps. This is primarily due to the failure of the experiment to produce steady-state conditions for parameter identification. The fact that the model manages to stay close during the transient period is more important, as filtering can be used to help match steady state periods. The effect of this mismatch can be seen more clearly in the overall temperature error plots shown in Section 4.5.2. Models based on FE/CFD data or more complete experimental results will have access to more data making the steady conditions easier to identify.

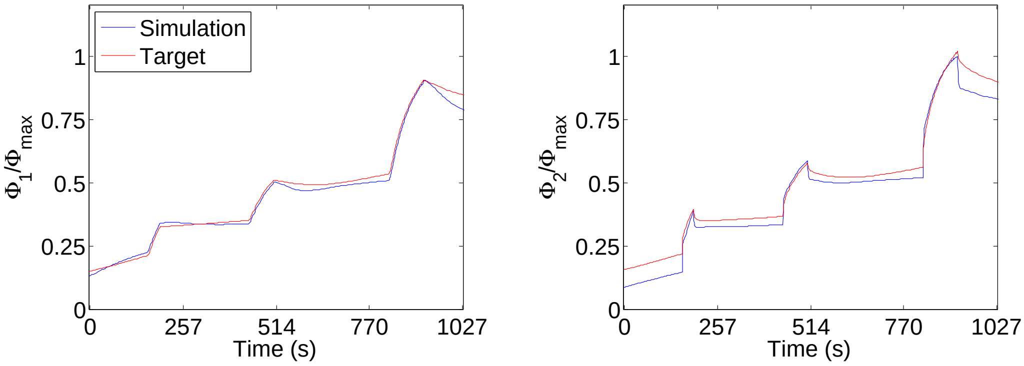

(a) Outer Surface

(b) Inner Surface

Figure 4.14: Comparison of Φ_i with target data, normalised to $\Phi_{i,max}$.

4.5.2 Split Model compared with Original Data

These results start by demonstrating how well the split model matches the original Test Q data that has been used throughout the chapter so far. The temperature plots of the inner and outer surfaces are shown in Figures 4.15a and 4.15b, and their respective error plots are shown in Figures 4.15c and 4.15d. The plots' x-axes have been limited to a period from roughly 30s after the heater has been turned on until it has been turned off, as is the scope of the model.

The overall temperatures behave similarly to the real system. The temperature range across all points tends to spread out in proportion to the average temperature. In particular, the spread of temperatures on the outside of the casing at 900s in Figure 4.15a leads to some of the error shown at the same position in Figures 4.15c. The same effect is seen on the inner surface. The error due to the mismatch of $\Phi_{inner,1}$ at steady state is clearly shown in Figure 4.15d.

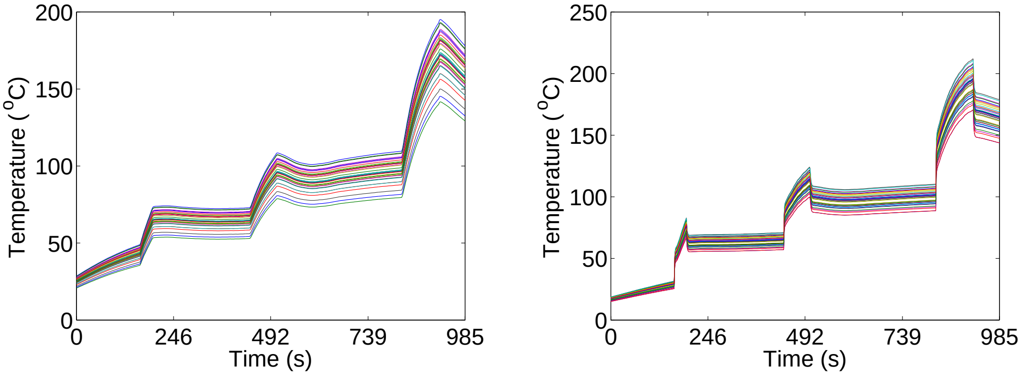

(a) Temperatures on Outer Surface

(b) Temperatures on Inner Surface

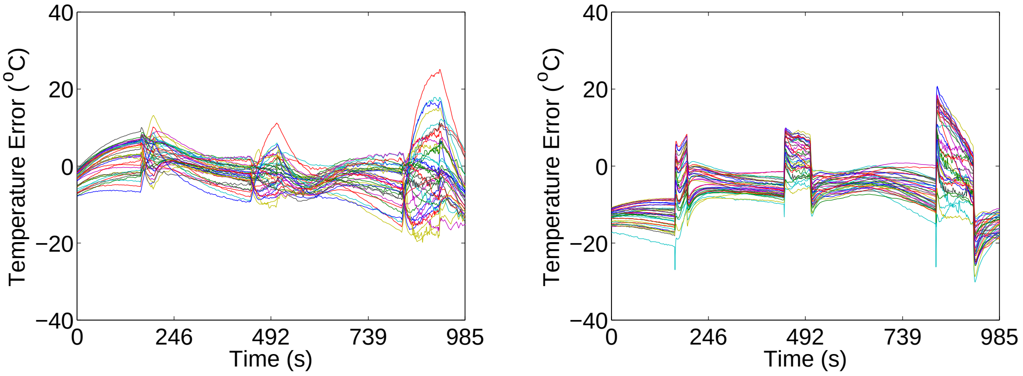

(c) Errors on Outer Surface

(d) Errors on Inner Surface

Figure 4.15: Results from simulation of Test Q using a split model. The errors are between the model output and the TC data.

Overall, the maximum error encountered for both inner and outer functions is about $30^\circ C$, mostly confined to a very limited number of points, and the majority of points stay within an error bound of $20K$. This is in agreement with the SVD analysis shown earlier in Figures 4.5 and 4.6.

Unfortunately, the trend does not continue quite so effectively in the other tests, as shown in Figure 4.16. These plots show the resulting error for both surfaces when simulating the full test results. Note that Tests P, Q and S were used for training, and Test R was not. The behaviour of each surface is clearly visible in the plots. The model shows particular trouble in matching Test P, as the temperatures never reach a steady condition, and the inner surface error varies quite distinctly.

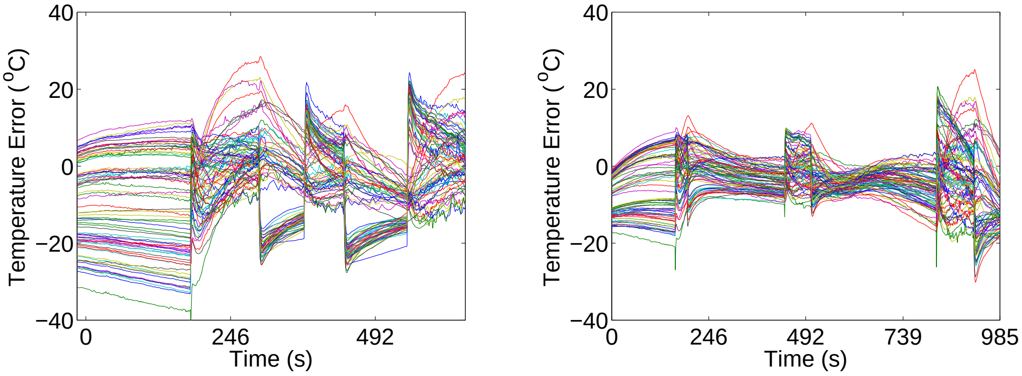

(a) Test P

(b) Test Q

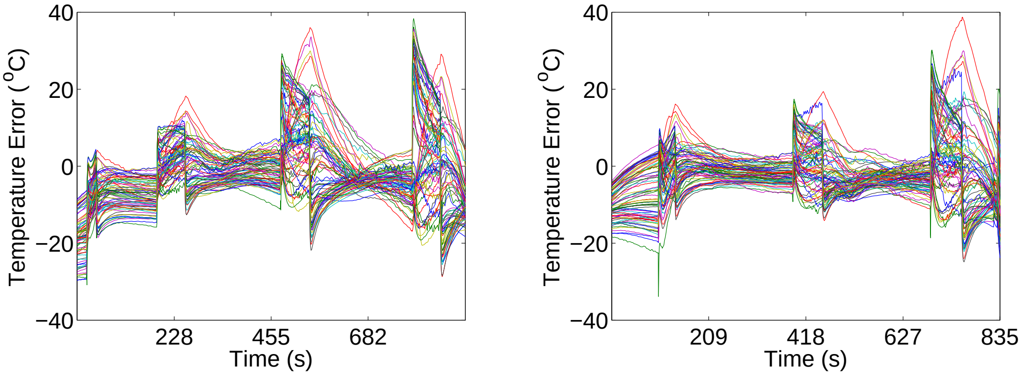

(c) Test R

(d) Test S

Figure 4.16: Comparison of model accuracy across all major tests.

4.5.3 Split Model vs Combined Model

The split model does not appear to match the experimental results as well as hoped, so instead we compare it to the combined system where all TCs are modelled using a single function. One problem with the split model is that it does not guarantee that the inner

TCs are always above their neighbouring outer TC. Without this, physically impossible temperature predictions can occur. The combined model does not have this problem.

Again, only $\sigma_1 V_1$ was used in building the combined model, following an SVD analysis and system identification process much like the one for the split system above. A direct comparison of the results are shown in Figure 4.17. The overall range of error appears to be similar, though the clustering is different. The combined result noticeably drifts from the target model towards the end of the test. Overall, there doesn't appear to be any obvious advantage looking at all the TCs at once. Instead, we consider how the models can simulate the average temperature of the casing.

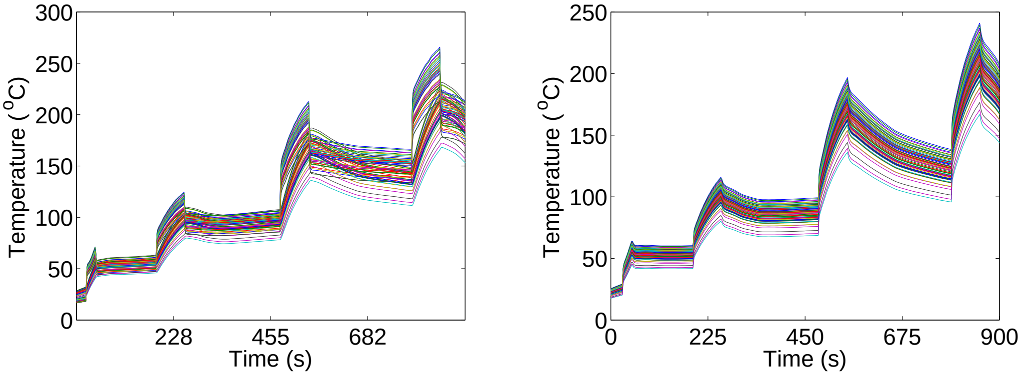

(a) Split System

(b) Combined System

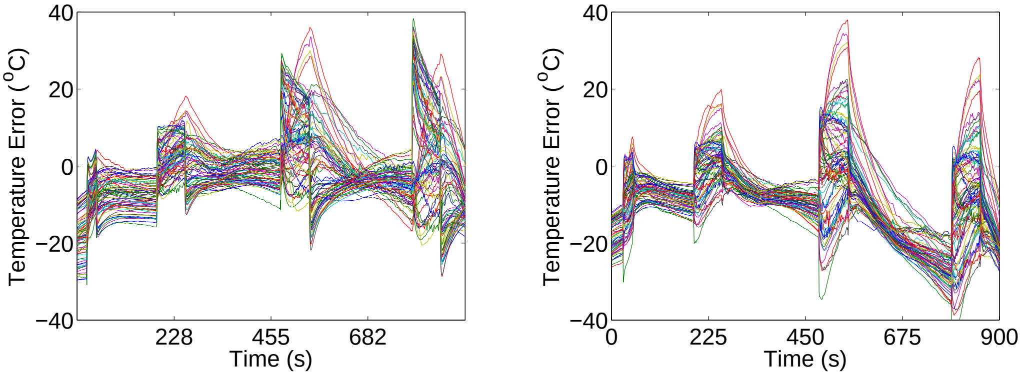

(c) Error of Split System

(d) Error of Combined System

Figure 4.17: Comparison of the split model and combined model for Test R.

4.5.4 Average Temperature of Casing

The ultimate goal of the THTF, and the LPV-SVD model, is to track changes in the average temperature of the casing in order to model thermal growth and thus the tip clearance. Thermal growth is not axisymmetric in real engines, but for the purposes of axisymmetric clearance control it is useful to be able to track the average temperature change of the casing volume. In particular, the location of greatest interest is the axial region between the impingement holes where the segment hooks are located.

The average temperature of the casing using both the combined and split models has been calculated for Test R, and the final results are shown in Figure 4.18. Both systems behave reasonably well for the first 420s. However, after 420s, the lack of local data to support the interpolated parameters leads to the combined system falling away quickly from the target. For reference, for an unsupported ring of stainless steel with radius 650mm, and thermal expansion coefficient of 17.5$\mu m/mK$, a 20K difference in temperature would result in a 0.23mm change in radius. This is the same order of tip clearance benefit that the SCA system is trying to capture. In the real engine however, Waspalloy has a lower coefficient of thermal expansion (13.9$\mu m/mK$, see Table 2.2), and the casing as a whole provides a lot of structural support. Therefore an LPV-SVD model of the engine casing could be expected to produce a prediction of clearance better than 0.23mm, however, further thermomechanical analysis would need to be undertaken in order to refine this prediction.

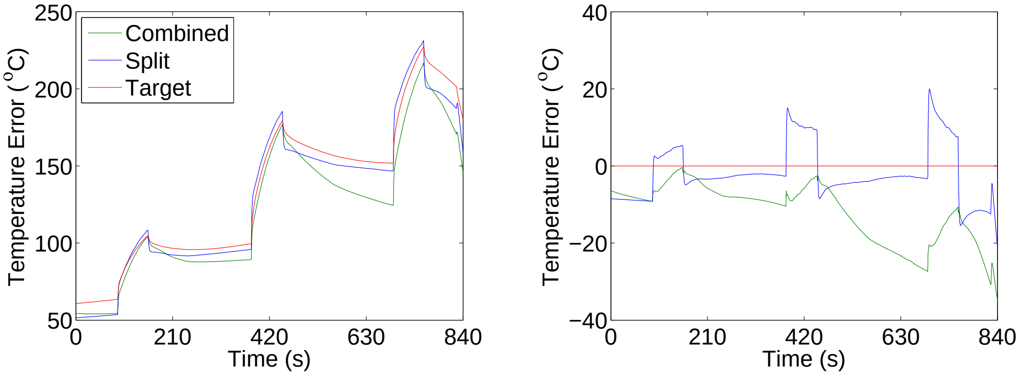

(a) Average Temperatures

(b) Error

Figure 4.18: Comparison of $\bar{T}$ near impingement rows 5 and 7 under both systems.

4.5.5 Early Experiment Comparison

The split model is now evaluated against experiments from the THTF experimental program, where the SCA valves are actuated more often, with less time for the system to settle. The results are shown in 4.19. These tests are much more difficult for the model to follow, as the hot bypass had not yet been calibrated properly, so there is significant PID controlled dynamics in the heater output. The mass flow through CV1 has been increased by the operator at 1400s mark which leads to a temporary drop in heater output temperature, and a greater spread in the temperature range of the casing. The opening angle of

CV1 (α_{CV1}) could possibly be incorporated into θ, however, this would have increased the amount of training data required and is not representative of engine operation.

With those caveats in mind, it is interesting to look at the effectiveness of the model. Figure 4.19a shows the original data, Figure 4.19b shows the model output, and the error between the two is shown in Figure 4.19c. The contour plots of the temperature of the model at time 1249s, and the associated error, are shown in Figures 4.20a and 4.20b. This is the point of maximum error before the CV1 flow changes and invalidates the model scope.

The error spread about the mean at steady state is much larger than for similar conditions in previous tests. This is driven by the reduced temperature of the flow entering the system when the SCA valves are switched on. This introduces a large volume of air that likely falls to the bottom of the annulus, while the hot air already in the inner cavity remains buoyant. This effect can be compensated for by the bypass system, and is unlikely to be a real effect in the engine.

4.6 Conclusions

An LPV-SVD model of the THTF has been constructed using raw step response data collected from the facility. The model has demonstrated that it can reproduce experimental measurements to an accuracy of $\pm 30K$ near training data points, and $\pm 40K$ away from those points, using only a rank 1 truncation model. This supports the idea that the SVD analysis can be used to predict final model accuracy. The difference between a split and combined system approach appears minimal in this case, favouring the split model in most instances. However, no method is shown to necessarily align the inner and outer temperatures within the split system approach, meaning that temperatures on the outer surface may exceed the inner surface in a physically impossible manner. This problem is avoided in the combined model.

There have been a few difficulties in constructing the model from experiments which could be avoided using simulated data. The experiments had a limited supply of air, which led to reduced experiment time meaning that it was impossible to run the facility to steady state conditions under reasonable circumstances. Thus, the spatial vectors that were identified for the first singular values showed contour variations present in transient conditions that might not be evident in steady state situations. Secondly, steady state condition at the peak of the impingement heating is never achieved, so it is not possible to use a standardised baseline for system identification of the non-impingement conditions. The tempera-

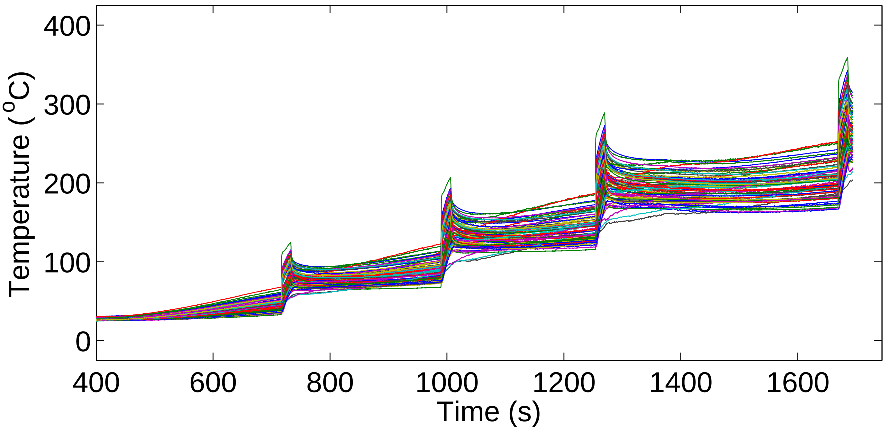

(a) Original Data

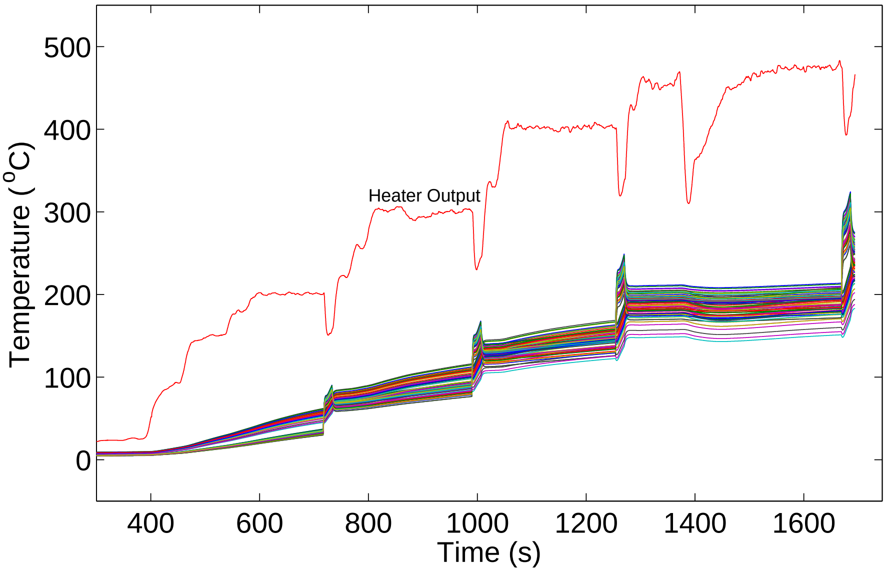

(b) Simulation and Heater Output

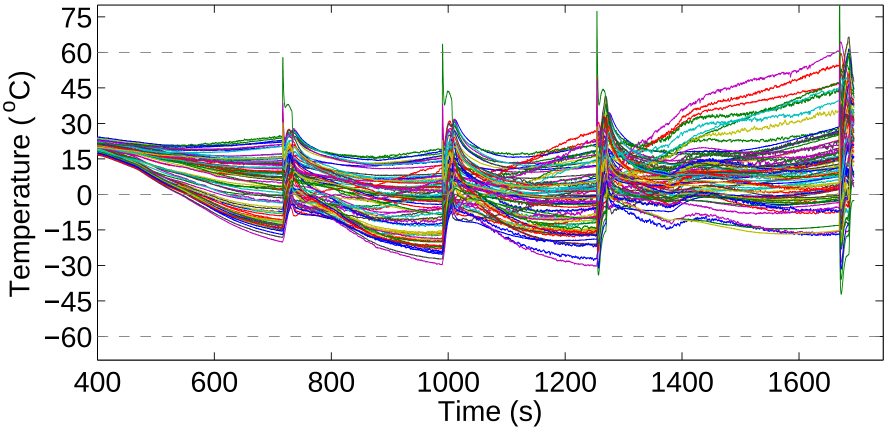

(c) Error

Figure 4.19: An early THTF experiment compared with the equivalent model simulation.

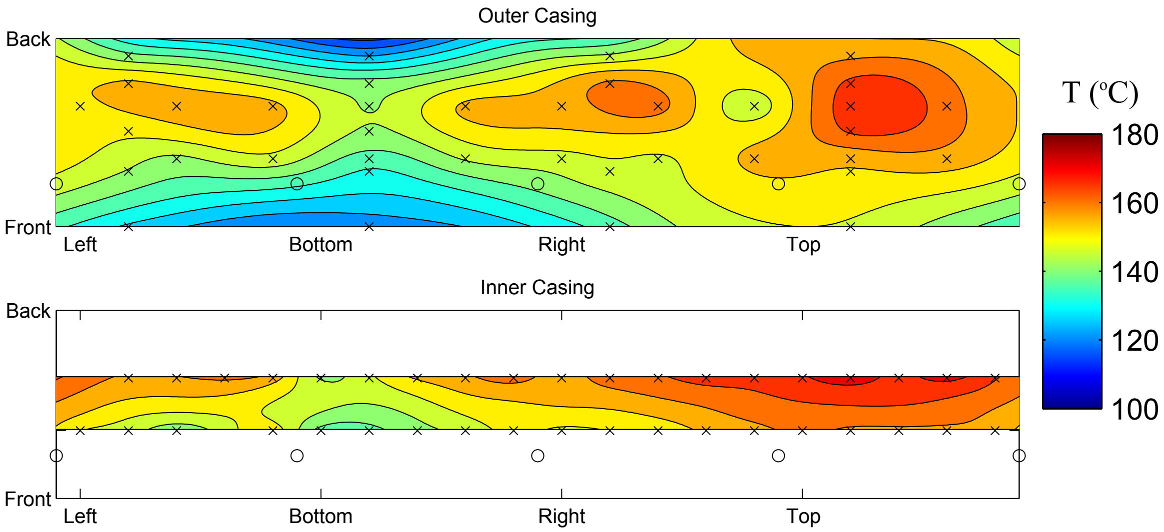

(a) Original Temperature

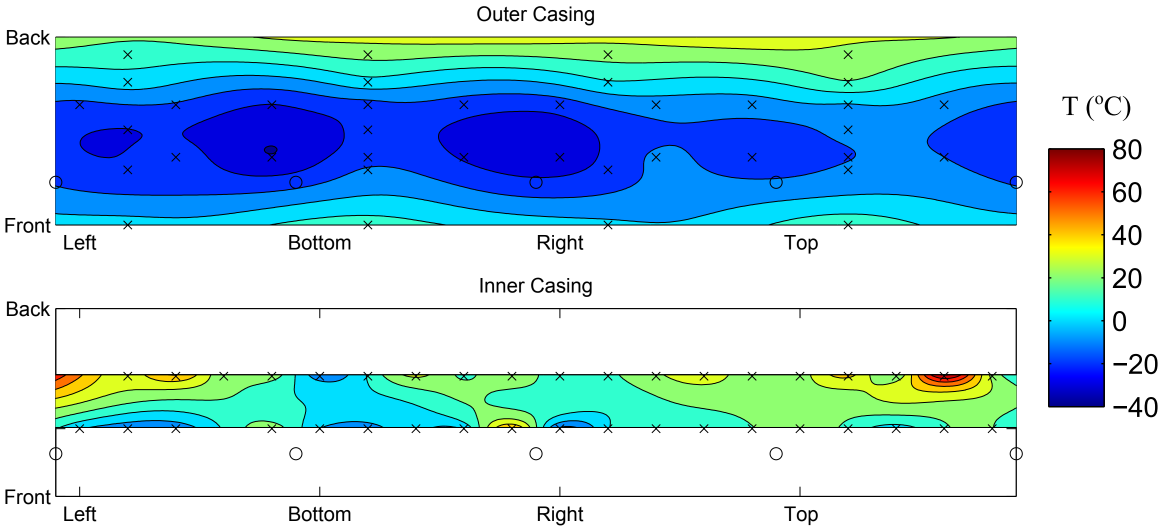

(b) Model Error

Figure 4.20: The surrface temperature and error at 1249*s* as shown in Figure 4.19.

tures during the non-impingement periods never truly reach steady state either. Finally, the control system that governs the heater would not be present in a real engine, and this can be more adequately accounted for in a simulated tests.

To help eliminate the facility effects that are not present in the real engine, the LPV-SVD model can be applied directly to SC03 model data. Simulated data provides a richer variation in parameters and test cases, however, it does not provide realistic insight into the number of available TC measurements, and the FE output has less noise than might be expected from raw data. This will be considered further in the next chapter.

Chapter 5

LPV-SVD Model of IP Turbine Disc

5.1 Introduction

The LPV-SVD methodology developed in the previous chapter was shown to be effective in modelling temperatures in an experimental application. This chapter presents the LPV-SVD model as applied to an axisymmetric FE simulation of an IP turbine disc from a large civil engine. This serves as a pre-emptive step towards controlling the disc's temperature distribution using cooling air, which can ultimately be used to reduce stresses and manage tip clearance growth. The fact that the data comes from SC03 simulations rather than experiments, allows for a much larger range of conditions for which training data can be gathered, and a more detailed sampling of the internal temperature field. This is useful, because the internal profile is much better suited to modelling with the LPV-SVD methodology than the casing surface. In bringing the LPV-SVD concept to a rounded conclusion, this chapter will also compare and contrast several methods for developing a Kalman filter for the model. The filter allows the LPV-SVD method to be readily adapted for practical applications where there is significant process and measurement noise.

Section 5.2 provides some background on the disc to be modelled, and considers some useful targets for producing ROMs for active flow control. The theory behind the LPV-SVD model has been detailed in Chapter 4, thus it will not be repeated here. Instead, Section 5.3 will present how the LPV-SVD methodology is applied to data generated with SC03 simulations and discuss the natural limitation of the model. Section 5.4 presents the final model as used to simulate disc temperatures. Section 5.5 presents the validation tests for both the identified temporal functions and the temperature simulations. Section 5.6 presents a brief background on Kalman filters and the development of a Kalman filter for the LPV-SVD model. This also includes a further validation and discussion of the selected filter. Section 5.7 presents the conclusions.

5.2 Background

5.2.1 Geometry and Source Data

A simplified profile of the IP disc is shown in Figure 5.1. The purpose of this disc is to transfer the work from the IP turbine blades via the drive-arm to the IP shaft, which in turn powers the IP compressor. Aerodynamically this subsystem is represented by two rotor-stator disc wells at both the front and back of the disc. Both wells draw air from the compressors and the air is pumped radially outward along the disc's surface. Air injected near the rim for cooling the blade is usually pre-swirled to decrease the temperature of the coolant relative to the blades and therefore improve its effectiveness. The mass flow, pressure and temperature of the air in these wells are not actively controlled but follow from the overall state of the engine and flight conditions. It is possible that future engines could control these flows independently, thereby guiding the temperature profile of the disc itself, which in turn can lessen the thermomechanical stress. Intelligent modulation of the flows would then allow for mitigating these stresses and monitoring fatigue.

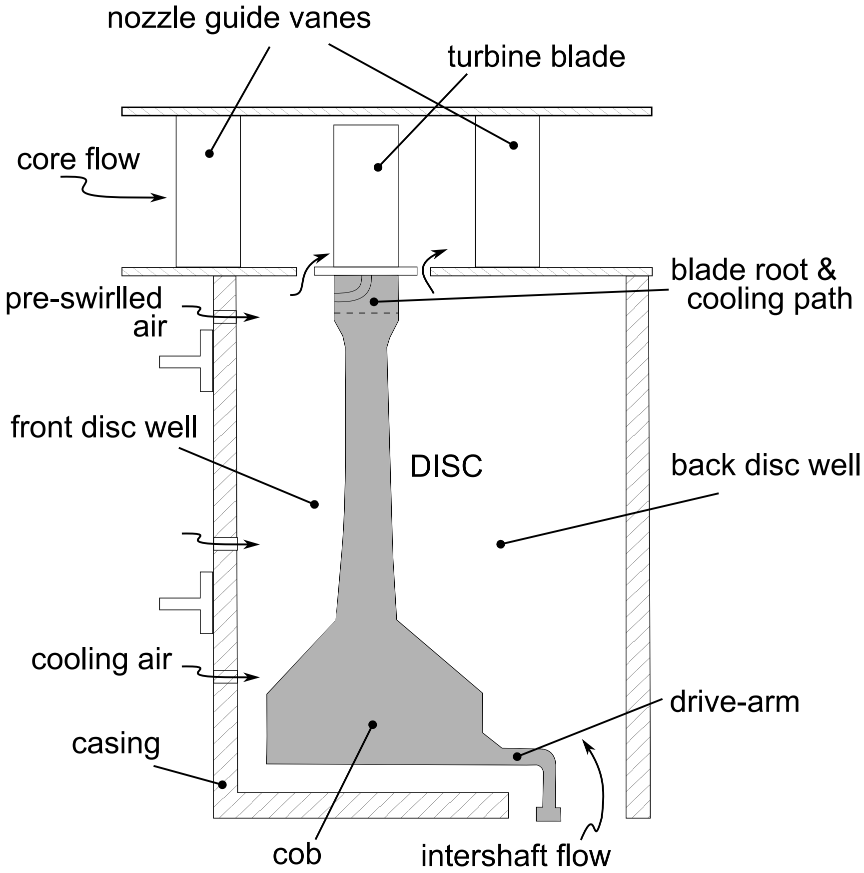

Figure 5.1: Schematic of turbine rotor, disc wells and casing structure.

Results from SC03 simulations have been used in this chapter (and Chapter 6) to both train and validate the model. The SC03 model incorporates the entire air system from the fan and compressors to the turbine exit, as well as all of the structures supporting those components. The fluid dynamics is informed by CFD studies and 1D air system models, and appropriate correlations applied at boundaries of the solid components. The solid model is capable of simulating both the thermal and mechanical response, and these results have been validated against engine tests. More information on SC03 can be found in papers such as [4, 8, 63, 126, 127].

5.2.2 Modelling Objectives and Requirements

The advantage of managing thermomechanical fatigue by monitoring disc temperature has been discussed in Section 1.4.3, yet it is clear from the literature that there is no specific relation between model accuracy and possible life extension. Therefore, targets have been based on desire to control the cooling flow to the disc. The following criteria were used in guiding the development of the model;

1. It must have a sufficiently low number of states to be suitable for real-time simulation. This is defined as executable on a standard FADEC 100ms sample task, which in turn can be tested by compiling the model in a real-time, dedicated computer that emulates the FADEC architecture.

2. It must have both a steady state and dynamic temperature error of less than $20K$ within volumes of interest compared with the SC03 reference model. This value was chosen with reference to Lu *et al.* [85] and under advice from Rolls-Royce life management specialists. The volumes are averaged from points that have been modelled directly, so individual points may have errors up to $\pm 30K$ provided it is not for an extended period of time. The volume averaged approach is discussed further in Chapter 6.

3. It must rely only on the standard existing measurement suite in the engine. Though optimal estimation can be improved with direct measurement of the disc, it is first assumed that no such measurement exists.

4. The model architecture must be suitable for use over a standard flight profile, such that the method could in theory be expanded to an aircraft's entire flight envelope, or to include reference to performance degradation and the run-on effects to local conditions at the disc.

These criteria have been applied in both the present LPV-SVD model and in the physics-based model presented in Chapter 6.

5.3 Methodology

5.3.1 Basic Equations for the LPV-SVD Model

To reiterate from previous chapters, the basic setup of the LPV-SVD model is;

$$T(\chi,t) = \sum_{i=1}^{m} \Psi_i(\chi)\Phi_i(\theta,t) \tag{5.1}$$

which can be expressed in state-space form as;

$$\begin{aligned}
\begin{bmatrix} \dot{\boldsymbol{x}}_1(t) \\ \dot{\boldsymbol{x}}_2(t) \\ \vdots \\ \dot{\boldsymbol{x}}_m(t) \end{bmatrix} &= \begin{bmatrix} \mathbf{A}_1(\theta) & & & 0 \\ & \mathbf{A}_2(\theta) & & \\ & & \ddots & \\ 0 & & & \mathbf{A}_m(\theta) \end{bmatrix} \begin{bmatrix} \boldsymbol{x}_1(t) \\ \boldsymbol{x}_2(t) \\ \vdots \\ \boldsymbol{x}_m(t) \end{bmatrix} + \begin{bmatrix} \mathbf{B}_1(\theta) \\ \mathbf{B}_2(\theta) \\ \vdots \\ \mathbf{B}_m(\theta) \end{bmatrix} \boldsymbol{u}(t) \\
T(\theta,\chi,t) &= \begin{bmatrix} \Psi_1(\chi) & \Psi_2(\chi) & \dots & \Psi_m(\chi) \end{bmatrix} \begin{bmatrix} \boldsymbol{x}_1(t) \\ \boldsymbol{x}_2(t) \\ \vdots \\ \boldsymbol{x}_m(t) \end{bmatrix}
\end{aligned} \tag{5.2}$$

5.3.2 Signal Selection

A signal must be selected from the existing engine measurement suite to serve as input to the model. There are several variables that govern a particular turbines temperature, the most important being the temperature of the gas in the disc wells and in the core flow. These can be consolidated by using the compressor exit temperature (T_{30}). Normalising this by the maximum and minimum temperatures provides a good input variable for the LPV-SVD model;

$$u(t) = \frac{T_{30}(t) - T_{30,min}}{T_{30,max} - T_{30,min}} \tag{5.3}$$

Several other variables still form an important part of parameterising the temperature profile itself. The next most important parameter that defines the non-linear boundary conditions is perhaps the rotational Reynolds number (Re_ϕ) which drives the Nusselt number (Nu) and the local heat transfer coefficients. Working backwards, the most important parameters would be the engine spool speed (Ω), and the inlet air thermodynamic properties. The latter are directly related to atmospheric conditions, which are captured as pressure altitude (alt) within the engine measurement suite. Thus we choose $\theta = \theta(\Omega, alt)$. It is assumed that other parameters such as the aircraft Mach number, other shaft speeds, fuel flow and power extraction will vary in a near fixed relation to these two, and that the model will capture the transient dynamics associated with them because it is trained to match the time constants found between steady state conditions.

5.3.3 Acquisition of Training Data

The thermal profile of the 2D disc geometry was subsampled at 121 discrete query points for each training cycle. The points were arbitrarily selected by imposing a square grid pattern on the profile and selecting all the points that fell within the boundary (see Figure 5.2). There is a natural limit to the accuracy imposed by the SVD truncation that is difficult to surpass, so it is unlikely that a more sophisticated, topologically guided selection of points would create a more accurate model.

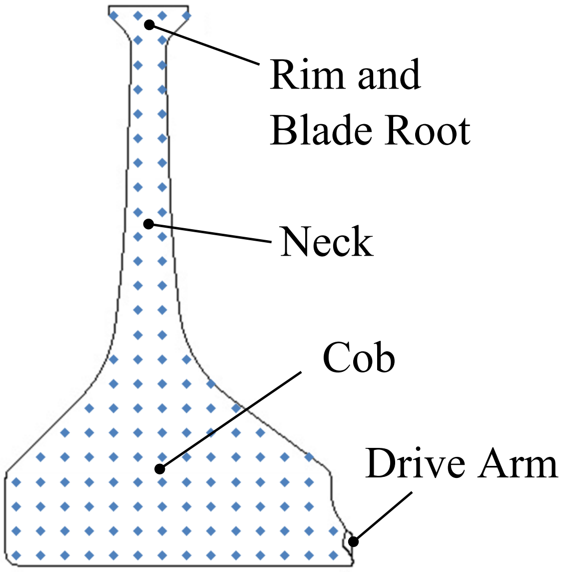

Figure 5.2: Grid of points used for subsampling the SC03 model.

The SC03 simulations were run with step cycles starting from steady Sea-Level-Static (SLS) conditions, rising to one of nine other conditions (see Table 6.2) and returning back to SLS. A tenth point was investigated for conditions at descent approaching 1.5kft, however because the temperatures at the start of the step cycle are so similar to these conditions, the simulation and resulting SVD failed to capture the full responses of the system. Instead, the parameters at this point have been heuristically determined based on other nearby points.

The model scope is limited to simulate only the temperature response above a baseline temperature (T_{base}) set at SLS conditions. This means that only temperatures above T_{base}

Condition	Ω (rad/s)	alt (kft)
Maximum Take-Off	915.0	0
Climb after Take-Off	901.2	1.5
Cruise	840.8	36
Reacceleration	889.2	36
Cruise	832.4	38
Reacceleration	883.6	38
Cruise	836.0	40
Deacceleration	591.8	40
Cruise (Low Hold)	788.9	1.5
Descent*	484.4	1.5

*Point derived from other nearby conditions

Table 5.1: The operating points used in the 'frozen value' training data.

were stored for analysis and used to build the model. The assumption is that the taxi period and SLS conditions are the same in every case. By restricting the range of temperatures that the SVD needs to reproduce, the error range can be reduced.

5.3.4 SVD Analysis

Figure 5.3 shows a representation of the spatial singular vectors (U_i) produced from an SVD of the full set of step response data. U_1 and U_2 appear to correlate with the disc temperature profiles at steady state and mid-transience respectively (more so than the casing temperatures did in Chapter 4). U_3 could be interpreted as the effect of local HTC spikes due to impingement. However, only the first two modes are used to create Ψ_1 and Ψ_2 in the final model based on the analysis of the temporal vectors below. U_3 and U_4 are shown here because they appear transiently within the error plots of the recombined profile (see Section 5.5.3 for further details).

Figure 5.4 shows a plot of the first six temporal modes ($\sigma_i V_i$) as identified from the SLS-MTO step cycle. These have been normalised to the maximum value of $\sigma_1 V_1$ to show the relative contribution of each vector. A closer view of the plot is shown in Figure 5.5 where $\sigma_1 V_1$ has been removed. Only the ascent (step-up) portion of the data is used for identification of state-space parameters at other operating points. The descent step (step-down) has only been used here for the identification of parameters at SLS. This full response also serves as a good comparison of the contribution of each $\sigma_i V_i$ to the final model.

As can be seen in Figure 5.5, $\sigma_3 V_3 \rightarrow \sigma_6 V_6$ are of all of similar magnitude in ascent and descent. This implies that they all contribute a similar component to the final model, which means that the benefit can only be achieved by incorporating all of them. Another way to

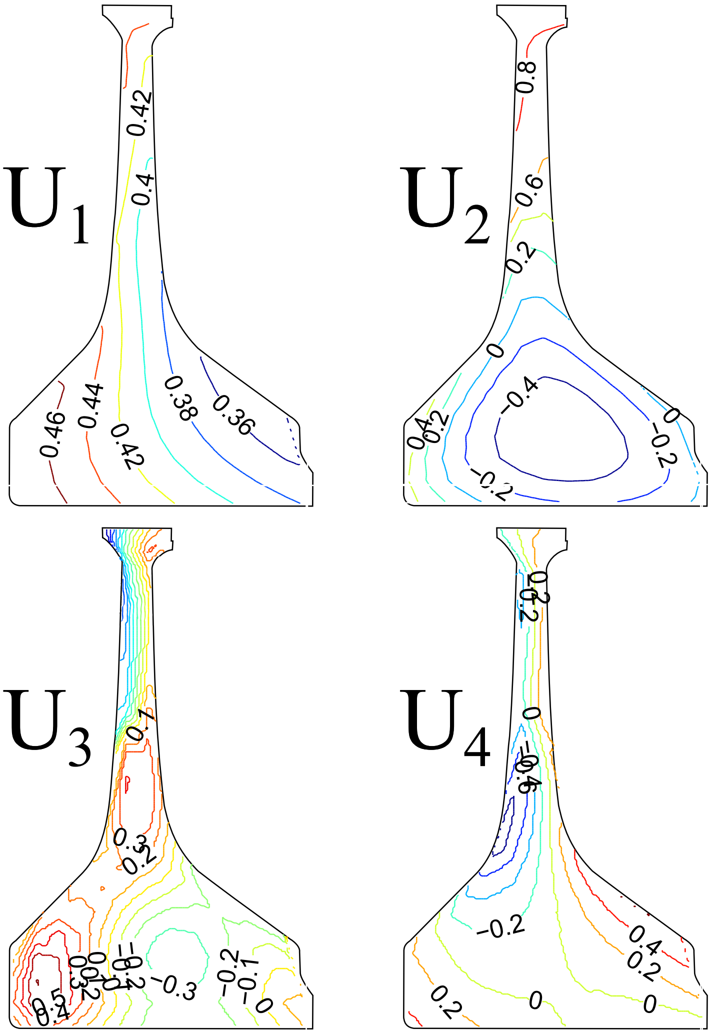

Figure 5.3: Contour representation of the first four spatial vectors (U_i).

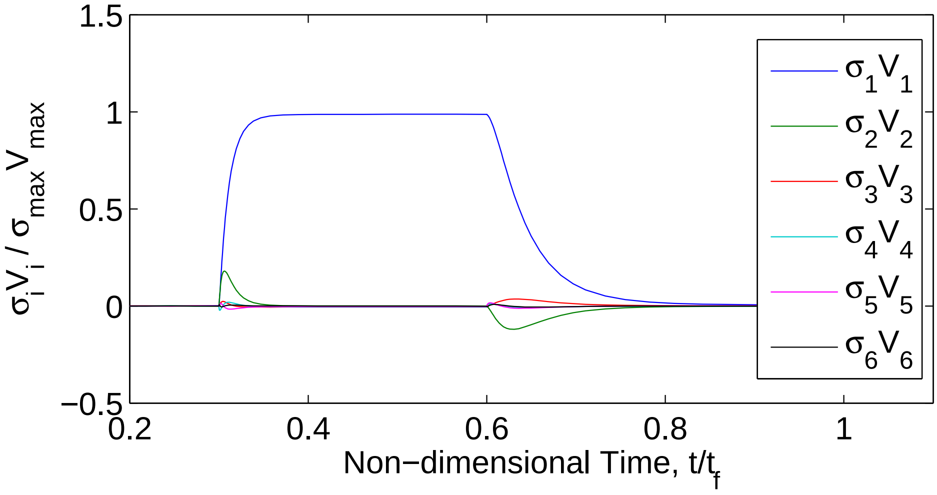

Figure 5.4: First six temporal modes ($\sigma_i V_i$) of a SLS-MTO step cycle.

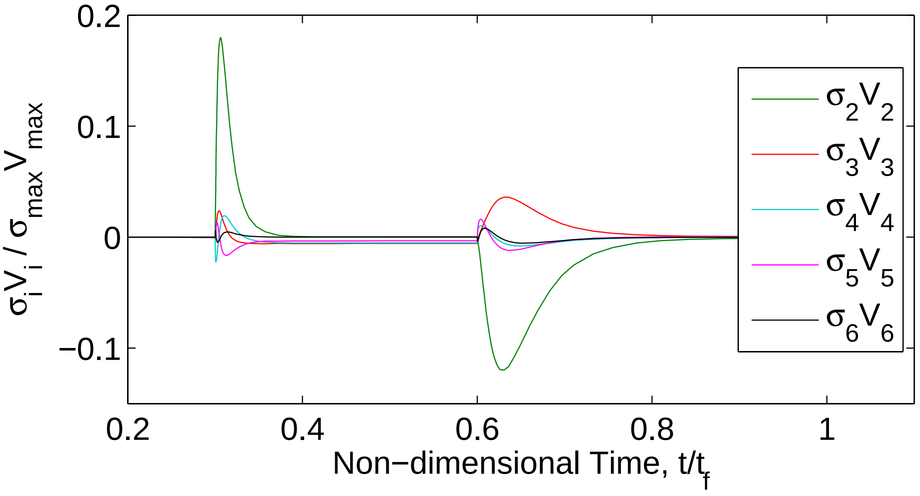

Figure 5.5: A close up of Figure 5.4 without ($\sigma_1 V_1$).

understand this, is to consider the e_{max} that occurs when recombining the truncated SVD. This is shown in Figure 5.6. From this plot, it is clear that the benefit of including modes above rank 2 are diminished, thus the final model is limited to a rank 2 truncation. There is a second reason for this choice; $\sigma_1 V_1$ and $\sigma_2 V_2$ are identified consistently as first and second order responses respectively. This trend does not continue over the subsequent modes, nor is it consistent across all data sets. If the order of the response is not consistent, it makes it extremely difficult to model them using the LPV-SVD methodology as described.

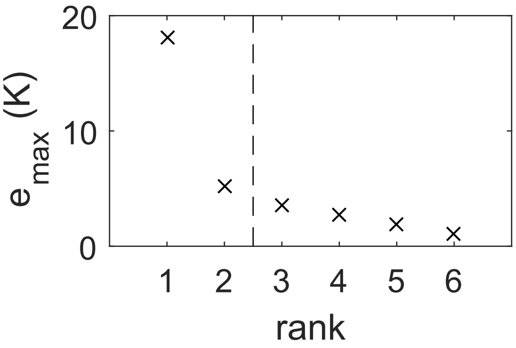

Figure 5.6: The e_{max} calculated for an SVD recombination of the SLS-MTO step data. The dashed line indicates the cut-off used in the model.

5.3.5 System Identification

It is necessary to identify the form of the transfer functions Φ_1 and Φ_2 that best model $\sigma_1 V_1$ and $\sigma_2 V_2$ respectively. For Φ_1 this is a transfer function with a single-pole (p_1) and gain (k_1). In state-space form, this is realised as;

$$\mathbf{A} = \begin{bmatrix} \mathrm{p_1} \end{bmatrix}\ , \quad \mathbf{B} = \begin{bmatrix} \mathrm{k_1} \end{bmatrix}\ , \quad \mathbf{C} = \begin{bmatrix} 1 \end{bmatrix} \tag{5.4}$$

The second function, Φ_2, is best represented by a dual-pole ($\mathrm{p_2}$,$\mathrm{p_3}$), single-zero (z) structure, with gain ($\mathrm{k_2}$), which in state-space form is;

$$\mathbf{A} = \begin{bmatrix} \mathrm{p_2} & 0 \\ \mathrm{p_3} - \mathrm{z} & \mathrm{p_3} \end{bmatrix}\ , \quad \mathbf{B} = \begin{bmatrix} \mathrm{k_2} \\ 0 \end{bmatrix}\ , \quad \mathbf{C} = \begin{bmatrix} 1 & 1 \end{bmatrix} \tag{5.5}$$

These matrices can be concatenated into a single state-space to make it more succinct. Further, the elements of **C** combine with U to give the vector Ψ, as;

$$\mathbf{A} = \begin{bmatrix} \mathrm{p_1} & 0 & 0 \\ 0 & \mathrm{p_2} & 0 \\ 0 & \mathrm{p_3} - \mathrm{z} & \mathrm{p_3} \end{bmatrix}\ , \quad \mathbf{B} = \begin{bmatrix} \mathrm{k_1} \\ \mathrm{k_2} \\ 0 \end{bmatrix}\ , \quad \Psi = \begin{bmatrix} U_1 & U_2 & U_2 \end{bmatrix} \tag{5.6}$$

The parameters of the functions are again identified through the 'frozen value' approach. That is, for each set of data, the gains ($\mathrm{k_1}$,$\mathrm{k_2}$), poles ($\mathrm{p_1}$,$\mathrm{p_2}$,$\mathrm{p_3}$) and zero (z) are identified in relation to the parameter vector (θ) and stored in a set for later interpolation. To visualise how this interpolation works in this case, a typical map of the results is shown in Figure 5.7. This plot shows $\mathrm{p_1}$ at both the training data locations (grey circles) and the interpolated values (contours). The arrowed line shows a typical flight cycle as it varies with Ω and alt.

The corners where no data exists are estimated to ensure smooth interpolation of the rest of the results. It was found after validation that similar model accuracy can be achieved with fewer data points, particularly in the upper-right corner of this plot, however the aim of the research is not to minimise the number of training points because it is not crucial to improving the speed of the model.

5.3.6 Truncation Limit of Model

The final model has an accuracy limit imposed by the nature of the truncated SVD. As a reference for the final model, a rank 2 SVD of a full flight profile across 121 points has been compared with the original data. The difference between the two is shown in Figure 5.8. The maximum error associated with this truncation is $34.8K$, with a root-mean-square error of $2.14K$ (when sampled at approximately $1Hz$). The major peaks in error occur at the start of take-off ($4980s$), at mid climb ($5000s$), and during descent ($35\,000s$). Though the maximum error is close to the $30K$ target, it is only for a single point and only lasts a short time (less than 5 seconds).

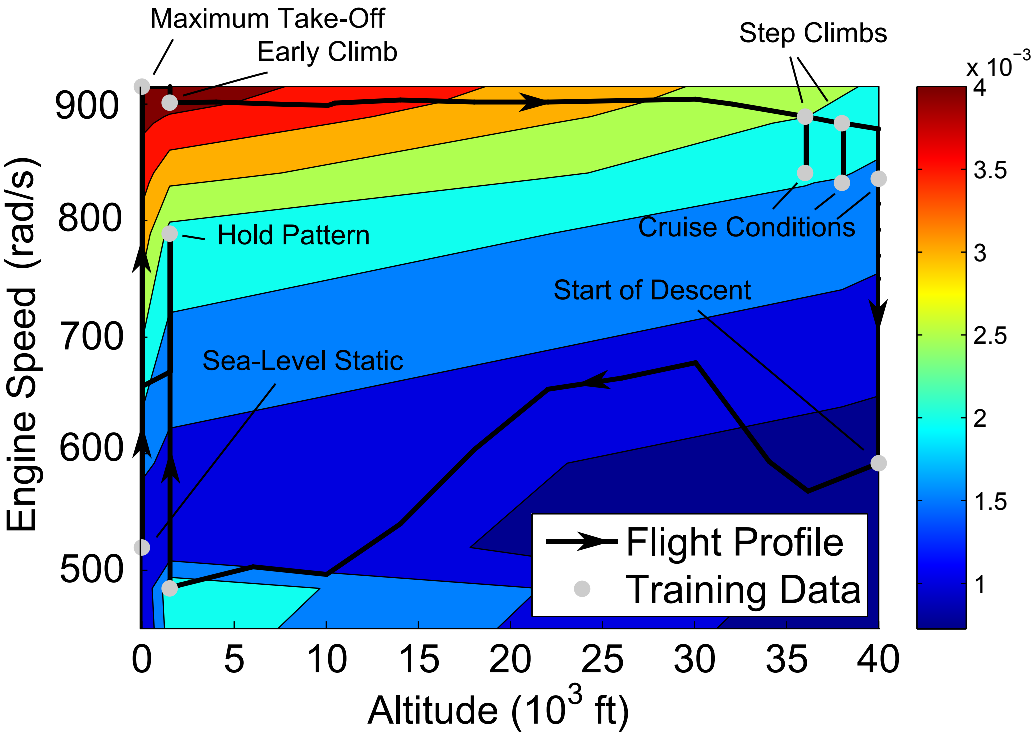

Figure 5.7: Contour plot of $\mathrm{p}_1 = \mathrm{p}_1(\theta)$ with a standard flight cycle superimposed. Note that the data for p_1 has been generated at the grey circles, which are shown also shown in Table 6.2. The corners have been estimated by the author to ensure smooth contours, and that the rest of the data has been interpolated, particularly between climb and cruise at $36kft$.

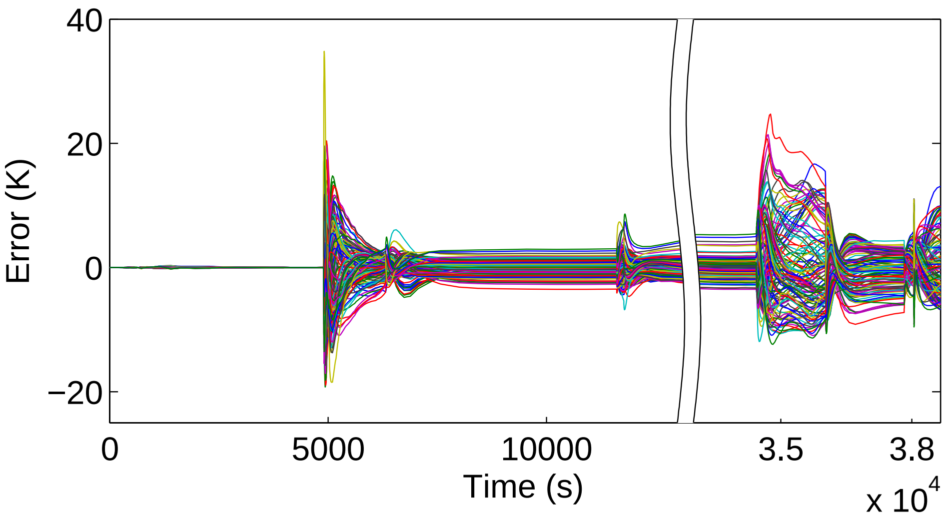

Figure 5.8: Difference between original data (T) and truncated data ($\hat{T}_{r=2}$). MTO and climb occur at 5000s, descent occurs at 35000s.

5.4 Final Model Structure

There are two model architectures important to the final model. The first is shown in Figure 5.9 and the second (and final) model is shown in Figure 5.10. Each architecture produces the same result overall, but the first was used primarily to produce each output Φ_i in isolation, making it possible to validate the system identification process. The first model can be expressed by the set of equations shown in Equation 5.7. The second architecture incorporates the simplification $\Psi = U\mathbf{C}$ can be expressed by the set of equations shown in Equation 5.8.

$$
\begin{gathered}
\dot{\boldsymbol{x}}(t) = \begin{bmatrix} \mathrm{p}_1(\theta) & 0 & 0 \\ 0 & \mathrm{p}_2(\theta) & 0 \\ 0 & \mathrm{p}_3(\theta) - \mathrm{z}(\theta) & \mathrm{p}_3(\theta) \end{bmatrix} \boldsymbol{x}(t) + \begin{bmatrix} \mathrm{k}_1(\theta) \\ \mathrm{k}_2(\theta) \\ 0 \end{bmatrix} \frac{T_{30}(t) - T_{30,min}}{T_{30,max} - T_{30,min}} \\
\begin{bmatrix} \Phi_1(\theta,t) \\ \Phi_2(\theta,t) \end{bmatrix} = \begin{bmatrix} 1 & 0 & 0 \\ 0 & 1 & 1 \end{bmatrix} \boldsymbol{x}(t) \\
\hat{T}(\theta,\chi,t) = \begin{bmatrix} U_1(\chi) & U_2(\chi) \end{bmatrix} \begin{bmatrix} \Phi_1(\theta,t) \\ \Phi_2(\theta,t) \end{bmatrix} + T_{base}(\chi,t)
\end{gathered} \tag{5.7}
$$

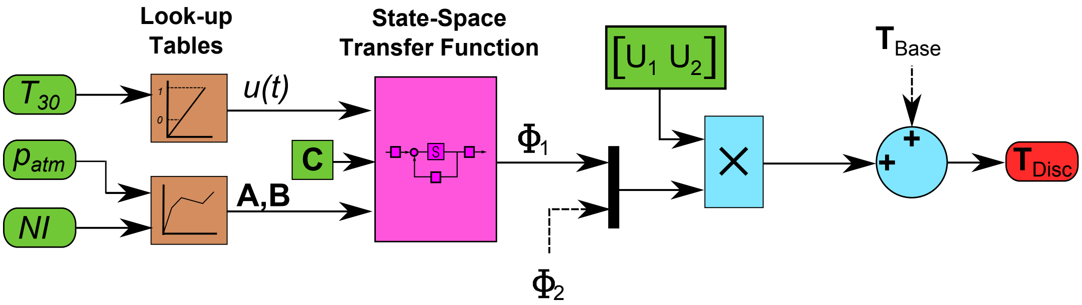

Figure 5.9: LPV-SVD model used to validate the identified transfer functions (Φ_i). In this case, $\mathbf{C}$ is a simple Boolean matrix as required by the realisation of the state-space.

$$
\begin{gathered}
\dot{\boldsymbol{x}}(t) = \begin{bmatrix} \mathrm{p}_1(\theta) & 0 & 0 \\ 0 & \mathrm{p}_2(\theta) & 0 \\ 0 & \mathrm{p}_3(\theta) - \mathrm{z}(\theta) & \mathrm{p}_3(\theta) \end{bmatrix} \boldsymbol{x}(t) + \begin{bmatrix} \mathrm{k}_1(\theta) \\ \mathrm{k}_2(\theta) \\ 0 \end{bmatrix} \frac{T_{30}(t) - T_{30,min}}{T_{30,max} - T_{30,min}} \\
\hat{T}(\theta,\chi,t) = \begin{bmatrix} \Psi_1(\chi) & \Psi_2(\chi) \end{bmatrix} \boldsymbol{x}(t) + T_{base}(\chi,t)
\end{gathered} \tag{5.8}
$$

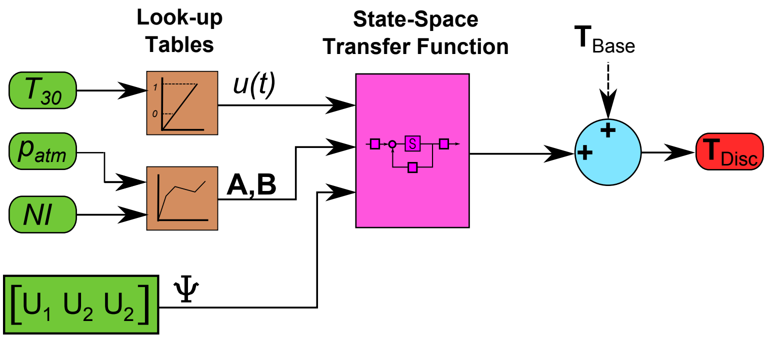

Figure 5.10: Overview of the final LPV-SVD model for the disc.

5.5 Validation and Discussion

5.5.1 Reproduction of Temporal Singular Vectors

Each of the identified Φ_i are validated against the relevant $\sigma_i V_i$ as produced by an SVD of the full flight cycle as shown in Figure 5.11. For the purposes of visual comparison, given these vectors are supposed to be orthonormal, each profile is normalised to the maximum value of Φ_1 in order to highlight their relative size. Both transfer functions appear to match reasonably well during take-off, cruise and mid-cruise reacceleration, but the descent period (from 0.9) does not match as well. This is due to the lack of local data to support the interpolation of the parameters (k,p,z). It is also likely to be due to the fact that cooling is a slower process than heating which leads to more complex interactions. However, a full discussion is best conducted alongside the realisation of the temperature profiles.

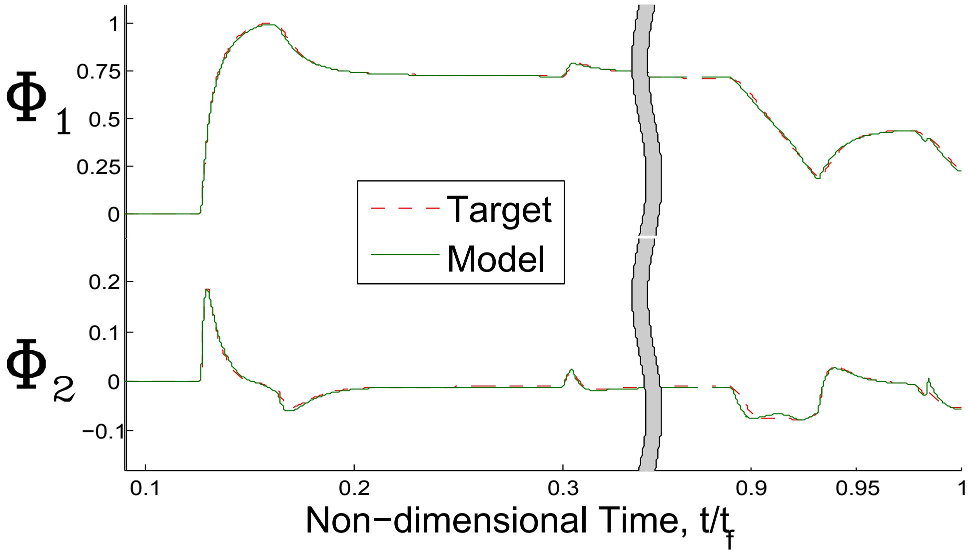

Figure 5.11: Comparison of the LPV transfer functions with their target output ($\sigma_i V_i^{\mathsf{T}}$).

5.5.2 Temperature vs Time

A number of validation studies help to identify the strengths and weaknesses of the model as a whole. As an example, the temperature profile for an arbitrary point selected at the centre of the disc cob is shown in Figure 5.12. This plot demonstrates the accuracy of the model any one point, and this particular point has $e_{rms} = 1.45K$ when sampled at $1Hz$. The least accurate point, which has $e_{rms} = 5.88K$, is located at the front of the disc where the neck meets the cob (see Figure 5.15e). The average e_{rms} for the entire model is $2.18K$, which is not statistically different from the truncation limit of $2.14K$ found in Section 5.3.6. This lends further support to the idea that the SVD analysis can be used to predict the final model accuracy.

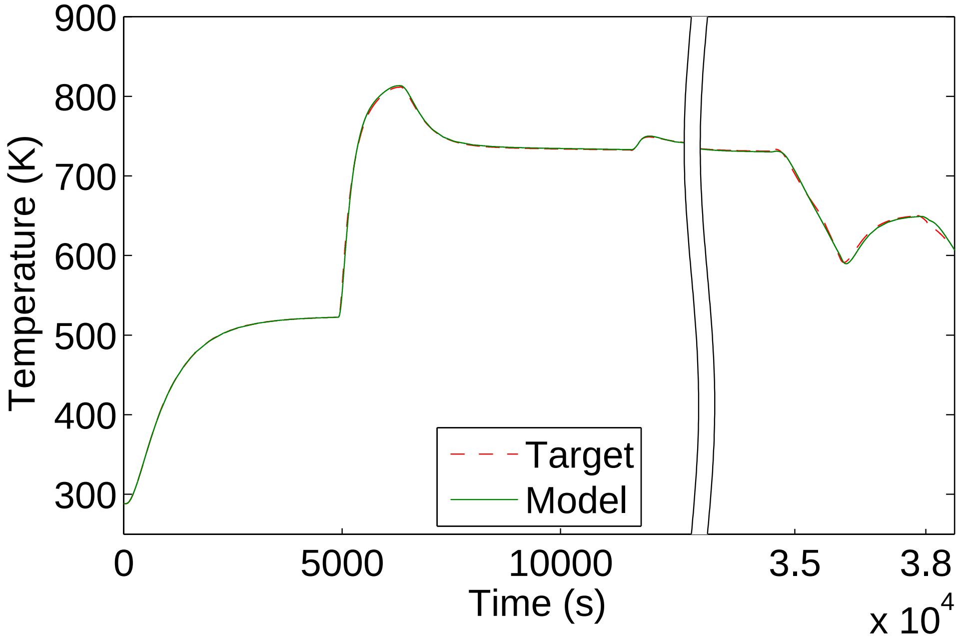

Figure 5.12: Comparison of a single point ($\hat{T}_{50}$) against the original (T_{50}).

The temperature profile of all 121 points is shown in Figure 5.13a and the error for each point is shown in Figure 5.13b. The initial warmup period ($0 < t < 5000s$) has no discernible error. This is because the model's range only starts above SLS conditions, and this early period only shows the T_{base} which is the same across all tests. The point of maximum error occurs just after MTO at point (a/e). The error here is $32.0K$, which is in agreement with the truncation limit of $e_{max} = 34.8K$ as identified in Section 5.3.6. By the time the simulations reaches maximum temperature at (b/f), the error reaches a minimum across the entire model. This is due to the way that Ψ is defined from the U_i vectors, which in turn is based on the overall training data. The model has been optimised to simulate the temperature at this point. Using a different set of training data, with different steady-state maximum temperatures and residence times, would shift this optimisation (e.g. to the cruise conditions). However, optimising to the maximum temperature conditions is most beneficial for life management.

The steady state error at cruise (c/g) and during mid-flight reacceleration is very low, well within the $20K$ target that would imply volume averaged accuracy. During descent (d/h) the error grows again. This is partially due to the lack of data used to identify the local parameters, and will be discussed further using the 2D profiles in the next section.

The overall width of the error spread in Figure 5.13b is similar to that found in the truncation limit shown in Figure 5.8. The difference being that the error in the truncated matrix case is centralised, whereas the model error drifts high and low with the simulation. This effect is partially corrected with the Kalman filter presented in Section 5.6.

5.5.3 Reconstructed Axisymmetric Disc Profile

From the point data shown above it is possible to look at snapshots of the disc temperature at specific time points and remap the temperature distribution onto the original disc geometry. An example of this is shown in Figure 5.14 alongside the equivalent profile from the SC03 simulation. The data between points in the LPV-SVD model have been interpolated assuming a linear gradient between nearest neighbours. This has the mistaken effect of interpolating data that falls along the edge of the geometry within the concave sides. However for the purposes of visualisation, and bearing this in mind, we can still pursue a reasonable analysis of the results. Figure 5.14 highlights the incredible detail that can be reconstructed from the SVD methodology. An appropriate extrapolation of surface points is presented in Section 5.5.4.

Figure 5.15 shows the temperature profile (a-d) and respective error (e-h) for the series of time points shown in Figures 5.13a and 5.13b. Focusing on the temperature profiles first, there is an obvious similarity between (b,c) and the contour plot of U_1 (Figure 5.3). These are examples of quasi-steady conditions that tend towards the dominant ‘steady-state’ mode. Similarly, (a) and (d) look much more like U_2 contours, as they are examples of transient conditions. From a physical perspective, the steady-state plots show the near linear temperature profile that dominates the geometry from front to back due to the steady heat transfer between the disc wells. During transients, the cob of the disc lags behind the temperature change of the rest of the disc due to its greater mass and heat capacity, so the contours have a local minimum/maximum near to the centre of the cob.

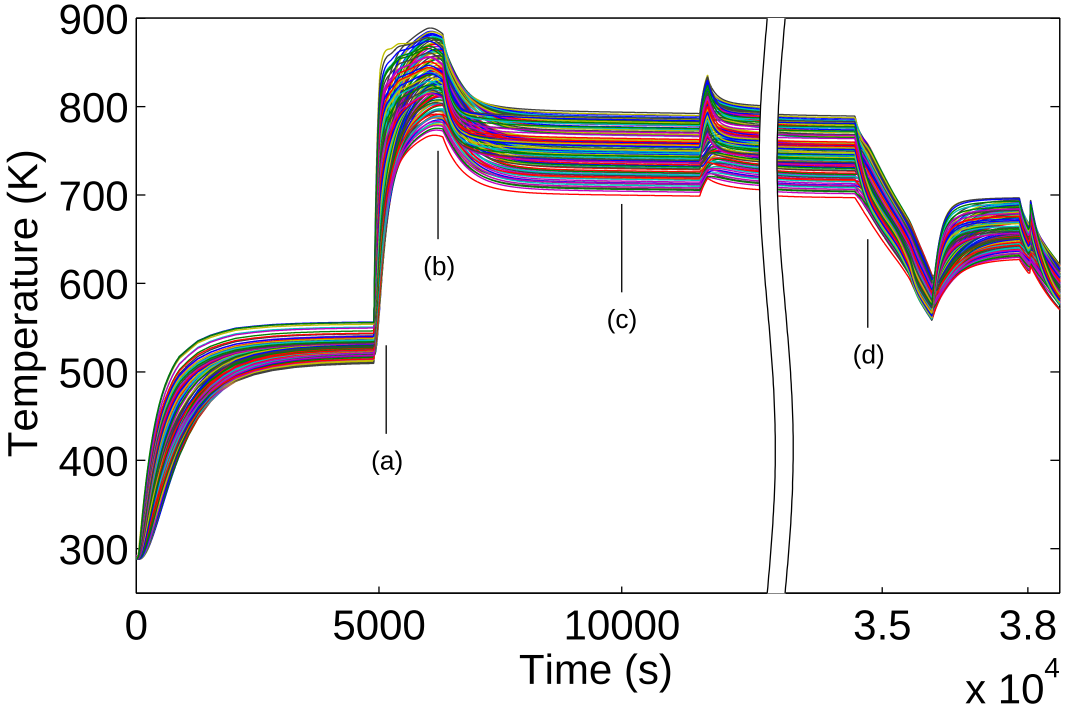

(a) Temperature

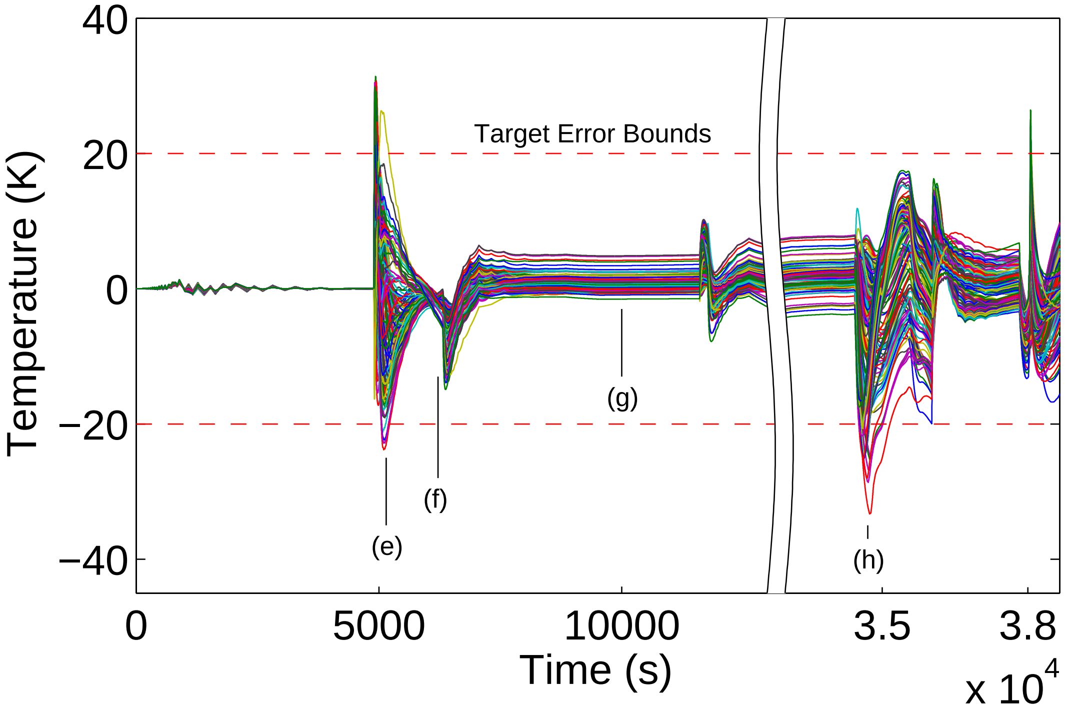

(b) Temperature error

Figure 5.13: Temperature results for all 121 model points, and how they compare with the original SC03 data.

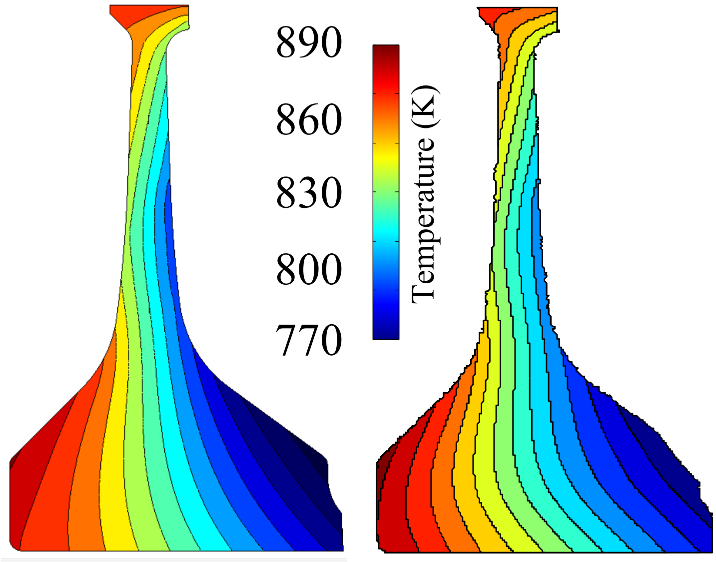

(a) SC03 Data (b) Model Data

Figure 5.14: Comparison of disc temperature contours at maximum conditions. Contour levels are the same for each.

Consider now the absolute error plots shown in Figure 5.15 (e-h). The first thing to notice is that the distribution of the error in (f) and (g) correspond very closely with U_2. Similarly, (e) corresponds very much with U_3, while (h) appears to have some similarity to both U_3 and U_4, particularly with the latter when observing the high contour on the rear surface of the cob.

Physically, plots (e) and (h) reflect the locations of local convective forces that have been ignored in the model by selecting only a rank 2 truncation of the SVD. For plot (e), an impingement mechanism exists on the front of the cob, where both flow is injected and the core region circulates back towards the disc surface. On the rear side of the disc in plot (h), there is a strong convective force across the entire surface. This is due to a heat transfer mechanism that is only partially dependent on the T_{30} air, and thus has not been properly incorporated into the model. There is an adjustable flow to this cavity that invalidates the assumption that the thermal field can be parameterised by T_{30}, Ω and alt alone. Adding a third measurement to θ should improve the result, and this could be a measurement of the air that feeds this cavity (T_{26}) or more likely a measurement of the valve position that provides the actuation of the flow. The addition of a third measurement to model a modulated flow is an area of future research.

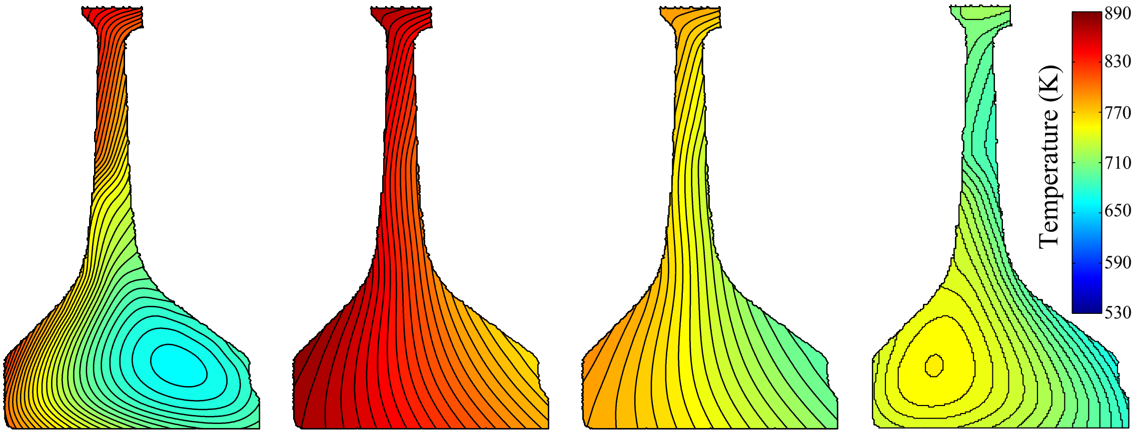

(a) Start of Take-Off (b) Maximum *T* (c) Cruise at 36 000 ft (d) Descent

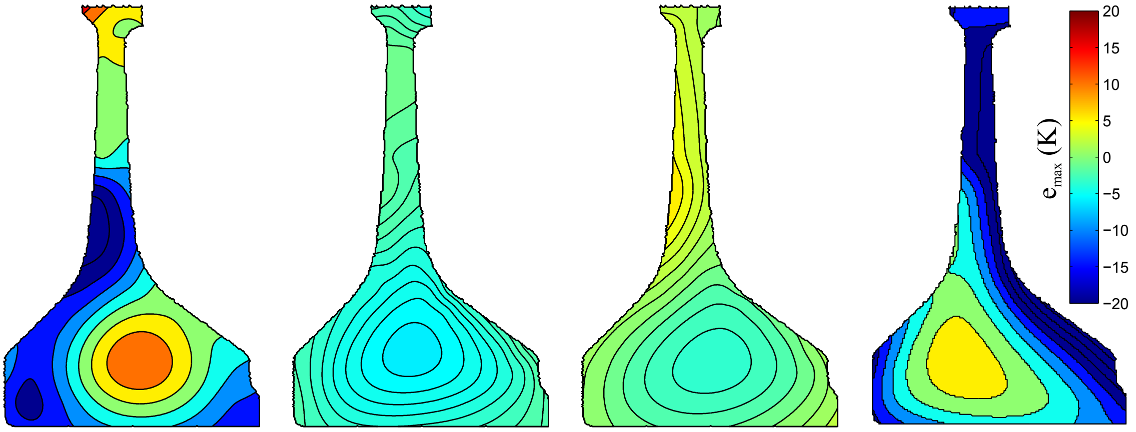

(e) Start of Take-Off (f) Maximum *T* (g) Cruise at 36 000 ft (h) Descent

Figure 5.15: Normalised temperature profile of the disc (a-d), and the respective error in *K* of the model relative to the original data (e-h). The scales are the same across the row for each of the four figures.

5.5.4 Extrapolated Surface Points

An important consideration in the practical application of this method is how well the temperatures on the surface of the disc can be extrapolated from the available data. This analysis considers five points spaced around the disc's surface as identified in Figure 5.16. The extrapolation technique for the simulated points involves minimising differences in the local temperature gradient, effectively smoothing the temperature towards a local linear profile. This is consistent with temperature distributions in an isotropic material under quasi-steady conditions. The comparison data from SC03 can be extracted directly.

The temperature data for the five points is shown in Fig. 5.17a and the relative error plots are shown in Fig. 5.17b. The extrapolated points do not perform as well as the points that are simulated directly, but some perform better than others. Point 1 (blue - inner cob

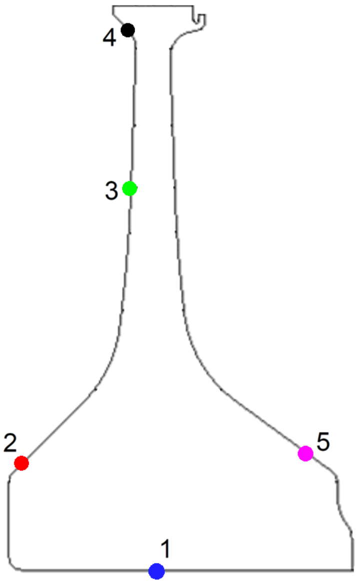

Figure 5.16: Five points on the disc's surface where temperature data has been extrapolated. Labels match Figure 5.17a and 5.17b.

surface) and Point 2 (red - front cob surface) still perform within the natural limitation. Point 3 (green - centre radius front) and Point 4 (black - front of rim) appear to be the worst affected at the start of take-off. Both are very close to impingement areas from secondary flows so they face large nonlinearities. Point 5 (purple - back of disc) is most affected by the variation in the flow entering the disc well that was identified in Figure 5.15h.

The ability of the model to resolve surface points appears to be good in this instance. Future work should consider how this can be combined with an experiment based LPV-SVD model that would necessarily utilise surface data.

5.5.5 Compilation on a Real-Time Computer

The model has been compiled on a NI PXIe-8115 Express Controller. This controller has a $2.5GHz$ dual-core Intel Core i5-2510E processor, with up to $1GB/s$ system bandwidth and $250MB/s$ slot bandwidth. This capability is on par with an aircraft FADEC. The model successfully executed at $10kHz$, validating that it is suitable for execution online within the $100ms$ sample task requirement.

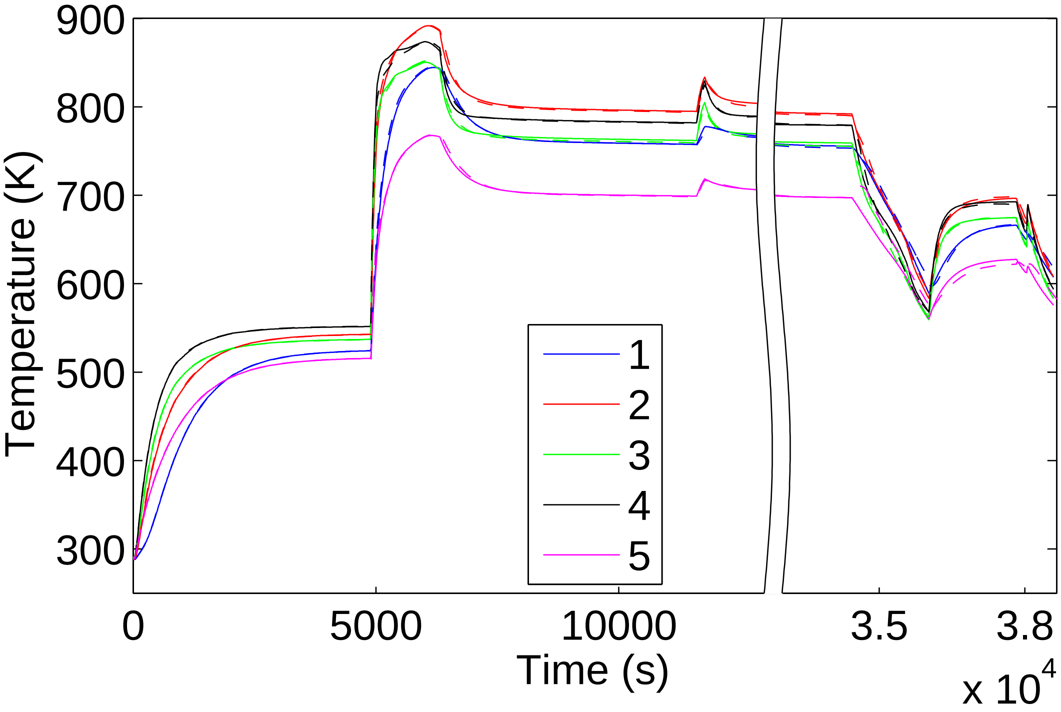

(a) Temperature

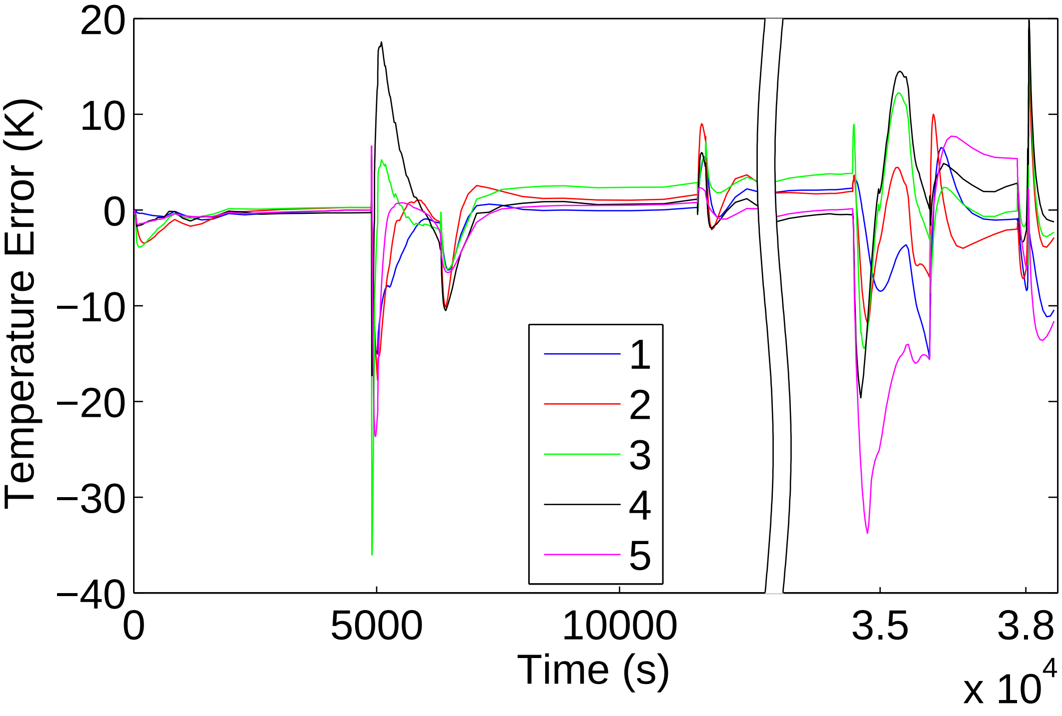

(b) Relative error compared with the FE/CFD solution

Figure 5.17: Temperatures for the five extrapolated points.

5.6 Kalman Filter

5.6.1 Background

A filter is a form of controller applied to a model in order to update and correct the output ($\bar{\boldsymbol{y}}$) based on some measurement of the plant ($\boldsymbol{y}$). Multivariable systems, such as the LPV-SVD model, do not have straight forward techniques or exact solutions to create optimised controllers. This is unlike SISO control systems, which can be devised analytically with root locus diagrams and frequency response [46]. To apply a filter to a model, the state-space equations are given an update between time steps based on the new information. The *current* state estimate ($\hat{\boldsymbol{x}}$) is found from the previous, or *predictor*, state estimate ($\bar{\boldsymbol{x}}$) and the residual of $\bar{\boldsymbol{y}}$ and $\boldsymbol{y}$;

$$\hat{\boldsymbol{x}} = \bar{\boldsymbol{x}} + \mathbf{L}(\boldsymbol{y} - \bar{\boldsymbol{y}}) \tag{5.9}$$

This is shown in block diagram for in Figure 5.18. The design of the Estimator matrix ($\mathbf{L}$) is the key to optimising the model. The solution to finding an appropriate $\mathbf{L}$ depends on the balance between the model accuracy and the plant observability. Neither are well understood, especially when process noise ($\boldsymbol{w}$) and measurement noise ($\boldsymbol{v}$) are not explicitly defined. Best practice techniques include Least-Square Estimation, Weighted Least Square Estimation, Recursive Least Square estimation, and Kalman filters [46]. The discussion here is limited to the Kalman filter, which is a common method based on a balance of $\boldsymbol{w}$ and $\boldsymbol{v}$ in real-time, assuming they have a stochastic distribution. The mean-square noise levels of each are defined from their expectation values;

$$R_w = E\{\boldsymbol{w}(k)\boldsymbol{w}(k)^\mathsf{T}\} \tag{5.10}$$

$$R_v = E\{\boldsymbol{v}(k)\boldsymbol{v}(k)^\mathsf{T}\} \tag{5.11}$$

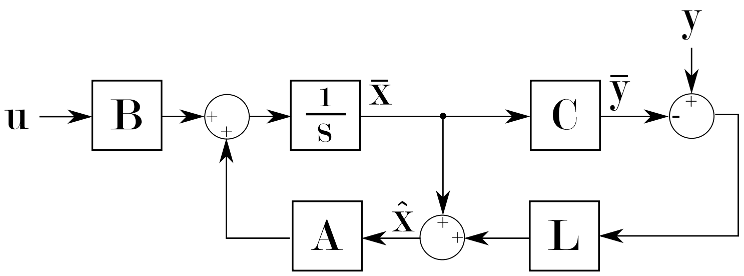

Figure 5.18: The implementation of estimator correction in a state-space model.

There has been a number of reported Kalman filters used in real-time models to understand the core-flow performance degradation in gas turbines [87, 122, 123, 141]. These examples mostly focus on the use of performance indicators such as losses in efficiency and capacity and relate this to overall system forecasting for failure and/or maintenance regimes. For example, Luppold *et al.* [87] propose Kalman filter based methods to understand the deterioration in core-flow parameters such as turbine efficiencies and nozzle capacities. Simon and Garg [122] have applied this method to the NASA C-MAPPS high-bypass turbofan engine model [47] and develop a selection process for a multi-input/multi-output filter. Simon and Armstrong [123] went further to concentrate on the methods to select the optimum Kalman filter gains for the purposes of gas path fault isolation (i.e. detection of which of the parameters have deteriorated). Volponi [141] focuses on a multi-layer neural network model that uses measurements of pressure and temperature directly, rather than observations of various stage efficiencies that are typically used.

5.6.2 New Model setup

The LPV-SVD model for a simulated environment can be improved using a virtual "measured" signal to better estimate the temperature field. This section presents a Kalman filter based on the assumption that a sensor could be manufactured such that the temperature of the disc could be measured to an accuracy of $\pm 5K$, as proposed by Garg *et al.* [48]. For simplicity, we assume that the measurement is taken directly at one of the model outputs (y_i) [1]. Measurements are more likely to be at the surface of the disc, however, extrapolating a 'measurement' from the surface back to a y_i point introduces an unnecessary estimation for the sake of identifying a best-practice approach. The error associated with such an estimation could be mitigated in practice by assuming larger measurement noise, or creating a disc model based on surface measurements only.

Figure 5.19 shows the setup for the Kalman filter, with the original LPV-SVD model in the bottom-left, the Kalman filter $\mathbf{L}$ on the bottom-right, and the artificial "Plant" at the top providing measurements y_i. The process noise ($\boldsymbol{w}$) must account for the random fluctuations in the temperature of the air leaving the compressor, the fluctuation of the heat transfer effects as the air passes from the compressor to the disc well, and the noise of the measurement of T_{30} in the first place. We assume that the noise associated with the T_{30} sensor is roughly equivalent to the fluctuations between T_{30} and the disc wells. Therefore, we assume $\boldsymbol{w}$ has a zero mean and $10K$ variance. The measurement noise ($\boldsymbol{v}$) occurs at the theoretical "sensor" that measures the temperature of the disc's surface. Raw data from

---

[1] For discussion on the Kalman filter in this section, y_i will be used to define the model output temperature at point i, rather than T_i . This is to avoid any confusion with the compressor exit temperature T_{30}.

the SC03 simulations is used as the measurement with $\boldsymbol{v}$ having a variance of $5K$ applied artificially.

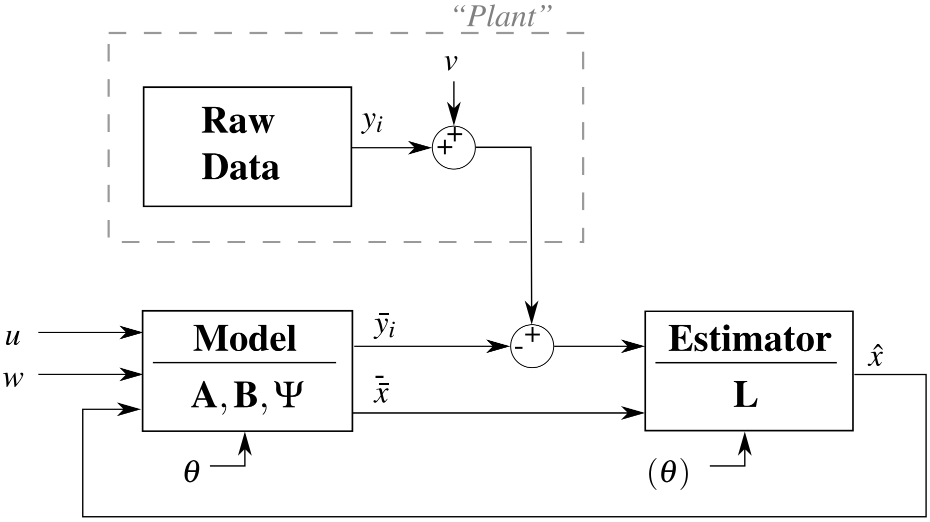

Figure 5.19: Setup of LPV-SVD model using raw SC03 data and artificial measurement noise v to create a "Plant" for filtering.

5.6.3 Filter Generation

The matrix $\mathbf{L}$ can be calculated from the solution to the *Linear Quadratic Gaussian* (LQG) problem. Details of the derivation can be found in Franklin *et al.* [46]. Here we simply present the formula as;

$$\mathbf{L}_{\infty} = \mathbf{L}_{\infty}(\mathbf{A}, \mathbf{B}, \mathbf{C}, R_v, R_w) \tag{5.12}$$

as given by MATLAB's `kalman.m`. However, as the model is based on an LPV system, and the output is a vector 121 points long, there is no clear method to optimise the solution based on either the operating point θ and/or measurement point y_i. The approach taken here is to evaluate filters at a selection of different θ and y_i, and then compare each filter's ability to correct the model over a known trajectory. From this comparison an optimal filter can be selected, and then be validated against an independent trajectory to confirm its effectiveness.

Two methods for evaluating $\mathbf{L}$ are presented. The first is constant, and is calculated using values of $\mathbf{A}, \mathbf{B}$, and Ψ (in place of $\mathbf{C}$) based on a single parameter vector θ. The second considers a filter based on LPV systems, where $\mathbf{L} = \mathbf{L}(\theta)$ and varies with the trajectory of the model like $\mathbf{A}(\theta)$ and $\mathbf{B}(\theta)$. Each method is evaluated across multiple y_i.

The complete θ map is based on 12 engine spool speeds (Ω) and five pressure altitudes (alt), giving a total of 60 operating points. However, these were mostly interpolated and extrapolated from the 10 original operating points that span the flight envelope of the validation cycle. As such, in choosing θ for evaluating the constant filter, only the original 10 points are considered. Furthermore, we start by prioritising accuracy at the extremes of operation (e.g. peak temperatures and long cruise periods) so only MTO and $38kft$ cruise conditions are considered initially. These represent two very different flight conditions, and should highlight any differences that the choice of θ might have on the overall effectiveness of the filter. The resulting constant filters are called $\mathbf{L}_{MTO,i}$ and $\mathbf{L}_{38k,i}$ respectively, and calculated as;

$$\mathbf{L}_{MTO,i} = \mathbf{L}_{MTO}(\mathbf{A}(\theta_{MTO}), \mathbf{B}(\theta_{MTO}), \psi_i, R_v, R_w) \tag{5.13}$$

$$\mathbf{L}_{38k,i} = \mathbf{L}_{38k}(\mathbf{A}(\theta_{38k}), \mathbf{B}(\theta_{38k}), \psi_i, R_v, R_w) \tag{5.14}$$

The parameter ψ_i is used to isolate different measurement points. It is defined by zeroing all the rows of $[\Psi_1 \Psi_2]$ apart from row i. This means that only the measurement T_i is considered when filtering the model, but still affects all other points.

Each constant value filter has been evaluated at nine different y_i. Only points near the surface of the disc make sense for the location of a virtual measurement, as shown in Figure 5.20. Any location not near the surface doesn't make practical sense and generally produces an unstable filter. It will be shown that the choice of measurement point is far more important than the choice of θ for defining $\mathbf{L}$. This is why only $\mathbf{L}_{MTO,i}$ and $\mathbf{L}_{38k,i}$ are presented.

The LPV-based filter has been trialled with the same nine measurement points as defined above. The filter is constructed by evaluating $\mathbf{L}$ at all 60 θ where $\mathbf{A}(\theta)$ and $\mathbf{B}(\theta)$ have been identified in the original model;

$$\mathbf{L}_{\theta,i} = \mathbf{L}_{\theta}(\mathbf{A}(\theta), \mathbf{B}(\theta), \psi_i, R_v, R_w) \tag{5.15}$$

$\mathbf{L}_{\theta,i}$ can then be evaluated in the model with a look-up table similar to $\mathbf{A}(\theta)$ and $\mathbf{B}(\theta)$. The motivation for this method was that the filter could be optimised at different operating points throughout a flight.

5.6.4 Filter Selection by Measurement Point

First consider how the choice of y_i affects the filter by comparing the results of different $\mathbf{L}_{MTO,i}$ alone. The profile used for comparing the filters is the same flight profile used

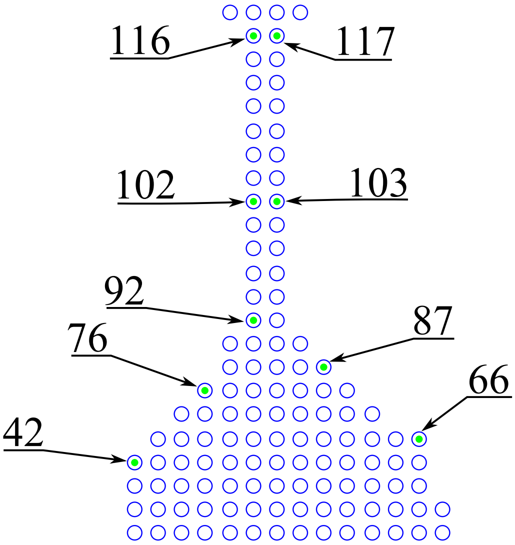

Figure 5.20: Points on the disc investigated to find the best possible Kalman filter virtual sensor location.

for validation in Section 5.5. The desire is that the filter will contain both large singular spikes in the error, and significant extended offsets. To that end, two basic analyses were generated. The first considers the maximum absolute error (e_{max}) experienced at each point throughout the entirety of the simulation. The second analysis considers the root-mean-square error (e_{rms}) at each point in order to identify where there is significant sustained drift in the accuracy.

The e_{max} and e_{rms} contour plots for each $\mathbf{L}_{MTO,i}$ are shown in Figure 5.21 and Figure 5.22. Blue indicate regions where the output is nearly an exact match to the training data, and red indicates either significant over- or under-estimation. The contour levels have been chosen to highlight the difference between results. It is important to acknowledge that the contours are included for aesthetics, and that the interpolated data away from the sample points is less significant than the values at the points themselves (yellow points). This is particularly apparent when considering the significance of the error at the top left corner of Figure 5.21a, compared with the error at the top right of Figure 5.21f.

It was found that the greatest factor affecting the results is the large difference in the dynamic response between the rim and the cob. Using a filter measurement at the cob will lead to gross inaccuracies at the rim because the cob responds much slower to thermal mechanisms than the neck and rim do. The exception to this observation is shown in Figure

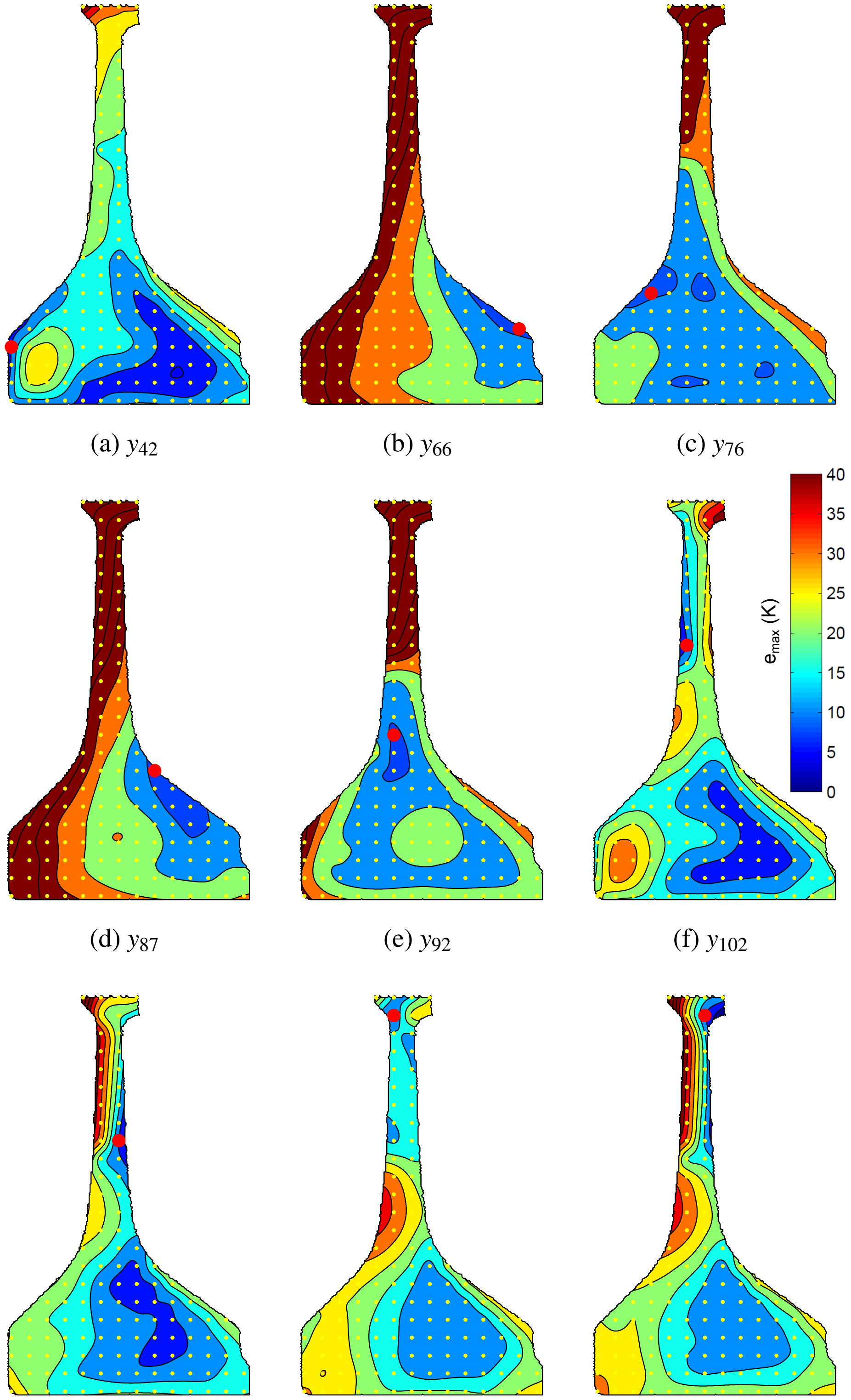

(a) y_{42} (b) y_{66} (c) y_{76}

(d) y_{87} (e) y_{92} (f) y_{102}

(g) y_{103} (h) y_{116} (i) y_{117}

Figure 5.21: Contour plot of the e_{max} at every point in the disc profile using a $\mathbf{L}_{MTO}$ with measurements at the red dot.

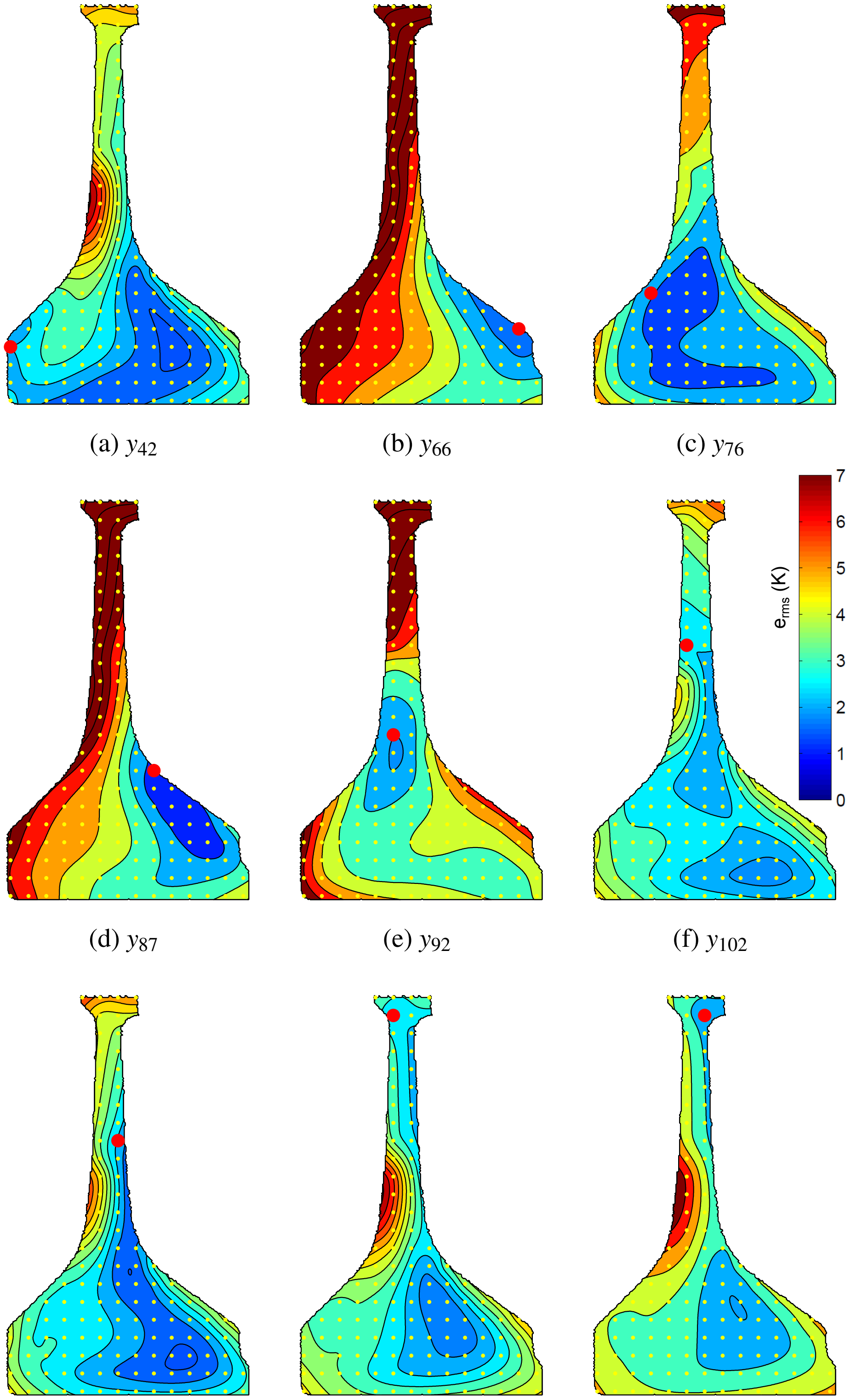

(a) y_{42} (b) y_{66} (c) y_{76}

(d) y_{87} (e) y_{92} (f) y_{102}

(g) y_{103} (h) y_{116} (i) y_{117}

Figure 5.22: Contour plot of the e_{rms} at every point in the disc profile using a $\mathbf{L}_{MTO}$ with measurements at the red dot.

5.21a, where a point at the front edge of the cob does a reasonable job of controlling the temperature error distribution across all points. This is because the front of the cob has dynamics similar to the rim due to a local impingement of air from the disc well.

On the other hand, a measurement near the rim of the disc will tend to over correct the cob for extended periods, as indicated by Figures 5.22(f-i). The closer the measurement is to the rim, the more yellow areas appear in the cob. Another feature that can be seen from both Figure 5.21 and Figure 5.22 is that there is a slight benefit to choosing a measurement at the front side of the disc. This is because the rear of the disc is known to be affected by flows that haven't been modelled properly (see Section 5.5.3). If this issue was resolved, a sensor that measures the back of the disc would be favourable because it would be easier to install.

Based on the above observations the location of y_i should be a point that reflects the dynamics of the disc on average. However, it is not yet clear how to derive this location analytically. The best compromise between the extremes has been found heuristically. As such, the best choice is a measurement at the mid span of the neck - y_{102} (see results shown in Figures 5.21f and 5.22f).

5.6.5 Filter Selection by Operating Condition

It could be assumed that the choice of y_i primarily affects the spatial resolution of the error, whereas the choice of θ would affect the error distribution over time. The latter point is true, however, the effect is almost negligible in the cases studied here. This is illustrated in Figure 5.23. Figure 5.23a shows the validation flight profile including some important time points such as MTO and cruise conditions. Figure 5.23b shows e_{max} as calculated for all points in the disc's profile at those time points using the three filters. Overall, there is no clear difference in the results that would suggest one technique over another. To consider this from another point of view, consider the e_{max} and e_{rms} considerd across all points at all times as shown in see Table 5.2. No one filter type shows a distinct benefit across all points, which suggests that the choice of θ is not very important. As such, and for simplicity, $\mathbf{L}_{MTO,102}$ has been chosen for the validation against the independent profile in the final model.

5.6.6 Validation and Discussion of $\mathbf{L}_{MTO,102}$

A new flight profile has been introduced to validate the final filter selection. This is shown in Figure 5.24 and represents a flight that has been aborted after take-off. For reference, the

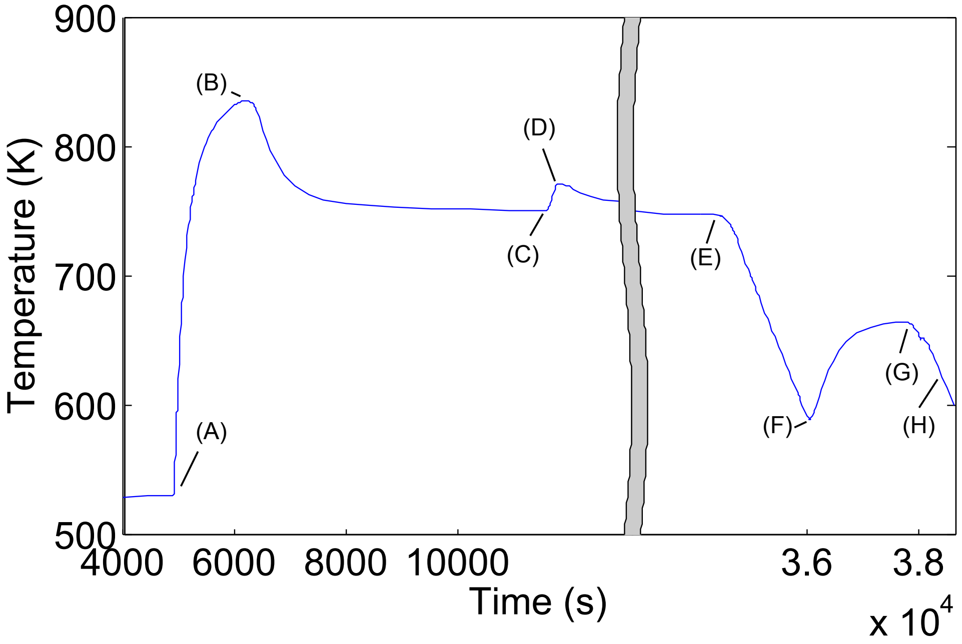

(a) Time Points

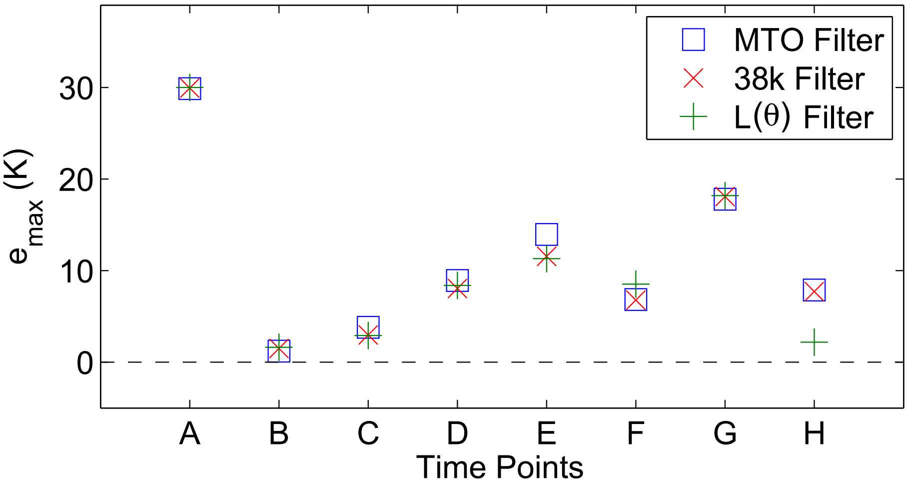

(b) Error Maximum

Figure 5.23: The similarity of Kalman filters based on different θ for Point 102. The maximum error recorded for any point in the disc is shown in (a) for the time points in (b). The time points align with; (A) MTO, (B) Max temperature, (C) Cruise at 36000ft, (D) Step Climb, (E) Start of descent, (F) End of descent, (G) Hold pattern, (H) Descent to landing.

	y_i	42	66	76	87	92	102	103	116	117
e_{max}	$\mathbf{L}_{MTO,i}$	44.5	86.1	69.8	85.9	102.3	36.8	54.9	34.4	56.2
	$\mathbf{L}_{38k,i}$	39.8	72.6	59.4	63.0	85.5	37.2	54.3	34.5	51.0
	$\mathbf{L}_{\theta,i}$	41.8	102.0	64.7	110.9	97.1	39.0	58.9	34.5	53.2
e_{rms}	$\mathbf{L}_{MTO,i}$	2.76	5.16	2.93	4.59	4.45	2.99	2.70	3.27	3.75
	$\mathbf{L}_{38k,i}$	2.63	5.36	2.89	4.39	4.24	2.73	2.62	2.93	3.44
	$\mathbf{L}_{\theta,i}$	2.93	5.95	3.33	5.17	4.78	3.00	2.90	3.19	3.75

Table 5.2: The e_{max} and e_{rms} for all three filters calculated across all points and all time based on a range of measurement points y_i.

error that occurs when simulating this profile without the Kalman filter is shown in Figure 5.25. The errors are much greater than previously observed for the LPV-SVD model due to the trajectory operating far outside the original training data. Even the initial temperature of the disc does not align with a typical take-off.

The data from the original SC03 simulation is used as a measurement signal for the Kalman filter. The signal has an artificial measurement noise $v(t)$ to emulate the sensor error that might exist in a real engine. A similar process noise $w(t)$ is applied to the model's input signal to replicate the sensor error associated with the upstream measurement.

The error associated with the complete, filtered results are shown in Figure 5.26. The improvement in accuracy compared to the unfiltered results is stark. The error is now bounded to $\pm 30K$, and most points perform far better. The signal is noisy, but this can be improved in downstream processing.

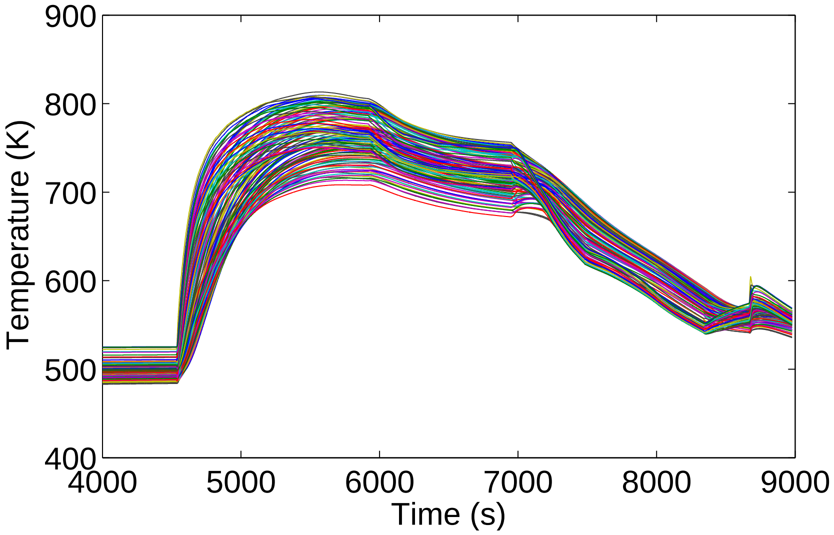

Figure 5.24: Flight profile used for validating the Kalman filter LPV-SVD model. Each point in the profile is represented by a different coloured line.

Figure 5.27 shows the results of the filtered model as applied to singular points. Specifically, Figure 5.27a shows how the filter works on y_{102} where the virtual measurement is taken, and Figure 5.27b shows the process on a neighbouring point (y_{88}) that has not been directly measured. The filter allows a large influence on the measurement point, so $\bar{y}_{102}$ follows the measured value precisely, albeit with a lower variance. This appears to work against the accuracy of point 88 at take-off, but the absolute accuracy of all points has improved as shown in Table 5.3, and between Figures 5.25 and 5.26. The filtering process has shown the greatest improvement through the descent period where the model would otherwise over predict the temperature.

Point	42	50	66	76	87	92	102	103	116	117
Original	26.9	20.6	19.6	25.7	21.1	25.3	26.6	25.6	29.0	28.6
Filtered	5.15	4.17	4.84	4.49	4.34	5.83	1.90	2.9	3.40	4.01

Table 5.3: The root-mean-square error before and after application of $\mathbf{L}_{MTO,102}$.

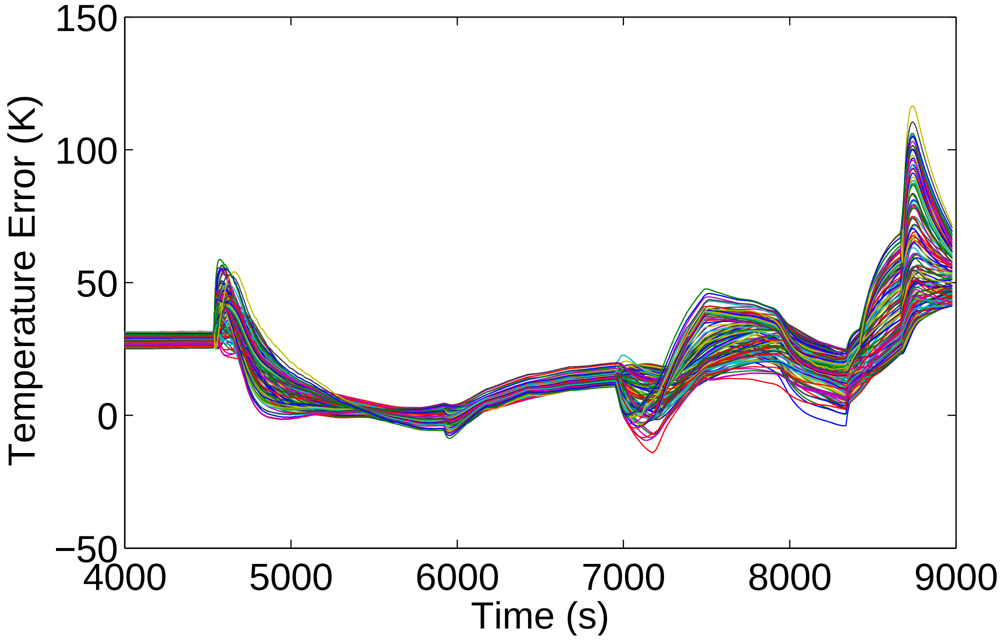

Figure 5.25: Error in simulating the new flight profile without the Kalman filter.

5.7 Conclusions

The aim of this chapter was to apply the LPV-SVD model to a turbine disc based on SC03 simulations, and develop a Kalman filter for the LPV-SVD model to improve online monitoring of the temperature. The final model is based on a rank 2 truncation of the SVD analysis. Higher order modes proved to be too difficult to work with as the spatial modes

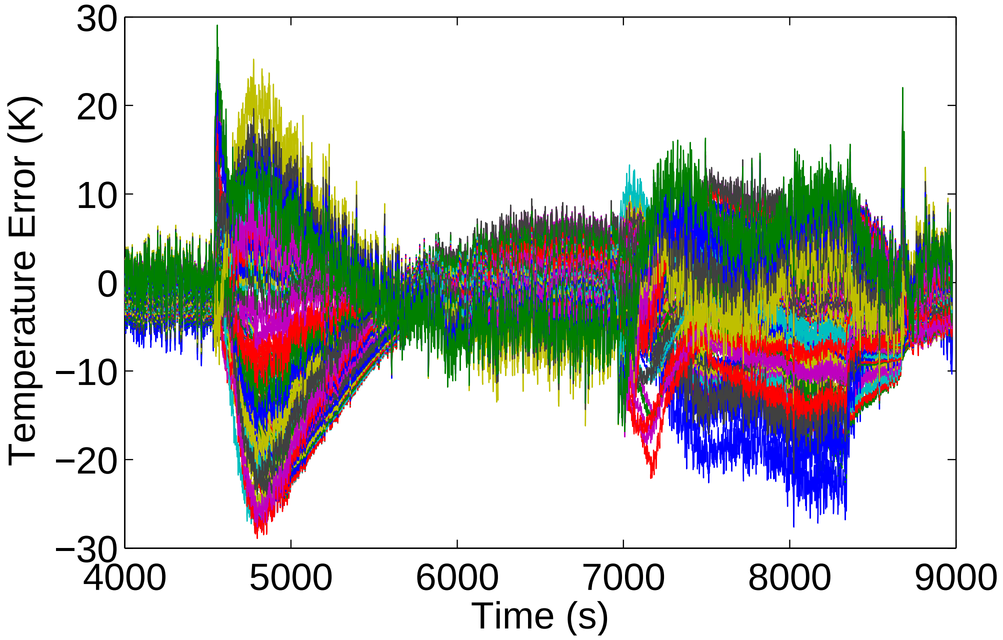

Figure 5.26: Error in simulating the new profile with the Kalman filter in place.

were less consistent across different training sets. The final model produces temperatures with an accuracy of $\pm 32K$, when there is no noise present. This model has been compiled in a real-time controller and successfully run at $10kHz$, suggesting that it is suitable for execution on an online FADEC system.

This chapter presented several methods for constructing a Kalman filter to support an LPV-SVD model of the disc. The filter selection procedure has shown that the measurement point for a filter is far more important than the operating conditions at which the filter is trained. Further, the measurement point should be chosen at a location that reflects the thermal dynamics of the disc on average. In this case, the point is chosen approximately halfway between the rim and cob. The filter allows the model to track an unknown flight trajectory that lies outside the original training data space to an accuracy of $\pm 30K$.

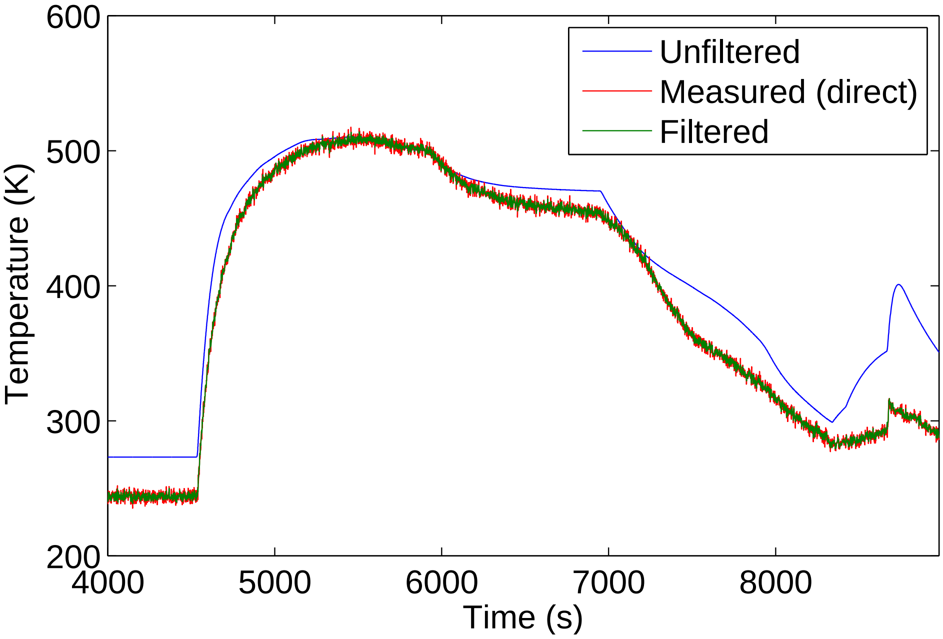

(a) Measurement point (102)

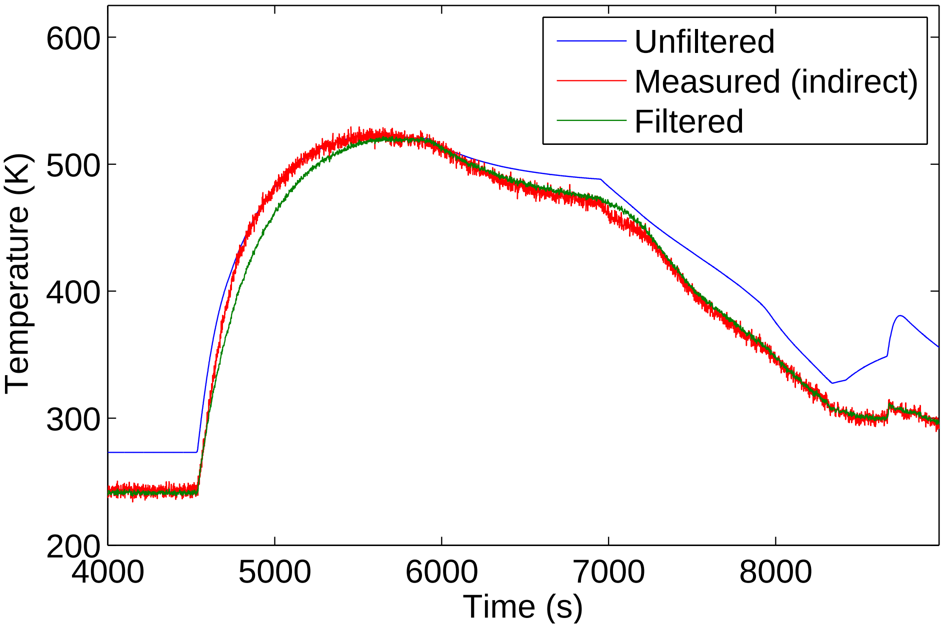

(b) Comparison point (88)

Figure 5.27: Unfiltered model, measured signal and filtered output for a single point.

Chapter 6

Physics Based Model of IP Turbine Disc

6.1 Introduction

This chapter introduces a physics based model of the IP turbine disc. The previous chapter has presented the LPV-SVD model of the disc, which is an example of a black box approach. The physics based model presents a counter example, a form of grey-box approach that incorporates the material properties of the system. It draws on three major backgrounds of study; LPV system identification, lumped capacitance conduction modelling, and the aerodynamics of rotor-stator disc wells. The aerodynamics in particular have not yet been discussed in detail, so a full analysis is presented here.

Section 6.2 will present the analytical theory behind the aerodynamics of rotor-stator disc wells. In Section 6.3, the overall method behind the model is presented, then each of the three parts are presented individually. This starts with an analysis of the disc-well aerodynamics in Section 6.4. Section 6.5 will present the model of the disc's internal heat diffusion based on lumped capacitance modelling, and Section 6.6 will present the simple LPV system used to model the inputs for the two other subsystems. A final overview of the architecture of the model is presented in Section 6.7. A series of validation studies are presented in Section 6.8, and Section 6.9 compares the grey-box model with the LPV-SVD model developed in Chapter 5. The conclusions about the model and the comparison study are presented in Section 6.10.

6.2 Background - Rotor-Stator Disc Well Aerodynamics

The flow structure and heat transfer effects found in rotor-stator disc systems has been subject of much study [32, 33, 38, 37, 44, 66, 82, 102, 114]. Generally, it is not possible to isolate the rotor and stator geometries, so they are considered as a whole. This allows for many different configurations depending on the flow input and output locations. However, simple rotor-stator systems do display many consistent flow patterns that can be categorised and defined by a small selection of non-dimensional parameters. A basic system that matches the configuration of the present geometry is shown in Figure 6.1 and highlights the typical notation of the axes and dimensions.

In particular, the rotor spins around the z-axis with speed Ω, the inner radius of the disc well is length a, and the outer radius is b. If we assume the air entering the well has density ρ and viscosity μ, the rotational Reynolds number of the system is defined as $\mathrm{Re}_\phi = \rho\Omega b^2/\mu$. Furthermore, the rotor surface is defined as $z = 0$ while the stator is at a distance s. The temperature at the disc and stator surfaces are defined as T_0 and T_s respectively, and the gap ratio is defined as $G = s/b$.

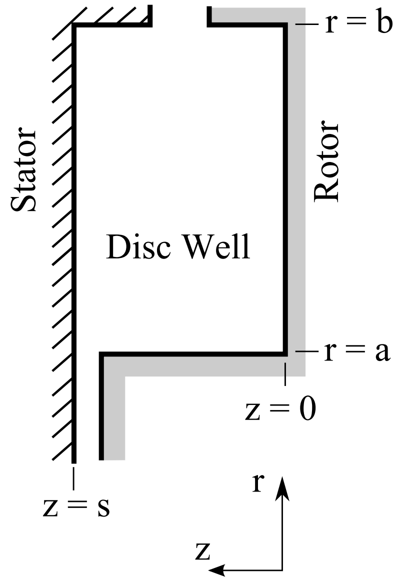

Figure 6.1: Standard rotor-stator disc well configuration.

The mass flow entering the inner radial opening is called the superposed flow ($\dot{m}$). Let the mass flow that is pumped out of the well from the rotor surface be $\dot{m}_o$ and the ingress at the stator surface be $\dot{m}_s$. The mass flow balance is thus $\dot{m} = \dot{m}_o + \dot{m}_s$. Generally this value is positive, which is called *positive superposed flow*. If the ingress is greater than the pumped flow, then there would be *negative* superposed flow ($\dot{m} < 0$). It is also possible for the ingress and pumped flow to be perfectly balanced, usually when there is no inner opening, and such a system has no superposed flow ($\dot{m} = 0$). The non-dimensional flow rate is defined as $C_w = \dot{m}/\mu b$.

So far, three non-dimensional parameters have been defined (Re_ϕ, G, C_w). There are two more that are typically used to characterise the flow; the core swirl ratio (β) and the turbulent flow parameter (λ_T). For these we consider the typical flow structure as shown in Figure 6.2. The structure consists of five key areas. The boundary layers that develop on the rotor surface have a large effect on the local recovery temperature, while the boundary layers on the stator surface may be very small by comparison. The outer and inner source regions show where mixing occurs, and their sizes depend on the amount of ingress to the system (with ingress at the outer opening being undesirable). These four regions confine the central core region which rotates about the axis with stream lines that form toroidal patterns. The average speed of the core rotation is defined as ω, which is always $0 < \omega < \Omega$. The fourth non-dimensional parameter is the core swirl ratio which can be defined as $\beta = \omega/\Omega$.

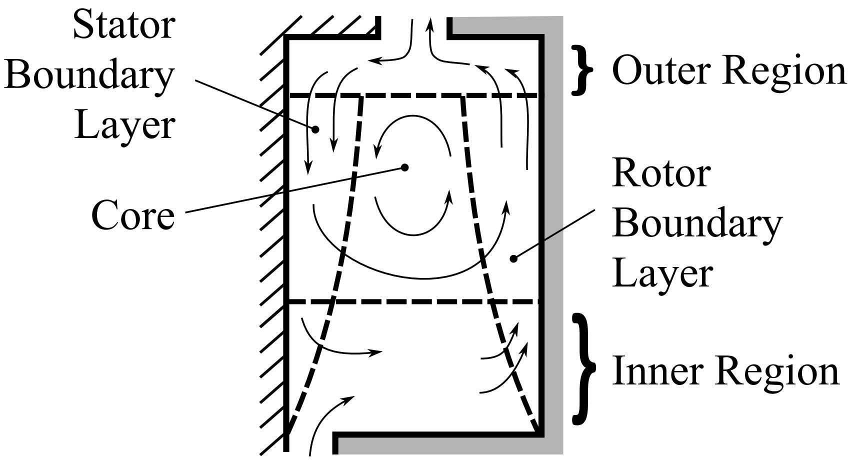

Figure 6.2: Simplified flow structure from rotor-stator system with ingress and superposed flow. Adapted from Sangan *et al.* [114].

Historically, Daily and Nece [38] showed that disc wells with no superposed flow can be generally defined by four basic regimes which depending on the rotational Reynolds number (Re_ϕ) and the gap ratio (G) as shown in Figure 6.3. This delineation of regimes was based on the moment, M, created on the surface of the rotor, which varied distinctly based on whether the flow was laminar (I,II) or turbulent (III,IV) and whether the boundary layers had merged (I,III) or left a core region (II,IV). Though these regimes were originally designed for closed systems, the same approach was later applied to systems with superposed flow. Daily and Nece chose M (and later, the moment coefficient - $C_M = M/\frac{1}{2}\rho\Omega^2 b^5$) as the delimiter because it is a measure of the work done by the air on the disc. Another way to think about it, is that it is a measure of the momentum flux or skin friction. The Reynolds Analogy (see Equation 6.1 as applied to a disc) postulates that the momentum flux and heat flux are related, thus a measure of one allows us to make a reasonable prediction of the other, provided that there is a zero pressure gradient and that $\mathrm{Pr} = 1$ [38]. Thus, by measuring C_M we can make a prediction about the local HTCs.

$$\frac{\mathrm{Re}_\phi C_M}{2\pi} = \mathrm{Nu} \tag{6.1}$$

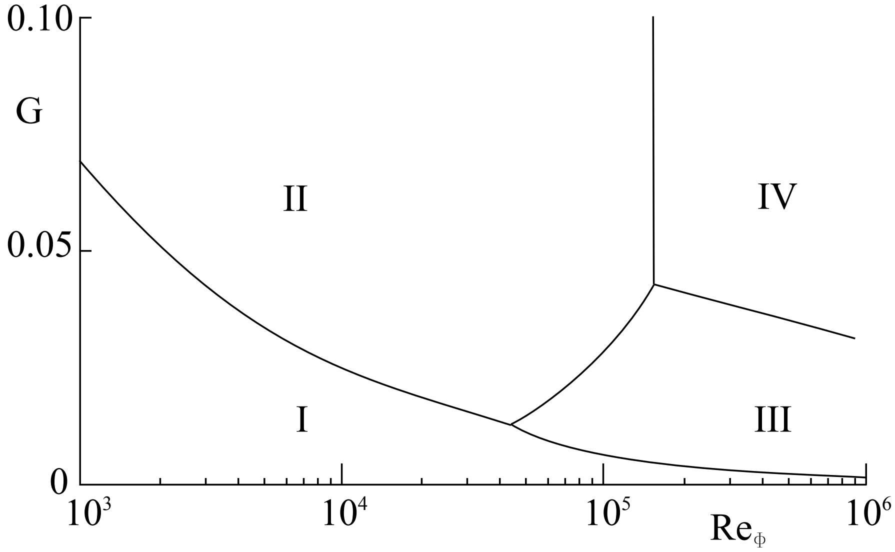

Figure 6.3: Flow regimes for rotor-stator system with no superposed flow. Adapted from Daily and Nece [38].

Daily *et al.* [37] showed that, for discs with superposed flow (i.e. positive $\dot{m}$), the local flow structure can be nearly completely defined by the core swirl ratio (β) and turbulent flow parameter (λ_T) which was simply defined as the product $\lambda_T = C_W \mathrm{Re}_\phi^{-\frac{4}{5}}$ (giving us the fifth non-dimensional parameter). As λ_T decreases (i.e. C_W decreases or Re_ϕ increases), more fluid is entrained at the stator to satisfy disc pumping, which leads to a smaller inner source region, and larger β. Such flows are said to be rotationally dominant. They occur when $\lambda_T < 0.22$. The upper limit, $\lambda_T = 0.22$, is the value associated with the free disc entrainment rate. Systems with $\lambda_T > 0.22$ are dominated by the source region. For systems with $\lambda_T = 0$, the core swirl ration tends to $\beta^* = 0.4258$. The relationship between λ_T and β has been correlated by Daily *et al.* [37];

$$\frac{\beta}{\beta^*} = \frac{1}{1 + 12.74 \frac{\lambda_T}{(r/b)^{13/5}}} \tag{6.2}$$

This can be used to predict the adiabatic wall temperature at the rotor surface ($T_{0,ad}$) which is calculated from the incoming flow temperature (T) as;

$$T_{0,ad} = T + R\frac{\Omega^2 r^2}{2c_{p,air}}(1-\beta)^2 \tag{6.3}$$

where R is the recovery factor and is equal to 0.88 for turbulent boundary layers. Note that the relationship between λ_T and β is heavily geometry dependent; this includes the number of inlets to the cavity, the placement of the inlets, and the direction of the inlet velocities (usually calculated as a pre-swirl ratio). It is possible to predict the local Nusselt number (Nu) by relating the C_M to the convective heat transfer rate, though it is best applied with some knowledge of the target system.

Coren, Childs and Long [32] evaluated the strong relationship between λ_T and C_M by comparing a vast collection of previous studies and with new data for a range of $Re_\phi < 10^7$. In particular they outlined the robustness of empirical models for rotationally dominant flows which are relevant to the flow regimes in this chapter. An example of their results is shown in Figure 6.4. Flow structure and the total pressure drop due to mixing has been investigated by complimentary CFD and experimental simulations by Yan *et al.* [147]. Haddadi and Poncey [52] have performed detailed CFD modelling of Regime III flows, including with negative, positive, and no superposed flow, for a wide range of rotational Reynolds numbers ($1.8 \times 10^5 \leq \mathrm{Re} \leq 1 \times 10^7$). Experiments and CFD continue to demonstrate the strong relationship between Re_ϕ, λ_T, and Nu in disk well flows [33, 44, 66, 82, 114]. These relations will be used to develop a model of the air system in the IP turbine disc.

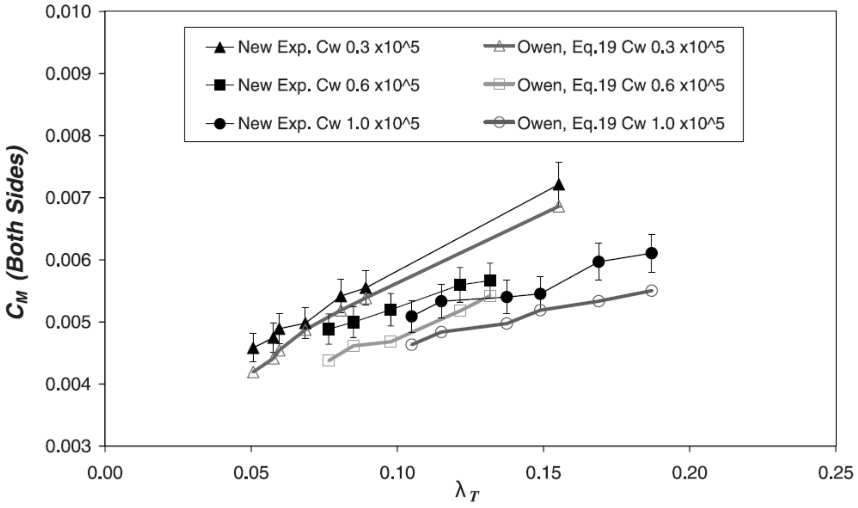

Figure 6.4: Comparison between experiment and theory for flows with $\lambda_T < 0.2$ from Coren, Childs and Long [32].

6.3 Methodology

The physics based model is developed through three majors systems, as discussed individually in the following sections. In order to build a ROM of the disc, the topology has been simplified by dividing it into 8 discrete solid control volumes that contain specific geometry and material properties. These are bounded at the inner and outer extremes by a two further solid control volumes, and on either side by a pair of air control volumes. This approximation of the disc is shown in Figure 6.5. The figure also highlights three flow structures of interest; Area 1 and Area 3 are examples of rotor-stator disc wells, while Area 2 is a more complex mix of both rotor-stator disc, and rotor-stator concentric cylinder interaction. The areas are divided into the blocks that are represented by the 16 air control volumes. Each air block also contains specific geometry information, as well as the mass flow rate, pressure, and temperature. From this the local HTCs can be found using empirical relations. The control volumes maintain mass and energy continuity, thus there is an approximation for the work done by the stator surface on the control volume, called the windage.

6.4 Modelling the Disc Air System

6.4.1 Analysis of Flow Structure

Formulae from the literature have been applied to the present geometry in order to calculate the local Nu from known parameters. In order to improve the model, corrections have been applied based on the results of the SC03 simulations. Similar to the LPV-SVD model, the effectiveness of the grey-box model is measured by the accuracy with which it simulates the SC03 results, and not with regards to the real engine data. This means uncertainties in this SC03 data are not considered. Both Area 1 and Area 3 have radial flow out along the disc surface, with a positive flow out via the leak paths and some recirculation of the air radially inwards far from the disc surface. Both areas have large boundary layers on the disc surface where the air has been entrained. The combined effect of the entrainment and recirculation pulls the inviscid core region into a toroidal flow path about the engine axis in the same direction as the disc. The range of non-dimensional numbers that define the flow in Area 1 and Area 3 are shown in Table 6.1.

The values of Re_ϕ and G imply that both areas fall into Regime IV of Daily and Nece's [38] definitions; turbulent flow ($Re_\phi > 10^5$) with a large gap ratio ($G > 0.05$). Both areas have $\lambda_T < 0.22$ meaning that the character of the local flow is dominated by the swirl component of velocity, and have some identifiable core. The lower value of λ_T in Area

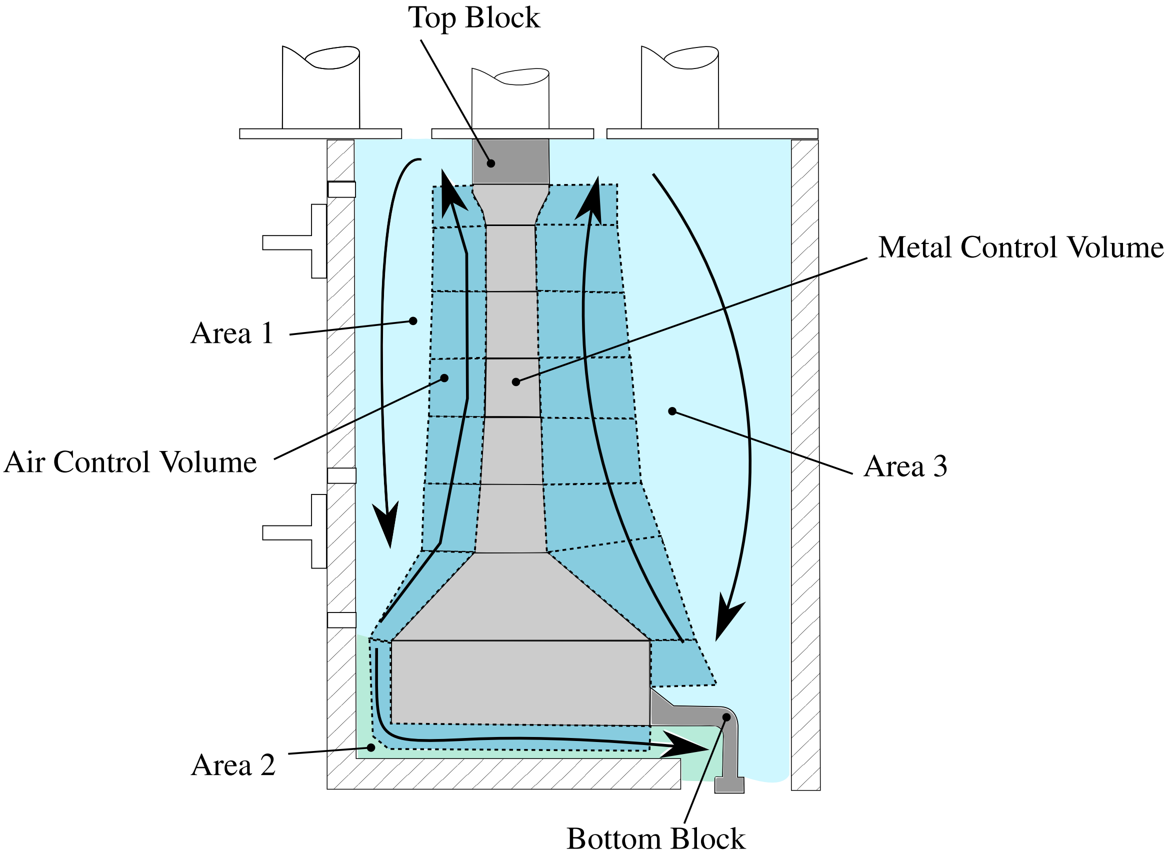

Figure 6.5: Schematic of the disc as modelled in the grey-box method. This shows the 3 aerodynamic regimes (light blue) and 1 of the 16 air control volumes (dark blue). The 8 metal control volumes (light grey) are numbered $1 \rightarrow 8$ starting from the inner radius. The Bottom Block and Top Block (dark grey) correspond to metal control volumes 0 and 9 respectively, but are modelled differently to the 8 disc volumes.

Parameter	Area 1	Area 3
$Re_\phi(\times 10^{-6})$	$2.0 \rightarrow 10$	$2.0 \rightarrow 10$
G	~ 0.12	~ 0.9
$C_W(\times 10^{-3})$	$7.0 \rightarrow 18$	$19 \rightarrow 61$
λ_T	$0.048 \rightarrow 0.059$	$0.15 \rightarrow 0.17$
β	$0.1 \rightarrow 0.5$	$0.2 \rightarrow 0.36$

Table 6.1: Range of non-dimensional numbers present on the front and back side of the disc.

1, as compared to Area 3, also implies that a great amount of air is entrained at the stator surface, which causes the greater value of β.

Area 2 corresponds to two very different flow regimes, firstly a rotor-stator system with negative superposed flow, and then a concentric rotating shaft cavity. Both have a very small clearances compared with the other areas, which suggests that heat would be exchanged more readily between the surfaces (i.e. windage would be high). It was attempted to model this region with two air volumes to match the two regimes, however the model suffered from severe feedback issues when working with the conduction model. As such, this area uses the same relations as for Area 1, but with an added correction factor as explained below.

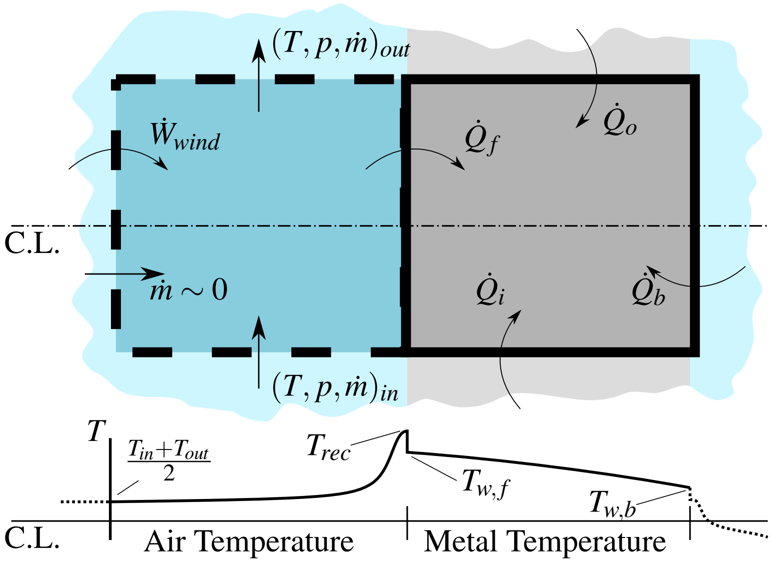

Figure 6.6: Heat transfer around adjacent air and metal control volumes. The temperature profile along the centre line (C.L.) is shown at bottom. Heat subscripts are $f = front$, $b = back$, $o = outer$ and $i = inner$.

6.4.2 Heat Transfer to the Disc

Consider again the control volumes representing the juxtaposed air and metal blocks, and particularly the axial temperature profiles as shown in Figure 6.6. A control volume of air for the rear side would mirror that shown for the front. The model assumes mass continuity for the air flow through each air volume. It also assumes that at each discrete time step each volume exists in some quasi-steady state for energy flow, both internally and between neighbouring volumes. For this analysis, the equation for the moment co-efficient of a disc in Regime IV is;

$$C_M = 0.0510 G^{\frac{1}{10}} \mathrm{Re}_{\phi}^{-\frac{1}{5}} \tag{6.4}$$

while the Reynolds Analogy allows the disc Nusselt number to be expressed as;

$$\mathrm{Nu} = \chi \, \mathrm{Pr} \frac{\mathrm{Re}_{\phi} C_M}{\pi} \tag{6.5}$$

In this case, χ is a correction factor for heat flux and is $\sim \mathrm{Pr}^{-\frac{2}{3}}$ as identified by Owen and Rogers [102]. These values are for the disc average, but we assume that we can choose them to be applicable to local conditions as well by using local Reynolds number, calculated as $\mathrm{Re}_{\phi,r} = \rho \Omega r^2 / \mu$. We gather the terms as;

$$\mathrm{Nu} = 0.051 \frac{\chi \, \mathrm{Pr}^{\frac{1}{3}} G^{\frac{1}{10}}}{\pi} \mathrm{Re}_{\phi,r}^{\frac{4}{5}} \tag{6.6}$$

For the purposes of fine-tuning, the model requires a built-in local correction factor which is introduced as $\psi_{f,n}$ where f is for front side (Area 1) which could also be replaced with b for back (Area 3) and n is the block number. By introducing individual values of $\psi_{f,n}$ into the Nu equation, they can absorb the values of the co-efficient, π, G, Pr and χ which are reasonably constant. Each value of $\psi_{f,n}$ is first estimated using these constants, but later can be fine-tuned by direct comparison with the SC03 results. Combining Eq. 6.6 with the definition $\mathrm{Nu} = hr/k_{air}$, a function for the local heat transfer co-efficient can be expressed as;

$$h_{f,n} = \psi_{f,n} \frac{\mathrm{Re}_{\phi,r}^{0.8} k_{air}}{r} \tag{6.7}$$

The bulk air temperature (T) for each control volume is assumed to be;

$$T = \frac{T_{in} + T_{out}}{2} \tag{6.8}$$

Then, to calculate the total local heat flux, the total relative temperature of the air at the disc surface $T_{0,ad}$ is required. This is given by the formula for recovery temperature;

$$T_{0,ad} = T + R \frac{\Omega^2 r^2}{2 c_{p,air}} (1 - \beta_{f,n})^2 \tag{6.9}$$

The recovery factor R is equal to 0.88 for a turbulent boundary layer [102]. The local core swirl ratio $\beta_{f,n}$ has been determined from SC03, which shows that $\beta_{f,n}$ is relatively constant for the range of Ω considered (with the exception of $\beta_{f,1}$, as corrected below). The total rate of heat flow from the air to the metal surface, using the known surface area $A_{f,n}$, becomes;

$$\dot{Q}_{f,n} = h_{f,n} A_{f,n} (T_{0,ad} - T_W) \tag{6.10}$$

Finally, in order to correct for the fact that Area 2 has a different flow regime to Area 1, the local correction factor $\psi_{f,1}$ references a look up table of values based on the spool speed that has been derived from study of the high fidelity simulations ($\psi_{f,1} = \psi_{f,1}(\Omega)$). This has not been applied generally as it was intended that the model could be developed with as little information available as possible. However, it is likely that using this approach would improve the overall result.

6.4.3 Energy Balance

The change in air temperature as it passes through the control volume uses the steady flow energy equation;

$$T_{out} = T_{in} + \frac{1}{\dot{m} c_p} \left(\dot{W}_{wind} - \dot{Q}_{f,n} \right) \tag{6.11}$$

where T_{in} and T_{out} static temperatures, are the windage ($\dot{W}_{wind}$) is calculated as;

$$\dot{W}_{wind} = \varepsilon_n \, \mathrm{Re}_\phi \tag{6.12}$$

The model uses a series of values for ε_n that have been determined heuristically, and shown in Figure 6.7. This equation is based on the assumption that the windage is proportional to Re, which showed the best results in simulations. It might appear that this relationship should be similar the equation for the moment coefficient (Eq.6.4) as this calculates the work done on the disc face, however there is no literature to support this when considering the placement of the control volume boundary. The windage is the work done by the far surface, but only as transferred through the intervening flow. Thus choosing a more complex relationship given the control volumes used in the present work has no basis.

The values of ε_n decrease steadily with radius, with the exception of $\varepsilon_{2,f}$. This anomaly is likely due to the local impingement of the flow on to the disc surface. The value of using the windage term, despite the simple approach, is expanded on in Section 6.8.5.

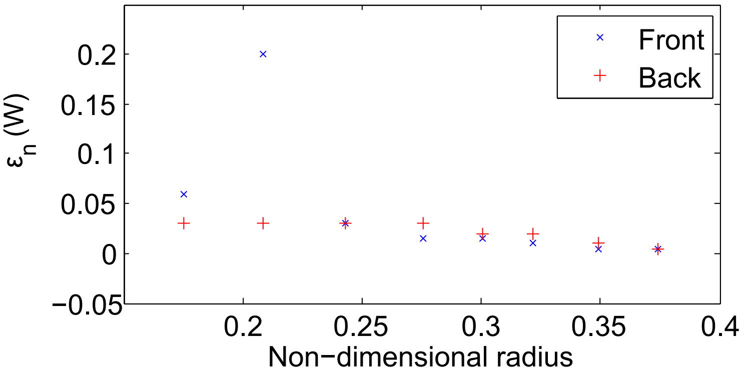

Figure 6.7: The windage correction factor for the front and back surfaces of the disc.

6.5 Modelling the Disc Metal Temperature

6.5.1 Lumped Capacitance

To model the disc temperature, the Conduction System uses a mixture of lumped capacitance models with approximate solutions to the heat equation. Lumped capacitance models are usually applied to situations where the Biot number $\mathrm{Bi} < 0.1$, implying that a solid's temperature can be modelled as uniform, and that the temperature is dominated by convection. For higher Biot numbers, such is the case for the disc modelling problem considered here (where $0.8 < \mathrm{Bi} < 1.3$), it is necessary to consider some transient conduction. This can be achieved using a polynomial approximation of the temperature profile in 1D cases, however generalising this to a 2D axisymmetric case proved to be more difficult. Instead, the model presented here separates the solutions for each of the axial and radial dimensions, by employing a quadratic approximation to the axial temperature profile (applied across a single block), and a linear approximation to the radial temperature profile (applied sequentially across multiple blocks). This effectively creates two overlaying 1D solutions rather than a continuous 2D solution. This approach was chosen as an optimisation between accuracy and computational efficiency, and justified by the observation that under steady state conditions (i.e. cruise) the temperature profile is very close to linear in both directions, and during transience the profile is close to quadratic.

6.5.2 Basic Method

When $\mathrm{Bi} < 0.1$, the temperature of a lump of metal can be modelled with a simple lumped capacitance approach as given shown in Chapter 3. The Top and Bottom Blocks have $\mathrm{Bi} \sim 0.2$, which is not low enough by traditional standards for modelling with the simple lumped capacitance approach, however, the relatively small time constant of these volumes compared with the rest of the model means that the relative errors are also small and do not contribute much to overall error of the simulation. As such, the Top and Bottom Blocks have been modelled assuming lumped capacitance via an LPV system approach as described in Section 6.6.

6.5.3 Improved Method

Each metal block represents a ring of material, and in selecting the dimensions of each volume it was noted that characteristic length of a ring with square sides is $L_C = w/2$, independent of the outer and inner radius. As such, choosing the height of each volume was governed by the need to have a low number of blocks overall and could not be exploited to improve the working Biot number. The forced convection rate around the disc means the volumes have Bi in the range of $0.8 - 1.7$. This means that it is important to model an internal temperature profile. The present analysis assumes that the radial and axial temperature profiles can be considered independently. (With the exception of the cob, this assumption appears to be validated by the results in Section 5.5.) This greatly simplifies the analysis, especially when the primary target of the model is to match volume average temperatures rather than point matching.

The rate of change of average temperature of each block is calculated using the lumped capacitance approach;

$$\frac{dT_{av}}{dt} = \frac{\dot{Q}_{net}}{mc_{p,metal}} \tag{6.13}$$

where $\dot{Q}_{net}$ is the sum of the convective heat flows $\dot{Q}_f$ and $\dot{Q}_b$, and the conductive heat flows $\dot{Q}_o$ and $\dot{Q}_i$ (see Figure 6.6).

6.5.4 Axial Conduction

The axial temperature profile is fitted by assuming a parabolic curve of the form;

$$T_n = C_1 x_n^2 + C_2 x_n + C_3 \tag{6.14}$$

The three coefficients (C_1, C_2, C_3) require three equations. Assuming Fourier's Law at the surface, the temperature gradient at the front of each block is given by the local flux as:

$$\left.\frac{dT_n}{dx}\right|_f = -\frac{\dot{Q}_{f,n}}{A_{f,n}k_{metal}} \tag{6.15}$$

Which can similarly be applied at the back (‘b’) surface to give a second equation;

$$\left.\frac{dT_n}{dx}\right|_b = -\frac{\dot{Q}_{b,n}}{A_{b,n}k_{metal}} \tag{6.16}$$

The average temperature of the block can be enforced by integrating the temperature profile over the width of the block, providing the third equation;

$$T_{n,av} = \frac{C_1}{3}w_n^2 + \frac{C_2}{2}w_n + C_3 \tag{6.17}$$

6.5.5 Radial Conduction

The model assumes a linear temperature profile between adjacent blocks to simulate the rate of heat conduction in the radial direction. The calculation uses a linearised form of Fourier’s Law;

$$\begin{aligned} \dot{Q}_{o,n} &= k_{metal}A_c\left(\frac{T_{av,n+1} - T_{av,n}}{r_{n+1} - r_n}\right) \\ \dot{Q}_{i,n} &= k_{metal}A_c\left(\frac{T_{av,n} - T_{av,n-1}}{r_n - r_{n-1}}\right) \end{aligned} \tag{6.18}$$

where $T_{av,n}$ is the average temperature of Block n as calculated by the lumped capacitance model, r_n is the midpoint radius of each volume and A_c is the relevant cross-sectional area between them.

6.6 Modelling the Cooling Flows

6.6.1 Overview of the Input System

The Input System uses a number of methods to model the 16 local parameters (see Figure 6.8) based on the measured upstream conditions; the compressor exit temperatures (T_{26}, T_{30}) and pressures (p_{26}, p_{30}). The inlet air pressures are interpolated from 1D look-up tables that correlate between p_{26}, p_{30} and local conditions. Mass flows rates are interpolated from look-up tables based on Ω and alt (similar to that shown in Table 6.2). These instantaneous changes with respect to upstream conditions are considered practical as the time constants related to changes in mass flow rate and pressure are much smaller than those associated with the temperature of the disc.

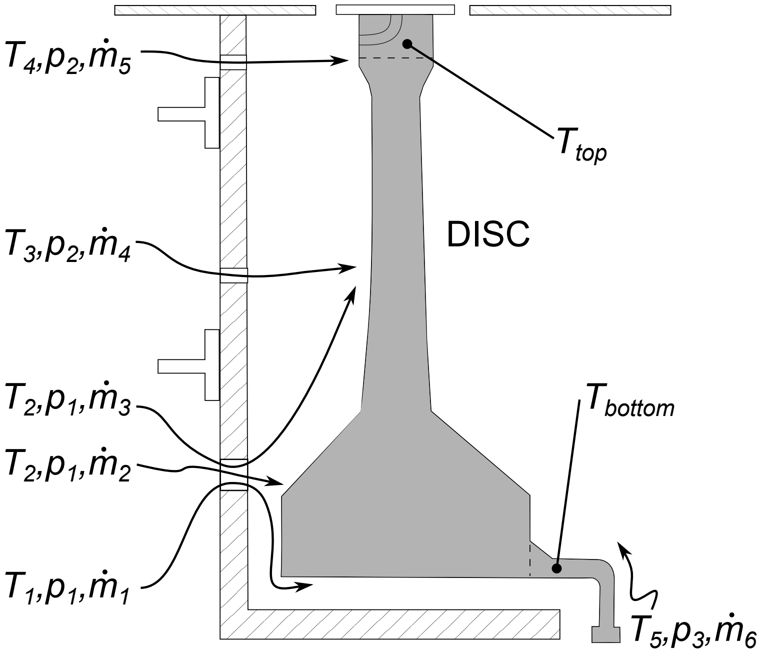

Figure 6.8: The local conditions that have been modelled by transfer functions. $T_2 \rightarrow T_5$ represent the temperature of the air as it enters the local inlets. On the other hand, T_1 represents the temperature of the air directly at the cob surface at the point shown, as this is the only temperature needed on this flow path.

6.6.2 System Identification

The temperatures of the air inlets, and top and bottom blocks have been identified using the quasi-LPV frozen value approach as used previously. The parameter vector is still defined as $\theta = \theta(\Omega, alt)$, and the form of the transfer functions have been trialled as both first order transfer functions,

$$G_i(s) = \mathrm{k}(\theta)\frac{1}{s+\mathrm{p}_1(\theta)} \tag{6.19}$$

and second order transfer functions with a zero,

$$G_i(s) = \mathrm{k}(\theta)\frac{s+\mathrm{z}(\theta)}{(s+\mathrm{p}_1\theta))(s+\mathrm{p}_2(\theta))} \tag{6.20}$$

where $G_i(s)$ represents the transfer function between the most relevant measured input ($u_i \in \{T_{26}, T_{30}\}$) and the corresponding local temperature inlet to the disc well (y_i). The most appropriate form of the function was chosen by inspection of the results as discussed in Section 6.6.3. To identify $G_i(s)$, SC03 data is gathered for three step cycles starting at ground idle conditions. The step down portioned is required because the time constant associated with heating is much shorter than that for cooling, and this is used to verify the transient parameters of the ground idle conditions. For each step the conditions are held long enough to achieve steady state, and the step can be considered instantaneous for practical purposes. Steady state data has also been taken at three cruise conditions.

Transient Conditions	Ω (rad/s)	alt (kft)
Maximum Take-Off	915.0	0
Reacceleration	889.2	36
Reacceleration	883.6	38
Ground Idle	519.6	0

Steady State Conditions	Ω (rad/s)	alt (kft)
Cruise	840.8	36
Cruise	832.4	38
Cruise (Low Hold)	788.9	1.5

Table 6.2: The operating points used in the ‘frozen value’ training data.

System identification is performed using the optimisation;

$$\begin{aligned} &\underset{\mathrm{k},\mathrm{p}_1\ldots\mathrm{p}_n,\mathrm{z}_1\ldots,\mathrm{z}_m}{\text{minimise}} && e \\ &\text{subject to} && e = \frac{1}{N}\sum_{i=1}^{N}\big(G(s)u(t_i) - y(t_i)\big)^2 \end{aligned} \tag{6.21}$$

The following 7 parameterised transfer functions have been found (see also Figure 6.8);

$$\begin{aligned}
G_1(s) &= \tfrac{T_1}{T_{30}} & G_6(s) &= \tfrac{T_{top}}{T_{HP3}} \\
G_2(s) &= \tfrac{T_2}{T_{30}} & G_7(s) &= \tfrac{T_{bottom}}{T_{26}} \\
G_3(s) &= \tfrac{T_3}{T_{HP3}} & & \\
G_4(s) &= \tfrac{T_4}{T_{HP3}} & {}^{*}T_{HP3} &= \tfrac{T_{26}+T_{30}}{2} \\
G_5(s) &= \tfrac{T_5}{T_{26}} & &
\end{aligned} \tag{6.22}$$

Using this methodology each $G_i(s)$ was identified with the corresponding k,p_1,p_2,z at three values of *alt* and seven values of Ω. Although the dynamics of the relationship between the measured inputs and the relevant output variables are non-linear, they are smooth and so are amenable to the interpolation approach, allowing us to form interpolation tables shown in Table 6.3 and Table 6.4.

k	alt_1	alt_2	alt_3
Ω_1	X	i	i
Ω_2	X	i	i
Ω_3	i	i	X
Ω_4	i	X	i
Ω_5	i	i	X
Ω_6	i	X	i
Ω_7	X	i	i

Table 6.3: Distribution of scaling factors (k) as found from the simulation data. 'X' marks data points, 'i' marks points that have been interpolated from that data.

p,z	alt_1	alt_2	alt_3
Ω_1	X	X	X
Ω_5	i	i	X
Ω_6	i	X	i
Ω_7	X	i	i

Table 6.4: Distribution of poles and zeroes (p_1,p_2,z) as found from the simulation data. 'X' marks data points, 'i' marks points that have been interpolated from that data.

6.6.3 Function Comparison

In general, the gain (k) was found to vary by $1\% \rightarrow 8\%$ for all combinations of Ω and *alt*. The exception was at ground idle conditions where there is comparatively lower spool speed and HTCs which lead to scaling factors that can be up to 40% different. This would have caused significant errors in interpolating the map when flying at low spool speed, even at high altitude, so the steady state data for a low altitude hold pattern (Ω_2,alt_1) was included to create a buffer between the ground idle state and high altitude cruising.

The accuracy of the higher order transfer function used to model an entire flight profile is shown in Figure 6.9. It was found that the second order transfer function can more accurately predict the transient response in a step cycle, however, when considered over an entire flight profile, the model had larger spikes in error under the most extreme conditions. This is due to the zero which makes the model sensitive to the rate of change of conditions prior to a step taking place. As the overall accuracy did not improve noticeably, the final model uses only first order transfer functions as they were considered sufficiently accurate yet computationally faster.

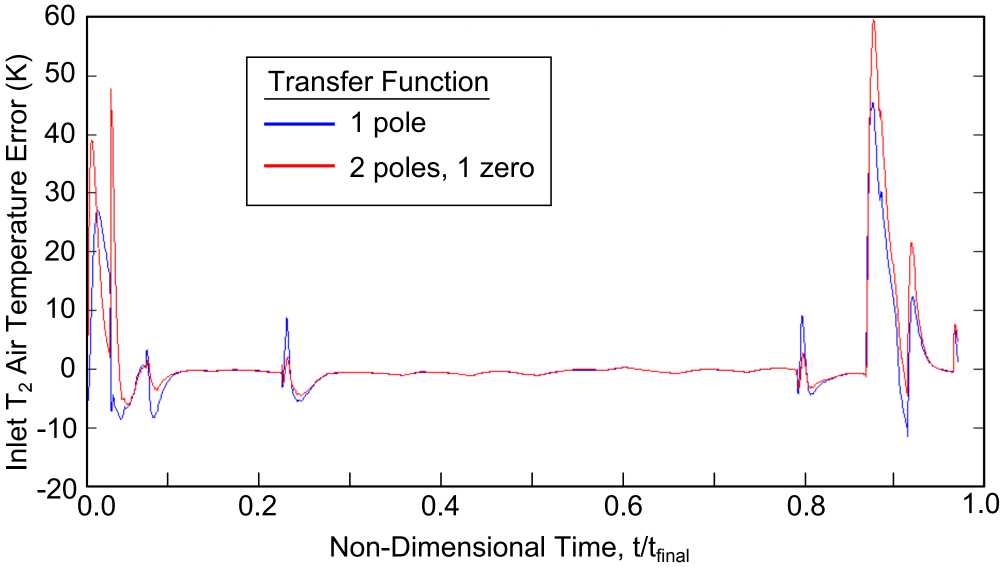

Figure 6.9: Comparison of transfer function identified for modelling the input system. The blue line uses a single pole transfer function, and the red uses two poles and a zero.

6.7 Final Model Structure

The overall model architecture is constructed from the three basic subsystems as shown in Figure 6.10. The precise number of blocks was chosen to satisfy criteria 1 of the model requirements, yet still provide some insight into the radial temperature variation. To recap, the three systems are as follows;

1. **Input System** (Inlet Blocks, Top Block and Bottom Block); each of these blocks take the “measured” input signal and use LPV functions to convert it to the local conditions. Each Inlet Block models a local air inlet, and the full model contains

four Inlet Blocks that relate to different delivery paths of the T_{26} and T_{30} air. (see Section 6.6)

2. **Air Flow System**; (Air Blocks) each block takes the local Flight Conditions and geometry data to calculate the total local convective heat transfer rate. These blocks work in tandem with the conduction model, exchanging $T_{0,ad}$ and q for T_w. (see Section 6.4)

3. **Conduction System** (Metal Blocks and Conduction Blocks); based on the modified lumped capacitance model, the Metal Blocks use the net heat flux to calculate the average temperature of each control volume. (see Section 6.5)

6.8 Validation and Discussion

6.8.1 Individual System Validation

Each of the three model subsystems; the Input System, Air Flow System, and Conduction System were individually validated against the SC03 data by isolating them from the other systems where possible. Isolation is straight forward for the Input System and it produces temperatures with $e_{rms} < 1K$. The e_{rms} for the Air Flow and Conduction Systems are shown in Table 6.5. The Air Flow System was isolated by feeding in the SC03 air data in place of the Input System, and the SC03 average block temperature data in place of the Conduction System, however the metal surface temperatures were allowed to vary naturally with the axial quadratic approximation. Similarly, the Conduction system was isolated by using the SC03 air temperature and relative total temperature in place of the Air System.

e_{rms} (K)	Block							
System	1	2	3	4	5	6	7	8
Air (front)	0.0*	19.6	19.5	16.4	8.7	11.9	14.3	12.7
Air (back)	6.5	9.7	8.1	8.5	7.7	7.6	7.8	7.8
Conduction	16.0	10.8	8.1	6.6	6.9	6.4	6.3	10.0

Table 6.5: Error generated in each of the air and metal blocks in the simulation. * Block 1 front air is modelled directly by the Input System.

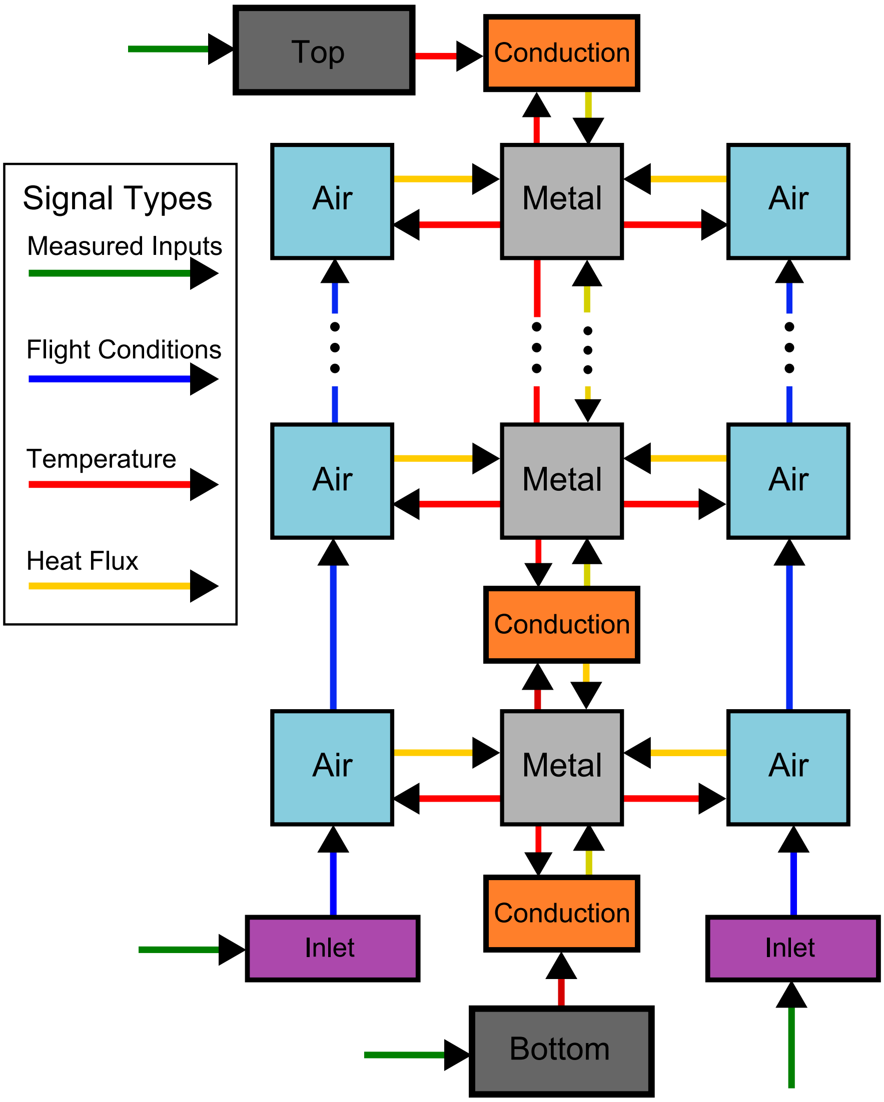

Figure 6.10: Overall breakdown of the grey-box model elements including data flow. The full model contains all 16 air volumes, and 8 metal volumes. Each element contains unique geometry information. Where air streams mix, fundamental mass and energy balances are used to resolve the final air conditions

6.8.2 Temperature vs. Time

The rest of the results shown here are for the full model. The primary objective is to match the disc's volume averaged temperatures. Figure 6.11 shows the average temperatures for the validation flight profile as calculated by the grey-box model, and Figure 6.12 shows the total error between this and the SC03 validation data. The errors are largest during transient periods, notably during the take-off and descent (5000*s* and 35 000*s* respectively). The transient error is largely due to the local temperature conversion in the Input System (as seen in Figure 6.9). The descent period is worse because the longer time constants associated with cooling augment the complex interactions of the real system, thus the error in assuming a first-order response is amplified. There are also far less training data used at near these conditions.

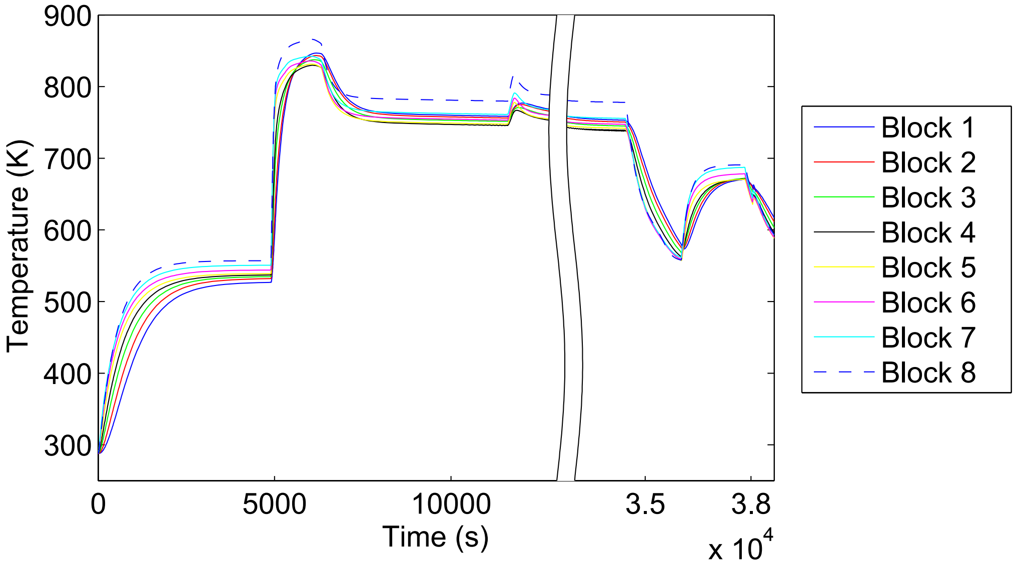

Figure 6.11: Simulation of the average metal temperature of the 8 metal volumes.

Metal Blocks 1 and 2 consistently have a the largest error in both transient and steady state. This is because the calculated heat flux into the "front" face of Block 1 has been averaged over a considerably larger area than for other volumes. The conduction between these two blocks is also problematic as noted in Section 6.8.3. The steady state error for blocks 3-7 starts positive and gets progressively more negative. Further analysis has shown that this pattern in steady state error occurs because each successive air volume decreases in temperature too much. This is particularly true on the front side because the windage correction has not been calibrated precisely (see Section 6.8.5). Block 8 is very accurate as it is tightly controlled by the adjacent Top Block (See also Figure 6.13). Block 1 doesn't receive the same influence from the Bottom Block because their shared conductive interface is much smaller relative to the size of the respective volumes.

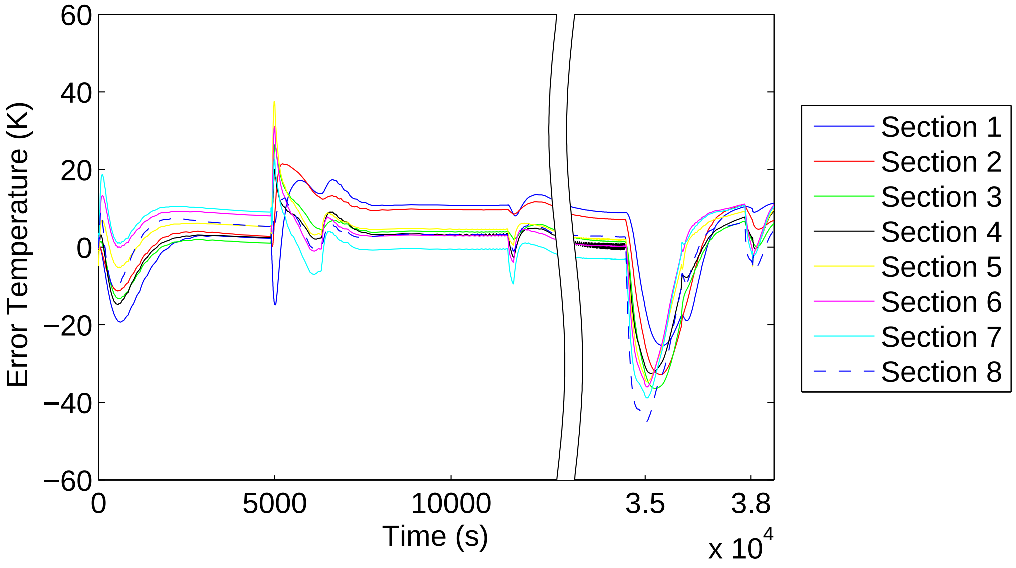

Figure 6.12: The error associated with the data in Figure 6.11. The greatest error occurs during the descent.

6.8.3 Temperature vs. Radius

Figure 6.13 is a representation of the disc's radial temperature profile as it transitions from SLS (a), through climb (b,c), and up to peak temperature (d). Whilst it is important to predict the overall temperature of these blocks, it is also important to accurately replicate the relative temperatures between adjacent blocks. This is because the temperature gradient is responsible for conduction and thermal stress calculations. As each data point on the line represents a block average temperature, the line itself gives an approximation of the gradient between blocks.

The temperature gradient ($\Delta T/\Delta r$) between blocks 1 and 2 is much greater in the transient cases than the in SC03 data. This suggests that the conduction between these blocks is not being modelled accurately, which in turn is likely to be distorting the temperature of blocks 3-7. Aside from the effect of the cob, Blocks 3-7 appear to capture much of the qualitative subtleties of the data profile.

6.8.4 Axial Temperature Profile

Figure 6.14 shows the axial temperature profile of Block 4 at difference stages of a step cycle from sea level conditions to MTO. The quadratic nature of the profile is evident in

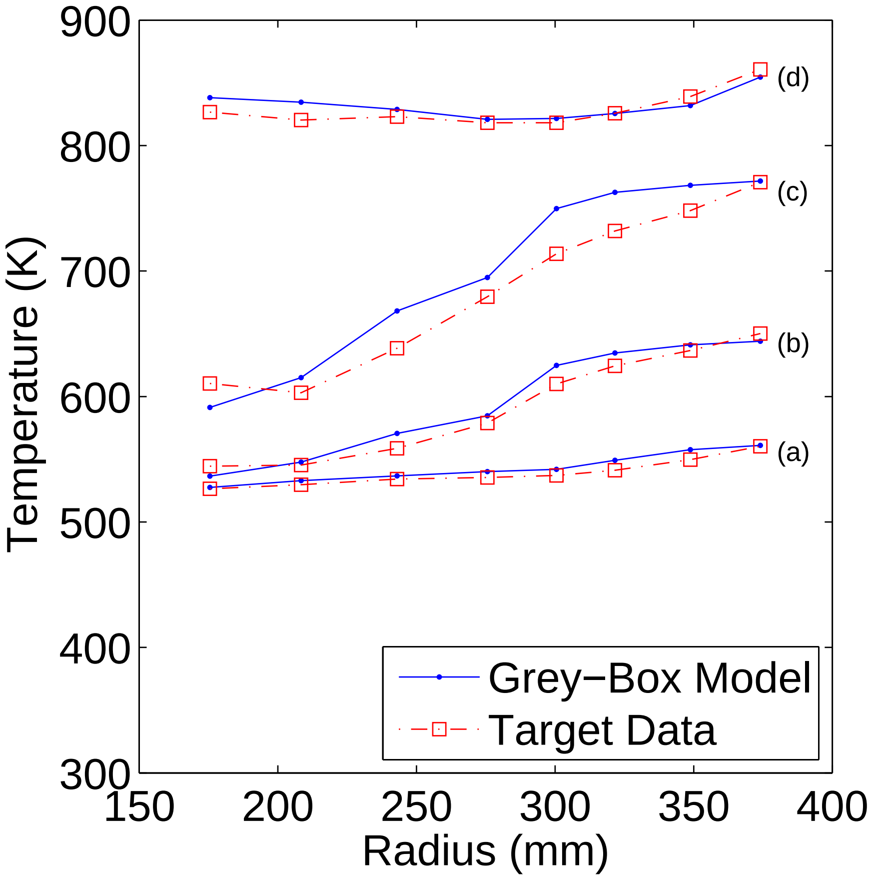

Figure 6.13: Radial temperature profile of the disc at different times. Data points mark the average temperature of each Block. Lines (a,b,c) represent stages in the transient period of take-off. Line (d) represents the near steady state case at peak temperature.

lines (b,c,d). Block 4 has been chosen for the example, although Blocks 3 to 8 show similar results. The steady state conditions, lines (a) and (e), match very well to the linear profile. The transient stages appear to capture the correct quadratic shape of the profile even if the average temperature is out by some near constant amount, most likely due to the error in modelling the cob and adjacent air system rather than the axial profile methodology.

It is well understood from the literature and experiment that the profile near the very surface of the metal can change very rapidly when observed over short periods of time ($< 2s$), such that the local temperature distribution follows an error function profile. However, capturing such detail is outside the scope of the current research, and unlikely to lead to large differences in the life consumption calculation.

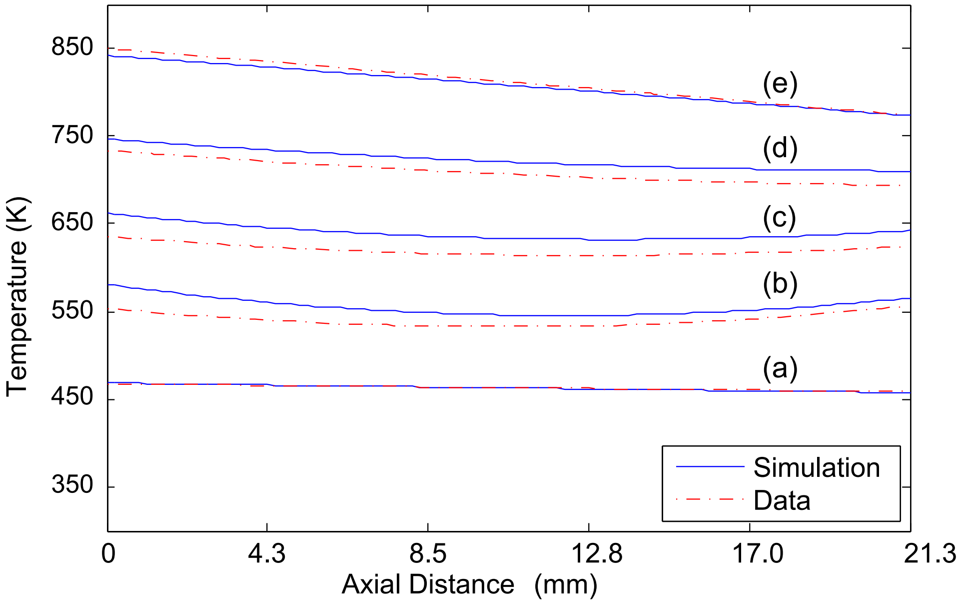

Figure 6.14: Axial temperature profile of Block 4 at different times through a SLS to MTO step profile. Lines (a) and (e) are steady state, while lines (b,c,d) are transient.

6.8.5 Effect of Windage Correction

It is instructive to consider the results of the simulation without the $\dot{W}_{wind}$ term. The average e_{rms} of the results shown in Figure 6.12 is $9.2K$. The error plot for the model without the windage correction function is shown in Figure 6.15, where average $e_{rms} = 26.8K$. The improvement caused by the windage correction appears to affect both the steady state and transient regions. Particularly, the improvement at the transient regions of take-off and descent are dramatic. This indicates that perhaps the corrections should be a function of more than just Re_ϕ. However, further work to correct this has not been explored as the LPV-SVD model was soon showing to be a much more promising methodology.

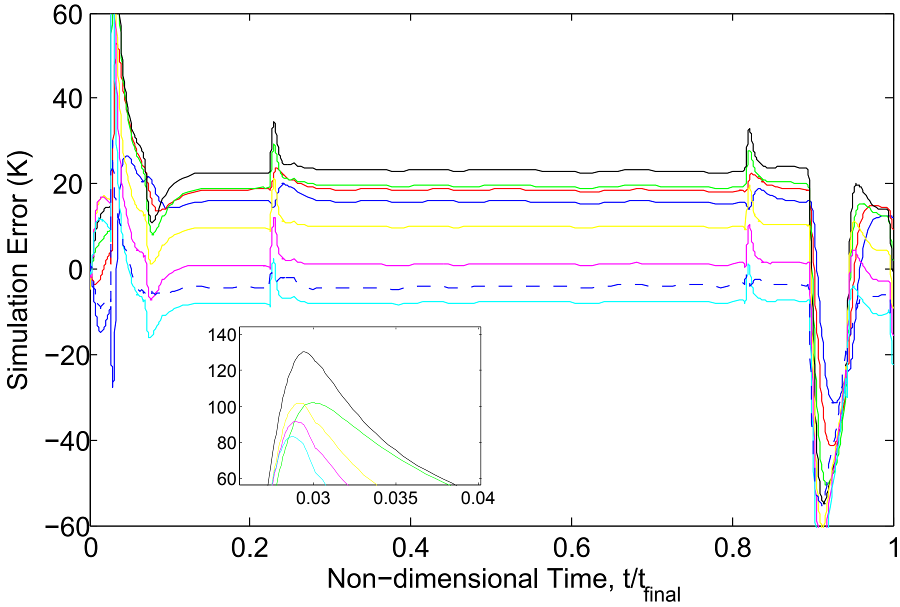

Figure 6.15: Error in the simulated model without the windage correction function. The colours match the key in Figure 6.11 and Figure 6.12. The insert shows detail of the peak at $t/t_{final} = 0.03$.

6.8.6 Compilation on a Real-Time Computer

The model has also been compiled on the NI PXIe-8115 Express Controller, and again successfully executed at $10kHz$, validating that it is suitable for execution online the FADEC system.

6.9 Comparison with LPV-SVD Model

6.9.1 Analogous Temperature Profiles

In order to compare the grey-box model with the LPV-SVD model, the data from the 121 points of the latter have been split into eight groups based on their location within the sections defined in the grey-box study. The average temperature of each volume was calculated by weighting each point with its radius in order to emulate the volume averaged temperatures. For section n that covers points from i to j, the average temperature of the section is calculated as;

$$T_{av,n} = \frac{\sum_i^j T_i \times r_i}{\sum_i^j r_i} \tag{6.23}$$

A comparison of the error for each model is shown in Figure 6.16, and snap shots of the radial temperature profile through take-off are shown in Figure 6.17.

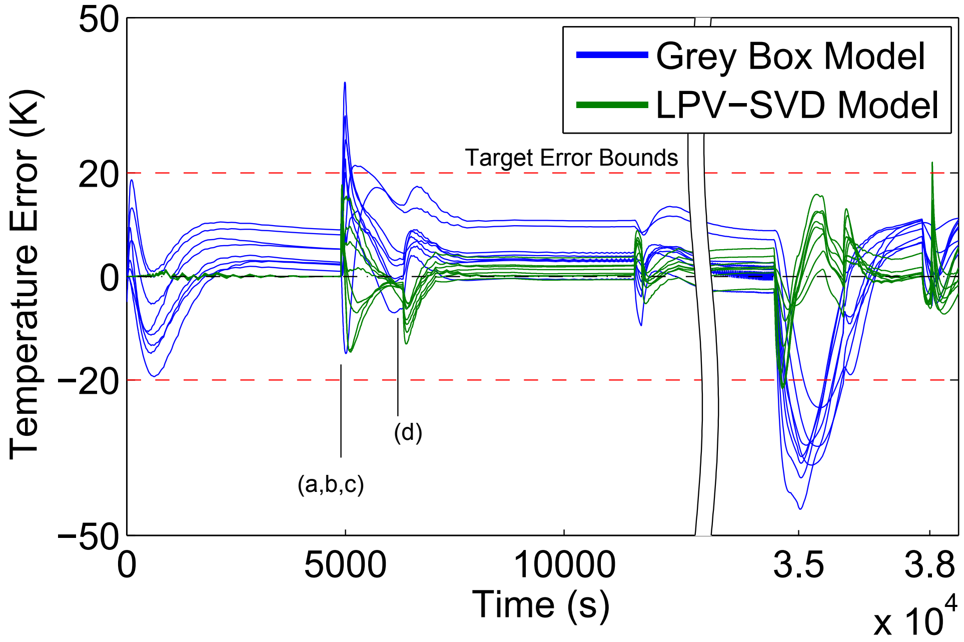

Figure 6.16: Comparison of results from LPV-SVD model and the grey-box model. Points (a,b,c,d) are related to Figure 6.17.

It is immediately apparent from the two figures that the LPV-SVD model achieves a greater overall accuracy than the grey-box model. There is an improvement at both transient and steady conditions. There are four key features of the LPV-SVD model that leads to this improvement; (1) the temperatures have been averaged over many points, which helps to eliminate some variability, (2) the disc temperatures have been modelled directly, involving less equations and stacked approximations, (3) the use of both first and second order transfer functions (rather than just first) that captures greater subtlety in the thermal dynamics, and (4) the parameter identification had more training data to draw upon, which has also improved the interpolation near those points.

6.9.2 Methods Discussion

There are other advantages to the LPV-SVD method compared to the grey-box model. It doesn't require specialist knowledge of the disc well inlet conditions, the flow field surrounding the disc, the relevant non-dimensional parameters, or the metal and gas thermal properties. The LPV-SVD model requires far fewer calculations per time step, and thus is less computationally expensive. The LPV-SVD model has the added benefit that it can

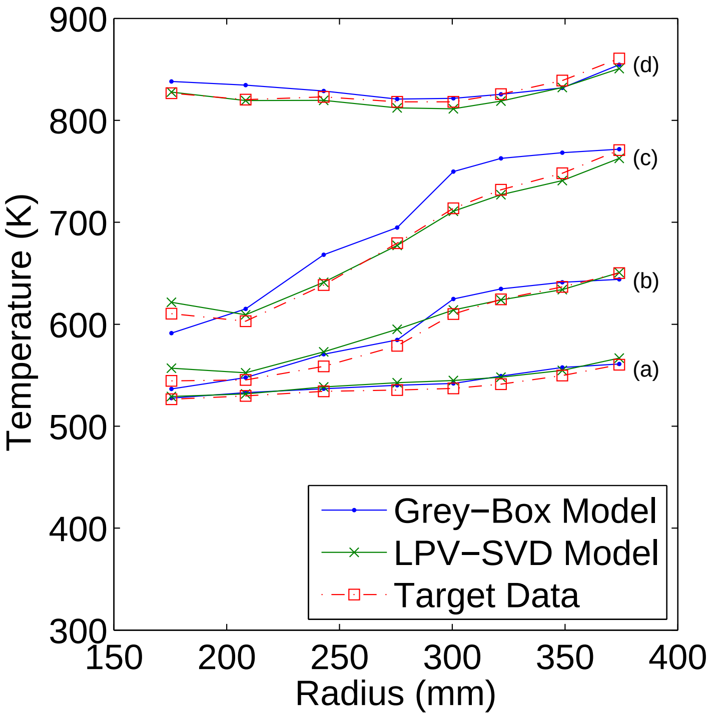

Figure 6.17: Radial temperature profiles from (a,b,c) start of take-off up to (d) peak temperature.

resolve greater detail with regard to the temperature distribution throughout the disc, particularly in the cob, which is a short-coming in the grey-box model. Finally, the LPV-SVD methodology is more generic and applicable to a wide range of components.

6.10 Conclusions

This chapter has presented a novel approach to modelling the temperature of a turbine disc using the standard existing measurement suite; the engine speed, atmospheric pressure and compressor exit temperatures and pressures. The model uses a combination of transfer functions and aerothermodynamic theory to evaluate the local air conditions in front of and behind the disc. It then uses lumped capacitance theory and simplified conduction models to simulate the average temperature of the disc for a multiple of discrete volumes such that both axial and radial profiles can be assessed. The model tracks the temperatures transiently and is able to predict steady state and transient temperatures to $\pm 20K$ for the majority of cases, except for at the start of take-off and in descent where the transient errors are up to 40K. The model computes at a speed consistent with the requirements for real-time simulation on an in-flight engine, and the example flight profile used for validation proves that the model architecture should be robust for application for an entire aircraft envelope. This approach, with some minor improvement, should allow the online tracking of thermal stresses so that the fatigue life of discs can be closely monitored in order to extend the lifetimes of both the discs and engines. However, the LPV-SVD model produces a temperature field with far greater resolution than the grey-box model can achieve. In a like-for-like comparison, the LPV-SVD model can predict average section temperatures to $\pm 20K$, better than the grey-box model. Overall, this study further supports that the LPV-SVD model is a robust and versatile methodology for an online monitoring system.

Chapter 7

Conclusions

7.1 Summary

This thesis has presented the design and commissioning of the Transient Heat Transfer Facility (THTF), a new facility capable of producing engine realistic test conditions. The test piece is representative of a full size HP turbine casing from a large civil engine. The test air has been successfully run at $13.5bar$ pressure, $770K$ temperatures and $1kg/s$ mass flow rates under test conditions. A preheat cycle has demonstrated that the test casing can be preheated with a controlled warm up of the facility, such that the average starting temperature is $526K$. This allows the facility to carry out up to two transient impingement tests of $10s$ each in a single experiment run at maximum conditions. More tests can be undertaken if intermediate conditions are also tested. It is predicted, with high confidence, that tests could be run at starting temperatures close to $670K$ if the SCA valves were used to their full capacity. The design life of the pressure vessel that houses the test casing is 20 000 cycles at maximum test conditions based on an extensive finite element analysis. Some buoyancy effects have been observed creating hot spots and temperature gradients in the test piece and vessel. It is known that these affects can be seen in the engine, however, as yet there has been no attempt to compare the Gr and Ra of the engine and the THTF. A non-dimensional analysis has shown that the SCA system should be successful and that a warm up rate of $25K$ in $5s$ can be achieved in the engine (Chapter 2).

The THTF has been designed specifically to investigate the SCA concept for tip clearance control. In support of this research, a new methodology called the LPV-SVD model has been developed for simulating the temperature distribution of engine components in online applications. The model uses singular value decomposition (SVD) to identify the dominant thermal modes, and a linear parameter varying (LPV) system to match those modes to a non-linear plant. The model needs only a small number of inputs, and these can be chosen from those that are already available in the engine measurement suite. It is based on an extensive review of the state-of-the-art literature on thermal modelling (Chapter 3).

The LPV-SVD model has been validated by applying it to the THTF. It has been constructed using 'frozen-value' quasi-LPV identification and raw data collected from the facility. Two models were produced, a split model where inner and outer measurements were considered separately, and a combined model where they were considered together. Each model demonstrated that it can reproduce experimental measurements to an accuracy of $\pm 30K$ near training data points, and $\pm 40K$ away from those points, using only a single thermal mode. The difference between the split and combined models appears to be minimal in this case. However, the split method does not correctly align the inner and outer temperatures, meaning that temperatures on the outer surface may exceed the inner surface in a physically impossible manner. This is avoided in the rank 1 combined model.

Using higher order modes would likely lead to a greater accuracy. However, there have been a few difficulties in constructing the model from experimental data. The experiments have a limited supply of air, which leads to reduced experiment time meaning that it is impossible to run the facility to steady state conditions under reasonable circumstances. Thus, the first spatial vectors contain modes characteristic of transient conditions rather than pure steady state conditions. This also makes it difficult to standardise the starting conditions of the step cycles. Finally, the PID control system that governs the heater would not be present in a real engine, yet it is difficult to isolate it fully from the model data (Chapter 4).

The LPV-SVD model has been applied to an IP turbine disc based on SC03 simulations in order to overcome some of the control problems in the experiments. It also allows a greater access to broad range of operating conditions and trajectories. The input is based on the compressor exit temperatures and the parameter vector is based on the engine speed and pressure atmosphere. The final model is based on a rank 2 truncation of the SVD vectors and achieves an accuracy of $\pm 32K$ at point locations throughout the axisymmetric profile, with all but a few points performing to an accuracy of $\pm 20K$. Higher order vectors produce inconsistent spatial modes across different operating conditions, so they cannot be included in the quasi-LPV identification process. The model has been successfully compiled on a FADEC similar controller, which validates its suitability for online use.

Several methods for constructing a Kalman filter to support the LPV-SVD model of the disc have been presented. The filter selection procedure has shown that the measurement point for a filter is far more important than the operating conditions at which the filter is trained. Further, the measurement point should be chosen at a location that reflects the thermal dynamics of the disc on average. In this case, the point is chosen approximately halfway between the rim and cob. The filter allows the model to track an unknown flight trajectory that lies outside the original training data space to an accuracy of $\pm 30K$ (Chapter 5).

Finally, a novel approach to modelling the temperature of a turbine disc using a physics based model is presented. The model uses LPV functions to relate measured inlet temperatures to the relevant air temperatures in the disc cavities. The aerodynamics and heat transfer from the air to the disc are modelled using rotor-stator aerothermal theory matched to CFD simulations. It then uses lumped capacitance theory and simplified conduction models to simulate the average temperature of the disc for a multiple of discreet volumes such that both axial and radial profiles can be assessed. The model tracks the temperatures transiently and is able to predict steady state and transient temperatures to $\pm 20K$ for the majority of cases, except for at the start of take-off and in descent where the transient errors are up to 40K. This approach gives an accurate estimate of the temperature distribution both radially and axially, whilst being computationally efficient enough for real-time Engine Health Management implementation. However, the LPV-SVD model produces a temperature field with far greater resolution than the grey box model can achieve. Further, in a like-for-like comparison of volume averaged temperatures, the LPV-SVD model can predict average temperatures to $\pm 20K$ even through MTO, which suggests it is the superior model (Chapter 6).

7.2 Future Work

The THTF is continuing to be upgraded to both improve the delivery of hot air to the test section, and improve the resolution of the thermal measurements. Most recently, a flow deflector has been installed between the $900mm$ flange surface and the bullet to help reduce the residency time of the flow between the vessel inlet and the test section (see Figure 7.1). Early results have shown an improvement of 10°. It is possible that entire bullet section could be replaced with more engine representative geometry if it was deemed important.

Following on from the study of the convection in the outer annulus, considerations are being made on improving the insulation around the test piece in order to replicate the engine geometry here as well. New instrumentation is also being considered, with the installation of a laser measurement system on a circumferential traverse in the outer cavity for recording casing expansion. There has also been some investigation into IR camera

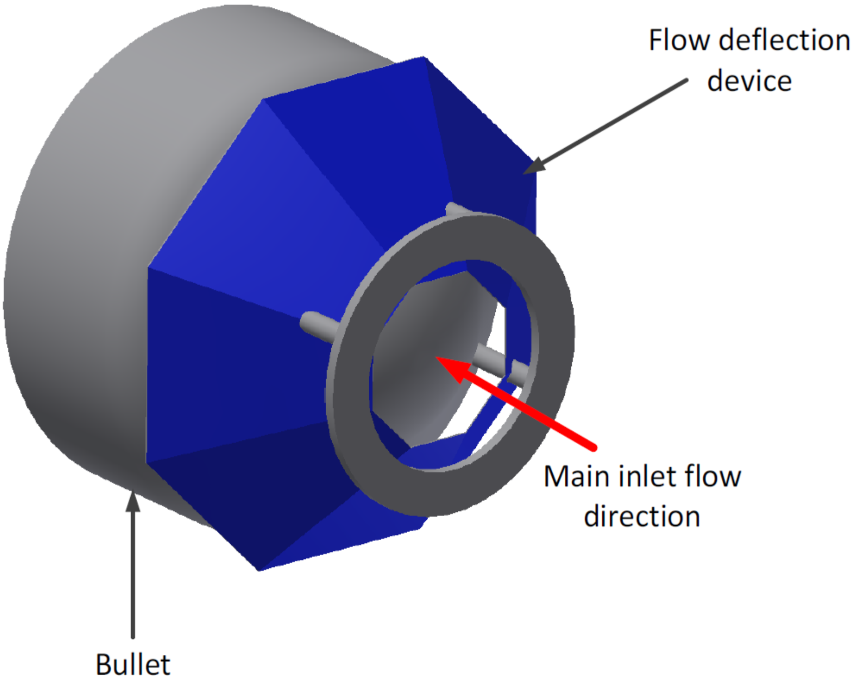

Figure 7.1: ‘Bullet’ with inlet flow deflector. Air entering the vessel in the direction of the red arrow, impacts the bullet and is deflected between the flow deflector device and the bullet to the annulus.

thermography. For such a camera to be installed, it needs to be housed within vacuum style pressure vessel to withstand the high pressure environment. A new set of impingement plates have been installed with circumferential variation, in order to trial multiple hole configurations at once.

The LPV-SVD model of the IP disc will be further investigated for use with a modulated air system. Based on experience, it is suggested that a third measurement, such as the valve opening angle, to be included in the parameter vector. Further, it is likely that SVD analysis will suggest extending the truncation to the third modes.

There are many improvements that could be made to the physics based model. It is likely that the inlets could be modelled more accurately with a second order approach if handled with greater care. However, principle focus should be on modelling the windage as accurately as possible, and creating a suitable 2D temperature distribution for the cob. The model would greatly benefit from a closer inspection of the available CFD and SC03 analysis, and focus less on generic empirical formulae.

Appendix A

Impingement Plate Design and Instrumentation

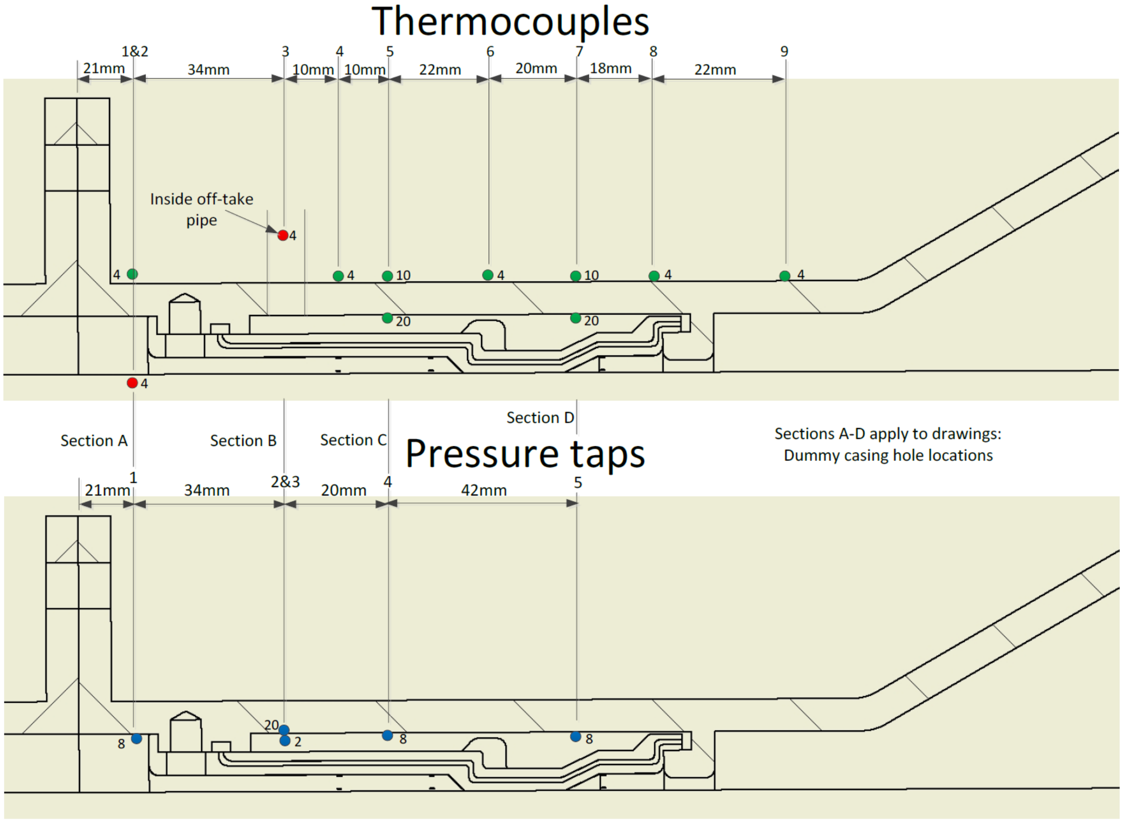

Figure A.1: Axial positions of the thermocouples and pressurement points.

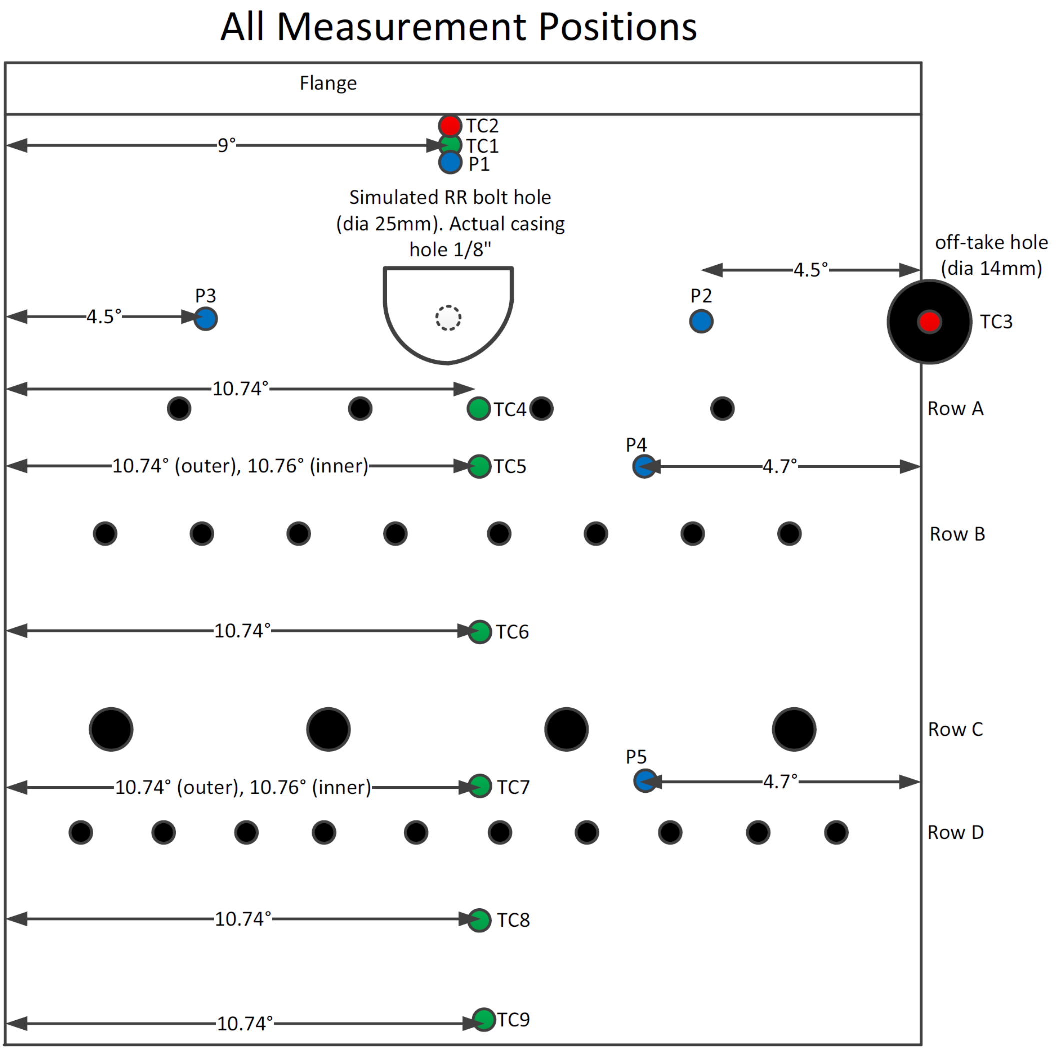

Figure A.2: Hole arrangement and approximate spanwise position of thermocouples and pressure measurements.

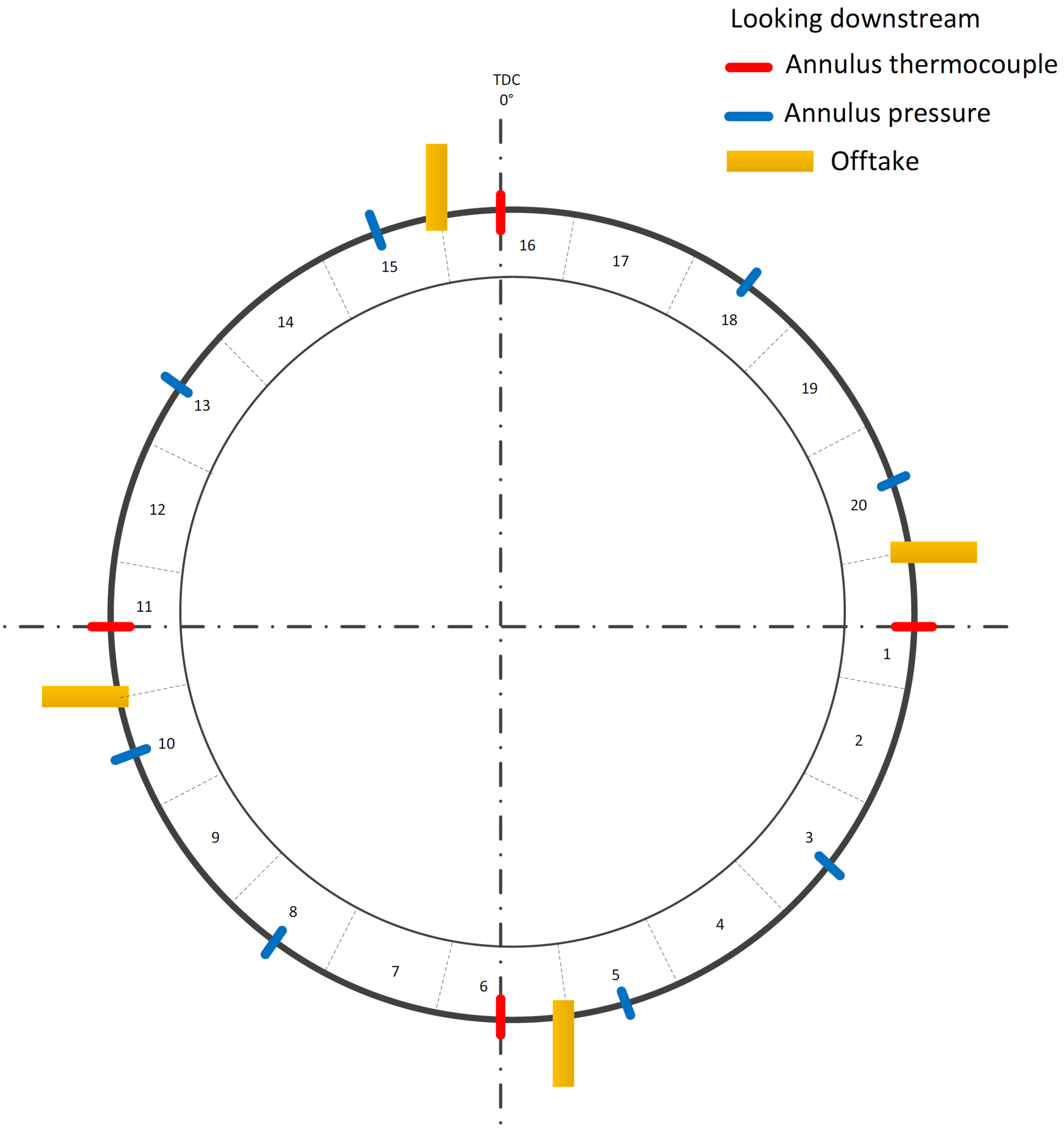

Figure A.3: Front view of all 20 plates in relation to the offtakes position.

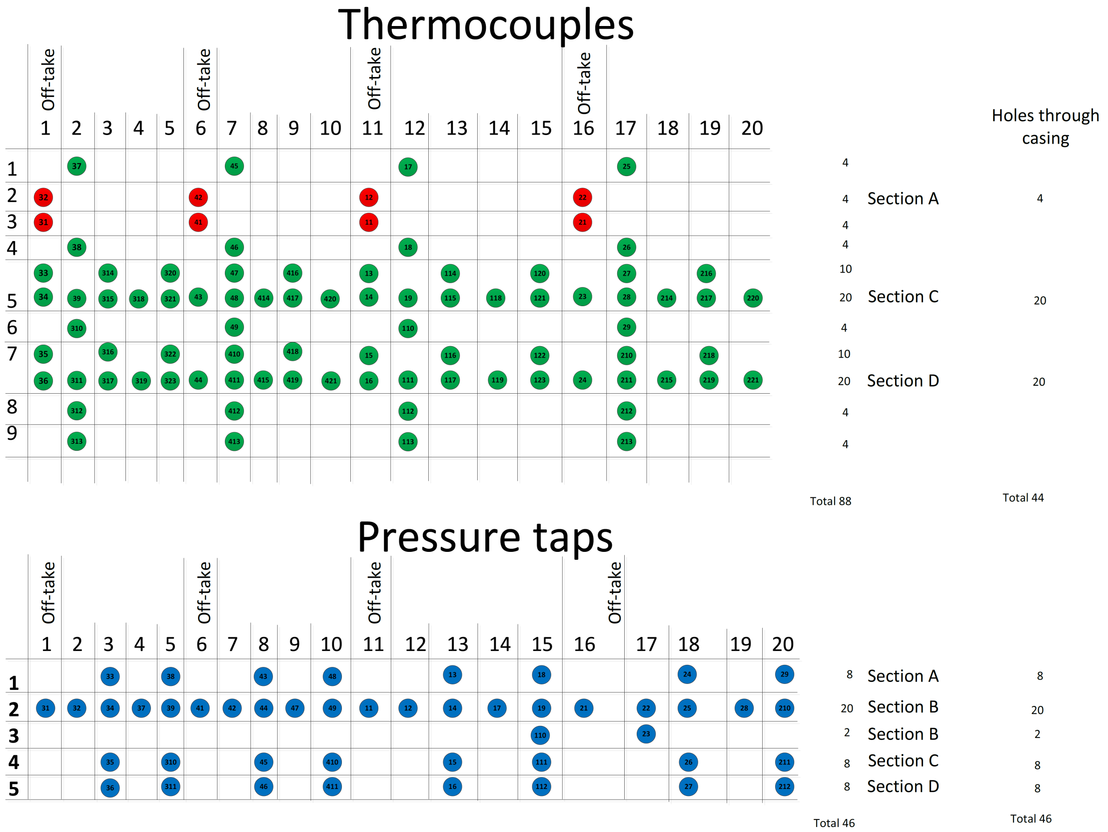

Thermocouples

	Off-take 1	2	3	4	5	Off-take 6	7	8	9	10	Off-take 11	12	13	14	15	Off-take 16	17	18	19	20			Holes through casing
1		37					45					17					25				4		
2	32					42					12					22					4	Section A	4
3	31					41					11					21					4		
4		38					46					18					26				4		
	33		314		320		47		416		13		114		120		27		216		10		
5	34	39	315	318	321	43	48	414	417	420	14	19	115	118	121	23	28	214	217	220	20	Section C	20
6		310					49					110					29				4		
7	35		316		322		410		418		15		116		122		210		218		10		
	36	311	317	319	323	44	411	415	419	421	16	111	117	119	123	24	211	215	219	221	20	Section D	20
8		312					412					112					212				4		
9		313					413					113					213				4		
																					Total 88		Total 44

Pressure taps

	Off-take 1	2	3	4	5	Off-take 6	7	8	9	10	Off-take 11	12	13	14	15	Off-take 16	17	18	19	20			
1			33		38			43		48			13		18			24		29	8	Section A	8
2	31	32	34	37	39	41	42	44	47	49	11	12	14	17	19	21	22	25	28	210	20	Section B	20
3															110		23				2	Section B	2
4			35		310			45		410			15		111			26		211	8	Section C	8
5			36		311			46		411			16		112			27		212	8	Section D	8
																					Total 46		Total 46

Figure A.4: List of all thermocouples and pressure tap positions for each of the 20 plates, including labels.

Appendix B

Pressure Vessel Material Design Strengths

Standard design strength of PN355NL1 and 316SS vs temperature as provided in OhmTech VVD [9]. The yield strength of the material is 1.5× the design strength.

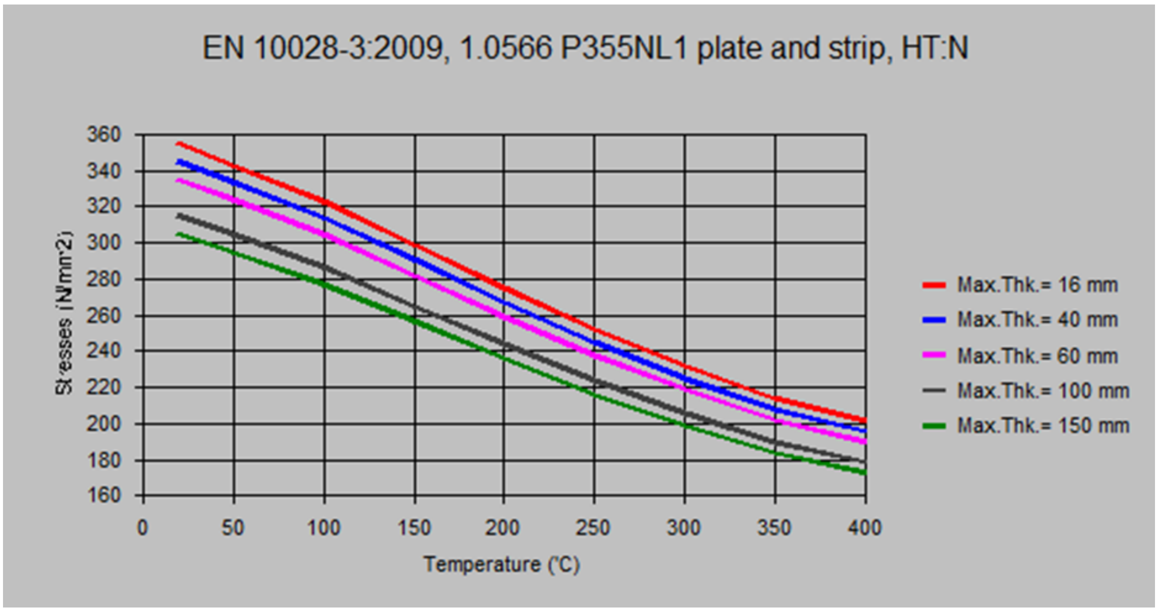

Figure B.1: Design strength vs temperature of PN355NL1.

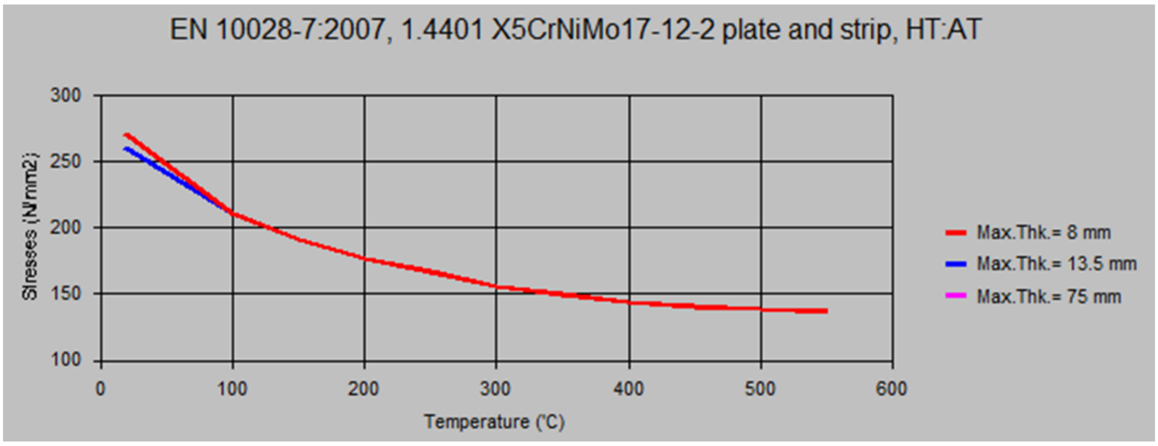

Figure B.2: Design strength vs temperature of 316SS.

Appendix C

Full Test Results

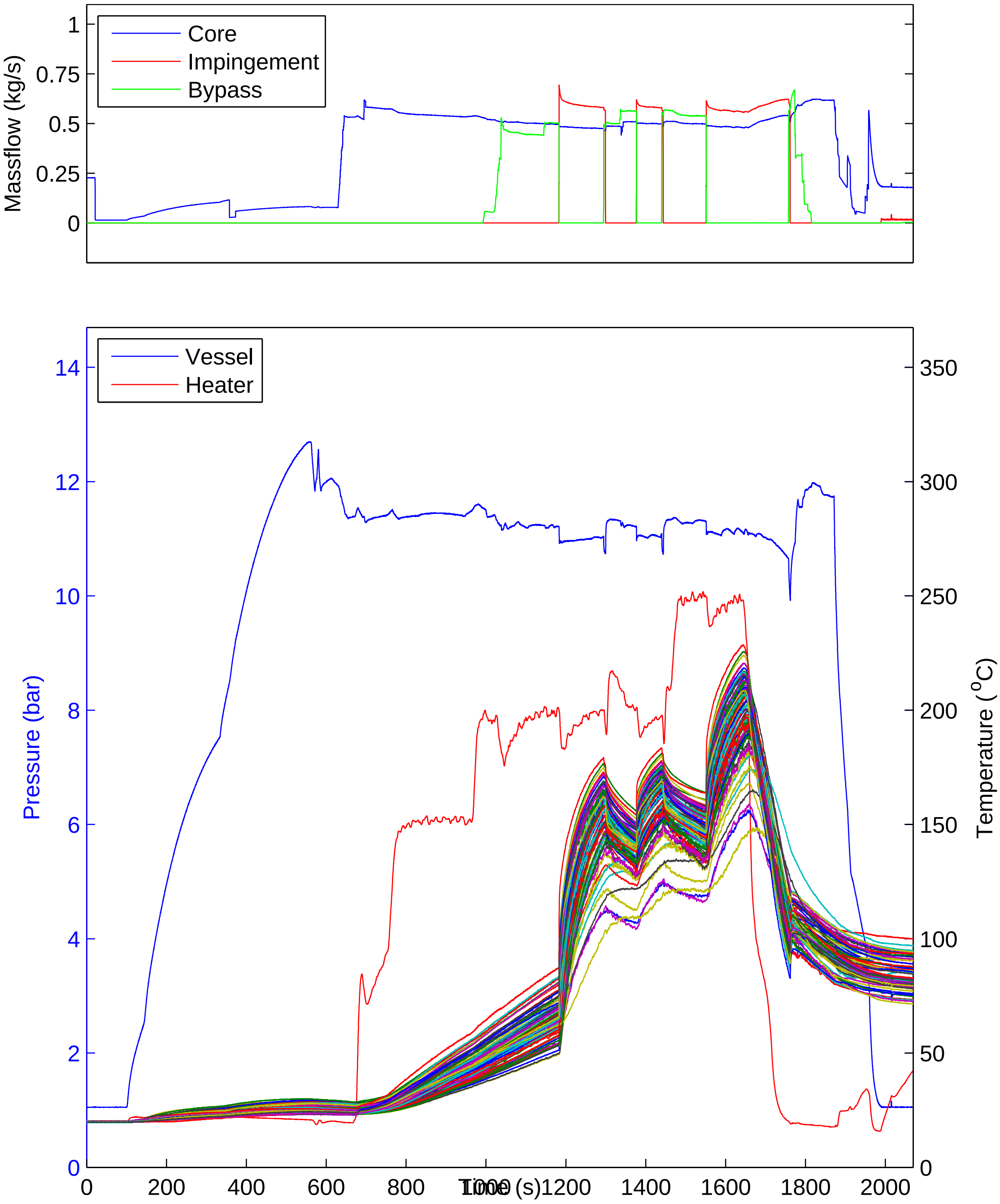

Figure C.1: Full Results for Test P.

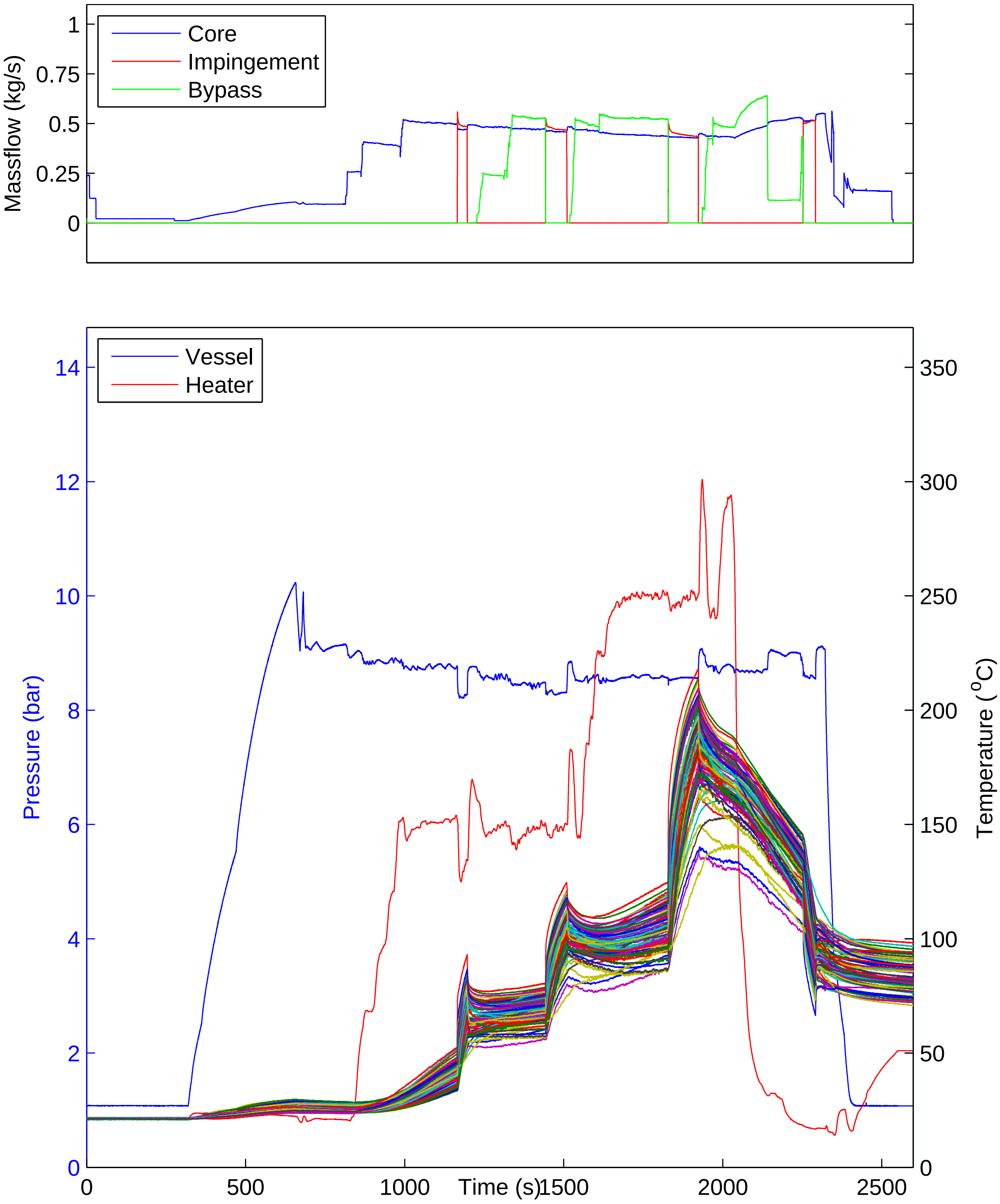

Figure C.2: Full Results for Test Q.

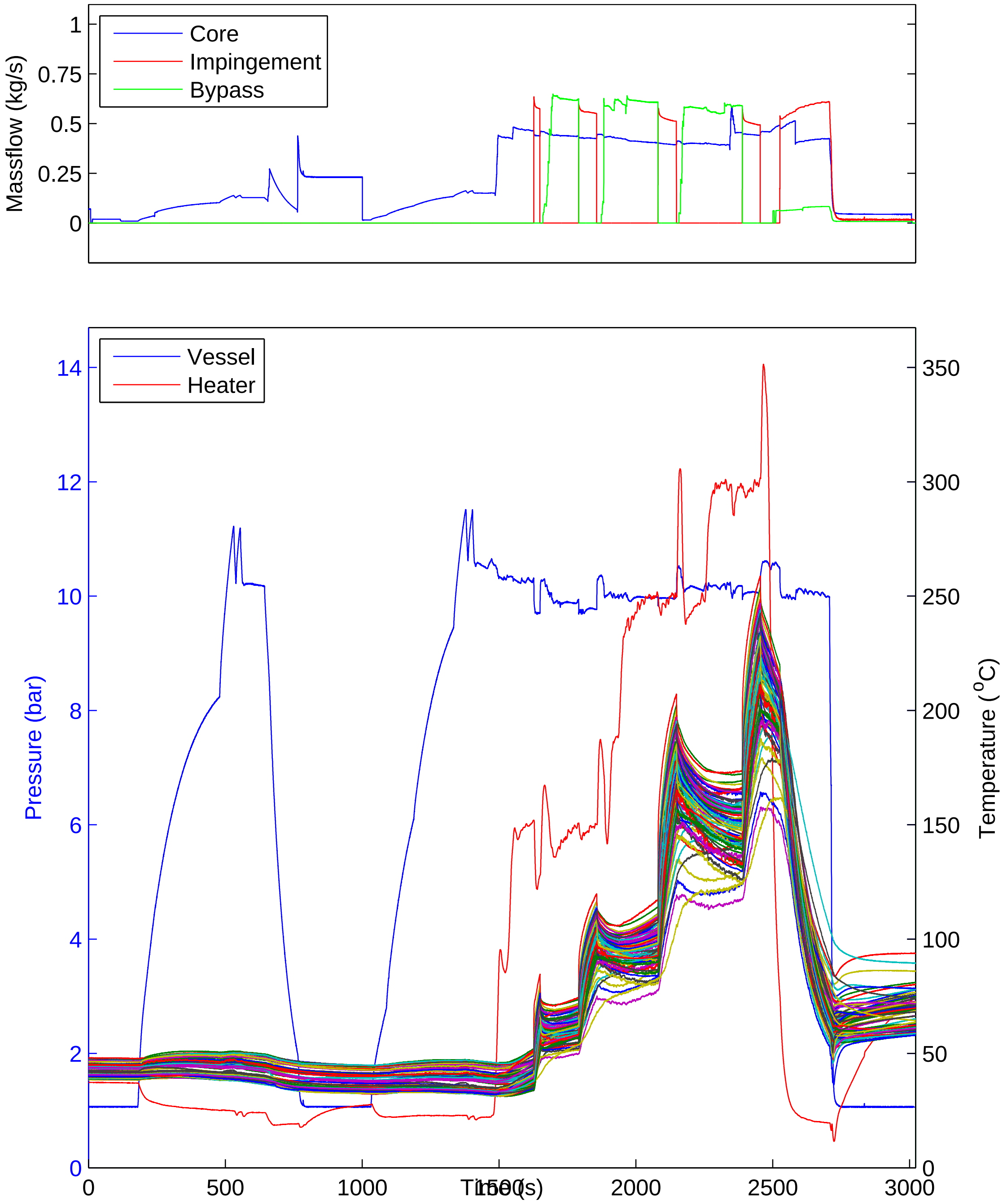

Figure C.3: Full Results for Test R.

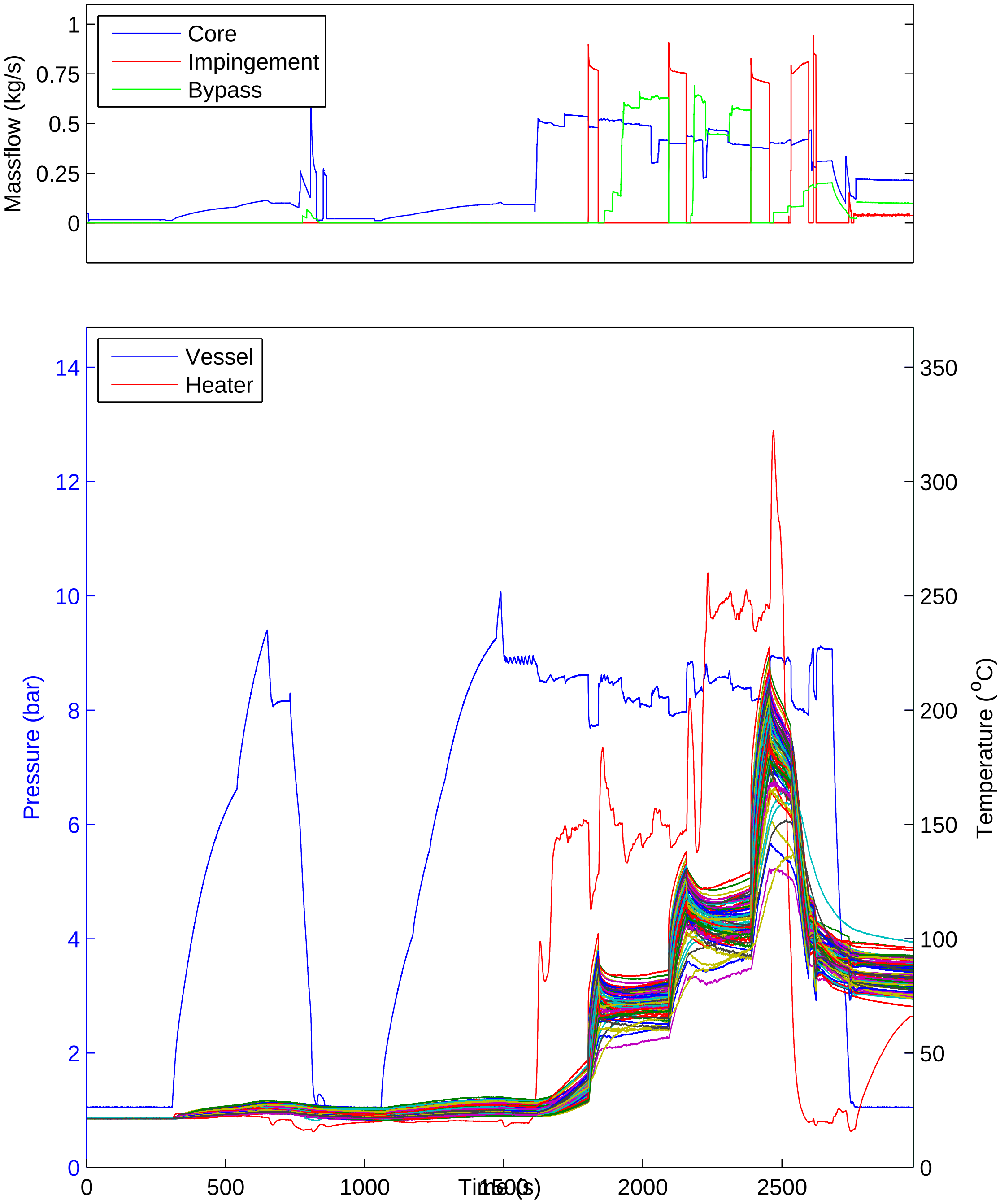

Figure C.4: Full Results for Test S.

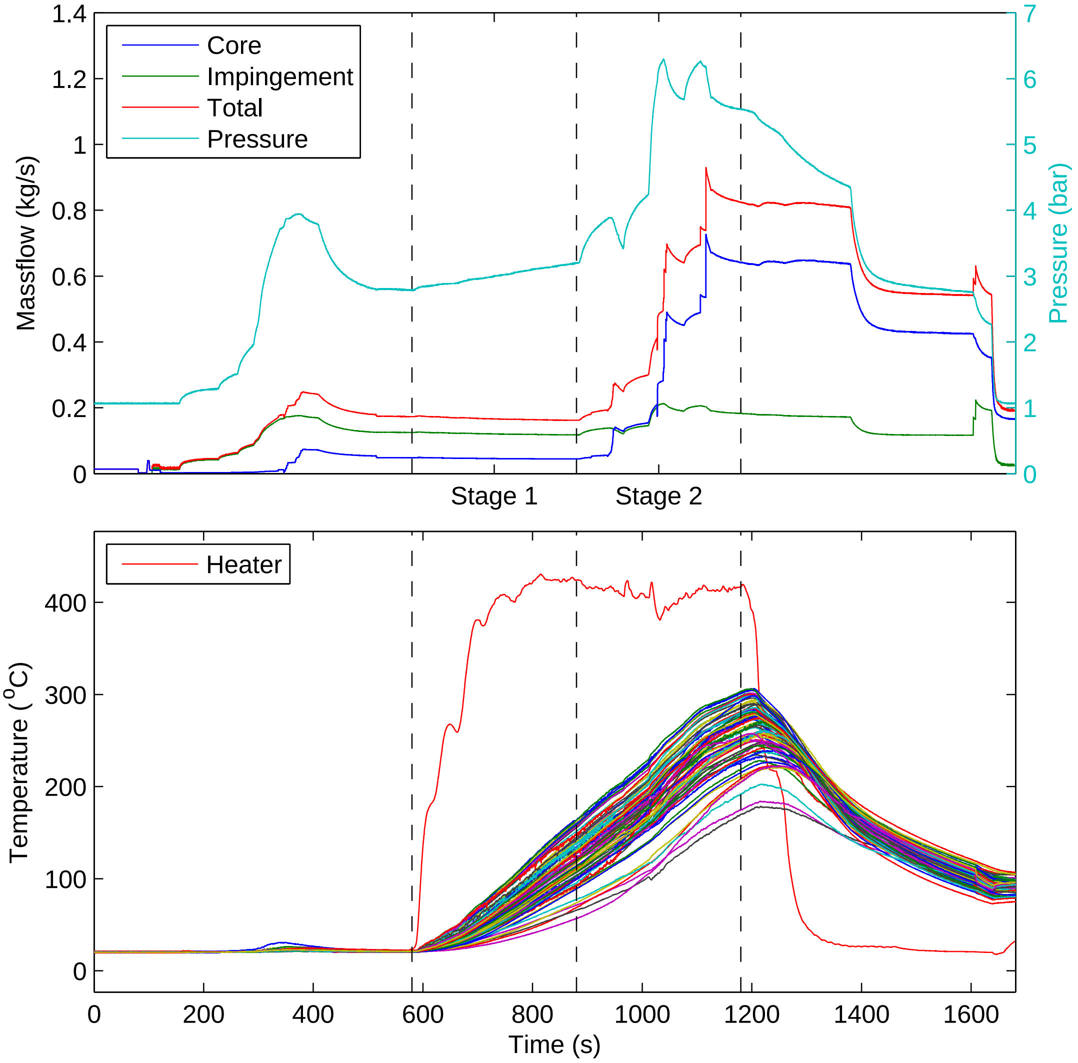

Figure C.5: Full Results for Preheating Test.

Bibliography

[1] Strategic Research & Innovation Agenda. Technical report, Advisory Council for Aviation Research and Innovation in Europe (ACARE), September 2012.

[2] Waleed Mohammed Abed, Amer Jameel Shareef, and Ahmed Ali Najeeb. Natural convection heat transfer in horizontal concentric annulus between outer cylinder and inner flat tube. *Anbar Journal for Engineering Sciences Natural*, 3(2):31–45, 2010.

[3] F.B. Ahmed, R. Tucholke, B. Weigand, and K. Meier. Numerical investigation of heat transfer and pressure drop characteristics for different hole geometries of a turbine casing impingement cooling system. In *Proceedings of ASME Turbo Expo 2011*, Vancouver, Canada, 2011.

[4] Dario Amirante, Nicholas J. Hills, and Christopher J. Barnes. Thermo-mechanical finite element analysis/computational fluid dynamics coupling of an interstage seal cavity using torsional spring analogy. *Journal of Turbomachinery*, 134(5):051015, 2012.

[5] Antonio Andreini, Riccardo Da Soghe, Bruno Facchini, Francesco Maiuolo, Lorenzo Tarchi, Torino To, and S Marta. Experimental and numerical analysis of multiple impingement jet arrays for an active clearance control system. *Journal of Turbomachinery*, 135(May 2013):031016, 2012.

[6] Pierre Apkarian and Pascal Gahinet. A convex characterization of gain-scheduled h controllers. *IEEE Transactions on Automatic Control*, 40(5):853–864, May 1995.

[7] Pierre Apkarian, Pascal Gahinet, and Greg Becker. Self-scheduled h_\infty control of linear parameter-varying systems: a design example. *Automatica*, 31(9):1251–1261, 1995.

[8] I. Armstrong and T. M. Edmunds. Fully automatic analysis in the industrial environment. In *Proceedings of the Second International Conference on Quality Assurance and Standards*, pages 74–84, Stratford-upon-Avon, May 1989.

[9] OhmTech AS. Ohmtech VVD, 2012.

[10] Air Transport Action Group (ATAG). The right flightpath to reduce aviation emissions. *UNFCCC Cop17*, (November):1–6, 2011.

[11] Omid Bagherieh, Karl Hedrick, and Roberto Horowitz. Nonlinear control of floating offshore wind turbines using input/ output feedback linearization and sliding control. In *Proceedings of ASME Turbo Expo 2014*, San Antonio, 2014.

[12] Gary J. Balas. Linear, parameter-varying control and its application to a turbofan engine. *International Journal of Robust and Nonlinear Control*, 12:763–796, 2002.

[13] Bassam Bamieh and Laura Giarré. Identification of linear parameter varying models. *International Journal of Robust and Nonlinear Control*, 12:841–853, 2002.

[14] Mark Baptista, Aditya Kumar, Brent Brunell, and Daniel Viassolo. Model-based life extending control for aircraft engines. In *AIAA 1st Intelligent Systems Technical Conference*, Chicago, September 2004.

[15] Paul F. Beard, Thomas Povey, and Kamaljit S. Chana. Turbine efficiency measurement system for the QinetiQ turbine test facility. *Journal of Turbomachinery*, 132(1):011002, 2010.

[16] G. Becker and A. Packard. Robust performance of linear parametrically varying systems using parametrically-dependent linear feedback. *Systems & Control Letters*, 23(3):205–215, 1994.

[17] Gregory Becker, Andy Packard, Doug Philbrick, and Gary Balas. Control of parametrically-dependent linear systems: A single quadratic lyapunov approach. In *Proceedings of the American Control Conference*, pages 2795–2799, San Francisco, 1993. IEEE.

[18] Gal Berkooz, Philip Holmes, and J.L. Lumley. The proper orthogonal decomposition in the analysis of turbulent flows. *Annual Review of Fluid Mechanics*, 25:539–575, 1993.

[19] Chongke Bi, Kenji Ono, Kwan-Liu Ma, Haiyuan Wu, and Toshiyuki Imamura. Proper orthogonal decomposition based parallel compression for visualizing big data on the k computer. *IEEE Symposium on Large-Scale Data Analysis and Visualization*, pages 121–122, 2013.

[20] F. D. Bianchi, R. J. Mantz, and C. F. Christiansen. Control of variable-speed wind turbines by LPV gain scheduling. *Wind Energy*, 7(1):1–8, 2004.

[21] Vedran Bobanac, Mate Jelavić, and Nedjeljko Perić. Linear parameter varying approach to wind turbine control. In *Proceedings of 14th International Power Electronics and Motion Control Conference (EPE/PEMC)*, pages T12–60 – T12–67, Ohrid, 2010. IEEE.

[22] D. Botto, S. Zucca, M.M. Gola, E Troncarelli, and G. Pasquero. Component modes synthesis applied to a thermal transient analysis of a turbine disc. In *Worldwide Aerospace Conference and Technology Showcase*, 2002.

[23] A.D. Boyd-Lee, G.F. Harrison, and M.B. Henderson. Evaluation of standard life assessment procedures and life extension methodologies for fracture-critical components. *International Journal of Fatigue*, 23, Supple(0):11–19, 2001.

[24] A.D. Boyd-Lee, D. Painter, and G.F. Harrison. Life extension methodologies and risk-based inspection in the management of fracture critical aeroengine components. Technical Report II, Manchester, October 2001.

[25] F. Bruzelius, C. Breitholtz, and S. Pettersson. LPV-based gain scheduling technique applied to a turbo fan engine model. *Proceedings of the International Conference on Control Applications*, 2:3–8, 2002.

[26] BSI. Specification for unfired fusion welded pressure vessels, 2012.

[27] Carl S. Byington, Michael J. Roemer, Matthew J. Watson, Thomas R. Galie, and Christopher Savage. Prognostic enhancements to diagnostic systems (peds) applied to shipboard power generation systems. In *Proceedings of ASME Turbo Expo 2004: Power for Land, Sea and Air*, volume 2, pages 825–833, Vienna, June 2004.

[28] Lance H. Carter and Jeff S. Shamma. Gain-scheduled bank-to-turn autopilot design using linear parameter varying transformations. 19(5), 1996.

[29] C. Changan, P.K. Liaw, M. Ye, and J. Yu. Recent developments in the thermomechanical fatigue life prediction of superalloys. *Journal of Metals*, 51(4), 1999.

[30] Myeonggeun Choi, Orpheas Tapanlis, Leo Lewis, Carlo Ciccomascolo, and David Gillespie. The effect of impingement jet heat transfer on casing contraction in a turbine case cooling system. In *Proceedings of ASME Turbo Expo 2014*, volume GT2014-267, Düsseldorf, June 2014.

[31] R.A. Cláudio, C.M. Branco, E.C. Gomes, J. Byrne, G.F. Harrison, and M.R. Winstone. Fatigue life prediction and failure analysis of a gas turbine disc using the finite-element method. *Fatigue & Fracture of Engineering Materials & Structures*, 27(9):849–860, September 2004.

[32] D. Coren, P.R.N. Childs, and C.A. Long. Windage sources in smooth-walled rotating disc systems. In *Proceedings of the Institution of Mechanical Engineers Part C-Journal of Mechanical Engineering Science*, volume 223, pages 873–888, April 2009.

[33] D.D. Coren, N.R. Atkins, J.R. Turner, D.E. Eastwood, S. Davies, P.R.N. Child, J.A. Dixon, and T.J. Scanlon. An advanced multiconfiguration stator well cooling test facility. *Journal of Turbomachinery*, 135(1):11003, 2013.

[34] Roy R. Craig Jr. and Mervyn C. C. Bampton. Coupling of substructures for dynamics analyses. *AIAA Journal*, 6(7):1313–1319, 1968.

[35] Nicholas Cumpsty. *Jet Propulsion*. Cambridge University Press, 2nd edition, 2003.

[36] Riccardo Da Soghe and Antonio Andreini. Numerical characterization of pressure drop across the manifold of turbine casing cooling system. *Journal of Turbomachinery*, 135(3):031017, 2013.

[37] J W Daily, V V Asbedian, and W D Ernst. *Enclosed rotating disks with superposed throughflow: mean steady and periodic unsteady characteristics of induced flow*. Hydrodynamics Laboratory Cambridge, Mass: Report. Defense Documentation Center, Cameron Station, 1964.

[38] J.W. Daily and R.E. Nece. Chamber dimension effects on induced flow and frictional resistance of enclosed rotating disks. *Journal of Basic Engineering*, 82(1):217–230, 1960.

[39] Andrew Dann, Priyanka Dhopade, and Marko Bacic. Step climb alleviation (SCA) rig report. Technical Report Unpublished, 2014.

[40] Andrew G. Dann, Steve J. Thorpe, Leo V. Lewis, and Peter Ireland. Innovative measurement techniques for a cooled turbine casing operating at engine representative thermal conditions. In *Proceedings of ASME Turbo Expo 2014*, Düsseldorf, June 2014.

[41] D. De Klerk, D.J. Rixen, and S.N. Voormeeren. General framework for dynamic substructuring: History, review and classification of techniques. *AIAA Journal*, 46(5):1169–1181, 2008.

[42] Jonathan A. DeCastro and Kevin J. Melcher. A study on the requirements for fast active turbine tip clearance control systems. Technical report, NASA Glenn Research Centre, July 2004.

[43] Air Transport Department. Fuel and air transport - a report for the european commission. Technical report, Cranfield University, 2008.

[44] C.J. Elkins and J.K. Eaton. Turbulent heat and momentum transport on a rotating disk. *Journal of Fluid Mechanics*, 402:225–253, 2000.

[45] Nicholas D. Francis Jr., Michael T. Itamura, Stephen W. Webb, and Darryl L. James. CFD calculation of internal natural convection in the annulus between horizontal concentric cylinders. Technical Report SAND2002-3132, Sandia National Laboratories, October 2002.

[46] Gene F. Franklin, J. David Powell, and Michael Workman. *Digital Control of Dynamic Systems*. Addison Wesley Longman, 3rd edition, 1997.

[47] D.K. Frederick, J.A. DeCastro, and J.S. Litt. User's guide for the commercial modular aero-propulsion system simulation (C-MAPSS). Technical Report TM-2007-215026, NASA, Cleveland, Ohio, October 2007.

[48] Sanjay Garg, Klaus Schadow, Wolfgang Horn, Hugo Pfoertner, and Ion Stiharu. Sensor and actuator needs for more intelligent gas turbine engines. In *Proceedings of ASME Turbo Expo 2010: Power for Land, Sea and Air*, Glasgow, June 2010.

[49] David H. Gay and W.Harmon Ray. Identification and control of distributed parameter systems by means of the singular value decomposition. *Chemical Engineering Science*, 50(10):1519–1539, May 1995.

[50] Manuel Girault, Laurent Cordier, and Etienne Videcoq. Parametric low-order models in transient heat diffusion by MIM. estimation of thermal conductivity in a 2D slab. *Journal of Physics: Conference Series*, 395:012019, November 2012.

[51] R.J. Goldstein and W.S. Seol. Heat transfer to a row of impinging circular air jets including the effect of entrainment. *International Journal of Heat and Mass Transfer*, 34(8):2133–2147, 1991.

[52] Sofia Haddadi and Sébastian Poncet. Turbulence modeling of torsional couette flows. *International Journal of Rotating Machinery*, 2008.

[53] Jeroen Van Helvoort, Maarten Steinbuch, and Paul Lambrechts Ren. Analytical and experimental modelling for gain-scheduling of a double scara robot. *Proceedings of the 3rd IFAC symposium on Mechatronic Systems*, pages 61–66, 2004.

[54] Didier Henrion, Luc Reberga, Jacques Bernussou, and Florian Vary. Linearization and identification of aircraft turbofan engine models. In *Proceedings of the IFAC Symposium on Automatic Control in Aerospace*, St Petersburg, June 2004.

[55] B.R. Hollworth and R.D. Berry. Heat transfer from arrays of impinging jets with large jet-to-jet spacing. *Journal of Heat Transfer*, 100:352–357, 1978.

[56] N.X. Hou, Q.M. Yu, Z.X. Wen, and Z.F. Yue. Low cycle fatigue behavior of single crystal superalloy with temperature gradient. *European Journal of Mechanics - A/Solids*, 29(4):611–618, July 2010.

[57] Yizhe Huang, Srinath V. Ekkad, and Je-Chin Han. Detailed heat transfer distributions under an array of orthogonal impinging jets. *Journal of Thermophysics and Heat Transfer*, 12(1):73–79, 1998.

[58] W.C. Hurty. Dynamic analysis of structural systems using component modes. *AIAA Journal*, 3(4):678–685, 1965.

[59] IATA. British Airways plc annual report and accounts. (December), 2012.

[60] Frank P. Incropera, David P. DeWitt, Theodore L. Bergman, and Adrienne S. Lavine. *Fundamentals of Heat and Mass Transfer*. John Wiley and Sons Inc., 6th edition, 2006.

[61] Peter Ireland. The potential impact of propulsion technology on emissions and energy security. In Oliver Inderwildi and David King, editors, *Energy, Transport, & the Environment*, pages 435–448. Springer-Verlag, London, 2012.

[62] Peter Ireland and Terry Jones. Detailed measurements of heat transfer on and around a pedestal in fully developed passage flow. In L Tien Chang, P Carey Van, and K. Ferrell James, editors, *Proceedings of the International Heat Transfer Conference*, volume 3, pages 975–980, San Francisco, 1986. Hemisphere Publ Corp.

[63] Umesh Javiya, John Chew, Nick Hills, and Timothy Scanlon. Coupled FE-CFD thermal analysis for a cooled turbine disk. *Journal of Mechanical Engineering Science (Part C, Proc. IMechE)*, 2015.

[64] C. Johnson, D. Karampinos, D. Chen, B. Sutton, W. Olivero, and J. Georgiadis. Proper orthogonal decomposition for improved assessment of brain MR elastography: Initial results. *Proceedings 17th Scientific Meeting, International Society for Magnetic Resonance in Medicine*, Honolulu(5232):718, 2009.

[65] Paul D.A. Jones, Stephen R. Duncan, Tim Rayment, and Patrick S. Grant. Control of temperature profile for a spray deposition process. *IEEE Transactions on Control Systems Technology*, 11(5):656–667, September 2003.

[66] Hasan Karabay, Michael Wilson, and J. Michael Owen. Predictions of effect of swirl on flow and heat transfer in a rotating cavity. *International Journal of Heat and Fluid Flow*, 22(2):143–155, 2001.

[67] S. Kenjereš and K. Hanjalić. Prediction of turbulent thermal convection in concentric and eccentric horizontal annuli. *International Journal of Heat and Fluid Flow*, 16(5):429–439, 1995.

[68] P. Keshavarz and M. Taheri. An improved lumped analysis for transient heat conduction by using the polynomial approximation method. *Heat and Mass Transfer*, 43(11):1151–1156, 2007.

[69] E.H. Knight. *Knight's American Mechanical Dictionary*. Hurd and Houghton, New York, 1876.

[70] T.H. Kuehn and R.J. Goldstein. An experimental and theoretical study of natural convection in the annulus between horizontal concentric cylinders. *Journal of Fluid Mechanics*, 74(04):695–719, 1976.

[71] T.H. Kuehn and R.J. Goldstein. An experimental and theoretical study of natural convection heat transfer in concentric and eccentric horizontal cylindrical annuli. *Journal of Heat Transfer*, 100:1127–1134, 1978.

[72] Andreas Kwiatkowski, Marie-Theres Boll, and Herbert Werner. Automated generation and assessment of affine LPV models. *Proceedings of the 45th IEEE Conference on Decision and Control*, (2):6690–6695, 2006.

[73] Scott B. Lattime and Bruce M. Steinetz. Turbine current engine clearance control systems : Practices and future directions. (September), 2002.

[74] Scott B. Lattime, Bruce M. Steinetz, and Malcolm G. Robbie. Test rig for evaluating active turbine blade tip clearance control concepts. *Journal of Propulsion and Power*, 21(3):552–563, 2005.

[75] L. Laurenti, F. Marcotullio, and A. Ponticiello. Multidimensional transient conduction analysis by generalized transfer function tables. *Journal of Heat Transfer*, 119(2):238–241, 1997.

[76] D. J. Leith and W. E. Leithead. Survey of gain-scheduling analysis and design. *International Journal of Control*, 73:1001–1025, 2000.

[77] Leo V. Lewis and Marko Bacic. Rotor blade tip clearance control. *US Patent 13/050,367*, 2011.

[78] Han-Xiong Li and Chenkun Qi. Modeling of distributed parameter systems for applicationsa synthesized review from timespace separation. *Journal of Process Control*, 20(8):891–901, September 2010.

[79] Shu Qing Li and Sheng X. Zhang. A modified LPV modeling technique for turbofan engine control system. *ICCASM 2010 - 2010 International Conference on Computer Application and System Modeling, Proceedings*, 5, 2010.

[80] Jonathan S. Litt, Donald L. Simon, Richard Millar, and Daniel T. Jensen. A survey of intelligent control and health management technologies for aircraft propulsion systems. Technical Report May, NASA Glenn Research Centre, 2005.

[81] C.L. Liu, Z.Z. Lu, Y.L. Xu, and Z.F. Yue. Reliability analysis for low cycle fatigue life of the aeronautical engine turbine disc structure under random environment. *Materials Science and Engineering: A*, 395(12):218–225, 2005.

[82] G.D. Lock, M. Wilson, and J.M. Owen. Influence of fluid dynamics on heat transfer in a preswirl rotating-disk system. *Journal of Engineering for Gas Turbines and Power*, 127(4):791–797, 2005.

[83] Carl F. Lorenzo, Michael S. Holmes, and Asok Ray. Design of life extending controls using nonlinear parameter optimization. (April), 1998.

[84] Bei Lu and Fen Wu. Control design of switched LPV systems using multiple parameter-dependent lyapunov functions. In *American Control Conference, 2004. Proceedings of the 2004*, volume 4, pages 3875–3880, June 2004.

[85] Z.Z. Lu, C.L. Liu, Z.F. Yue, and Y.L. Xu. Probabilistic safe analysis of the working life of a powder metallurgical turbine disc. *Materials Science and Engineering: A*, 395(12):153–159, 2005.

[86] J. Luo and P. Bowen. Statistical aspects of fatigue behaviour in a PM Ni-base superalloy Udimet 720. *Acta Materialia*, 51(12):3521–3535, July 2003.

[87] R.H. Luppold, J.R. Roman, G.W. Gallops, and L.J. Kerr. Estimating in-flight engine performance variations using kalman filter concepts. In *Proceedings of the AIAA 25th Joint Propulsion Conference*, volume 5, July 1989.

[88] Chris Lykins, Dan Thomson, and Chris Pomfret. The air force's application of probabilistics to gas turbine engines. In *35th Structures, Structural Dynamics, and Materials Conference*, number AIAA-94-1440, April 1994.

[89] R.H. MacNeal. A hybrid method of component mode synthesis. *Computers & Structures*, 1:581–601, 1971.

[90] Rajib Mahamud and Chanwoo Park. Spatial-resolution, lumped-capacitance thermal model for cylindrical Li-ion batteries under high biot number conditions. *Applied Mathematical Modelling*, 37(5):2787–2801, 2013.

[91] John C. Mankins. Definition of technology readiness levels. Technical report, NASA, April 1995.

[92] Andrés Marcos and Gary J. Balas. Development of linear-parameter-varying models for aircraft. *Journal of Guidance, Control, and Dynamics*, 27(2):218–228, 2004.

[93] Chris Markou, Geraldine Cros, and Eunsuk Yang. US DOT form 41 airline operational cost analysis report. Technical Report March, International Air Transport Association, March 2011.

[94] R.M. Mathison, C.W. Haldeman, and M.G. Dunn. Aerodynamics and heat transfer for a cooled one and one-half stage high-pressure turbine - part I: Vane inlet temperature profile generation and migration. *Journal of Turbomachinery*, 134(1):011006, 2012.

[95] R.M. Mathison, C.W. Haldeman, and M.G. Dunn. Aerodynamics and heat transfer for a cooled one and one-half stage high-pressure turbine - part II: Influence of inlet temperature profile on blade row and shroud. *Journal of Turbomachinery*, 134(1):011008, 2012.

[96] R.M. Mathison, C.W. Haldeman, and M.G. Dunn. Aerodynamics and heat transfer for a cooled one and one-half stage high-pressure turbine - part III: Impact of hot-streak characteristics on blade row heat flux. *Journal of Turbomachinery*, 134(1):011008, 2012.

[97] C. Ménézo, H. Bouia, J.J. Roux, and J. Virgone. Adaptation of the balanced realization to the coupling of reduced order models for the modelling of the thermal behavior of buildings. *Mathematics and Computers in Simulation*, 53(4-6):395–401, October 2000.

[98] Adam H. Monahan, John C. Fyfe, Maarten H.P. Ambaum, David B. Stephenson, and Gerald R. North. Empirical orthogonal functions: The medium is the message. *Journal of Climate*, 22:6501–6514, 2009.

[99] B. Moore. Principal component analysis in linear systems: Controllability, observability, and model reduction. *IEEE Transactions on Automatic Control*, 26(1):17–32, February 1981.

[100] Noel Morris. SCA rig preliminary simulations, August 2012.

[101] W. Nunner. Heat transfer and pressure drop in rough tubes. *VDI-Forschungsheft 455*, Series B(22):5–39, 1956.

[102] J.M. Owen and R.H. Rogers. *Flow and Heat Transfer in Rotating-Disc Systems*. John Wiley and Sons Inc., New York City, New York, 1989.

[103] Bart Paijmans, Wim Symens, Hendrick Van Brussel, and Jan Swevers. Identification of interpolating affine LPV models for mechatronic systems with one varying parameter. *European Journal of Control*, 14(1):16–29, 2008.

[104] M. Potter and M. Bacic. Design and control of hardware-in-the-loop simulations for testing non-return-valve vibrations in air systems. *IEEE Transactions on Control Systems Technology*, 20(1):98–110, 2012.

[105] Muruhan Rathinam and Linda R. Petzold. A new look at proper orthogonal decomposition. *SIAM Journal on Numerical Analysis*, 41(5):1893–1925, 2003.

[106] Luc Reberga, Didier Henrion, Jacques Bernussou, and Florian Vary. LPV modeling of a turbofan engine. *IFAC Proceedings Volumes (IFAC-PapersOnline)*, 16:526–531, 2005.

[107] Roger C. Reed. *The Superalloys: Fundamentals and Applications*. Cambridge University Press, Cambridge, UK, 1 edition, 2008.

[108] Rolls-Royce. *The Jet Engine*. Rolls-Royce PLC, London, 6th edition, 2005.

[109] Reinout Romijn, Leyla Özkan, Siep Weiland, Jobert Ludlage, and Wolfgang Marquardt. A grey-box modeling approach for the reduction of nonlinear systems. *Journal of Process Control*, 18(9):906–914, October 2008.

[110] Damiano Rotondo, Fatiha Nejjari, and Vicenç Puig. Quasi-LPV modeling, identification and control of a twin rotor MIMO system. *Control Engineering Practice*, 21:829–846, 2013.

[111] Wilson J. Rugh and Jeff S. Shamma. Research on gain scheduling. *Automatica*, 36:1401–1425, 2000.

[112] Ryanair. Final annual report. Technical report, 2014.

[113] Ramadan Y. Sakr, Nabil S. Berbish, Ali A. Abd-Aziz, and Abdalla Said Hanafi. Experimental and numerical investigation of natural convection heat transfer in horizontal elliptic annuli. *Journal of Applied Sciences Research*, 4(2):138–155, 2008.

[114] C.M. Sangan, Y. Lalwani, J.M. Owen, and G.D. Lock. Fluid dynamics of a gas turbine wheel-space with ingestion. *Proceedings of the Institution of Mechanical Engineers, Part A: Journal of Power and Energy*, 228(5):508–524, 2014.

[115] Michael Sapsard (Ed.). Recommended practices for monitoring gas turbine engine life consumption. Technical Report RTO-TR-28, NATO RTO Working Group AVT-017 Report, April 2000.

[116] Jeff S. Shamma. *Analysis and Design of Gain Scheduled Control Systems*. PhD thesis, Massachusetts Institute of Technology, 1988.

[117] Jeff S. Shamma. An overview of LPV systems. In Javad Mohammadpour and Carsten W. Scherer, editors, *Control of Linear Parameter Varying Systems with Applications*, chapter 1, pages 3–26. Springer, 2012.

[118] Jeff S. Shamma and Michael Athans. Guaranteed properties of gain scheduled control for linear parameter-varying plants. *Automatica*, 27(3):559–564, 1991.

[119] Jeff S. Shamma and James R. Cloutier. Gain-scheduled missile autopilot design using linear parameter varying transformations. *Journal of Guidance, Control, and Dynamics*, 16(2):256–263, 1993.

[120] J.S. Shamma and M. Athans. Gain scheduling: potential hazards and possible remedies, 1992.

[121] Raymond P. Shreeve and J.K. Richmond. Design and operation of the BSRL pebble bed heater-windtunnel facility. (October 1966), 1966.

[122] D.L. Simon and S. Garg. Optimal tuner selection for kalman filter based aircraft engine performance estimation. *ASME Journal of Engineering for Gas Turbines and Power*, 132, July 2010.

[123] Donald L. Simon and Jeffrey B. Armstrong. An integrated approach for aircraft engine performance estimation and fault diagnoses. *ASME Journal of Engineering for Gas Turbines and Power*, 135(7):071203, July 2013.

[124] Maarten Steinbuch, René Van De Molengraft, and Aart-jan Van Der Voort. Experimental modelling and LPV control of a motion system. *Proceedings of the 2003 American Control Conference*, 2(1):1374–1379, 2003.

[125] D.G. Stephenson and G.P. Mitalas. Calculation of heat conduction transfer functions for multi-layer slabs. *ASHRAE Transactions*, 77(2):117–126, 1971.

[126] Zixiang Sun, John W. Chew, Nicholas J. Hills, Leo Lewis, and Christophe Mabilat. Coupled aerothermomechanical simulation for a turbine disk through a full transient cycle. *Journal of Turbomachinery*, 134(1):011014, 2012.

[127] Zixiang Sun, John W. Chew, Nicholas J. Hills, Konstantin N. Volkov, and Christopher J. Barnes. Efficient finite element analysis/computational fluid dynamics thermal coupling for engineering applications. *Journal of Turbomachinery*, 132(3):031016, 2010.

[128] Weehong Tan, A.K. Packard, and G.J. Balas. Quasi-LPV modeling and LPV control of a generic missile. *Proceedings of the 2000 American Control Conference. ACC (IEEE Cat. No.00CH36334)*, 5(June), 2000.

[129] Shawn C. Taylor, Bruce M. Steinetz, and Jay J. Oswald. Further characterisation of an active clearance control concept. In *43rd Joint Propulsion Conference and Exhibit*, July 2006.

[130] Shawn C. Taylor, Bruce M. Steinetz, and Jay J. Oswald. High temperature evaluation of an active clearance control system concept. In *42nd Joint Propulsion Conference and Exhibit*, Cleveland, Ohio, November 2006. NASA Glenn Research Center.

[131] Alexandros Terzis, Peter Ott, Jens von Wolfersdorf, Bernhard Weigand, and Magali Cochet. Detailed heat transfer distributions of narrow impingement channels for cast-in turbine airfoils. *Journal of Turbomachinery*, 136(9):091011, 2014.

[132] R. Tóth. *Modeling and Identification of Linear Parameter-Varying Systems; an Orthonormal Basis Function Approach.* Master of engineering, University of Pannonia, 2008.

[133] Roland Toth, Marc Van De Wal, Peter S.C. Heuberger, and Paul M.J. Van Den Hof. Lpv identification of high performance positioning devices. *Proceedings of the 2011 American Control Conference*, pages 151–158, 2011.

[134] Sebastien Tourillon. Aviation Gazette - Trent 1000 TEN makes first flight, 2015.

[135] The Sir Frank Whittle Commemorative Trust. Frank Whittle - founder of the jet age. www.frankwhittle.co.uk/ *Accessed* 16 Jan 2015.

[136] Andrew van Paridon, Marko Bacic, and Peter T. Ireland. Kalman filter development for real time proper orthogonal decomposition disc temperature model. June 2016.

[137] Andrew van Paridon, Marko Bacic, Peter T. Ireland, Christopher Barnes, and Leo V. Lewis. Reduced order transient disc temperature models for online health monitoring. In *Proceedings of ASME Turbo Expo 2014*, Düsseldorf, 2014.

[138] Andrew van Paridon, Marko Bacic, Peter T. Ireland, and Ron Daniel. Disc temperature modelling using reduced order proper orthogonal decomposition models. In *Proceedings of ASME Turbo Expo 2015*, Montreal, June 2015.

[139] Andrew van Paridon, Andrew Dann, Peter Ireland, and Marko Bacic. Design and development of a full-scale generic transient heat transfer facility (THTF) for air system validation. In *Proceedings of ASME Turbo Expo 2015*, June 2015.

[140] Etienne Videcoq, Manuel Girault, and André Piteau. Thermal control via state feedback using a low order model built from experimental data by the modal identification method. *International Journal of Heat and Mass Transfer*, 55(5-6):1679–1694, February 2012.

[141] A. Volponi. Enhanced self-tuning on-board real-time model (eSTORM) for aircraft engine performance health tracking. Technical Report CR-2008-215272, NASA, July 2008.

[142] John M. Wallace, Catherine Smith, and Christopher S. Bretherton. Singular value decomposition of wintertime sea surface temperature and 500-mb height anomalies. *Journal of Climate*, 5(6):561–576, 1992.

[143] Michael Widrich, Alok Sinha, Eva Suarez, and Brice Cassenti. Applications of neural networks to the real-time prediction of metal temperatures in gas turbine engine components. In *Proceedings of ASME Turbo Expo 2006: Power for Land, Sea and Air*, volume 2, pages 561–569, Barcelona, 2006.

[144] M.W. Wiseman and Ten-Huei Guo. An investigation of life extending control techniques for gas turbine engines. In *Proceedings of the American Control Conference*, volume 5, pages 3706 –3707 vol.5, 2001.

[145] Xijia Wu. Life prediction of gas turbine materials. In Gurrappa Injeti, editor, *Gas Turbines*, chapter 9, pages 215–282. InTech, 2010.

[146] Ali Ait Yahia and Elena Palomo Del Barrio. Thermal systems modelling via singular value decomposition: direct and modular approach. *Applied Mathematical Modelling*, 23(6):447–468, 1999.

[147] Y. Yan, M.F. Gord, G.D. Lock, M. Wilson, and J.M. Owen. Fluid dynamics of a pre-swirl rotor-stator system. 125(October 2003):641–647, 2003.

[148] D. Zheng and K.A. Hoo. Low-order model identification for implementable control solutions of distributed parameter systems. *Computers & Chemical Engineering*, 26(7-8):1049–1076, August 2002.